Synthesis and characterization of activated carbon materials for supercapacitor applications

by

Farshad Barzegar

A thesis submitted in partial fulfillment of the requirements for the degree of

DOCTOR OF PHILOSOPHY (Ph.D.) IN PHYSICS

Faculty of Natural and Agricultural Sciences

University of Pretoria

Hatfield, Pretoria

November of **2015**

Supervisor/Promoter: **Prof. N. I. Manyala**

Declaration of Originality

I, **Farshad Barzegar** declare that the thesis/dissertation, which I hereby submit for the degree **Doctor of Philosophy (Ph.D.)** at the University of Pretoria, is my own work and has not previously been submitted by me for a degree at this or any other tertiary institution.

Signature: …… Date: ……

Dedicated

With unending love, to my parents

whom encouragement have been always with me.

I am indebted to them for their support, guidance and

encouragement.

Acknowledgements

My sincere gratitude goes to my supervisor, Prof. Ncholu Manyala, who was an excellent advisor, mentor, uncle, and friend throughout my Ph.D. research. He has not only guided and assisted through getting a good experimental thesis work done but has also constructively criticized my work that enabled me to work harder in the last couple of years.

My special gratitude goes to Dr. A. Bello, Dr. J.K. Dangbegnon and Dr. D.Y. Momodu, for giving me unending assistance both in the laboratory and making my postgraduate research a success. My special thanks to them for the role they played in working extra hours on weekends and public holidays in ensuring we were able to get good results and finish up my work in record time.

I would also like to thank the rest of my group members, Ms. F. Taghizadeh, Ms. T Masikhwa, Mr. M.J. Madito, Mr. A.A. Khaleed, Mr. O. Olaniyan and Ms. F. Ugbo for their ever-reliable support and assistance they rendered.

I would also like to appreciate head of the department Prof. C.C. Theron for some part-time work he offered me within the department to enable me to supplement my finances. I will also like to thank the University for their Financial Support through the UP-Postgraduate Bursary.

I am also thankful to the great friends I made here at the Physics Department, fellow students, staff, professors who put up with me throughout my stay. I would also like to thank especially my best friends Mr. K. Ostvar and Ms. S. Taghizadeh for their love, support, and encouragement. They have been my family away from home.

I also will like to thank specially Mrs. Antoinette Buys and Dr. Andre Botha at the Microscopy Department for their assistance in getting nice SEM images, Dr. Linda Prinsloo for all the assistance with the Raman measuring equipment and Mrs. Wiebke Grote for XRD analysis. Likewise to Mrs. Suzette Seymore and Mrs. Isbe Van DerWesthuizen at the Institute of Applied Materials, South Campus laboratory for their continuous support in procurement and laboratory work.

I would like to give endless gratitude to my family for their constant prayers and encouragement that kept me standing strong in the midst of the struggle.

Abstract

The unifying theme within this work is the production of porous activated carbon (AC) materials from different carbon-containing precursors for electrochemical supercapacitors (ES) applications. The activated carbon-based ES is an emerging storage technology that promises to play an important role in meeting the rising demands from the energy sector. Thus, it is necessary to study and produce various high-quality ACs by optimizing the micro/meso-porous architecture as electrodes and also study the effect of different electrolytes on the electrochemical behavior of the produced ACs. The produced ACs which are discussed in different sections in chapter 4 show specific surface area ranging from ~300 m^2 g^{-1} to ~3000 m^2 g^{-1}, specific capacitances in the range of ~179 F g^{-1} to ~335 F g^{-1} and energy density in the range of ~15 Wh kg^{-1} to ~38 Wh kg^{-1} at a current density of 0.5 A g. Both symmetric and asymmetric devices also showed excellent long term stability and no capacitance loss after 10,000 charge discharge and the stable operating potential ranging from 1.2 V to 2 V depending on the electrolyte used. All devices kept the important property of supercapacitors which is a high power density even at low current densities. All the results presented above showed the great potential in the adoption of the synthesized activated carbon material for supercapacitor applications.

Table of Contents

List of Figures

List of Abbreviations and Symbols

Activated carbons	ACs
Aqueous asymmetric supercapacitors	AASs
Brunauer–Emmett–Teller	BET
Specific capacitance	C_s
Cell capacitance	C_{cell}
Specific capacitance according to the diffuse layer	C_D
Double layer capacitance	C_{DL}
Carbon aerogels	CAGs
Cyclic galvanostatic charge–discharge	CGCD
Composite materials	CMs
Carbon nanotubes	CNTs
Carbon nanofibers	CNFs
Conducting (electronically) polymers	CPs
Constant Phase Element	CPE
Cyclic voltammetry	CV
Chemical vapor deposition	CVD
Double-layer	DL
Double-walled carbon nanotubes	DWCNTs
Maximum energy density	E_M
Electrochemical capacitors	ECs

Electrical double-layer capacitors	EDLCs
Equivalent distributed resistance	EDR
Expanded graphite	EG
Electrochemical impedance spectroscopy	EIS
Equivalent series resistance	ESR
Galvanostatic charge/discharge	GCD
Hybrid Electrochemical Capacitors	HECs
High-pressure carbon monoxide disproportionation	HiPco
Multi-walled carbon nanotubes	MWCNTs
Maximum power density	P_M
Polyaniline	PANI
Poly(3,4-ethylenedioxythiophene)	PEDOT
Polypyrrole	PPy
Pore size distribution	PSD
Polythiophene	PT
Polytetrafluoroethylene	PTFE
Polyvinylidene fluoride	PVDF
Charge transfer resistance	R_{CT}
Polarization Resistance	R_P
Solution (electrolyte) resistance	R_S
Ohmic resistance	R_Ω
Supercapacitors	SCs

Saturated calomel electrode	SCE
Specific surface area	SSA
Redox Electrochemical Capacitors	RECs
Warburg Impedance	W

CHAPTER 1

INTRODUCTION

1.1 BACKGROUND AND GENERAL MOTIVATION

The humanity problem today (increasing population) is associated with increasing consumption and demand for energy, which has left the energy sector with a huge challenge of meeting the increased demand for energy due to the ever-expanding population. Thus, energy research technologies have become an important area of focus in the global scientific community. Fossil fuels are the primary sources for many energy systems, however, in many countries the fossil fuels are being depleted leaving the energy sector with the search for alternative sources of energy that are renewable and cost effective. Secondly, this source of energy is associated with environmental degradation and may cause a hazard to human life. Hence, decreasing the use of fossil fuel that leads to the emission of greenhouse gas has become global objectives in all society. Thus, to achieve this goal, the use of renewable energy sources that can be easily restored by a natural process and further improves the energy efficiency is the most promising solution. Renewable energy technology sources like solar and wind energy are becoming interesting and promising energy sources that have large fluctuations in the generation of electricity. Various exciting renewable technologies are being developed, and they include

mechanical, thermal, physical, chemical and electrochemical energy storage systems.

Today batteries (such as lithium-ion or nickel–metal hydride) that have high energy density and electrochemical capacitors (ECs) that have high power density are the common energy storage devices. Thus, an efficient, high performance, low cost and environmentally safe all-in-one energy storage system that combines the properties of the batteries and capacitors is required. Furthermore, hybrid systems of the two devices might play complementary functions when they are combined with each other [1] and can give us a storage system with high energy and high power densities.

Electrochemical capacitors (ECs) are emerging technologies with a promising future for energy storage. Scientists have studied ECs for the past few decades. In 1957, capacitor based on high surface area carbon was described by Becker [2]. Figure 1-1 shows the reason ECs were able to gain significant attention in the scientific community. The figure presents the energy storage and conversion devices visualized in so-called ‘Ragone plot’ regarding their specific energy and specific power. ECs fills the gap (regarding specific energy as well as specific power) between batteries and conventional capacitors [3].

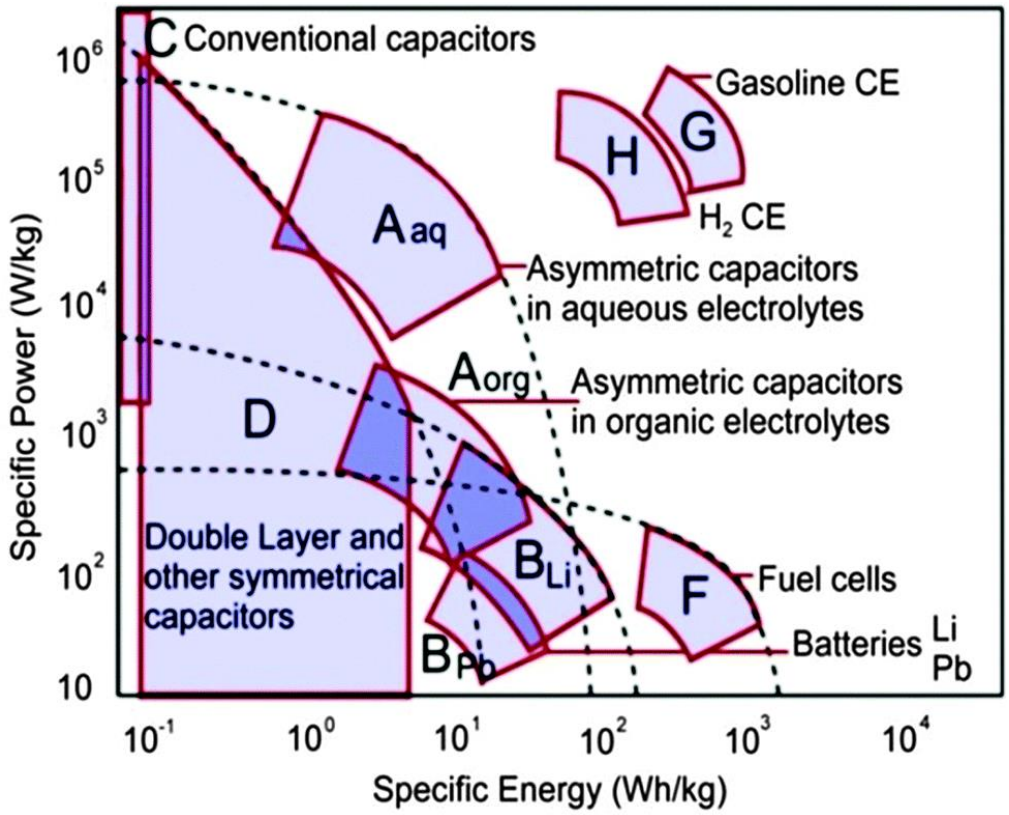

Figure 1-1 Sketch of Ragone plot with specific energy and power for different energy storage devices [4]

The initial benefits of ECs are that they offer excellent power capability (60–120 s is typical) offering solutions for energy storage and delivery applications in power systems and extended cycle life (>10^5). Normally they present 20–200 times higher capacitance per unit volume or mass than conventional capacitors [5]. Nevertheless, the energy density of the ECs is still small when compared with battery with an order of magnitude less. Hence, scientists focus on the fabrication of ECs devices that can match or compete with the batteries regarding specific energy and long cycle life. Improving the energy density and power density of ECs, scientist search for new

electrode materials, new electrolytes and new electrochemical concepts to meet the increasing demand [1,5–7].

ECs can be classified into two, namely; electrical double-layer capacitors (EDLCs) and faradaic capacitors [5] based on their mode of energy storage and the materials used for their fabrication. The EDLCs mainly focus on the use of different allotropes of carbon materials as electrode [8–10], while faradaic capacitor materials include a metal oxide and hydroxide [11,12], conductive polymers [13,14] and functionalized carbon [15].

Porous carbon materials are the usual materials for EDLCs because they have large specific surface area (SSA) [16,17], high electrical conductivity [18], different micro- and mesopores texture that are suitable for various electrolytes [1], highly stable giving rise to long cycle life [9] and enhanced capacitance values. For industrial applications, low cost and abundant availability of these porous carbons are necessary for use as electrode materials in EDLCs. Also, microporous carbons materials are available in a different form such as powders, fibers, cloths, monoliths, nanotubes, nanospheres and so on [1] and this availability helps the engineer to match the material in the correct form for a specific design. All the above reasons make microporous carbons the best and suitable candidate for ECs applications. This research work describes the design of microporous carbons from different precursors and electrochemical capacitor studies based on the produced carbon electrodes, with the main objective of enhancing the capacitance, potential voltage and the energy density of the device with a long cycle life.

Activated carbons (ACs) are forms of microporous carbon and have attracted great attention as an electrode material for ECs due to their highly porous nature, high SSA, chemical stability, relatively low synthesis cost, adjustable structural properties, and electrical conductivity [19]. The cost-effective and synthesis method for production of large amounts of ACs with high SSA is through chemical and physical activation technique from carbon containing materials such as polymers or natural biomass materials [16,20–22]. The chemical process leads to the formation of aerogel or hydrogel materials while the physical activation leads to the formation of porous ACs and is usually done with potassium hydroxide (KOH), zinc chloride ($ZnCl_2$) and phosphoric acid (H_3PO_4) [23,24]. Thus, for EDLCs purposes, it is necessary to produce high-quality ACs by optimizing the micro/meso-porous architecture as an electrode, study various carbon materials sources for the production of ACs and the effect of different electrolytes on the electrochemical behavior of ACs.

1.2 AIM AND OBJECTIVES

The aim and objectives of this research are divided into three parts as follows:

1. Synthesis and characterization of activated carbon (AC) for high-performance electrochemical capacitors from different carbon sources which includes:
    - Hydrothermal and chemical vapor deposition (CVD) synthesis and characterization of AC based on polymers and graphene foam for high-performance electrochemical capacitors.

- Effect of different carbon material on polymer based AC and their applications in high-performance supercapacitors electrodes
- Synthesis and characterization of eco-friendly supercapacitor electrodes based on AC derived from pine tree cones.
- Synthesis and characterization of new AC from expanded graphite (EG) for high-voltage supercapacitors.

2. Study the effect of different electrolytes on the electrochemical behavior of supercapacitors based on AC such as:
   - Effect of different aqueous electrolytes on AC based supercapacitors.
   - Effect of different gel electrolytes on AC supercapacitors.

3. Preparation and characterization of AC cathode material and α-MoO_3 transition metal oxide as anode material for high-performance asymmetric supercapacitors.

1.3 OUTLINE OF THESIS

The thesis is divided into five chapters:

Chapter 1 presents a general introduction of the energy storage systems, the aim and the objective of the study.

Chapter 2 presents a literature review on electrochemical capacitors.

Chapter 3 presents the growth and characterization techniques used in this study. Chapter 4 presents the results obtained and detailed discussion of the results. A summary and conclusions from each experimental result will be presented in different sections of Chapter 4.

Chapter 5 contains general conclusions and details of future work to be performed in this study.

CHAPTER 2

ELECTROCHEMICAL CAPACITORS

Electrochemical capacitors (ECs) also called supercapacitors (SCs) or ultracapacitors [25] store energy (charge) in the electric field of the electrochemical double-layer [3,5,26]. ECs possess excellent electrochemical properties such as; cycling performance, high rate capability and long lifespan thus considered as a promising candidate for energy storage [27].

The basic block of the ECs and batteries is an electrochemical cell that combined two active electrodes, one positive and one negative, separated by a separator such as microporous membrane or filter paper and sandwiched between two current collectors (leads) [28,29] as shown in Figure 2-1. The current collectors must be electronically conducting and ensure electrons transfer from and to the active electrodes. The separator must be electronically isolating to avoid self-discharge, but ionically conducting to allow the movement of ions through it during the charge and discharge time [30]. Active electrode materials inside the electrochemical cell are under electrochemical reactions; the electrodes are ionically connected to the separator and electronically connected to the current collector. The separator and the active masses need an ionically-conducting medium (electrolyte). The whole unit is generally contained in a sealed container [28,30].

Figure 2-1 Electrochemical cell schematic part

In the device setup shown above, each electrode-electrolyte interface represents a capacitor so that the complete cell can be considered as two capacitors in series. For a symmetrical capacitor (similar electrodes), the cell capacitance (C_{cell}), will therefore, be [23]:

$$\frac{1}{C_{cell}} = \frac{1}{C_1} + \frac{1}{C_2} \qquad 1$$

Where, C_1 and C_2 represent the capacitance of the first and second electrodes, respectively. The capacitance, measured in Farad (F), is defined as the ratio of total charge in Coulomb (Q) in each electrode to the potential difference (V) between the plates [28]:

$$\boldsymbol{C = \frac{Q}{V}} \qquad \textbf{2}$$

The capacitance is also proportional to the surface area (A) of the plates and inversely proportional to the distance (d) between the plates multiplied by a permittivity constant ε_0 (8.8542×10^{-12} C^2 Nm^{-2}) [28]:

$$\boldsymbol{C = \frac{\varepsilon_0 A}{d}} \qquad \textbf{3}$$

Also, the double layer capacitance at each electrode interface is given by [23]:

$$\boldsymbol{C = \frac{\varepsilon A}{4\pi d}} \qquad \textbf{4}$$

Where **ε** is the dielectric constant of the electrical double-layer region, **A** the surface area (cm^2) of the electrode and **d** is the thickness of the electrical double layer (cm). The stored energy of the capacitor in joules (J) is proportional to the capacitance (C) and voltage (V) square across the plates [28]:

$$\boldsymbol{E = \frac{1}{2} C V^2} \qquad \textbf{5}$$

It should be noted that the energy equation assumes that the initial voltage of the capacitor is zero. If the voltage is not zero, then the energy equation becomes [28]:

$$\boldsymbol{E_1 - E_2 = \frac{1}{2} C(V_2^2 - V_1^2)} \qquad \textbf{6}$$

Where V_2 is the final voltage and V_1 is the initial voltage.

2.1 CLASSIFICATION OF ELECTROCHEMICAL CAPACITORS

ECs may be classified by some criteria such as the electrical energy storage mechanisms, the electrode material utilized, the electrolyte or the cell design [3,5]. In this section, we give a brief description of each.

2.1.1 Electrical energy storage mechanisms

Depending on the charge-storage mechanism, ECs can be classified as follows [5]:

- Electric Double Layer Capacitors (EDLCs)
- Redox Electrochemical Capacitors (RECs) or faradaic capacitors
- Hybrid Electrochemical Capacitors (HECs)

The materials used for the fabrication of ECs devices include different forms of carbon [8–10], transition metal oxides [11,12], and conductive polymers [13,14]. The EDLCs mainly focus on the use of carbon materials which store energy by the charge separation at the electrode/electrolyte interface, while faradaic capacitors materials include metal oxide, conductive polymers and doped carbon [15], which not only store energy like an EDLC, but also in the appropriate potential window represent electrochemical faradaic reactions between electrode materials and ions [5]. Figure 2-2 presents an overview of each of these classes of electrochemical capacitors with their sub-groups and common electrode materials.

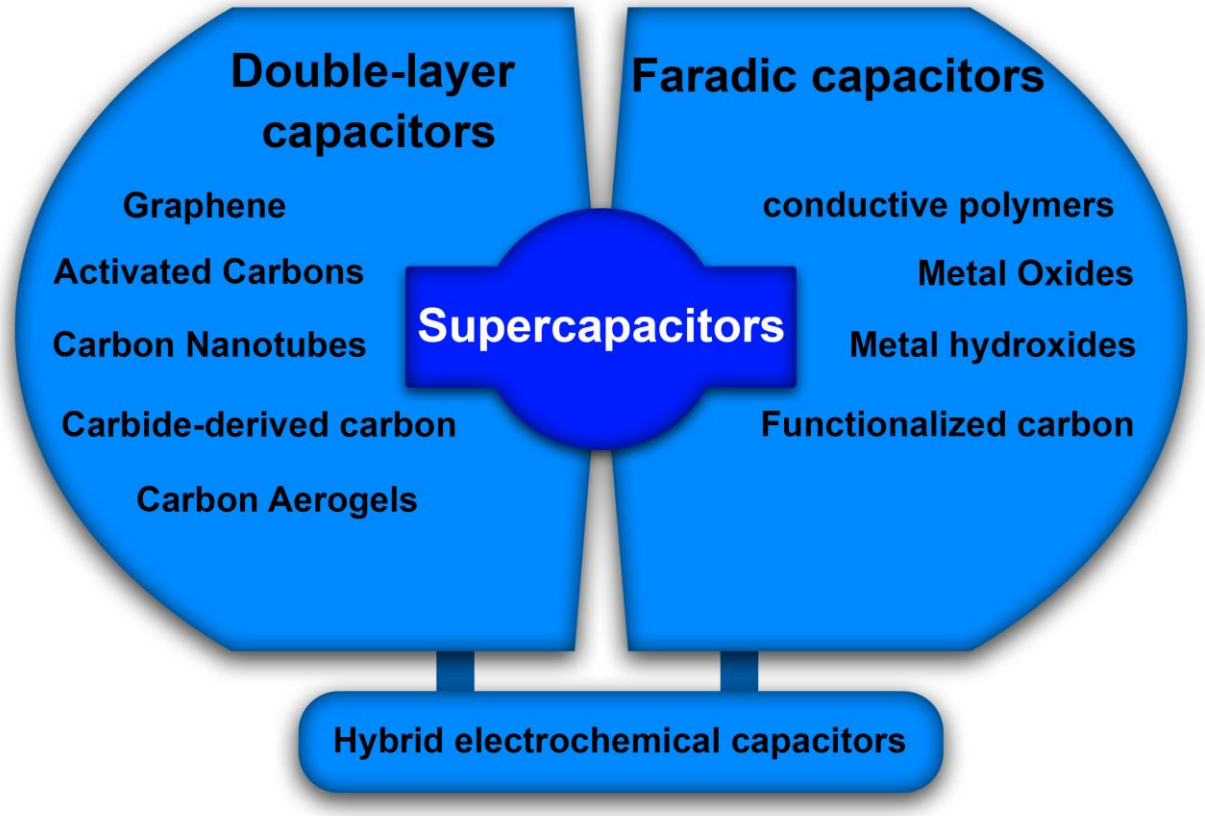

Figure 2-2 Classification of electrochemical capacitors depending on the charge-storage mechanism

2.1.1.1 EDLCs

The energy storage of EDLCs is generally based on the electric charge stored by adsorption of electrolyte ions directly across the double-layer (DL) of the electrode, in other words, EDLCs store the energy based on pure electrostatic charge accumulation at the electrode/electrolyte interface [5,31]. EDLCs show the true capacitance effect because there are no charge transfer and reduction–oxidation

reactions across the interface which can store or supply charges by non-Faradaic processes. The specifications of the EDLCs are dependent on the surface structure of the electrode, the electrolyte and the potential field between the charges at the interface [32]. The mechanism of surface electrode charge generation includes surface dissociation as well as ion adsorption from electrolyte and crystal lattice defects [5]. The ions distributed across the separator and align themselves uniformly on the pores of the whole active surface, thus creating an electric field that allows the storage of energy in the capacitor. Therefore, high surface areas and pores adapt to electrolyte ion sizes that are necessary for EDLCs [33]. Figure 2-3 represent the schematic illustration of simple EDLCs energy storage method.

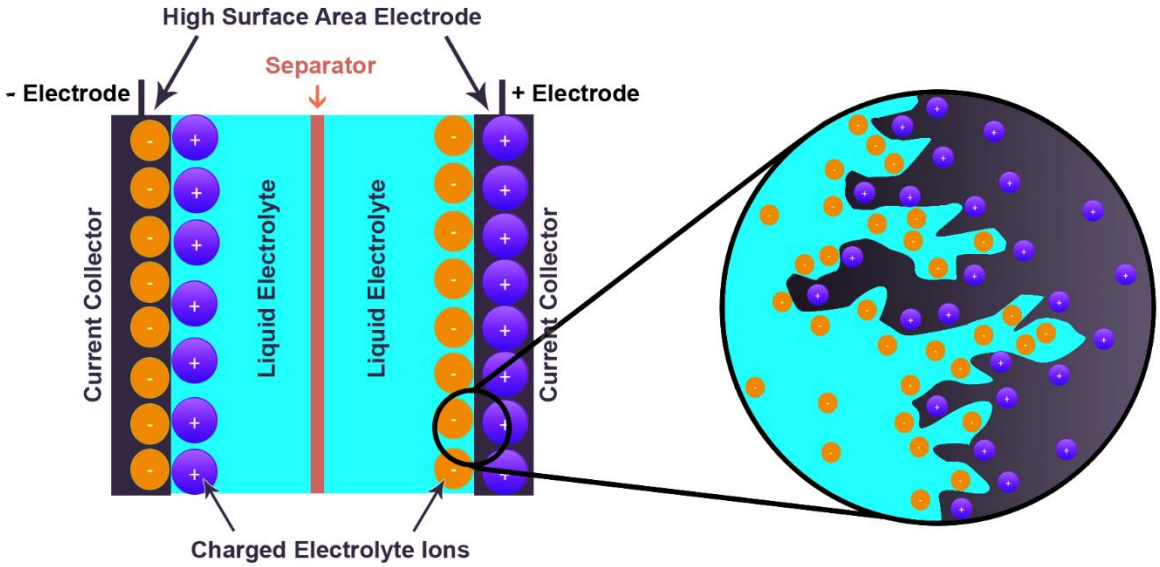

Figure 2-3 Schematic Illustration of simple EDLCs energy storage method

When adsorption of electrolyte ions starts at the surface of active materials, two phases appear. Hermann von Helmholtz described the model to explain this behavior in EDLCs [34,35]. This model is similar to the conventional dielectric capacitors with two metal planar electrodes. When the electrode surface get an excess or deficiency of charge, the ions of the opposite charge build at the wall near the electrode/electrolyte interface to provide electroneutrality (see Figure 2-4 (a)) [36]. The thickness of the Helmholtz DL depends on the concentration of the electrolyte and the size of ions [5].

By increasing the distance d (m) between the ions and the electrode (Figure 2-4 (a)) the potential in the vicinity of the electrode decreases. This simplified Helmholtz DL can be considered as an electrical capacitor of capacitance C_H defined by Equation (7) [1]:

$$\boldsymbol{C_H = \varepsilon_0^* \varepsilon_r S / d} \qquad \textbf{7}$$

Where $\boldsymbol{\varepsilon_0^*}$ is the vacuum permittivity ($\boldsymbol{\varepsilon_0^*}$ = 8.854·10^{-12} F m^{-1}), $\boldsymbol{\varepsilon_r}$ the relative permittivity of the dielectric electrolyte ($\boldsymbol{\varepsilon_r}$ is assumed as 10 for the water in the DL), d is the effective thickness of the DL, and the S is the surface area. The corresponding electric field in the electrochemical DL is as high as 10^6 V/cm [1,3,5].

Diffusion of ions in the solution and the interaction between the dipole moment of the solvent and the electrode is not taken into account in the Helmholtz model .Gouy and Chapman proposed a diffusion model of the EDL. This model treats the ions as point charges so that the ions' movements in the electrolytes are driven by the influence of

diffusion [37] (Figure 2-4 (b)). The diffuse charge is determined by the Poisson-Boltzmann equation in the Guoy-Chapman theory. The specific capacitance according to the diffuse layer, C_D, can be evaluated as [37]:

$$C_D = \left(\frac{n_0 \varepsilon e_0^2}{2\pi kT}\right)^{1/2} cosh \frac{e_0 V}{2kT} \qquad 8$$

Where n_0 is the number of ions in the bulk electrolyte, V is the potential drop between the electrode and the bulk electrolyte, e_0 is the charge of the ion, k is the Boltzmann constant, ε is the dielectric constant in the electrolyte, and T is the temperature.

The Gouy-Chapman model, however, failed for highly charged double-layers, and because of this in 1924, Stern proposed a model combining the Helmholtz and Gouy-Chapman models by taking into account the hydrodynamic motion of the ionic species in the diffuse layer and the accumulation of ions close to the electrode surface (Figure 2-4 (c)) [1].

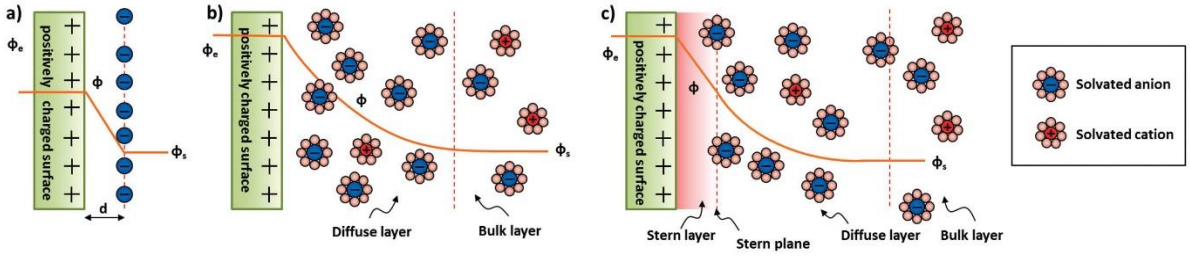

Figure 2-4 (a) Helmholtz, (b) Gouy-Chapman, and (c) Stern model of the electrical double-layer formed at a positively charged electrode in an aqueous electrolyte [1].

These two layers are equivalent to two capacitors in series, C_H (Stern layer) and C_D (diffuse layer), and the total capacitance of the electrode (C_{DL}) can be expressed as Equation (9) [1]:

$$\frac{1}{C_{DL}} = \frac{1}{C_H} + \frac{1}{C_D} \quad (9)$$

In an ideal EDLCs system, since there is no charge transfer between the electrode and electrolyte interface, there are no chemical or compositional changes associated with them and the electrolyte concentration and properties should remain the same while charging and discharging [6].

2.1.1.2 Faradaic capacitance

In 1971, a new type of electrochemical capacitance was discovered in ruthenium dioxide (RuO_2), called pseudocapacitance because that active material behaved like a capacitor, but not like an EDLCs and it involved faradaic charge-transfer reactions [38,39]. Faradaic capacitors or Redox Electrochemical Capacitors (RECs) store charge through the transfer of charges between the electrode and electrolyte Faradaically [5]. Different Faradaic mechanisms can occur in electrochemical charge storage in faradaic capacitors, and these include; electrosorption (underpotential deposition), reduction-oxidation reactions (redox pseudocapacitance) and intercalation (intercalation pseudocapacitance) [40]. These processes are illustrated in Figure 2-5 [38].

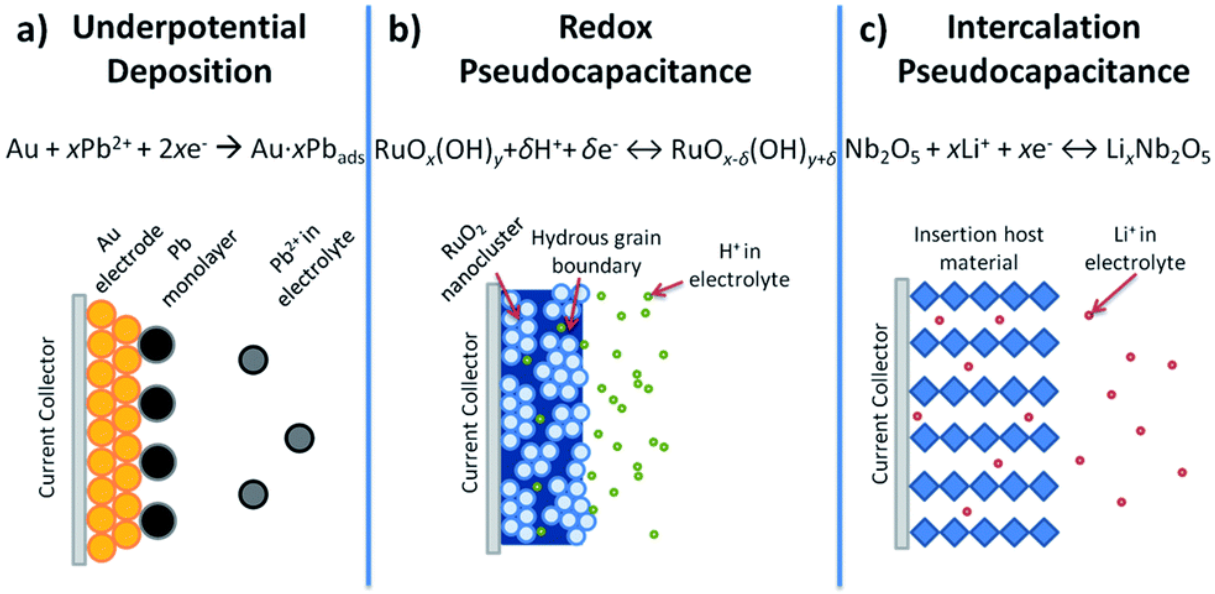

Figure 2-5 Schematic showing different types of reversible redox mechanisms that give rise to faradaic capacitance (pseudocapacitance) [33].

Underpotential deposition occurs when the onset of deposition of metal adatoms (adsorbed atom [41]) at various types of substrates in potential ranges positive to the reversible equilibrium potential (also referred to as the Nernst potential) [42]. A classic example of underpotential deposition, is the deposition of lead (Pb) on the surface of a gold (Au) electrode [43], while redox pseudocapacitance occurs when the electrochemical adsorption of ions near surface or onto the surface of a material with a concomitant Faradaic charge-transfer [38] (for example, surface redox reactions as in RuO_X [44]). Intercalation pseudocapacitance happens when ions intercalate into the pores or layers of a redox-active material accompanied by a Faradaic charge-transfer with no crystallographic phase change [38]. Underpotential

deposition and redox pseudocapacitance represent charge storage on the surface, however, in intercalation pseudocapacitance, charge storage does not occur on the surface but in the bulk material [44].

The remarkable difference between compatible materials for Faradaic capacitors and batteries are in the surface reactions, the charging and discharging behavior of faradaic capacitive materials which happens on the order of seconds and minutes. Battery materials utilize the bulk solid state to store charges that give them their high energy densities while faradaic capacitive materials are not limited by solid state diffusion, and the utility of energy storage is based on a kinetic behavior [38]. Figure 2-6 shows capacitive and non-capacitive Faradaic charge storage.

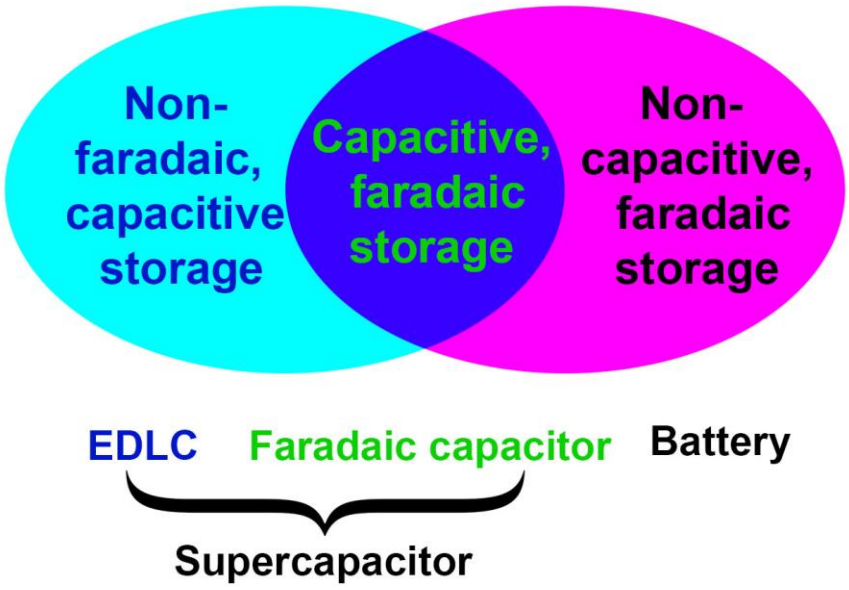

Figure 2-6 Capacitive and non-capacitive Faradaic charge storage

The most usually studied faradaic capacitors or Faradaic-like electrode [39] materials are transition metal oxides [6,45,46], transition metal hydroxides [47–49], transition metal nitrides [50,51], carbon material enriched with oxygen/nitrogen-containing functional groups [52,53], etc. A higher capacitance is observed for some of these materials as compared to EDLCs due to the Faradaic charge transfer process that takes place at the electrode surface. However, they have low power performance due to poor electrical conductivity and lower cycling stability when compared to pure EDLCs materials [54].

2.1.1.3 Hybrid electrochemical capacitors

Hybrid electrochemical capacitors (HECs) combine properties of both EDLCs and faradaic capacitors with an asymmetrical configuration. HECs can bridge the gap between ECs and batteries because they have higher power density than Li-ion batteries and higher energy density than ECs [5].

2.1.2 Electrode materials for ECs

The important parameters for selection of electrode materials for ECs are the following: (1) high SSA, important for the large capacitance, (2) small pore size, short pore length, and straight pathways pore connectivity for the high-speed ions diffusion, (3) low internal electric resistance to enable fast charging-discharging and low ohmic resistance, (4) low volume and weight, (5) low price and (6) environmentally friendly materials [5]. These materials section is divided into three

parts: electrode materials for EDLCs, electrode materials for faradaic capacitors and composite materials.

2.1.2.1 Electrode Materials for EDLCs

Carbon-based material such as activated carbons (ACs) [55], carbon aerogels (CAGs) [56], graphite's [57], graphene [58,59], carbon nanotubes (CNTs) [60], carbon nanofibers (CNFs) [61] and nano-sized carbon [62] have been examined as the electrode materials for EDLCs because of their accessibility, relatively low cost, non-toxicity, high chemical stability, good electronic conductivity and wide temperature range [5,30,63]. Carbon materials are available in a different form (powders, woven cloths, felts or fibers) with a specific surface area up to ~3500 $m^2 g^{-1}$. In general stability and conductivity of the porous carbon decrease with increasing surface area [3], the carbon structure including pore shape, surface functional groups, and electrical conductivity has to be considered for EDLCs. Based on carbon materials, different techniques have been used to increase their specific surface area (SSA) or improve on their pore size distribution (PSD) [5]. According to the energy storage mechanism of EDLCs, the SSA of carbon-based materials plays an important role. It is noted that to get higher specific capacitance, high SSA materials are needed. However, the main problem of high SSA carbon is that not all the Brunauer–Emmett–Teller (BET) surface area is electrochemically accessible when in contact with the electrolyte, meaning that the gravimetric capacitance of different carbon materials does not increase linearly with the SSA. Microporous carbon with a high

SSA is effective to obtain a high capacitance with a relatively slow charge–discharge, however, to obtain a high rate performance, the negative electrode carbon should have a relative amount of mesopores [5].

2.1.2.1.1 Activated carbon

One of the major attractions of using carbon as an electrode material is that it can be converted into different forms with very high SSA. Generally, the process engaged to increase surface area and porosity from a carbonized organic precursor is known as activation and the resulting groups of materials are referred to as activated carbons (ACs) [23]. Changing activation conditions, particularly such as temperature, time and gaseous environment, and the carbon precursor allow some control over the resulting porosity, pore-size distribution and the nature of the internal surfaces. The ACs materials are commercially available and have proven to have applications in water treatment [64,65], CO_2 capture [66], energy storage [23], and most typically heterogeneous catalysis [67,68]. Briefly, the processes of the activation of commercial carbons can be placed into two general categories; physical (Thermal) activation and chemical activation [23].

Physical (Thermal) activation uses hot gases to develop the structure into ACs. Physical activation is generally done by using one or a combination of the following steps: the first one is the carbonization, so-called pyrolysis of carbonaceous material at high temperature (~500-1100 °C) in an inert atmosphere to remove the maximum

of oxygen and hydrogen elements from the reaction chamber. The second one is the thermal activation at the same temperature as for pyrolysis or at a higher temperature in the presence of oxidizing gas such as steam, carbon dioxide, air or mixtures of these gases [23,24].

Chemical activation usually needs lower temperatures (~400-800 °C), and it is possible to make ACs in a single step. Pyrolysis and activation are carried out concurrently in the presence of dehydrating agents such as phosphoric acid (H_3PO_4), sulfuric acid (H_2SO_4), zinc chloride ($ZnCl_2$) and potassium hydroxide (KOH) [23,24]. This process can give high porous carbons with a high specific surface area (SSA) of over 2500 $m^2\ g^{-1}$. Remarkably high specific surface area materials (>2500 $m^2\ g^{-1}$) have been prepared with KOH activation techniques [23]. KOH activation has been known since 1978. The pore microstructures of ACs depend on the activation parameters (such as the mass ratio of KOH/carbon, activation temperature, and time) and carbon sources used as precursors to produce the ACs [21]. Figure 2-7 shows a scanning electron microscopy image of the activated carbon material.

ACs can be prepared from many carbon sources such as organic materials that they have a high carbon content, for example, wood [69], coal [70] and coconut shells [71,72]. In the recent years, many other carbon sources have been used for ACs production such as waste tea-leaves [73], potato starch [74], fish scale [75], waste coffee beans [76], etc. The main commercial producers of ACs in the world are Egypt, Iran, Saudi Arabia, United Arab Emirates, Pakistan, Algeria and other Mediterranean countries [24].

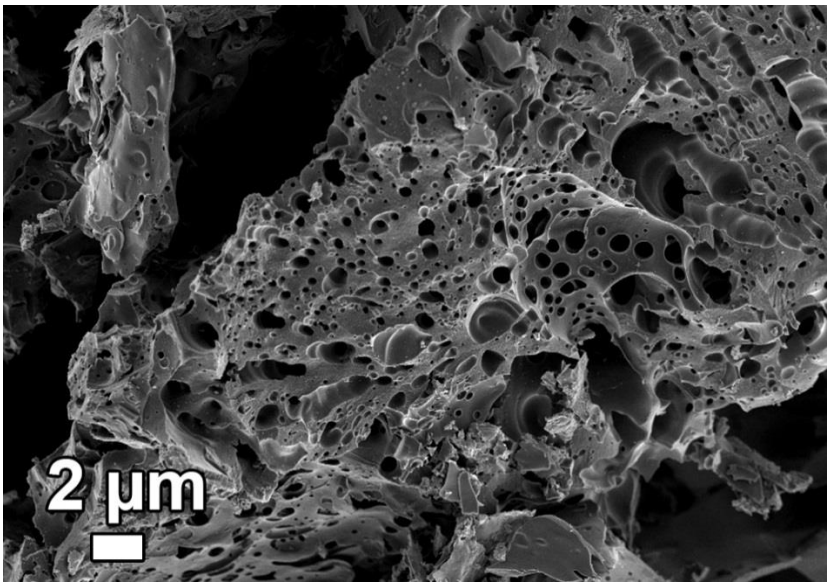

Figure 2-7 Scanning electron microscopy image of activated carbon

Carbon has different allotropes depending on the hybridization. Graphitic carbon has graphene layers that are settled parallel to each other in a three-dimensional crystalline network [77]. Non-graphitic carbon does not have a long-range three-dimensional network, even if it has been made in graphitization process. Franklin (in the 1950s) showed that the non-graphitic carbon material can be classified into two types, which are graphitized and non-graphitized carbon material [78]. Schematic representation of these non-graphitic carbons is shown in Figure 2-8 (a) and (b). The basic structural characters of ACs are close to the structural properties of pure graphite. The graphite crystal is formed by layers of bonded hexagons held approximately 0.335 nm apart by van der Waals forces (Figure 2-8 (c)).

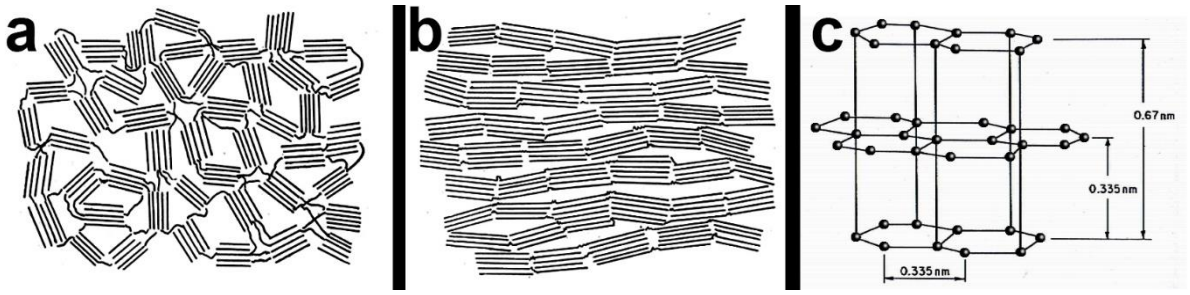

Figure 2-8 Schematic representation of the structure of (a) a non-graphitized carbon, (b) a graphitized (but non-graphitic) carbon [73] and (c) carbon atom arrangements in graphite crystal

However, the structure of the ACs can be different from the structure of graphite. The structure of ACs is totally disorganized compared to the graphite because of random oxidation of graphite layer. During the carbonization process, some aromatic nuclei with a structure similar to that of graphite are formed [79]. Carbon from ACs are non-graphitized, meaning that it cannot be converted into crystalline graphite even at temperatures of 3000 °C and above [80]. The non-graphitized carbons are shaped, normally, from materials containing little hydrogen or much oxygen in their structure. By heating these materials at low temperatures, one can create a strong system of cross-linking, which immobilizes the structure and unites the crystallites in a rigid mass. The random orientations of crystallites with crosslinking make up a porous structure [78].

ACs contains two types of admixtures: Inorganic part of the carbon source that is called ash after activation and chemically bonded elements which make the organic

structure with the carbon atoms. The chemically bonded structures, mainly oxygen and hydrogen elements. These structures remained in the ACs structure during carbonization or make chemical bonding to the surface during activation. Other atoms apart from the carbon atom into the network and on the surface of the ACs have a significant key role in the chemistry of ACs by influencing the adsorption properties [81]. The different behavior of the different ACs comes from the several surface functional groups which are formed by the interactions of the free radicals during carbonization and activation. Mainly oxygen and hydrogen containing functional groups are present on the surface of the ACs [82]. In the structure of ACs, carbon atoms at the edges of the basal planes are unsaturated because of the unpaired electrons [83] and the ratio of the edge to basal plane carbon atoms can be as high as 10-20% [84] and that causes a strong tendency for oxygen chemisorption. The chemisorbed area increases by chemical bonding of other atoms such as oxygen apart from the carbon atom and thus the surface functional groups have an effect on the surface characteristics and physicochemical properties of the ACs [85]. The amount of the oxygen generally decreases with increasing the activation temperature. The most common oxygen-containing surface functional groups found on carbon surfaces are given in Figure 2-9. Carbon source materials also have hydrogen in the form of hydrocarbon chain and rings that are attached to the edge atom of hexagon planes. Most of the hydrogen is removed from the structure of carbon during the carbonization time below 950 °C.

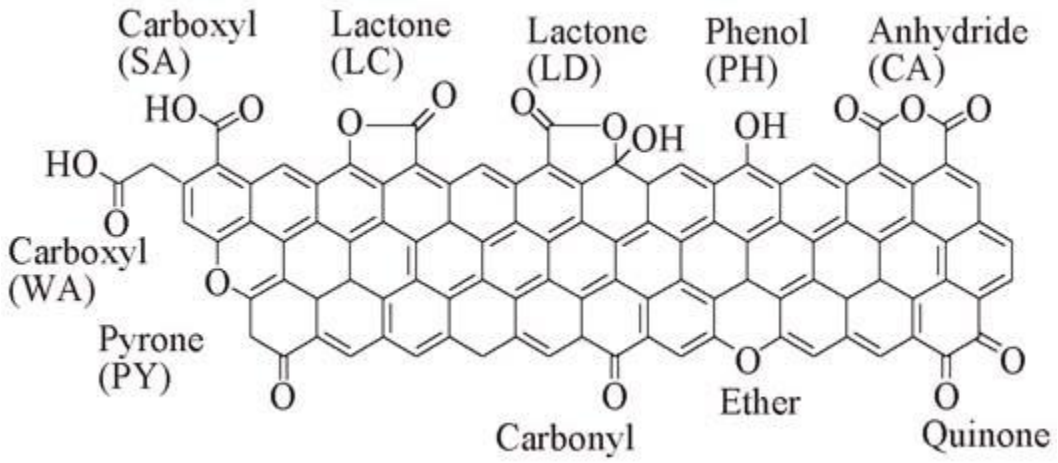

Figure 2-9 Oxygen Functional Groups on Carbon Surfaces [86]

ACs can be produced with different porous structure and relatively low density which is generally less than 2 g cm^{-3}. The International Union of Pure and Applied Chemistry (IUPAC) classified pores according to their size as follows [87]:

- Micropores (nanopores): smaller than 2 nm
- Mesopores: between 2 and 50 nm
- Macropores: larger than 50 nm

The pores of ACs can be in the shape of capillaries as shown in Figure 2-10. The macropores do not contribute to adsorption capacity and surface area of the adsorbent remarkably [87]. However, they are important in the kinetics of adsorption. The macropores act as broad transport arteries in the adsorption process with a minimum diffusional resistance [88,89].

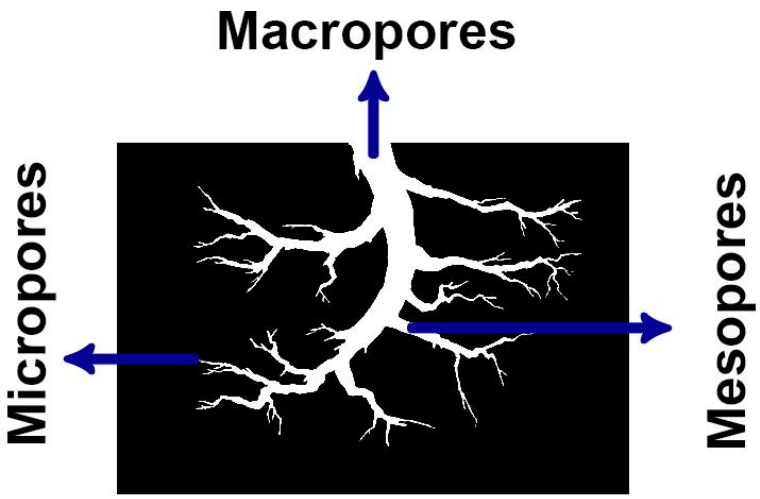

Figure 2-10 Pore Structure of Activated Carbon

The mesopores act as a transitional pore between the macropores and micropores. Usually, the surface area of AC is a combination of the micropores, mesopores, and macropores in the material. However, changing the parameters during the activation and carbonization can lead to ACs with different micropores, mesopores, and macropores area [87]. The micropores play an important role in the determination of the surface area and adsorption capacity of the material. Because of the proximity of the pore walls in micropores compare to the others, the interaction potential between adsorbent and adsorbate is higher than the other pores, therefore at a given relative pressure the amount of gas adsorbed is enhanced. Micropores and mesopores in ACs play a key role in the charge/discharge process of EDLCs as discussed above [90,91]. Earlier reports by Conway [40] showed that the larger pore sizes correspond

to higher power densities while smaller pore sizes correspond to higher energy densities.

2.1.2.1.2 Graphene

Graphene, discovered in 2004 [92,93], is a single flat layer of carbon atoms packed into honeycomb lattice and is regarded theoretically as the basis for the formation of all other sp^2 allotropes of carbon. It's unique and amazing properties such as excellent electronic transportability, great mechanical strength, large surface area (~2630 m^2 g^{-1}), tunable band gap, excellent optical characteristics and thermal conductivity (~3000 W mK^{-1}) [94–96], etc., has made it an exciting and suitable candidate for many applications [97,98]. Graphene can be synthesized by several methods such as Hummer's method [16,99], dispersion method [100], microwave method [101], chemical vapor deposition (CVD) method [102] and etc. The excellent theoretical surface area and the other amazing properties of graphene have made it suitable as a potential electrode material for EDLCs. However, the graphene synthesized by the above-mentioned methods in reality, supplied low capacitance performance, which cannot be adopted for practical applications [58,59,103]. For that reason, researchers adopted to doping graphene [104] or make a composite of graphene with a conductive polymer [105] or some oxide materials [106] to improve the electrochemical behavior of the materials.

2.1.2.1.3 Carbon nanotubes

Another allotrope of carbon is carbon nanotubes (CNTs). Theoretically, graphene can be rolled at certain axis to produce single-walled carbon nanotubes (SWCNTs) [107]. CNTs have one of the highest strength to weight ratios of any known material and are chemically and thermally resilient [108]. Some of the techniques that can produce CNTs are: arc discharge [109], laser ablation [110], high-pressure carbon monoxide disproportionation (HiPco) [111] and CVD [112,113]. Large amounts of CNTs can be synthesized by CVD method [114] as shown in Figure 2-11. CNTs can be produced as SWCNTs, double-walled carbon nanotubes (DWCNTs) and multi-walled carbon nanotubes (MWCNTs) [115].

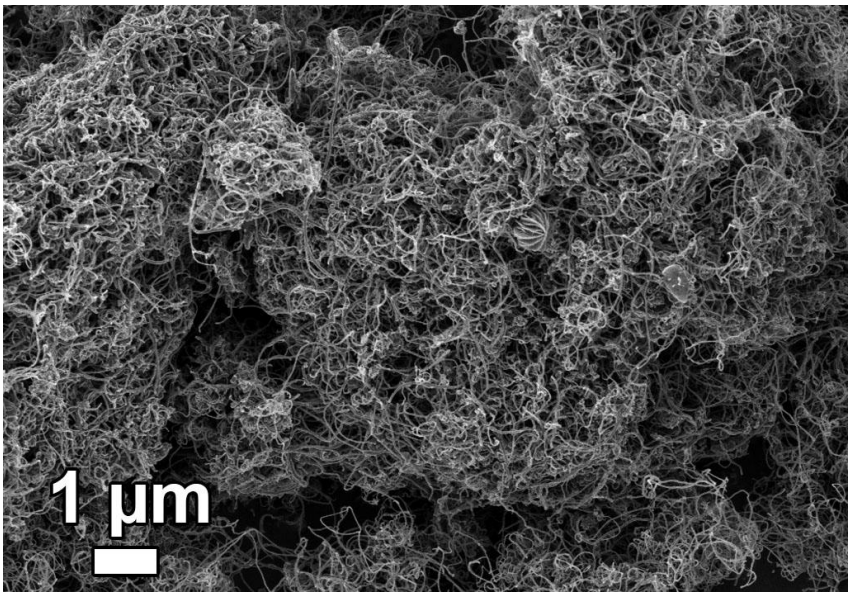

Figure 2-11 Scanning electron microscopy image of carbon nanotube

In the past few years, CNTs have been extensively studied for EDLCs [116,117]. CNTs have been used in two different ways in supercapacitor research. The first technique uses CNTs alone as the active electrodes [117] due to their unique beneficial pore and tubular structure. However, as the SSA of CNTs is generally lower than ACs, mostly their specific capacitance is much lower than ACs too, but their higher conductivity also gives them a lower equivalent series resistance (ESR) value as compared to ACs. In a second technique, CNTs are used as an additive in electrode materials [118], in order to enhance their electrical conductivity as well as provide mechanical stability. The internal resistance of the electrodes is decreased, thus increasing capacitance.

2.1.2.2 Electrode Materials for faradaic capacitors

2.1.2.2.1 Transition metal oxides/hydroxides (t-MO/t-MOH)

Transition metal oxides/hydroxides are considered to be very good materials for ECs due to their high intrinsic specific capacitance and high specific power, which makes them very attractive for commercial applications [5]. Because the electrons combine with other elements that are available in more than one shell, they are appropriate choices for faradaic capacitors electrode materials where the Faradaic reaction is taking place. The transition metal oxides also can be formed as a stable metal oxide (t-MO) and hydroxide (t-MOH) nanostructures. Numerous t-MOs and t-MOHs such as MnO_2 [119–121], $Ni(OH)_2$ [122], NiO [123–125], RuO_2 [126–128], $Co(OH)_2$ [129], Co_3O_4 [130–132], SnO_2 [133], V_2O_5 [134,135] and MoO_3 [136,137] have gained great attention because of their wide applications for storing charge in ECs .

Transition metal oxides/hydroxides require some properties to be successfully used as electrode materials for ECs applications [40]. They must be electronically conductive in nature, the constituting metals must also have the capability to exist in variable oxidation states with no phase change involving reversible modifications of its structure and lastly, their structure should be designed in such a way that during redox reactions protons can freely intercalate in/out of the lattice of the material.

As mentioned earlier, MoO_3 has been extensively studied as a material for ECs application. For example, MoO_3 had been used as a negative electrode by Peng *et al*. [138] in a 1 M H_2SO_4 aqueous electrolyte where they used a polymer material as the positive electrode. The assembled device with an extended operating voltage window of 2.0 V, showed excellent performance, such as a high specific capacitance of 518 F g^{-1} at a current density of 0.5 A g^{-1}, reaching an energy density 71.9 Wh kg^{-1} at a power density of 254 W kg^{-1}. On the other hand, Tang *et al.* [139] used MoO_3 as a positive electrode and activated carbon as a negative side in 0.5 M Li_2SO_4 aqueous electrolyte. The assembled device can deliver a high energy density of 45 Wh kg^{-1} at a power density of 450 W kg^{-1}. The nanostructures of MoO_3 have shown fascinating properties as well as exciting prospects for applications in energy storage. MoO_3 can be produced in different morphology and thickness by different physical and chemical methods. By producing hierarchical nanostructures with 2D building blocks of MoO_3 (e.g., nanoflake, nanoplate and nanosheet) can further improve their functionality in energy storage [140].

2.1.2.2.2 Conductive polymers (CPs)

Recently, conducting (electronically) polymers (CPs) have been investigated as faradaic capacitor electrodes materials [141–143]. Because of the π-conjugated polymer chains in CPs, they have fast and reversible oxidation and reduction processes during energy storage [5]. The conductivity of CPs can be raised to metallic levels by chemical or electrochemical p-doping (oxidation), or n-doping (reduction) [144]. The p-doped polymers are more stable against degradation than n-doped polymers [145]. Mostly, the doped polymer materials have the potential to exploit fully the maximum energy and power densities [146]. The most commonly studied CPs for EC applications are polyaniline (PANI) [147,148], polypyrrole (PPy) [149], polythiophene (PT) [150] and poly(3,4-ethylenedioxythiophene) (PEDOT) [141,151] because of their high conductivity, high storage ability, good thermal and environmental stability, high redox and capacitive current and biocompatibility [152]. The main problem of CPs is their low stability [153]. Mostly, for improved CPs for EC applications composites with carbon materials are usually produced [154,155].

2.1.2.3 Composite materials

Composite materials (CMs) for EDLCs (non-Faradaic) and faradaic capacitors show the best intrinsic characteristics of both components. As previously mentioned, each EDLCs and faradaic capacitor materials have their strengths and weaknesses and CMs try to take advantage of the strengths of each one to make a material that has best SSA and porosity, large active sites, extended potential window, protecting active materials from mechanical degradation and improving cycling stability

[156,157]. An *et al.* [152] used polypyrrole (PPy)/carbon aerogel (CAG) as a composite material with high specific capacitance of 433 F g^{-1}, while the capacitance of CAG electrode is only 174 F g^{-1}. Khomenko *et al.* [155] used a composite of conducting polymer with multiwall carbon nanotubes (MWNTs) and they have measured specific capacitance values of 190 F g^{-1} for PPy/MWNTs and 360 F g^{-1} for polyaniline (PANI)/MWNTs in the two-electrode cell. Zhang *et al.* [156] incorporated manganese oxide (Mn_2O_3) homogeneously into a templated mesoporous carbon to prepare Mn_2O_3/carbon nanocomposites with the high specific capacitance of over 600 F g^{-1}.

2.1.3 Electrolyte solutions for ECs

One of the important parameters for EC system is the electrolyte due to the fact that it comprises ions that are necessary for charge transport and storage. The electrolyte can affect the voltage window, electrochemical stability, ionic concentration, solvated ionic radius, cost, toxicity and resistivity of the ECs. There are three main categories of liquid electrolytes used for ECs application; organic, aqueous and liquid salts (commonly known as ionic liquids) electrolytes [1,26].

2.1.3.1 Organic

Since the energy of supercapacitors is related to the square of the operating voltage, organic electrolytes are commonly used in commercial supercapacitors and academic research. Organic electrolytes are regularly operated up to 2.3 V based on

acetonitrile (ACN) or propylene carbonate (PC) as solvents [26]. ACN can dissolve a lot of organic electrolytes and can improve the conductivity of the electrolytes [158]. However, the solubility of the salts in the organic solvents is comparatively low (their conductivity is ~100 mS cm^{-1} [159]), posting high internal resistance and there is an issue of electrolyte leakage [26,160]. They also suffer from environmental instability, toxicity problems and are highly flammable materials [161]. To keep large operating voltage window characteristic of organic electrolytes, the water content should also be kept to a minimum (normally below 3 – 5 ppm).

2.1.3.2 Aqueous

Aqueous electrolytes include acid, alkaline, and neutral media which are mostly used because of high conductivities and the special mechanism of proton transport (limited to ~1.2 V) [26]. Acid-based (e.g., H_2SO_4 [162]) and alkali (e.g., KOH [163]) aqueous electrolytes have a high conductivity (up to ~1 S cm^{-1}). To achieve a low equivalent series resistance of ECs, the high conductivity of current collectors and electrolytes is required, and the contact resistance between them should be minimal [26]. However, operating voltage is relatively low (~1 V) leading to the narrow electrochemical stability window (1.23 V) of water [164] and consequently, the energy that can be stored in the device is limited [1]. Aqueous electrolytes have the advantages of high ionic conductivity, low cost, non-corrosiveness, safety, non-flammability and convenient assembly in the air [165] which make ECs base on aqueous electrolyte attractive.

2.1.3.3 Ionic Liquids

Ionic liquids are salt which are molten at room temperature. They have good conductivity [7], high thermal and electrochemical stability [166], low vapor pressure [167], low flammability, wide voltage window (usually 4.5 V) [168] and high thermal stability [167]. Ionic liquids are composed of cations and anions. However, the ionic conductivity of these liquids is low at room temperature [169]. Some of the ionic liquids used are imidazolium, pyrrolidinium, aliphatic ammonium salts such as tetrafluoroborate, trifluoromethanesulfonate, bis(trifluoromethanesulfonyl)imide, bis(fluorosulfonyl)imide or hexafluorophosphate, cyclic amines such as aromatic pyridinium, imidazolium and saturated piperidinium, pyrrolidinium and quaternary ammonium salts such as tetraalkylammonium $[R_4N]^+$ [7,170–172].

2.1.4 Cell design for ECs

2.1.4.1 Symmetrical

Symmetrical ECs suggest that both electrodes have the same materials as anode and cathode, so they have the same capacitance value. If $C_1 = C_2$, then $C_{total} = C_1/2$. For symmetric capacitors, the total capacitance value equals half the value of a single electrode [173]. With the galvanostatic charge/discharge plots based on two-electrode cells, the specific capacitance (C_S) (F g^{-1}) of a single electrode, the

maximum energy density (E_M) (Wh kg^{-1}) and the maximum power density (P_M) (kW kg^{-1}) of the supercapacitors are calculated using equations below [174]:

$$C_S = 4C_t = \frac{4\,I\,\Delta t}{m\,\Delta V} \quad \textbf{10}$$

$$E_M = \frac{1}{2}\,C\,(\Delta V)^2 = \frac{1000 \times C_S \times \Delta V^2}{2 \times 4 \times 3600} = \frac{C_S \times \Delta V^2}{28.8} \quad \textbf{11}$$

$$P_M = \frac{3600 \times E_m}{1000 \times \Delta t} = \frac{3.6 \times E_m}{\Delta t} \quad \textbf{12}$$

where C_S is the total specific capacitance of the cell, I is the constant discharge current (A), $\Delta \mathbf{t}$ is the discharge time (s), and ΔV is the voltage window (V), and m is the total mass (g) of the active material in both electrodes, respectively.

We can calculate the maximum power density (P_M) (kW kg^{-1}) of the supercapacitors by using equivalent series resistance (ESR) [175] (that will be discussed in section 2.2.3.3) with the following equation:

$$D_P = \frac{1}{4 \times (ESR)}\,\frac{V^2}{m} \quad \textbf{13}$$

where ESR is the equivalent series resistance, m is the total mass of active material and V is the voltage window (V). The volumetric capacitance (F cm^{-3}) is calculated from:

$$C_v = C_S \times D \quad \textbf{14}$$

where D is the bulk density calculated as the average of the mass of many particles of the material divided by the total volume they occupy. The area capacitance (F cm^{-2}) of sample is calculated from:

$$C_a = \frac{C_s}{A_{BET}} \quad \textbf{15}$$

where A_{BET} is the SSA (m^2 g^{-1}) BET measurements.

2.1.4.2 Asymmetrical

Asymmetric capacitors make use of two different materials as anode and cathode respectively. One of the electrodes usually has a higher capacitance value than the other. In asymmetric ECs, the total capacitance may be approximately equal to the smaller capacitance electrode (If C_1 >> C_2, and then C_{total} ≈ C_2) [173]. For an asymmetric cell, charges at both electrodes should be balanced and also equals to the charge of ions consumed from the electrolyte. The maximum charge from ions available in the electrolyte can be expressed as:

$$Q_i = \frac{m_i}{\rho} c_0 F \quad \textbf{16}$$

where m_i and c_0 are the mass and ion concentration of the electrolyte, ρ is the mass density (mass per unit volume) of the electrolyte, and F= 96484 F mol^{-1} is Faraday's constant [176]. The swing voltage can be expressed as:

$$V = \gamma \frac{C_-}{C_+} \quad \textbf{17}$$

where γ = m_-/m_+ the mass ratio of the negative and the positive electrodes, V is the voltage swing during charge, C_+ and C_- the specific capacitance of the positive and the negative electrode material respectively [176]. In asymmetric ECs, the voltage window is dependent on the capacitance of the active material in each electrode. Therefore, the mass balancing of electrode materials is taken into account according to the equation: $Q_+ = Q_-$, where Q_+ and Q_- are the charges stored in the positive and negative electrodes, respectively. The charge can be expressed by [177]:

$$\boldsymbol{Q = C_s M \Delta U} \qquad \textbf{18}$$

where C_s is the specific capacitance of active material, M is the mass of the active material and ΔU is the potential range during charge-discharge process. In order to get $Q_+ = Q_-$, the mass balancing will follow the equation below:

$$\frac{\boldsymbol{M_+}}{\boldsymbol{M_-}} = \frac{\boldsymbol{C_{s-}\,\Delta U_-}}{\boldsymbol{C_{s+}\,\Delta U_+}} \qquad \textbf{19}$$

Once mass balancing has been taken care of, the capacitance of each electrode is same, meaning that the cell behaves like a symmetric cell and thus equation 10-12 can be used for calculating the specific capacitance, energy, and power densities [178].

2.2 ELECTROCHEMICAL TESTING OF ECS

2.2.1 Experimental testing of materials

Specific capacitance is regularly estimated for the capacitance of a single electrode, which is usually derived from a three-electrode laboratory test. Active materials

testing is usually conducted in a three-electrode configuration to find the best working parameters for ECs with the working electrode (materials to be tested), reference electrode (supposed to be operational in the electrolyte used) and a counter electrode (designed not to interfere with the working electrode). If successful results are obtained from three-electrode cell configuration, one can then proceed to the two-compartment cell [28].

2.2.1.1 Working Electrode

To obtain appropriate information about active materials, the working electrode is made as similar as possible to the electrode of an operational device (real practical device). Working electrode is generally coated on the current collector. Current collectors are generally made with corrosion resistant materials, with good electronic conductivity, a classic example of current collectors are gold, platinum, vitreous carbon and nickel foam [179]. The active mass normally mixed with electronically conducting materials such as carbon black (or acetylene black) to improve the conductivity of the active mass and mixed with a binder to protect the active mass during the test such as polyvinylidene fluoride (PVDF) or polytetrafluoroethylene (PTFE) [28].

2.2.1.2 Reference Electrode

Reference electrodes are electrodes that assist as experimental reference points. The reference electrode operates as a set-point electrode which measures and regulates the potential of the working electrode without allowing any current through it. Selection of an appropriate reference electrode is critical to the success of any experimental process. The right reference electrode is reliant on the medium used. mercury/mercury oxide (Hg/HgO) or silver/silver chloride (Ag/AgCl) are often the electrodes of choice in the aqueous alkaline medium while saturated calomel electrode (SCE) or silver/silver chloride (Ag/AgCl) are used in many non-aqueous media such as acetic acid, etc. When the experiment needs large currents to flow between the working and the counter electrodes, specific attention must be paid to placing the reference electrode at an equipotential line close to the working electrode [28].

2.2.1.3 Counter electrode

The counter electrode allows the required amount of current to be generated at the working electrode by varying its potential within the electrolyte. Suitable materials for CEs are conductive materials which do not react with the electrolyte during the experiment. Counter electrodes are usually made from Glassy carbon (vitreous carbon) or Platinum.

2.2.2 Electrode Experiments

2.2.2.1 Two-Electrode Experiments

Two-electrode experiments are the simplest cell setups. The experimental setup for two-electrode experiments will have the current and sensing leads connected together: Working and working sense are connected together as working electrode positive) and, reference and counter are connected together as a second electrode (negative). A diagram of two-electrode cell setup is shown in Figure 2-12. In this system, the potential difference between both electrodes is monitored, and additional electrochemical properties like the energy density, power density, and life cycle testing can be studied.

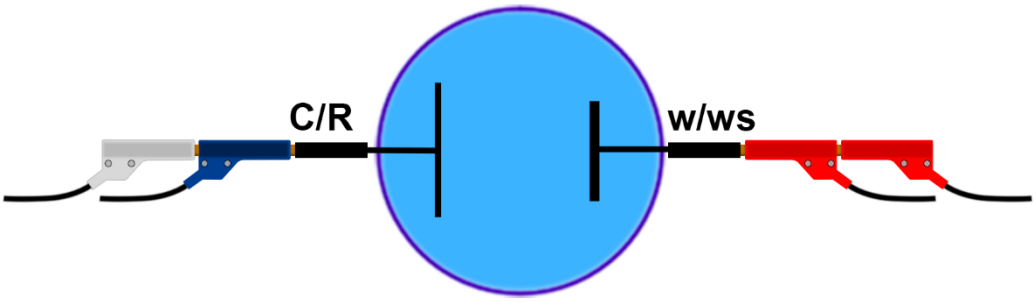

Figure 2-12 Schematic view of the 2-electrode cell setup (Working (W), Working Sense (WS), Reference (R) and Counter (C))

2.2.2.2 Three-Electrode Experiments

The three-electrode experiments are initially used in order to obtain the separate electrochemical properties of each electrode material without the effect of other interaction factors that might arise when they are combined in two- electrode cell. In three-electrode experiments, the reference is separated from the counter. The reference electrode is most often positioned so that it measures a point very close to the working electrode (which has both working and working sense leads attached). A diagram of a three-electrode cell setup can be seen in Figure 2-13.

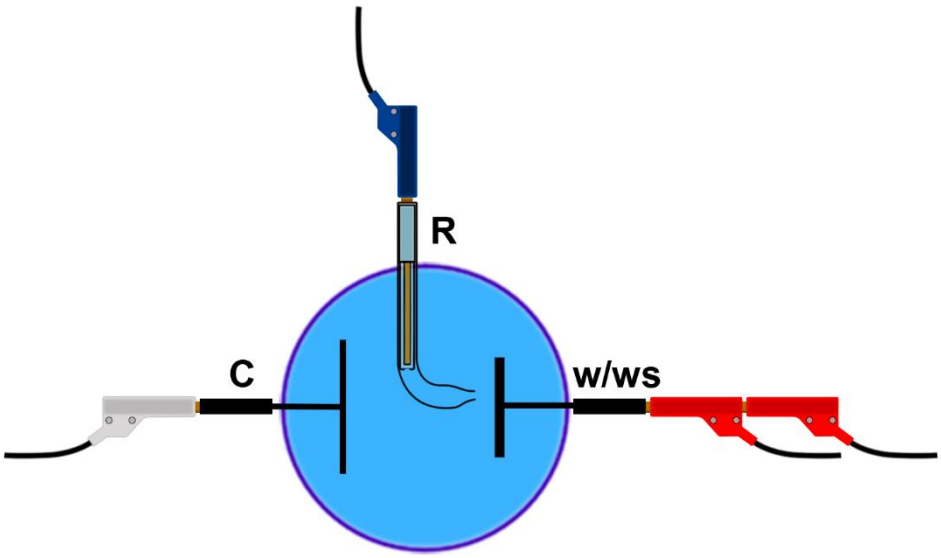

Figure 2-13 Schematic view of the 3-electrode cell setup (Working (W), Working Sense (WS), Reference (R) and Counter (C))

2.2.2.3 Four-Electrode Experiments

In the four-electrode mode, the working sense, working electrode, reference, and counter are separated from each other. A diagram of a four-electrode setup can be seen in Figure 2-14. This setup is relatively uncommon in electrochemistry. Four-electrode model measures the effect of an applied current, on the solution itself or some barrier in that solution. This setup is generally used for measuring impedance through some solution phase interface, like a membrane or liquid-liquid junction or to make very accurate measures of solution resistance or the resistance across the surface of some material (solid state cells).

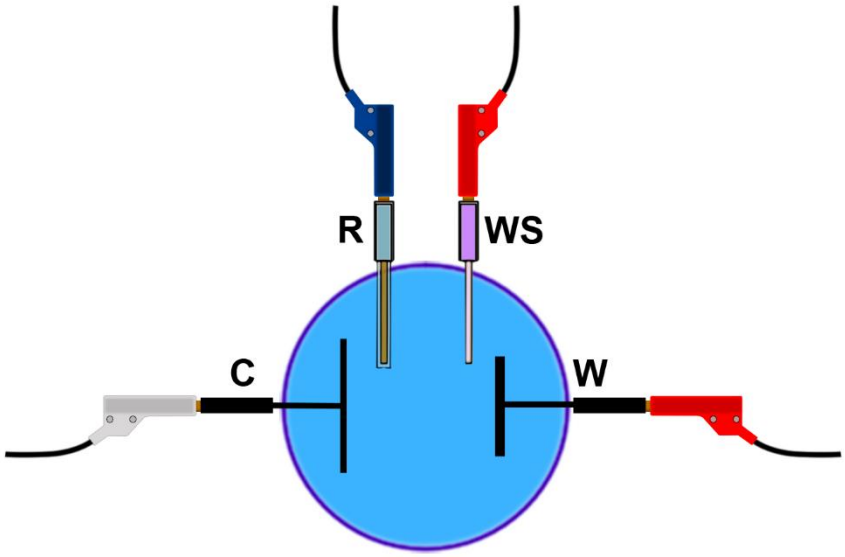

Figure 2-14 Schematic view of the 4-electrode cell setup (Working (W), Working Sense (WS), Reference (R) and Counter (C))

2.2.3 Testing the electrochemical behaviors

The most common techniques for testing electrodes are cyclic voltammetry (CV), galvanostatic charge/discharge (GCD), internal resistance, cyclic life, self-discharge and electrochemical impedance spectroscopy (EIS) and the basics of these techniques will be presented in the following sections.

2.2.3.1 Cyclic voltammetry (CV)

Cyclic voltammetry (CV) is a generally used electrochemical technique to study the role of thermodynamics and electron transfer kinetics of ECs at the interface between the electrode and electrolyte. In CV, the electrochemical cell is driven in a specific potential window, where the potential is applied to the working electrode and measured for different scan rates (e.g. 5, 20, 50, and 100 mV s^{-1}). Scan rate is defined as the change in potential as a function of time. The electrochemical performance of a material can be estimated by detecting the current change in a cathodic and anodic scan. The specific capacitance (C_s) can be calculated from CV curves according to the following equation [177]:

$$C_s = \frac{\int I\,dV}{vm\Delta V} \qquad 20$$

where I is the average current, ΔV is the voltage difference, v is the potential sweep rate (mV s^{-1}), m is the mass of total electroactive material of electrodes including a positive electrode and the negative electrode. The maximum energy density (E_M) and

maximum power density (P_M) of ECs can then be calculated from C_s according to the following equations 11 and 12 above.

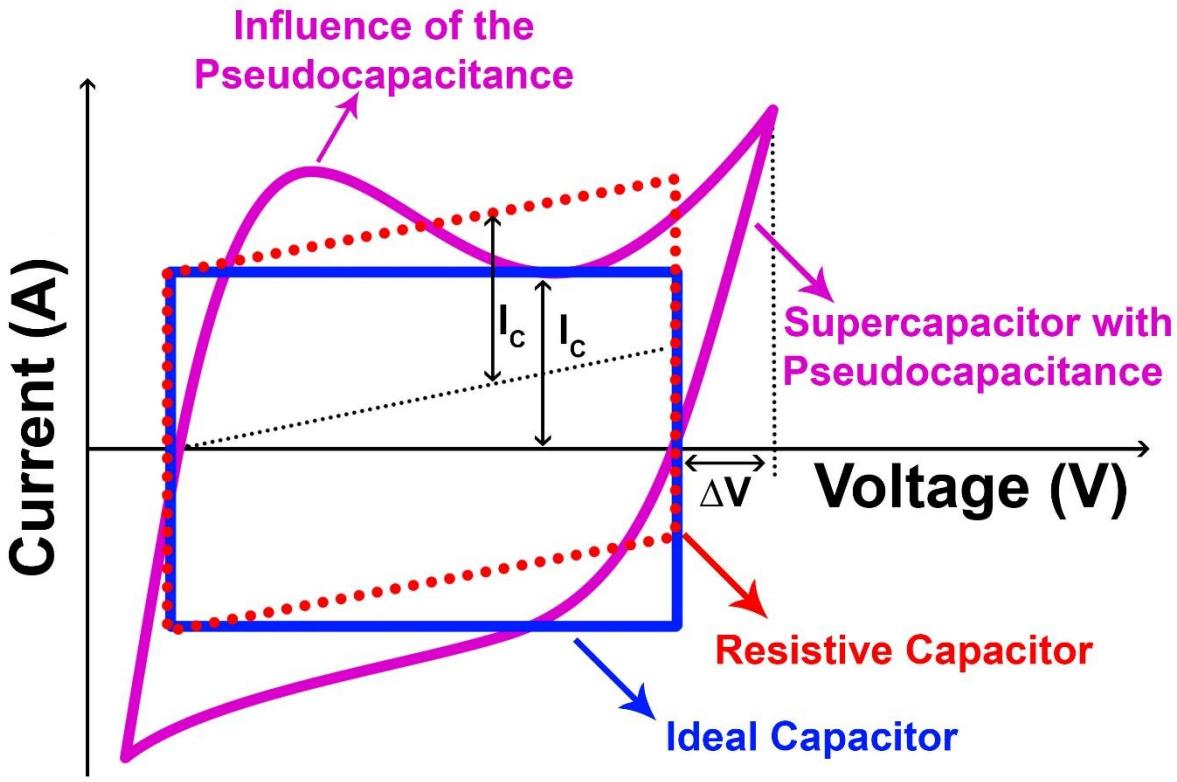

Figure 2-15 A cyclic voltammogram showing the fundamental differences between static capacitance (rectangular) and faradaic capacitance (curved)

For a reversible electrochemical process, the shape of the EDLCs should be close to the rectangular shape (Figure 2-15), while, faradaic capacitors have a curved shape with anodic and cathodic peak for a reversible electrochemical process. For a

reversible electrochemical process, the CV plots should have a peak voltage difference between the anodic and current cathodic peaks of ~ 59 mV. The peak positions do not change as a function of scan rate, the ratio of the peak currents should also be unity for a reversible electrochemical process. The peak current is related to the square root of the scan rate by the power law equation; $I=v^{0.5}$ where I is the current and v is the scan rate

2.2.3.2 Chronopotentiometry (CP) or Galvanostatic Charge/Discharge (GCD)

This calculation is critical to the analysis and prediction of the active materials' performance under practical operating situations. The working electrode is subjected to a constant current I (positive in charge or negative in discharge), and voltage versus time is recorded between minimal and maximal values [180]. The usual curve of galvanostatic charge-discharge process is in four regions as shown in Figure 2-16; (1) the cell behavior during charging, (2) the cell behavior during discharging, (3) the initial process, and (4) this section is responsible for the negative resistive ohmic loss associated with the resistance of the cell (Ohmic potential drop).

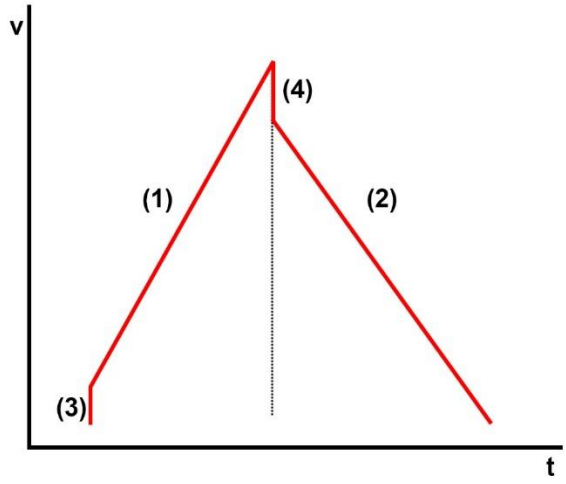

Figure 2-16 The typical curve of galvanostatic charge-discharge process

2.2.3.3 Internal resistance

An equivalent series resistance (ESR) and equivalent distributed resistance (EDR) can be considered as an internal resistance. ESR (pulse resistance) corresponds to all the resistive components within the ECs. The ESR would be fully elaborated and explained in the electrochemical impedance spectroscopy (EIS) section. EDR value comprises of ESR and extra contribution of the charge redistribution process in the non-uniform porous electrode [181]. EDR and ESR value, when charging/discharging the ECs with the constant current I (Ohm) can be calculated from the value of $\Delta \mathbf{V_T}$ for EDR and $\Delta \mathbf{V}$ (Ohmic voltage drop) for ESR with the following equation [182]:

$$\boldsymbol{EDR} = \frac{\Delta \boldsymbol{V_T}}{\boldsymbol{2I}} \qquad \textbf{21}$$

$$ESR = \frac{\Delta V}{2I} \qquad 22$$

where $\Delta \mathbf{V_T}$ (from Figure 2-17) is voltage difference from the interception of the straight line with the vertical line at the moment when the discharge is switched on giving the voltage drop ($\Delta \mathbf{V}$), and **I** is the current. Equation (13) clearly shows the dependence of maximum power of the capacitor on the ESR; thus it is ideal to ensure that this value remains as small as possible for high power density.

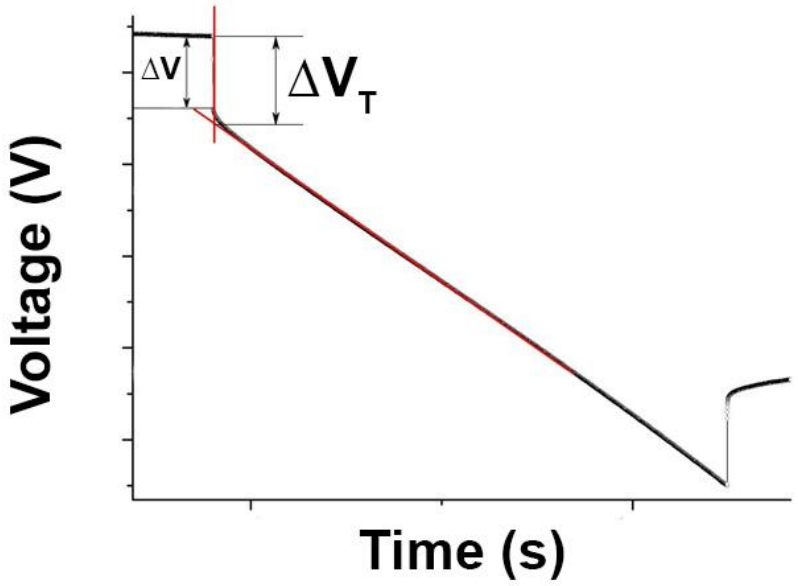

Figure 2-17 Measurement profile for ESR (from $\Delta \boldsymbol{V}$) or EDR (from $\Delta \boldsymbol{V_T}$) evaluation

2.2.3.4 Cyclic life

Ideal ECs can be charged and discharged for an infinite number of cycles. The cycle life for all rechargeable devices depends on the exact situations under which cycling takes place [173]. Applied current, voltage limits, device history, and temperature are

all important during cycling. Cyclic galvanostatic charge–discharge (CGCD) is the standard method used to test the performance and cycle life of ECs. The capacitance (from discharge time) of each cycle during the CGCD divided by the charging time multiplied by 100% give the coulombic efficiency as a function of cycle number. The coulombic efficiency of the ideal ECs stays at 100% for CGCD. However for normal ECs it can be observed that there is a reduction in capacitance after the period of the cycling.

2.2.3.5 Self-discharge

Self-discharge is the voltage drop on a charged cell without a load after a specified period of time. To get a realistic measure of the leakage or self-discharge currents, the capacitors need to be charged for several hours, after which it will be left without a load to discharge (Figure 2-18). The goal of the self-discharge test is to evaluate the energy loss over the test interval and to measure the decrease in capacitance of the capacitor's voltage during the test.

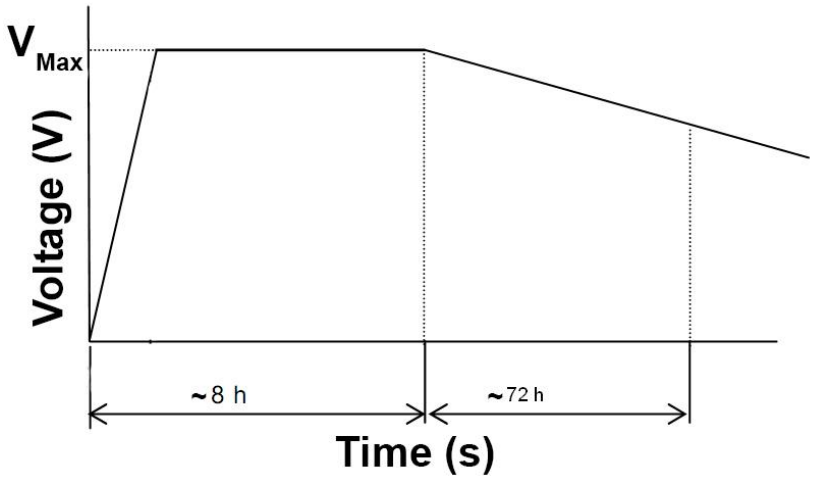

Figure 2-18 Self-discharge test diagram.

From Figure 2-18, the measured parameter is the voltage maintenance rate (VMR) (%), which is calculated by the following equation:

$$\boldsymbol{VMR} = \frac{\boldsymbol{V_{End}}}{\boldsymbol{V_{Max}}} \times \mathbf{100}\% \qquad \mathbf{23}$$

where V_{End} is the voltage between open capacitor terminals after ~72 h and V_{Max} is the rated voltage.

2.2.3.6 Electrochemical impedance spectroscopy (EIS)

Impedance spectroscopy is a technique which studies the behavior of small potential perturbations at different frequencies (mHz to MHz) at a constant AC signal or open circuit potential. The EIS is often represented by the Nyquist plot which presents the real and imaginary part of the impedance on the x and y-axis respectively. The Nyquist plot takes into account the different parameters (resistance, capacitance,

inductance and etc.) all being contingent on the frequency. Another important plot from the EIS measurements is the Bode plot. In EIS measurement, the Nyquist plot consists of the low-frequency region and the high-frequency region. In the low-frequency region, the capacitance (C(ω)) can be defined as the combination of imaginary (C″(ω)) and real (C′(ω))parts of capacitance respectively, and they can be expressed as the following equations [26,183]:

$$\boldsymbol{C(\omega) = C'(\omega) + jC''(\omega)} \quad \textbf{24}$$

$$\boldsymbol{C'(\omega) = -\frac{Z''(\omega)}{\omega|Z(\omega)^2|}} \quad \textbf{25}$$

$$\boldsymbol{C''(\omega) = -\frac{Z'(\omega)}{\omega|Z(\omega)^2|}} \quad \textbf{26}$$

where C′(ω) corresponds to the static capacitance which is tested during the constant current discharge, C″(ω) corresponds to energy dissipation of the ECs by IR drop and an irreversible Faradaic charge transfer process, which can cause the hysteresis of the electrochemical processes. |Z(ω)| is the impedance modulus, and **ω** is the angular frequency [26,183]. The real (C' (ω)) and imaginary (C" (ω)) specific capacitances as a function of frequency can be plotted. A relaxation time **τ** can be calculated from knee frequency in the real and imaginary plot; from **τ = 1/f** where f is the characteristic frequency of the cell, corresponding to the maximum on the C" (ω) curve versus frequency plot. τ is the time required to deliver efficiently the stored energy. This represents the boundary between a pure capacitive and resistive behavior of the ECs electrode.

The Nyquist plot (Figure 2-19) relates the imaginary part of impedance, Z(ω)“, with the real part of impedance, Z(ω)', [143]. The Nyquist plot is usually divided into three regions, low frequency, medium frequency and high-frequency region [184]. At the high-frequency region usually a small semicircle appears which normally for EDLCs material arises due to the kinetic phenomena and charge transfer resistance (R_{CT}) and double layer capacitance (C_{dl}) [185]. It can be possible to make an equivalent circuit for each EIS result. The equivalent circuit that represents the electrochemical system should be as simple and give the best possible match between the model's impedance and the measured impedance of the system [186]. Common circuit elements used in equivalent circuit models are resistance (R), capacitance (C), constant phase element (CPE), Warburg coefficient (W) and inductance (L). These parameters are described as follows:

I. Resistances:
    a. Solution (electrolyte) resistance, R_S, is the resistance of the electrolyte and it same as the ESR.
    b. Charge transfer resistance, R_{CT}, has to do with the process of charge transfer from the electrode to the electrolyte. This occurs on the electrode surface perpendicular to the electrochemical double layer.
    c. Ohmic resistance, R_Ω, is the potential drop between the reference electrode and the working electrode.
    d. Polarization Resistance, R_P, is the resistance when the potential of an electrode is forced away from its value at open-circuit.

II. Capacitances:

a. Double layer capacitance, C_{DL}, exists at the interface between an electrode and electrolyte. It is formed when ions from the electrolyte stick on the active surface.

b. Constant phase element, CPE, is an equivalent electrical circuit element that models the behavior of a double layer, and it happens when the capacitor behavior is not perfect. The electrical impedance can be calculated as follows:

$$Z_{(\omega)} = Q\,(j\omega)^{-n} \qquad 27$$

when $j=(-1)^{0.5}$, Q is is a constant with dimension F s^{n-1} ($Q=1/|Z|$ at $\omega=1$ rad/s) and $0 < n < 1$. when $n = 1$, the CPE behaves as a pure capacitor [187], while when $n = 0$, the CPE behaves a pure resistor and when $n= 0.5$, the CPE is the equivalent of the so-called Warburg element.

III. Warburg Impedance, W, is associated with CPE. Warburg impedance element represents diffusion element that can be used to model semi-infinite linear diffusion.

The diameter of the semicircle of the Nyquist plot in the high-frequency region is R_{CT} and the intercept of the impedance plot on the real |Z| axis gives information on the solution (electrolyte) resistance (R_S). However, in the low-frequency region the plot is due to the diffusion mechanism of ions in the material for the ideal supercapacitors and should be parallel to the y-axis [188].

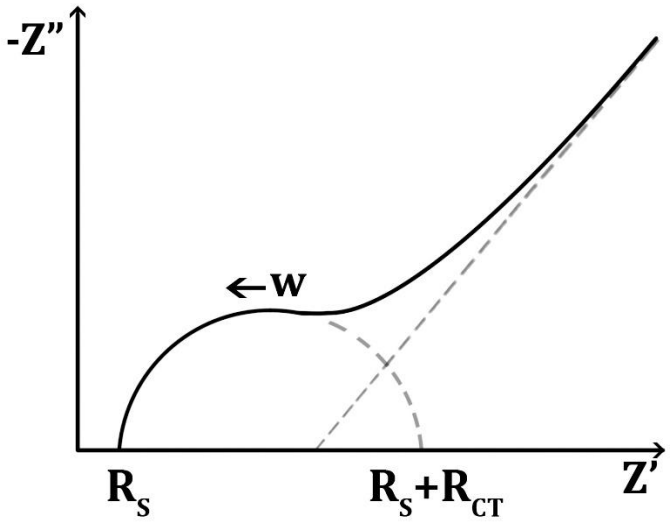

Figure 2-19 Nyquist impedance plot

There are two types of Bode diagram: one where $log\,|Z"|$ is plotted against $log\,|f|$ and the other where phase angle is plotted against $log\,|f|$. The capacitance (C) can be calculated from the linear portion of the Bode plot using the relation [6]:

$$\boldsymbol{C = \frac{1}{2\pi f|Z"|}} \qquad \textbf{28}$$

Unlike the Nyquist plot, the Bode plot explicitly shows frequency information. A tilted line with respect to the real axis with the angle of $45^{o} \leq \theta \leq 90^{o}$ is achieved, and this has been explained to correspond to ion diffusion mechanism between the Warburg diffusion and ideal capacitive ion diffusion [189,190].

CHAPTER 3

GROWTH TECHNIQUES AND CHARACTERIZATION

In this chapter all the experimental procedures used will be discussed. Detailed specific parameters for each material fabricated and tested will be discussed later in specific sections of chapter 4.

3.1 GROWTH TECHNIQUES

3.1.1 Chemical vapor deposition (CVD)

Chemical Vapor Deposition (CVD) was developed in the 1960s and 1970s to produce carbon fibers and carbon nanofibers [191,192]. Generally in CVD, a reactive gas mixture flows through a reactor chamber at a particular temperature, where the substrates are placed. This method is suitable for high purity, large scale and uniform layer deposition of materials. It is also reliable, cost effective and very efficient. [193]. The CVD system used in this study consists of a reaction chamber (a 2-inch diameter quartz tube) which was linked by flow meters to different gas supplies and enclosed in a furnace. Figure 3-1 shows a schematic diagram of the CVD system used in this study for the synthesis of graphene and for the production of activated carbon. The gases used in this study were of high purity and were as follows argon (Ar, grade 5 - 99.999%), hydrogen (H_2, grade 5 - 99.999%) and methane (CH_4, grade 4.5 – 99.995%).

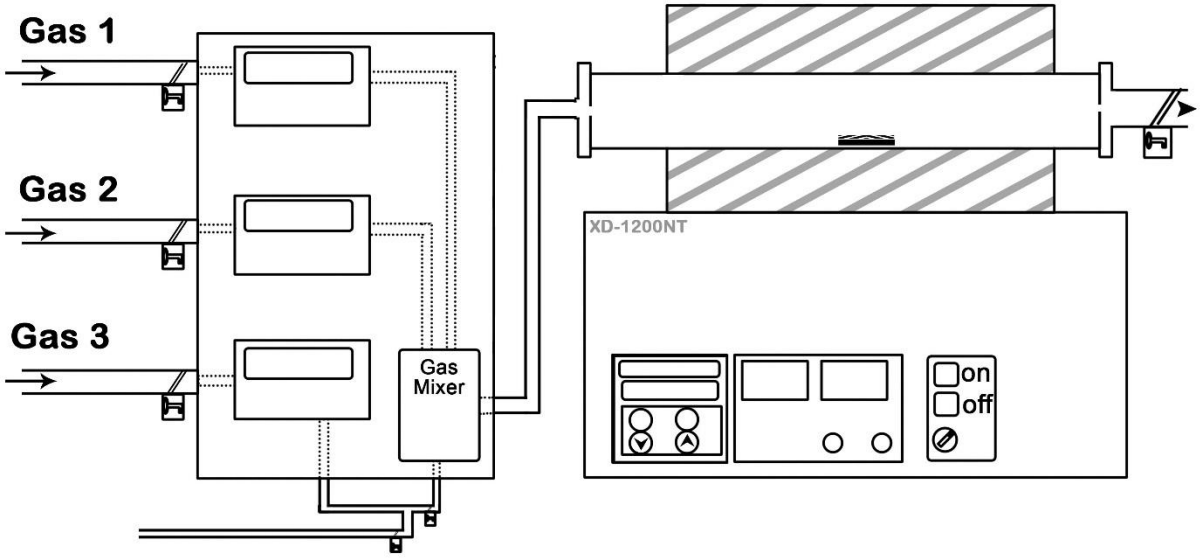

Figure 3-1 Schematic of the chemical vapor deposition system in our laboratory

Large area, high-quality graphene can be grown on catalytic transition metal surfaces such as nickel (Ni) and copper (Cu) by CVD [191,194,195]. Methane (CH_4) is one of the generally used carbon sources for the growth of high-quality graphene. In this work, CH_4 was used as the carbon source to grow graphene foam (GF) on Ni foam (NF) template. GF which is a three-dimensional foam-like structure of graphene was first reported by Chen et al. [196] using NF template directly in the CVD and subsequently quenching after the growth. Different cooling rates (quenching) [197], fast, medium and slow (are illustrated in figure 3-2), which strongly affects the thickness and quality of graphene films produced due to the non-equilibrium nature of the precipitation process [198]. Medium cooling rates is ideal for uniform carbon

segregation and produces few layer graphene. However, fast and slow cooling rates gives patches of graphene deposition on the substrate used for example Ni-substrate [199]. Also the microstructure of the nickel substrate plays an important role in the formation of the graphene film morphology [200,201].

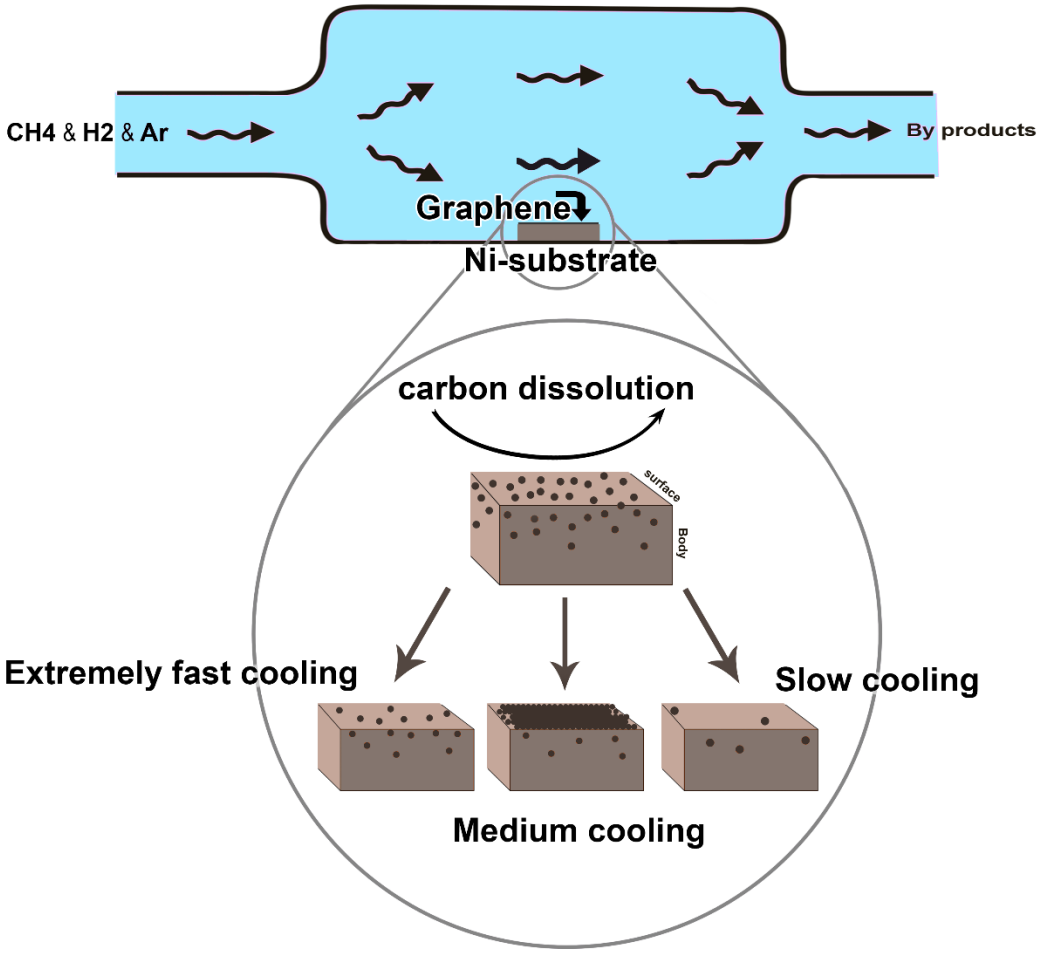

Figure 3-2 Illustration of the different cooling rates of graphene growth

This work mainly focuses on the synthesize of GF using CVD system as reported in reference [125]. Nickel foam substrate with 430 g m^{-2} areal density and 1.6 mm in

thickness was used as a template for the growth of graphene. Briefly, the NF was annealed at 800 °C in the presence of Ar and H_2 for 30 minutes to remove any surface contaminations like oil residues as well as inorganic materials that might have originated from the manufacturing or packaging process, before the introduction of the CH_4 gas at 1000 °C. The flow rates of the gases (CH_4:H_2:Ar) were 10:10:300 sccm. After 15 - 30 minutes of deposition, the sample was cooled (medium cooling) by pushing the quartz tube to a lower temperature region [125,202]. After growth, the nickel template was removed by chemical means. The sample was placed in 2 M hydrochloric acid (HCl) solution at 80 °C and left for 48 hours to ensure complete removal of the nickel. The resulting GF sample was washed with deionized water to remove completely the HCl and dried at 50 °C in an electric oven.

3.1.2 Hydrothermal synthesis

The hydrothermal technique is a very popular method in the last fifteen years for production of nanomaterials. It was initially used by the British geologist, Sir Roderick Murchison (1792-1871), to describe the action of water at high temperature and pressure in bringing about changes in the earth's crust leading to the formation of various rocks and minerals [203]. Hydrothermal synthesis takes into account the various techniques of crystallizing substances from high-temperature aqueous solutions at high vapor pressures where the synthesis is conducted in a stainless steel autoclave. The solvothermal process is a special case of hydrothermal synthesis. The solutions used in a solvothermal synthesis can be anything from water

(hydrothermal), ammonia (ammonothermal), alcohol (alcothermal, glycothermal) or any other organic or inorganic solvent [204]. One of the most important solvents in nature is Water. It has extraordinary properties as a reaction medium under hydrothermal conditions where it acts very differently from water at standard conditions. Hydrothermal synthesis is a cheap and direct synthesis route used to prepare bulk materials or composite materials with different nano-architectures with their unique chemical and physical properties. Such nanostructures include nanorods, nanowires, nanoflowers, nanosheets, etc. [205–209]. Figure 3-3 shows a complete system for the hydrothermal chemical growth.

Figure 3-3 Complete system for the hydrothermal chemical growth; (a) shows the stainless steel autoclave system with the Teflon lining (b) shows the electric oven used for heating

3.1.3 The microwave technique

The microwave technology (MT) is known to decrease reaction times and increase productivity yield of materials compared to some other technique such as the conventional hydrothermal system or the reflux systems. MT use a group of electromagnetic waves whose frequencies range from 0.3 GHz to 300 GHz (some industrial Microwave reactors can work at a frequency of 2.5 GHz or wavelength of 12.25 cm). This technology makes use of two heating mechanisms, namely dipolar polarization and ionic conduction. The dipoles in the reaction chamber are involved in the polarization effect while the charged particles in a reaction chamber (usually ions) contribute to ionic conduction effect. When reaction chamber is irradiated, the dipoles or ions in the sample align themselves in the direction of applied electric field. When the applied field oscillates, the dipole or ion field realigns itself with the alternating electric field thereby losing energy in the form of heat through friction and dielectric loss. The microwave irradiation induces a volumetric heating by direct coupling of microwave energy with the molecules that are present in the reaction chamber. This increases the temperature of the whole liquid volume in the chamber simultaneously, compared with the conventionally heating system, where the reaction chamber in contact with the hot vessel walls is heated first [210,211]. The example of microwave system used in this study is Samsung Combi CP1395EST (Figure 3-4).

Figure 3-4 the Microwave system that used for this study (Samsung Combi CP1395EST).

3.1.4 Synthesis of activated carbon (AC)

In this study, a different technique such as CVD, hydrothermal technique and Microwave were used to prepare AC, and they are discussed briefly below.

3.1.4.1 Hydrothermal synthesis of AC based on polymers and different carbon material

Figure 3-5 presents the preparation process of hydrothermal and CVD carbonization of ACs based on polymers and a different carbon material such as graphene foam (GF), carbon nanotubes (CNTs) and expanded graphite (EG). The CNTs used in the work was prepared by CVD according to reference [113]. The expanded graphite (EG) samples were synthesized by exfoliation of expandable graphite (grade ES 250

B5 from Qingdao Kropfmuehi Graphite) in a quartz boat using a home based microwave system (Samsung Combi CP1395EST) at a power of 900 W, irradiated for 1 minute. The starter material, as a hydrogel state was synthesized via the hydrothermal process. Briefly, the different mass of GF, CNT and EG were dispersed by ultrasonication in separate containers with 100 ml of water containing different masses of polyvinylpyrrolidone (PVP) and 11.11 g of polyvinyl alcohol (PVA) and. 1.50 ml of hydrochloric acid (HCl) was then added to the solution as a cross-linker [16]. The approachused based on the procedure by Wajid *et. al* [212] successfully demonstrated an effective method to disperse carbon material using PVP as stabilizer where it is also known to noncovalently functionalize carbon material (like graphene) surface. That should allow the carbon material to easily disperse in the PVP solution and subsequently in the PVA matrix. Furthermore, the nitrogen contained in the PVP can be bond to the carbon, enhancing the conductivity of the final material. The mixture was further sonicated for few minutes and stirred for 30 min to obtain a homogeneous dispersion before being transferred into a 150 ml Teflon-lined autoclave system. The solution was heated at 190 °C for 12 h. The hydrothermal process gave a porous network of the polymer hydrogel that allowed the loading of material to be activated inside the porous network. The resulting hydrogels were crushed and washed with deionized water and dried for 6 h. The hydrogels obtained was then soaked in aqueous KOH solution with a KOH/hydrogel mass ratio of 5, for 24 h and dried at 120 °C for 12 h before carbonization [16,213]. The composites were then placed in a horizontal tube furnace ramped from room

temperature to 800 °C at 10 °C/min under argon gas flow for 2 h. This procedure transforms the hydrogel into carbon materials consisting of a continuous pore network distribution created by the escape of the K^+ ions. The obtained powders were washed with 3 M HCl to remove the remaining KOH and subsequently washed with deionized water and dried at 60 °C.

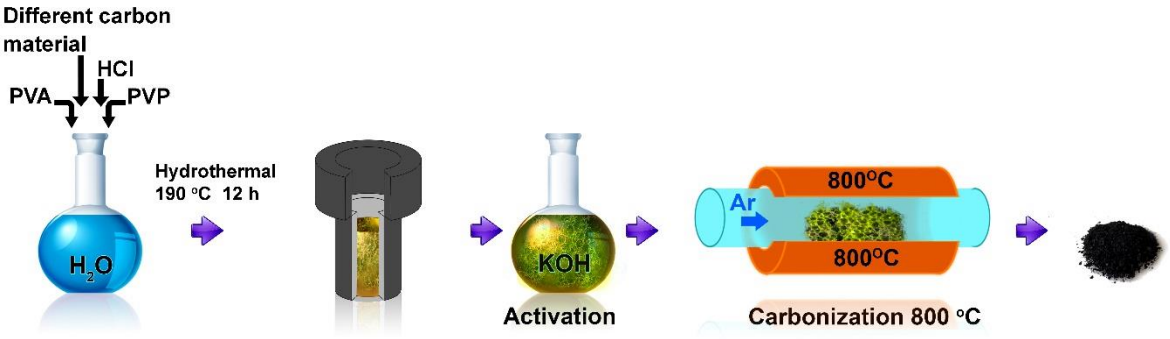

Figure 3-5 Schematic diagram of ACs based on polymers and different carbon material

3.1.4.2 Synthesis of AC based on expanded graphite (EG)

Figure 3-6 presents the preparation process of activation of expanded graphite (EG) to produce activated carbon (AC). Firstly, 1 g of expanded graphite (EG) was dispersed in 100 ml of 10 wt% polyvinylpyrrolidone (PVP) solution to create high-concentration dispersions [212], and the mixture was sonicated for 12 h. 5 g of KOH was then added to the solution, which was stirred for 2 h at 60 °C. After 2 h of stirring, the EG forms a solid precipitate at the surface of the solution. The solid precipitate obtained was collected and dried at 70 °C for 12 h. The dried solid

precipitate was then placed in a horizontal tube furnace which was ramped from room temperature to 800 °C at 5 °C/minute under argon and hydrogen gas flow and kept at this temperature for 2 h of carbonization. This procedure transforms the EG solid precipitate into flakes of carbon material denoted as activated expanded graphite (AEG). The black powder obtained was washed with 1 M HCl to remove the remaining KOH and subsequently with deionized water and dried at 60 °C.

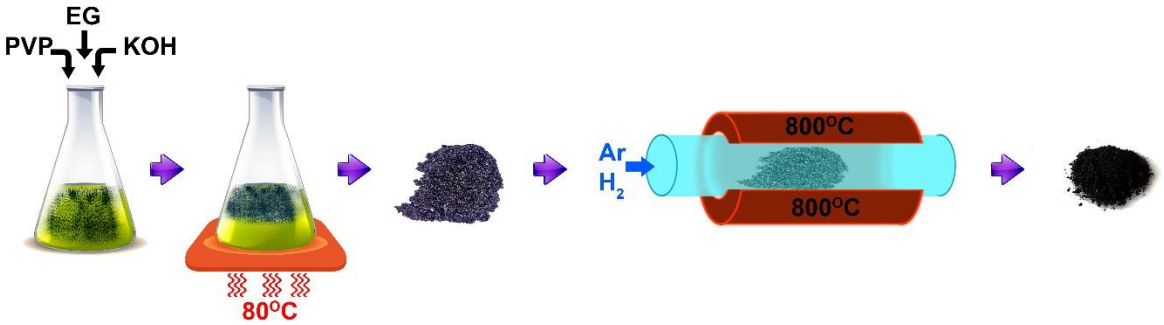

Figure 3-6 Schematic diagram of synthesis procedure of AC based on expanded graphite (EG)

3.1.4.3 Synthesis of AC based on Pinecone (PC)

Figure 3-7 presents an illustration of the preparation process adopted for the production of activated carbon derived from pine cone (PAC). Pine cones obtained from University of Pretoria campus Hatfield South Africa were first washed with acetone and deionized water to remove any adhering dirt and dried at 60 °C before being crushed. The crushed pine cone was then soaked in aqueous KOH solution with a KOH/pine cone mass ratio of 4 for 24 h and dried at 80 °C for 12 h before

carbonization. The mixture was then placed in a horizontal tube furnace ramped from room temperature to 800 °C at a constant rate of 10 °C/min. The tube containing the sample was subjected to argon and hydrogen gas flow for 2 h of carbonization. Thereafter, the sample was collected, washed with 3 M HCl to remove the remaining KOH and deionized water before final drying at 60 °C.

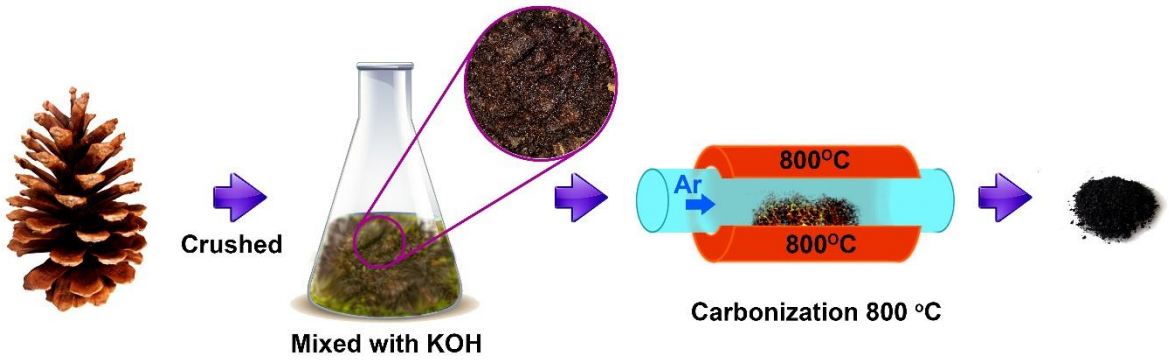

Figure 3-7 Schematic diagram of synthesis of AC based on Pinecone (PC)

3.1.5 Synthesis of α-MoO_3

Figure 3-8 presents the preparation process of α-MoO_3. α-MoO_3 prepared by the hydrothermal system by the procedure reported by Wang *et al.*[140]. First, ammonium paramolybdate ($(NH_4)_6Mo_7O_{24}\cdot 4H_2O$) and sodium diethyldithiocarbamate ($(C_2H_5)_2NCS_2Na\cdot 3H_2O$) were dissolved in deionized water and magnetically stirred for 12 h, and the solution mixture was kept stationary under the ambient condition for another 12 h. The resulting yellow precipitate ($Mo((C_2H_5)_2NCS_2)_2O_2$) was filtered, washed with deionized water and dried at 70 °C for 12 h. After, which the $Mo((C_2H_5)_2NCS_2)_2O_2$ was placed into a 100 ml Teflon-lined stainless steel autoclave,

and 85 ml deionized water was added with stirring. The autoclave was sealed and maintained at 200 °C for 24 h. The resulting precipitates was filtered, washed 1st with deionized water, then ethanol and washed with deionized water again and dried under vacuum at 100 °C for 6 h. Nanostructured α-MoO_3 was obtained by heating the hydrothermally synthesized powder in air at 370 °C for 6 h.

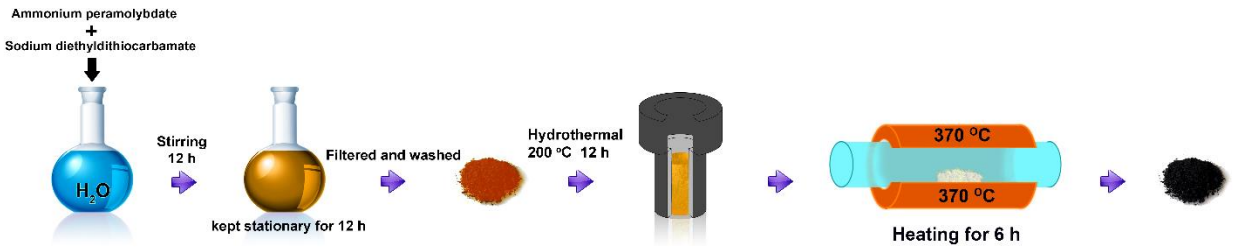

Figure 3-8 Schematic diagram of synthesis of α-MoO_3

3.2 MATERIALS CHARACTERIZATION

3.2.1 Morphological Analysis

In this study, we benefited from electron microscopes at the microscopy unit of the University of Pretoria for morphological analysis of the samples. An electron microscope uses a beam of accelerated electrons as a source of illumination. Scanning electron microscope (SEM) and Transmission electron microscopy (TEM) are briefly discussed below.

3.2.1.1 Scanning electron microscope (SEM)

Scanning electron microscopy (SEM) is one of the most useful instruments available to examine and analyze the microstructural morphology and chemical composition when using energy dispersive x-ray spectrometer (EDs) with the electron microscope. The SEM uses focused electron beams which are made with a Schottky field emission source that utilizes a high applied field in an ultra-high vacuum to generate a variety of signals at the surface of solid specimen's surface. The beam diameter is only a few nanometers which allow a great spatial resolution. When the electrons interact with the specimen's surface, creating a multitude of signals that have information about the sample's surface topography, composition and other properties such as electrical conductivity [214] are recorded as signals by suitable detectors. The produced signals (see Figure 3-9) include secondary electrons (SEs), characteristic X-rays (use for EDS analysis), bremsstrahlung X-rays, Auger electrons, backscattered electrons (BSEs), light, specimen current, electron beam induced current (EBIC) (in semiconductors) and transmitted electrons (thin samples).

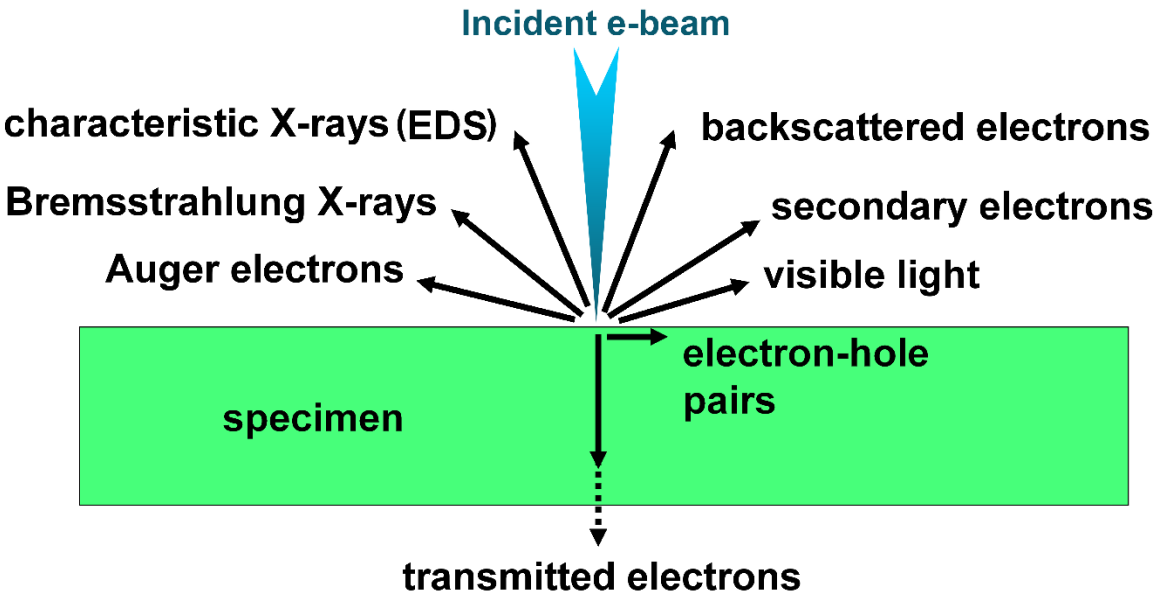

Figure 3-9 Schematic of the electron-specimen interaction in an SEM

The secondary electrons are used for imaging to obtain information about the morphology at the sample surface. High-resolution images of the order of 1 nm are visible with SEMs having secondary electron detectors for secondary electron imaging. X-ray emission involves electron reshuffling within the energy levels of the electronic structure and as such, the characteristic X-rays are used to identify composition and measure elemental abundance in the sample. The BSEs signal is linked to the atomic number of the signatory element at the sample surface. As such, the BSEs are often used for analytical SEM in conjunction with the X-ray to provide information about the elemental distribution of the sample. EDS characterization is typically combined into SEM instrument and includes a sensitive X-ray detector, a liquid nitrogen Dewar for cooling, and software to collect and analyze energy spectra.

EDS detector is used to separate the characteristic X-rays of different elements into an energy spectrum, and EDS software is used to analyze the energy spectrum in order to determine the specific elements present in the sample [214]. EDS can also be used to find the chemical composition of materials down to a spot size of a few microns, and to create an elemental composition. Normally for imaging in the SEM, the surface of the specimens must be electrically conductive and electrically grounded to prevent the accumulation of electrostatic charge on the surface and for nonconductive material they are coated with some material like gold, gold/palladium alloy, platinum, osmium, iridium, tungsten, chromium, or graphite.

The surface morphology of all samples was investigated using a Zeiss Ultra Plus 55 field emission scanning electron microscope (FE-SEM). “Image J” was used to measure the diameter of fibers from SEM images and for EDS, using a JEOL 5800LV scanning electron microscope equipped with energy dispersive operated at 20kV.

3.2.1.2 Transmission electron microscopy (TEM)

Transmission electron microscopy (TEM) also makes use of an electron beam for illuminating a sample area and creating an image [215] when the high accelerating voltage electrons passes through the sample. In TEM, the source of illumination is a beam of electrons with high energy (very short wavelength), released from a tungsten filament at the top of a cylindrical column. The electrons with high accelerating voltage pass through the sample and they are scattered in different degree, losing or

prevailing initial energy. The elastically scattered electrons within the sample form an imaging contrast [216] and this is magnified by a series of magnetic lenses until it is recorded by a photographic plate. This is then portrayed to a monitor for viewing real-time images. A JEOL JEM-2100F microscope operated at 200 kV was used in this work to analyze the nature of samples. TEM samples were prepared by dispersing the active material in powder form in ethanol and ultrasonicated to disperse the samples evenly. The ethanol solution containing the sample for the study was dropped on a lacey carbon-coated copper grid and left for some minutes to dry before being loaded into the chamber for analysis.

3.2.2 Gas Adsorption Analysis

Adsorption is surface phenomenon essential when adsorbate molecules (pollutants) attract to an adsorbent surface by the intermolecular force of attraction [217]. Liquid or gas phase can be used as an adsorbate molecules during the adsorption process. The pore analyzes of porous solid phase are mostly determined by methods belonging to gas adsorption [217]. To properly understand the pores structure desorption studies were carried out too. During adsorption/desorption, inert gases that do not have any form of interaction with the surface of the active materials are used. For this purpose, N_2, CO_2, Ar or He are commonly used gases [218]. Analysis of the adsorption/desorption isotherms gives information about the specific surface area, porosity, average pore volume and the general pore size distribution of a sample.

In this study, nitrogen adsorption/desorption isotherms were analyzed using a Micromeritics ASAP 2020 and a Micromeritics TriStar II 3020 (version 2.00) surface area and porosity analyzer. The surface area measurements were obtained using the Brunauer-Emmett-Teller (BET) method based on the Langmuir model. Pore size and pore volume were obtained by the Barrett-Joyner-Halenda (BJH) method from the desorption branch of the associated isotherm. The process for obtaining the isotherms involved initially degassing the pre-weighed sample at 180 °C for more than 12 h under vacuum conditions in order to remove any traces of moisture within the sample. The degassed sample was then transferred to the main chamber for the complete analysis using N_2 gas at specified pressure and temperature of 77 K. Originally, the sample is dosed with a specific amount of gas which is then evacuated to obtain the quantity of gas absorbed by the sample over a relative pressure range, P/P0 (e.g., $0.01 < P/P0 < 0.2$).

The adsorption isotherms are classified according to the molecular interactions between the gas and adsorbent surface. After Brunauer et al. [219] explanation of 5 adsorption isotherms in 1940, the International Union of Pure and Applied Chemistry (IUPAC) [220] published the types of the adsorption isotherms while Gregg and Sing [221] stated the differences among them with an additional isotherm. Typical shapes of isotherms are given in Figure 3-10 (a).

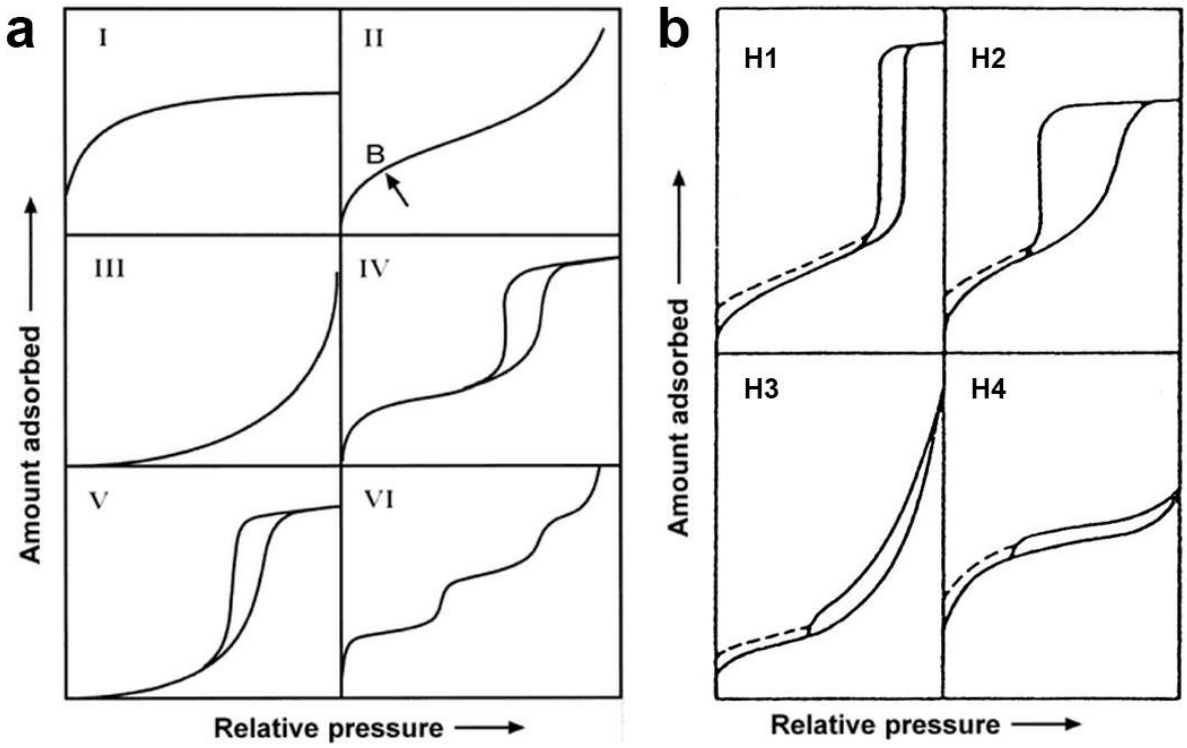

Figure 3-10 (a) The IUPAC classification of adsorption isotherms types for gas–solid equilibria [220], (b) the modern classification of hysteresis loops [222]

A type I (Langmuir type), roughly characterized by a uniform approach to a limiting adsorption that seemingly corresponds to a complete monolayer and is usually used to describe adsorption on microporous adsorbents. Types II and III belong to non-porous or macroporous adsorbents with strong and weak adsorbate–adsorbent interactions respectively. Types IV and V show hysteresis for strongly and weakly adsorbing surfaces. Type VI shows that the adsorption isotherms can have one or more steps. This isotherm represents stepwise multilayer adsorption on a uniform

nonporous surface. Figure 3-10 (b) shows the modern classification of hysteresis loops. H1 hysteresis, with the narrow hysteresis loop, presents porous materials made from agglomerates or compacts of almost uniform spheres and having a narrow pore size distribution. The H2 presents many porous adsorbents with narrow necks and wide bodies or when the porous material has an interconnected pore network. The H3 happens with aggregates of plate-like particles giving rise to slit-shaped pores. The H4 generally presents narrow slit-like pores [222].

3.2.3 Raman Analysis

Raman spectroscopy is a non-destructive technique used to observe vibrational, rotational, and other low-frequency modes in a sample [223]. This technique is based on inelastic scattering of monochromatic light usually produced from a laser source in the visible, near infrared or near ultraviolet region. Inelastic scattering means that the frequency of photons in monochromatic light changes upon interaction with a sample. The sample absorbed and then reemitted the photons of the laser light, and the reemitted photon's frequency is shifted up or down in comparison with original monochromatic frequency, which is called the Raman effect [224]. This shift of frequency provides information about rotational, vibrational and other low-frequency transitions in molecules. Raman spectroscopy can be used to study solid, liquid and gaseous samples. In particular for graphitic materials, Raman spectroscopy provides useful information on the in-plane vibrations of sp^2 carbon atoms (G-band), disorder

(D-band), out-of-plane stacking order (2D band), in-plane crystallite size, the crystallographic orientation of graphene and graphene doping [225–228].

In this study, all Raman spectra were recorded with a high-resolution Jobin–Yvon Horiba T64000 micro-Raman spectrometer equipped with a triple monochromator system to eliminate contributions from Rayleigh scattering. The samples were excited using the 514 nm wavelength of an argon excitation laser with a power of 1.5 mW at the source so that the heating effect on the sample is minimized. The laser was focused on the sample using a 50X objective with an acquisition time of 60 – 120 seconds for each spectrum. Further analysis of the obtained spectra was done using LabSpec (Ver. 5.78.24) analytical software.

3.2.4 Crystallinity and Qualitative Phase Analysis (XRD)

X-ray powder diffraction (XRD) is an analytical technique mostly used to identify the phases of crystalline materials [229] and other additional information such as lattice parameters and phase distribution using Rietveld confinement [230]. XRD system consists of three basic elements: an X-ray tube, a sample holder, and an X-ray detector. In this system, electrons are produced from a cathode by heating a filament and accelerated to an anode target (commonly made of copper or cobalt) where bombardment takes place to produce X-rays in a cathode ray tube. When electrons have enough energy to dislodge inner shell electrons of the target material, specific X-ray spectra are produced. Depending on the anode material, characteristic X-rays

of different wavelength (Cu-λ = 1.5406 Å or Co-λ = 1.7890 Å) is produced. When the X-rays interact with the sample, constructive interference occurs where Bragg's law is satisfied [231]:

$$\boldsymbol{n\lambda = 2d\,sin\,\theta} \qquad 29$$

where n is an integer value (1,2,3..), λ is the wavelength of the incident x-ray, d is the spacing between the planes in the atomic lattice and θ is the angle between the incident ray and scattering plane (The angle between the projection of the x-ray source and the detector is 2θ). This law relates the wavelength of electromagnetic radiation to the diffraction angle and the lattice spacing in a crystalline sample.

From XRD result, the crystallite sizes were estimated by using Equation 30, which is known as the Scherrer formula [232]:

$$\boldsymbol{G_{hkl} = \frac{k\lambda}{\beta\,Cos(\theta)}} \qquad 30$$

where G_{hkl} is the average linear dimension of the crystal perpendicular to the diffracting plane (hkl) (diameter of the particles), β (radians) is the full-width at half-maximum in the 2θ scan, k is a constant (0.89), λ is the wavelength of the X-rays and θ is the angle of the diffraction peak.

The measurements were performed at the Department of Geology, University of Pretoria, on a Panalytical X'Pert PRO X-ray diffractometer in θ–θ configuration, equipped with a Fe filtered Co-Kα radiation (1.789Å) and with a X'Celerator detector and variable divergence- and fixed receiving slits. Samples were prepared according

to the standardized Panalytical backloading system, which provides nearly random distribution of the particles. The data was collected in the angular range 5° ≤ 2θ ≤ 90° with a step size 0.008° 2θ and a 13-s scan step time. Some of the samples were measured on a zero background holder. Due to small sample size, the samples were top loaded onto the zero-background holder and analyzed. The zero-background is a silicon wafer, cut in such a way that it does not produce peaks with XRD. Some of the samples have been measured with a Cu-tube in that case a Ni filter was used. The phases were identified using X'Pert High score plus and Match software.

3.2.5 X-ray photoelectron spectroscopy (XPS)

X-ray photoelectron spectroscopy (XPS) is a surface-sensitive quantitative spectroscopic technique that measures the elemental composition at the parts per thousand range, empirical formula, chemical state and electronic state of the elements that exist within a material. A typical XPS spectrum is a plot of the number of electrons detected (sometimes per unit time) (Y-axis) versus the binding energy of the electrons detected (X-axis). Each element produces a characteristic set of XPS peaks at characteristic binding energy values that directly identify each element that exists in or on the surface of the material being analyzed. These characteristic spectral peaks correspond to the electron configuration of the electrons within the atoms, e.g., 1s, 2s, 2p, 3s, etc. The number of detected electrons in each of the characteristic peaks is directly related to the amount of element within the XPS sampling volume. For this study XPS analysis was performed on a physical

electronics VersaProbe 5000 instrument employing a 100 µm monochromatic Al-Kα to irradiate the sample surface. Photoelectrons were collected by a 180° hemispherical electron energy analyzer. Samples were analyzed at a 45° angle between the sample surface and the path to the analyzer. Survey spectra were taken at a pass energy of 117.5 eV, with a step size of 0.1 eV, which was used to obtain an estimate of the elemental analysis of the powders.

3.2.6 Electrochemical Analysis

The electrochemical properties of all samples coated on nickel foam (NF) and nickel foam graphene (NFG) templates were analyzed in two- and three-electrode test system on a Biologic SP-300 and VMP 300 PGSTAT workstation (Knoxville, TN 37930, USA) controlled by an EC-Lab v10.44 software. The PGSTAT workstation is an electronic instrument designed to control the potential difference (E) applied to the working electrode (WE) with a current flow (in the form of either a half cell or a full cell) and a reference electrode (RE) with no current. The PGSTAT generates characteristic cyclic voltammetry curves which give us information on the possible thermodynamics of electrochemical reactions of the system. All tests in a three-electrode configuration, active material serving as the working electrode, a rectangular glassy carbon rod serving as the counter electrode and a Ag/AgCl (3 M KCl) serving as the reference and in a two-electrode configuration, with coin-type cells (Glass microfiber filter paper was used as the separator) as shown in Figure 3-11.

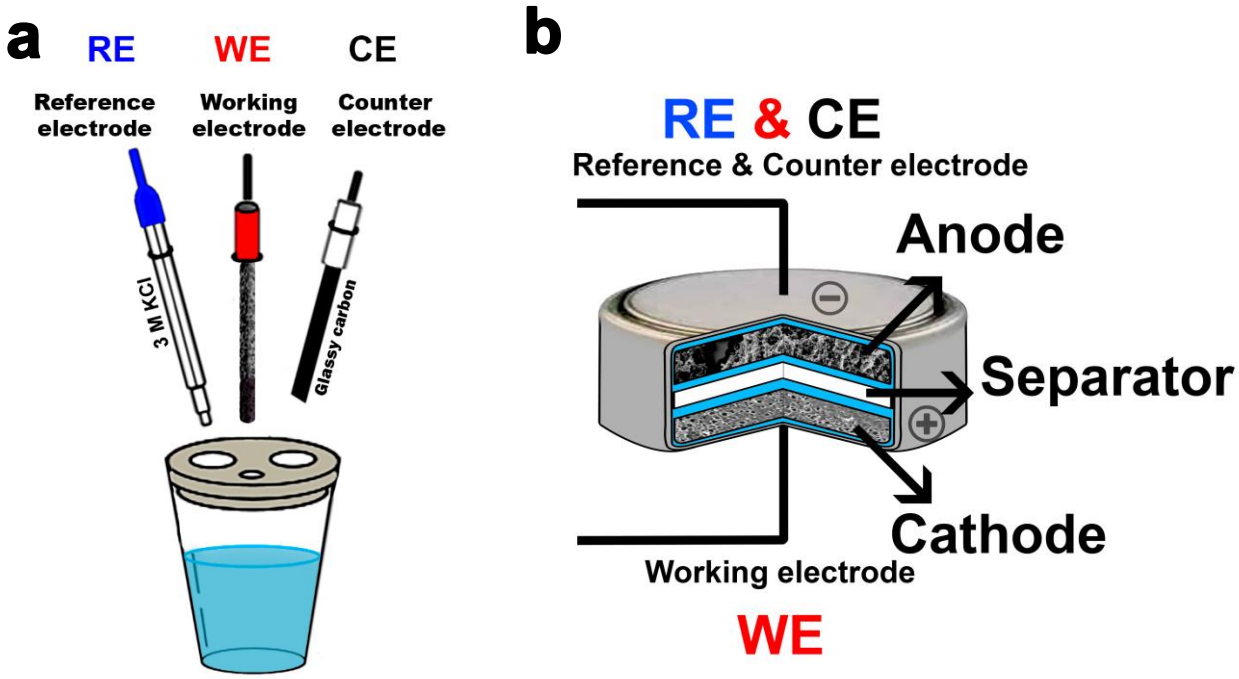

Figure 3-11 (a) Three-electrode and (b) Two-electrode set-up used for electrochemical testing of active materials electrodes

The electrodes for supercapacitor were prepared as follows: The synthesized material was mixed with polyvinylidene fluoride (PVdF) as a binder and carbon black (CB) to improve the conductivity of the material (if the material conductivity is not good) with a weight ratio of 8:1:1. The slurry was made using N-Methyl-2-pyrrolidone (NMP) solution and was uniformly coated on nickel foam current collector. The electrodes were dried at 60 °C in an oven for 8 hours to ensure complete evaporation of the NMP. Cyclic voltammetry (CV), chronopotentiometry (CP), electrochemical impedance spectroscopy (EIS) and cycling life tested for all the samples. The CV

tests were carried out at the different potential range and different scan rates ranging from 5 mV s^{-1} to 100 mV s^{-1}. EIS measurements were conducted in the frequency range from 0.1 Hz to 100 kHz with an open circuit potential (~ 0 V).

CHAPTER 4

RESULTS AND DISCUSSION

In this chapter, the results obtained from all experimental procedures outlined in the preceding chapter are fully explained. The resulting publications from each of the specific research studies are also presented afterward.

4.1 SYNTHESIS AND CHARACTERIZATION OF ACTIVATED CARBONS (ACS) FROM DIFFERENT CARBON SOURCES FOR HIGH-PERFORMANCE ELECTROCHEMICAL CAPACITORS

4.1.1 Hydrothermal and chemical vapor deposition (CVD) synthesis and characterization of AC based on polymers and graphene foam.

4.1.1.1 Introduction

Activated carbons (ACs) are the most commonly used material for EDLC applications due to their environmentally friendly nature, highly porous structure, large surface area, good adsorption property, and high electrical conductivity [5]. Recently, research activities have been focused on the use of porous ACs materials with high SSA from different sources so as to improve the electrochemical performance of EDLC [16,17]. The electrochemical performance of EDLCs are related to the pore structure, surface area and surface chemistry of the ACs. Thus, production of large amounts of ACs with optimum properties via a cost-effective synthesis method would be a step in the right direction for advancement of supercapacitor technology [16,20–22].

In this section, the hydrothermal synthesis of three-dimensional porous carbons with a high SSA from the dispersion of graphene foam (GF) into two different low-cost polymers namely polyvinyl alcohol (PVA) and polyvinylpyrrolidone (PVP) polymer matrix solution is presented. PVA and PVP are chosen because they are well-known polymer blends [233–235]. PVA has some outstanding physical properties which include electrochemical stability, non-toxicity, and mechanical strength. PVP is also non-toxic and has excellent absorption and complex forming capabilities [236].PVA possess OH groups which freely attach to carbons and may also serve as a source of hydrogen bonding during the reaction. On the other hand, PVP being a vinyl polymer with a pyrrolidine group is good at attracting other polar groups and forming other bonds which lead to the formation of hydrogels.

After the hydrothermal treatment as mentioned in (chapter 3.1.4.1), the hydrogels formed were collected and soaked in KOH for activation followed by carbonization to create a porous network of graphitic carbons. A systematic study was made on the effect of activation, the morphology and the SSA of the three-dimensional PVA-GF-PVP produced carbons designated as 3D-PGP. The electrochemical characteristics of the 3D-PGP were investigated using both the three- and two-electrode configurations. The 3D-PGP displayed remarkable electrochemical properties in a 6 M KOH aqueous electrolyte. Samples designated 3D-PG-1 represented when 50 mg of GF was added, 3D-PG-2 when 80 mg of GF was added, and 3D-PG-3 when 100 mg of GF was added in 100 ml of PVA matrix solution without PVP. After characterizing all the samples produced, it was realized that the 3D-PG-3 sample had

the best properties for electrochemical applications. Furthermore, 3D-PGP-1 denotes the addition of 1.76 g PVP sample to 3D-PG-3, and 3D-PGP-2 indicates samples produced when 3.5 g of PVP was added to sample 3D-PG-3.

4.1.1.2 Result and discussions

The produced 3D-PGP materials were tested in three- and two-electrode configurations setup for electrochemical measurements in different electrolytes and the results will be presented in section 4.2. This section presents results obtained in 6 M KOH electrolyte. A publication obtained from this work which details all the processes with the supporting information from the article is attached.

Electrochimica Acta 180 (2015) 442–450

Contents lists available at ScienceDirect

Electrochimica Acta

journal homepage: www.elsevier.com/locate/electacta

Synthesis of 3D porous carbon based on cheap polymers and graphene foam for high-performance electrochemical capacitors

Farshad Barzegar[a], Abdulhakeem Bello[a], Omobosede O. Fashedemi[b], Julien K. Dangbegnon[a], Damilola Y. Momodu[a], Fatemeh Taghizadeh[a], Ncholu Manyala[a,*]

[a] Department of Physics, Institute of Applied Materials, SARCHI Chair in Carbon Technology and Materials, University of Pretoria, Pretoria 0028, South Africa
[b] Department of Chemistry, University of Pretoria, Pretoria 0002, South Africa

ARTICLE INFO

Article history:
Received 13 July 2015
Received in revised form 27 August 2015
Accepted 28 August 2015
Available online 29 August 2015

Keywords:
Porous carbon
Supercapacitor
Equivalent circuit
Electrochemical performance

ABSTRACT

A scalable production of high surface area nanoporous carbon material (~2994 $m^2 g^{-1}$) with good distribution of micro-, meso- and macro-pores was hydrothermally synthesized using both cheap polymers and graphene foam as carbon sources. The as synthesised material shows a unique interconnected porous graphitic structure. The electrochemical double-layer capacitor fabricated from this nanoporous carbon material exhibited a superior supercapacitive performance of 188 $F g^{-1}$ at current density 0.5 $A g^{-1}$. This corresponded to areal capacitance of 6.3 $\mu F cm^{-2}$ coupled with a high energy of 0.56 $\mu Wh cm^{-2}$ (16.71 $Wh kg^{-1}$) and a power density of 13.39 $\mu W cm^{-2}$ (401 $W kg^{-1}$) due to extended potential window of 1.6 V in KOH aqueous electrolyte. Moreover, no capacitance loss after 10,000 cycles was observed, owing to the unique structure and large surface area of the active material. The outstanding performance of this material as supercapacitor electrode shows that it has great potential for high performance energy-related applications.

1. INTRODUCTION

As a result of the depletion of fossil fuels and the issue of greenhouse gas emission, cleaner sources of energy are being explored such as solar and wind energies. Furthermore, new technologies for minimizing CO_2 emission are developing rapidly and require the elaboration of highly reliable energy storage devices. Supercapacitors or electrical double layer capacitors (EDLCs) seem to be the most likely candidates for the next generation of energy storage devices. They are at the forefront of research on energy storage technology due to the limitations of batteries for many applications. They can help to optimize energy consumption by complementing batteries in a variety of applications. They are also regarded as possible replacements for batteries if their production costs are competitive enough and their energy densities surpass those of current batteries. At the same time, they must be able to retain their extraordinary properties of high power density, superior rate capability, rapid charging/discharging rate, long cycle life (>100, 000 cycles), simple principles, fast dynamics of charge propagation and low maintenance cost. These unique properties result from the storage harvesting mechanism of the primary charge, which relies on the electro-sorption of ions from an electrolyte onto a porous electrode [1].

Carbon materials are the materials of choice for EDLC applications. Their advantages as electrode materials were reported in previous work [2] some of which are the following: carbon has different allotropes, a variety of shapes, and good polarization, and its amphoteric behavior exhibits essential electrochemical properties from donor to acceptor states. It is also environmentally friendly. However, although low-cost nanoporous carbon electrodes with a tunable electrically conductive architecture and a highly active surface area exhibit high power density above 10 $kW kg^{-1}$ their energy density is still limited to less than 10 $Wh kg^{-1}$ [3]. Even though the operating voltage can be up to 4 V for ionic liquids (ILs) electrolytes for carbon electrodes, the ILs electrolytes are usually characterized by poor conductivity and high viscosity which significantly hinder their penetration in the electrode structure and decreases charge propagation which results in low energy density. Consequently, the capacitance of the capacitors operating in such electrolytes is usually low and is characterized by poor power rates [4]. On the other hand, aqueous electrolytes are cheap and ecological but suffer from the drawback of even smaller operating voltage as low as 1.0 V due to the thermodynamic decomposition of water at 1.23 V. However, this electrolyte has the highest specific capacitance compared to organic and ionic electrolytes owing to its high conductivity, low

* Corresponding author. Tel.: +27 0 12 420 3549; fax: +27 0 12 420 2516.
E-mail address: ncholu.manyala@up.ac.za (N. Manyala).

http://dx.doi.org/10.1016/j.electacta.2015.08.148
0013-4686/

viscosity and good charge propagation. In addition, this electrolyte is environmentally friendly which solves the problem of disposal of waste and used devices. Moreover, functional carbon materials or carbon materials enriched with heteroatom such as oxygen and nitrogen, demonstrate pseudocapacitance originating from redox reactions of these functional groups as well as from local changes in the electron density of the carbon matrix enriched by these heteroatoms. These functionalized or enriched carbon materials are more stable in an aqueous electrolyte, and their pseudocapacitive behavior further increases their specific capacitance. These advantages have encouraged research into producing novel designs that could increase the working potential of EDLCs in aqueous electrolytes close to that of organic electrolytes (i.e. ~2 V). Recently Fic et al. [5] designed an activated carbon (AC) symmetric supercapacitor exhibiting a specific capacitance of 120 $F.g^{-1}$ after 15 000 cycles in a working potential of 2.2 V in 1 M Li_2SO_4 aqueous electrolyte. Furthermore, novel asymmetric supercapacitors based on carbon in 1 M H_2SO_4 have demonstrated high stability after 10,000 cycles at 1.6 V [6]. The high over-potential of di-hydrogen evolution was used to improve the working voltage. These two reports were based on commercial activated carbon with a high specific surface area (SSA) but they gave no information on the pore sizes distribution (PSD). In fact, good PSD in the carbon materials can enhance the specific capacitance of the EDLCs since sub-nanometric pores size between 0.7 and 0.9 nm satisfy the ions electro-sorption. However mono-dispersion of these micropores adversely affects rapid transport of electrolyte ions by increasing the ion transport resistance in these small pores which leads to poor rate capability and power density. Therefore, the presence of mesopores and macropores is essential for ions transport and the ion buffering reservoir respectively [7]. Carbide derived carbons (CDCs), usually produced from chlorination of metal carbides, possess narrow and tunable PSDs between 0.6 and 2 nm and a high SSA up to 3000 $m^2 g^{-1}$. These properties can be controlled and tailored by the selection of the precursors and the chlorination conditions. These materials show extraordinary electrochemical performances in any electrolyte [8]. However, CDCs are very expensive and serious safety and environmental issues surrounding their production are limiting factors for their commercialization. On the other hand, polymers have been actively investigated as promising alternative precursors. They have received considerable interests in recent years due to their low cost, commercial availability, uniform structure, and high chemical purity. Mixed with graphene, they can act as spacers to form composites, preventing graphene agglomeration or re-stacking [9]. Thus, the high surface area of graphene will be accessible to ions and its high conductivity will also be advantageous for the performance of this graphene-based material. Furthermore, there have been previous reports on carbon derived hydrogel for various applications. For example, You et al. [10] prepared a hydrogel derived non-precious electrocatalysts for efficient oxygen reduction reaction (ORR) by freeze-drying and subsequent carbonization of a Tris/Boric acid/EDTA gel. In their more recent work [11], similar synthesis technique was used to produce multifunctional electroactive heteroatom-doped carbon aerogels. This material showed promising results when used as active material for ORR and lithium ion storage. Zhang et al. [12] synthesized N-doped carbon aerogels with high surface area. This electrode material demonstrated good electrochemical capacitor performance with a specific capacitance of 354 Fg^{-1} at a current density of 0.2 Ag^{-1}.

In this paper, we report on the hydrothermal synthesis of three dimensional porous carbons with a high SSA based on graphene foam (GF) with two different polymers namely Polyvinylpyrrolidone (PVP) and polyvinyl alcohol (PVA). We chose PVA and PVP as they are well-known polymer blends [13–15]. PVA has some outstanding physical properties which include its electrochemical stability, non-toxicity and mechanical strength. PVP is also non-toxic and has excellent absorption and complex forming capabilities [16]. While PVA with its free OH groups attached to methane carbons can be a source of hydrogen bonding, PVP being a vinyl polymer with a pyrolidine group is good at attracting other polar groups and forming other bonds. Thus a highly cross-linked polymer hydrogel with ionic bonds, inter and intra molecular hydrogen bonds and dipole interactions is easily formed with such blends. The hydrothermal treatment resulted in hydrogels that were further treated with KOH for activation followed by carbonization to create a porous network of graphitic carbons. A systematic study was made of the effect of activation on the morphology and SSA of the three-dimensional PVA-GF-PVP produced carbons designated as 3D-PGP. The electrochemical characteristics of the 3D-PGP were investigated using both the two- and three- electrode configurations. The 3D-PGP displayed remarkable electrochemical properties in a conventional 6 M KOH aqueous electrolyte.

2. EXPERIMENTAL

2.1. Synthesis and activation of the hydrogel.

Scheme 1 presents the preparation process of carbons. Graphene foam (GF) with a three dimensional network and relatively low defect density (Figure S1 (a)) was first prepared by chemical vapor deposition (CVD) following the procedure used in our previous work [17]. The hydrogel was synthesised via the hydrothermal process. Typically, different masses of GF were dispersed in 100 ml of water containing 11.11 g of polyvinyl alcohol

Scheme 1. Schematic diagram of the preparation process of 3D-PGP carbons.

(PVA) followed by the addition of different masses of Polyvinylpyrrolidone (PVP) (for PVA/GF/PVP samples) in a glass vial by ultrasonication, 1.50 ml of hydrochloric acid (HCl) was added to the solution as a cross linker [18]. The mixture was sonicated for few minutes and further stirred for 30 min to obtain a homogeneous dispersion before being transferred into a 120 ml Teflon-lined autoclave system operated at 190 °C for 12 h. The resulting hydrogel was crushed and washed with deionized water and dried for 6 h. The hydrogel obtained was then soaked in aqueous KOH solution with a KOH/hydrogel mass ratio of 5 for 24 h and dried at 120 °C for 12 h before carbonization [19]. The composite was then placed in a horizontal tube furnace ramped from room temperature to 800 °C at 10 °C/min under argon gas flow for 1 h of activation. This procedure transforms the hydrogel into carbon materials consisting of a continuous pore network distribution. After which samples were washed with 3 M HCl to remove the remaining KOH and then washed with deionized water. Samples were designated 3D-PG-1 when 50 mg of GF was added, 3D-PG-2 when 80 mg of GF was added, and 3D-PG-3 when 100 mg of GF was added in a PVA solution. 3D-PGP-1 denotes the addition of 1.76 g PVP sample to 3D-PG-3, and 3D-PGP-2 indicates samples produced when 3.5 g of PVP was added to sample 3D-PG-3.

2.2. Structural characterization

The SEM images were obtained using a Zeiss Ultra Plus 55 field emission scanning electron microscope (FE-SEM) operated at an accelerating voltage of 2.0 kV. The energy dispersive x-ray (EDX) obtained using scanning electron microscope (SEM) (JEOL 5800LV) equipped with an EDX spectrometer operated at 20 kV was used to estimate the elemental composition of the produced materials. X-ray photoelectron spectroscopy (XPS) was used to determine the chemistries of activated carbons obtained in powder form. A Physical Electronics VersaProbe 5000 instrument employing a 100 μm monochromatic Al-Kα to irradiate the sample surface was used. Photoelectrons were collected by a 180° hemispherical electron energy analyzer. Samples were analyzed at a 45° angle between the sample surface and the path to the analyzer. Survey spectra were taken at a pass energy of 117.5 eV, with a step size of 0.1 eV, which was used to obtain an estimate of the elemental analysis of the powders. High-resolution spectra of C1s, N1s, and O1s regions were taken at a pass energy of 23.5 eV, with a step size of 0.05 eV. All binding energies were referenced to that of the binding energy of C-C at 284.7 eV. Transmission electron microscopy (TEM) was carried out with a JEOL JEM-2100F microscope operated at 200 kV accelerating voltage. Nitrogen adsorption–desorption isotherms were measured at −196 °C using a Micromeritics ASAP 2020. All the samples were degassed at 180 °C for more than 12 h under high vacuum conditions. The surface area was calculated by the Brunauer–Emmett–Teller (BET) method from the adsorption branch in the relative pressure range (P/P_0) of 0.01 - 0.2. The X-ray diffraction (XRD) was recorded using an XPERT-PRO diffractometer (PANalytical BV, the Netherlands) with theta/theta geometry. The qualitative phase of samples was analyzed with the X'pert Highscore search match software at room temperature. Raman spectroscopy measurements were carried out using a Jobin Yvon Horiba TX 6400 micro-Raman spectrometer equipped with a triple monochromator system to eliminate contributions from Rayleigh lines. LabSpec (Ver. 5.78.24) analytical software was used to analyze the spectra. All the samples were excited with a 514 nm argon laser line with a laser power of 1.5 mW to avoid possible thermal effects.

2.3. Electrochemical testing

The electrodes for supercapacitor were prepared as follows: The synthesized carbon material was mixed with Polyvinylidene fluoride (PVdF), with a mass ratio of 90:10. The slurry was made using N-methylpyrrolidone (NMP) solution and was uniformly coated on nickel foam acting as current collector. The electrodes were dried at 60 °C in an oven for 8 hours to ensure complete evaporation of the NMP. The electrochemical test of the symmetric cell was carried out in a two-electrode cell configuration with coin-type cells. Both electrodes had a mass loading of ~3.3 mg with a thickness of 0.2 mm and a diameter of 16 mm. Glass microfiber filter paper was used as the separator in 6 M KOH aqueous electrolyte solution. The three-electrode measurement was performed with 3D-PGP-1 as the working electrode, a glassy carbon plate as the counter electrode and Ag/AgCl (3 M KCl) as the reference. All electrochemical measurements were carried out using a Bio-logic SP-300 potentiostat namely cyclic voltammetry (CV), chronopotentiometry (CP) and electrochemical impedance spectroscopy (EIS). The CV tests were carried out in the potential range of 0 to 1.6 V at different scan rates ranging from 5 mV s^{-1} to 100 mV s^{-1}. Electrochemical impedance spectroscopy (EIS) measurements were conducted in the frequency range from 0.1 Hz to 100 kHz with an open circuit potential (~0 V).

According to the galvanostatic charge–discharge tests based on a two-electrode cell, the gravimetric specific capacitance (C_{sp}: F g^{-1}), the maximum energy density (E_{max}: Wh kg^{-1}), and the power density (P_{max}: kW kg^{-1}) of the cell were calculated using equations 1 to 3 respectively:

$$C_{sp} = 4 \times I\Delta t/m\Delta V \quad (1)$$

$$E_{max} = 0.5C(\Delta V)^2 = (C_{sp} \times \Delta V^2)/28.8 \quad (2)$$

$$P_{max} = 3.6 \times E_{max}/\Delta t \quad (3)$$

where I is the discharge current (A), m is the total mass of the active material in both electrodes (g), Δt is the discharge time (s), and ΔV is the applied potential (V). The areal (C_{area}: F cm^{-2}) capacitances of 3D-PGP were calculated using equation 4:

$$C_{area} = 10^{-4} \times C_{sp}/A_{BET} \quad (4)$$

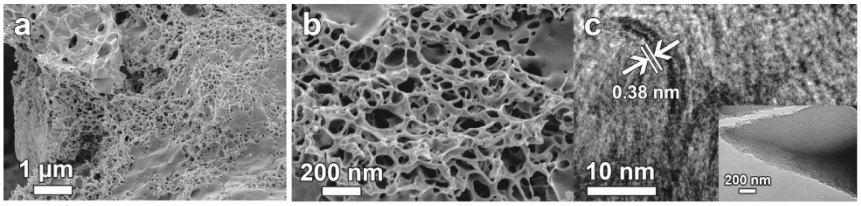

Fig. 1. SEM and TEM of 3D-PGP-1 sample: (a) low-magnification SEM image, (b) high-magnification SEM image and (c) TEM image.

where A_{BET} is the BET surface area ($m^2 g^{-1}$) of the 3D-PGP-1 sample. The energy (E_a: $Wh\,cm^{-2}$) and power (P_a: $kW\,cm^{-2}$) densities of the two electrode cell were calculated respectively using equation 5 and 6 below respectively:

$$E_a = (C_{area} \times \Delta V^2)/28.8 \quad (5)$$

$$P_a = 3.6 \times E_a/\Delta t \quad (6)$$

3. RESULTS AND DISCUSSION

Fig. 1 shows SEM and TEM micrographs of 3D-PGP-1 sample. SEM images of GF, 3D-PGP-2 and 3D-PGP-3 samples are shown in figure S1, in the supporting information. Fig. 1(a) shows a low-magnification image of 3D-PGP-1 sample, and Fig. 1(b) shows a high-magnification image of the sample, which reveals a highly dense and interconnected porous architecture which is beneficial in providing a large ion-accessible surface for fast ion transport for high performance supercapacitors. The TEM image (Fig. 1(c)) verifies that the pores are homogeneously and uniformly distributed throughout the highly porous structure of the sample with a d-spacing of about 0.38 nm as indicated by the distance between the white lines in the TEM image.

The mechanism of formation of the hydrogel which yielded the porous structure of 3D-PGP-1 sample could be explained as follows: The PVA, which is the template, consists of long molecular chains which are believed to promote physical cross-linking points with the PVP. The PVP promotes and ensures a high cross-linking density and denser packing of polymer chains in the PVP/PVA hydrogel network [20]. The deprotonating processes in the acid catalyzing medium enhances the formation of bonds between the two polymers. The hydroxyl OH groups of PVA readily deprotonate in an acidic medium, making a cross-link with carbonyl groups (CO) of PVP via hydrogen bonding [14]. Another form of cross linkage between the two polymers can occur as a result of free radicals produced at the main chains of both polymers. This can also be enhanced during the heating of the polymer mixtures. Thus other bonds can be formed via the free radicals of the PVP groups and the OH of PVA (as can be seen below in reaction Scheme 2) below leading to more cross-linking. This cross-linkage further assists in the interconnectivity and the porosity of the structure. The different repeating units in PVA and PVP also result in a steric stabilization of the hydrogel produced [21].

On the other hand the presence of graphene foam which has been shown to have excellent properties by Chen et al. [22], is believed to have a π-π or weak Van der Waal interaction with the hydrogel, which ensures a larger surface and enhanced conductivity. The activation of the preformed PVA/GF/PVP hydrogel by KOH further enhances the porosity of the hydrogel structure by the efficient intercalation of potassium ions in the carbon lattice of the polymer network. The role of KOH in the activation of carbon materials has been summarized as the result of a series of synergistic reactions, which include chemical activation, physical activation and carbon lattice expansion by the metallic K intercalation [23]. The resulting activated carbon obtained from the PVA/GF/PVP hydrogel after the carbonation process through annealing thus guaranteed a highly dense porosity which should be coupled with a highly improved conductive surface area.

The XPS elemental analysis and peak fitting results are shown in table S1 and S2 respectively in the supporting information. Carbon is considered the major element (89.4 at.%) in the sample, while oxygen takes the second place, the percentage of oxygen is 9.5 at. %. The sample also contains N at 1.1 at. %. The results of the peak fitting for the sample are shown in Fig. 2. The C1s region was fitted by four components corresponding to graphitic carbon, hydrocarbons (CH_x), alcoholic (C-O-) and/or carbon nitrogen structures (C-N-), and carboxyl or ester (COO). The graphitic carbon takes the largest fraction of the C1s region (0.45). The N1s region (Fig.. 2b) was fitted by one component corresponding to nitrile and/or pyrrole while the O1s region (Fig. 2c) was fitted by two components corresponding to C-O- and COO. The presence of all these functional groups on the surface of this activated carbon could prevent oxygen and hydrogen overpotential in aqueous electrolytes as mentioned by Bichat et al. [24].

The specific surface areas and pore size distributions of samples were measured by N_2 adsorption–desorption isotherms using the Barrett Joyner Halenda (BJH) method as shown in Fig. 3 for the 3D-PGP-1 sample, with other samples showing similar behaviour. It is observed that the 3D-PGP-1 sample shows a H4 isotherm that is characteristic of complex materials that contain micropores and mesopores. At high pressure, the inflection point occurs near completion of the first monolayer. The sample also exhibits a high Brunauer–Emmett–Teller surface area of 2994 $m^2 g^{-1}$. The average BJH pore size distribution (inset to the figure) is of 2 nm, with a substantial amount of mesopores present in the 3D-PGP-1 sample. The structural parameters, such as BET isotherm and pore volume of all the other samples are listed in Table S3 in the supporting information. Fig. 3(b) shows the XRD patterns for the 3D-PGP-1 powders. The wavelength used for the XRD analysis was Cu-Kα, 1·5405 Å. It is noted that all the XRD peaks are identified as graphite peaks (COD: 96-900-8570) which crystallize in the hexagonal structure with space group P63mc (186), and lattice parameters a = 2.4560 Å and c = 6.6960 Å. Figure S2 is the EDX of the 3D-PGP-1, which shows the presence of carbon only.

Figure S3 in the supporting information shows the Raman spectra of all as-synthesized samples. Figure S3 (a) shows the defect-free spectrum of GF with only two prominent peaks (G and 2D peaks) typical of graphene samples. This shows that the CVD-

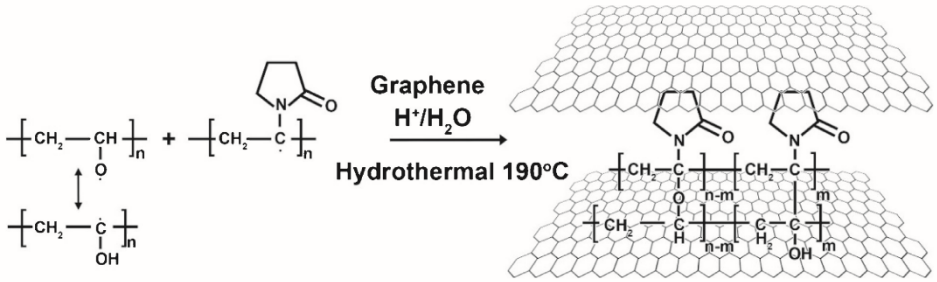

Scheme 2. Schematic of the reaction between PVA/GF/PVP in a hydrothermal system.

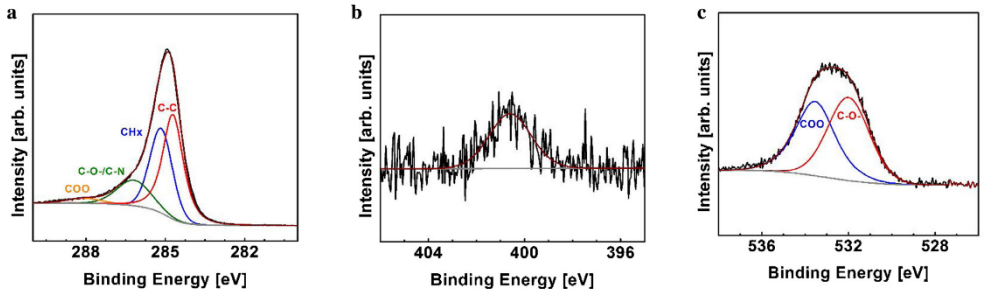

Fig. 2. XPS spectra of (a) C1s, (b) N1s and (c) O1s regions for 3D-PGP-1.

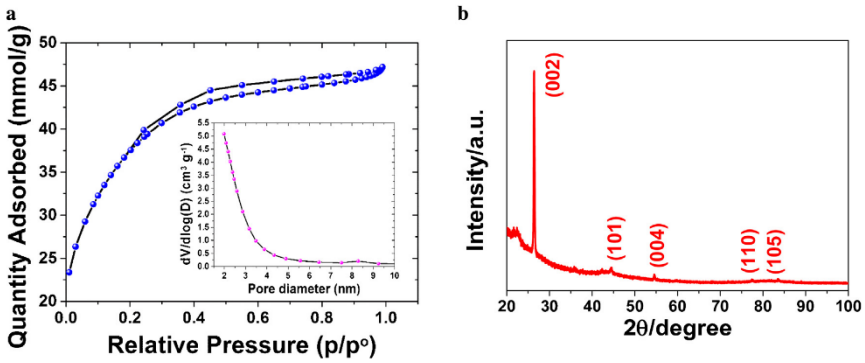

Fig. 3. (a) N_2 adsorption-desorption isotherm of the 3D-PGP-1 sample and (b) X-ray diffraction pattern of the 3D-PGP-1 sample.

grown GF consists of few layers. Figure S3 (b) shows the Raman spectra of the composites. Typically, all the Raman spectra show D and G bands, suggesting that the samples produced are made up of highly disordered graphitic structures. The D band is commonly ascribed to a series of structural defects, whereas the G band is observed in all graphitic structures. The intensity ratio of the D- and G-peak I_D /I_G is also used to estimate the concentration of sp^3 carbon relative to the concentration of sp^2 carbon.

The potential of the activated materials performance as an EDLC electrode was demonstrated using cyclic voltammetry (CV) and galvanostatic charge/discharge (CD) measurements in both three- and two- electrode cell configurations. Table S3 shows that the 3D-PGP-1 sample has superior listed properties as compared to the others, and hence based on this, it was the sample on which electrochemical measurements were done because its properties are ideal for such measurements. Herein, we show the results of

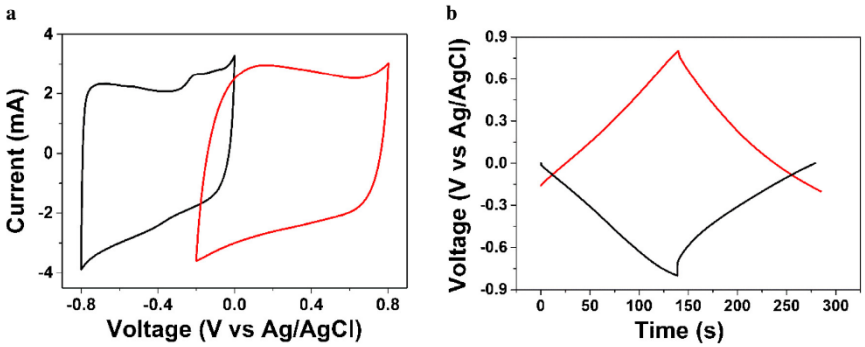

Fig. 4. (a) CV and (b) galvanostatic charge/discharge results the 3D-PGP-1 sample in a three-electrode system in the negative and positive voltage ranges.

the 3D-PGP-1 sample with SSA of 2994 $m^2 g^{-1}$. Fig. 4(a) shows the CV results of the 3D-PGP-1 as the active electrode material at two different voltage ranges of -0.8 - 0 V and -0.2 - 0.8 V vs Ag/AgCl. The CV curve in Fig. 4(a) is almost featureless and quasi-rectangular in these potential windows confirming the traditional double-layer capacitance characteristics. Fig. 4(b) shows the CD results of the 3D-PGP-1 sample in the three-electrode system; the same absolute values of the potential windows are shown. The specific capacitance values calculated from the CD in Fig. 4(b) are 175.27 $F g^{-1}$ for the negative potential and 182.32 $F g^{-1}$ for the positive potential. The variation in the values could be due to the distorted CV shape and possible increase in resistance as observed in the IR drop in the negative potential window. Due to these capacitance values, which might be related to the high SSA of this sample, further tests were done on a two-electrode symmetric configuration.

Fig. 5 presents the CV and Chronopotentiometry measurements of the symmetric AC/AC supercapacitor in a 6 M KOH electrolyte. Fig. 5(a) shows the CV curves of the symmetric cell at different scan rates, which range from 5 to 100 mV s^{-1} in a potential window of 1.6 V. The cell shows near-rectangular CV shapes at low scan rates, indicating ideal capacitive behavior, which demonstrates the formation of a double-layer capacitor and ideal polarization of the electrodes material. The shape of the CV indicates a pure capacitive characteristic behavior, suggesting reversible reaction at the electrode/electrolyte interface [25]. At a high scan rate, the CV shows a deviation from the pure EDLC shape with a characteristic resistive CV shape related to an increase in resistance attributed to the capacitance decay observed in Fig. 5(c). A symmetric triangular charge/discharge distinctive of ideal capacitor behavior was observed even at a high current density of 10 A g^{-1} (Fig. 5(b)). This linear behaviour indicates the reversible adsorption/desorption of ions at the electrode interface with a relatively small voltage drop. The gravimetric capacitance was 188 $F g^{-1}$ at a current density of 0.5 A g^{-1}, which can be expressed as areal capacitance from equation 4 as 6.28 μF cm^{-2}. These are reasonable values for double-layer capacitors and compare well with or are higher than previous values in the literature [5,26,27].

The Ragone plot and the specific capacitance as function of the current density of the symmetric device are shown in Fig. 5(c). The specific capacitance decreases from 188 $F g^{-1}$ to 111 $F g^{-1}$ with increasing current density from 0.5 to 10 A g^{-1}, retaining about 60% of the initial capacitance. We attribute this to the unique nanoporous architecture, where the wide meso/macro pore range from 10–60 nm could buffer the amount of electrolyte ions and promote ion transfer into the interior pore surface of the micropores at higher current densities [28]. The maximum energy density of the device was recorded as 17 Wh kg^{-1} with power density of 400 W kg^{-1} at a current density of 0.5 A g^{-1}. However, at this point it is worth stating that the gravimetric capacitance does not reflect the true performance metrics of the porous electrode materials [29] but rather the areal capacitance calculated according to equations 5 and 6. A high areal capacitance of 6.3 μF cm^{-2} was obtained, which resulted in high energy and power densities of 0.56 μWh cm^{-2} (16.71 Wh kg^{-1}) and 13.39 μW cm^{-2} (401 W kg^{-1}) respectively. This excellent electrochemical

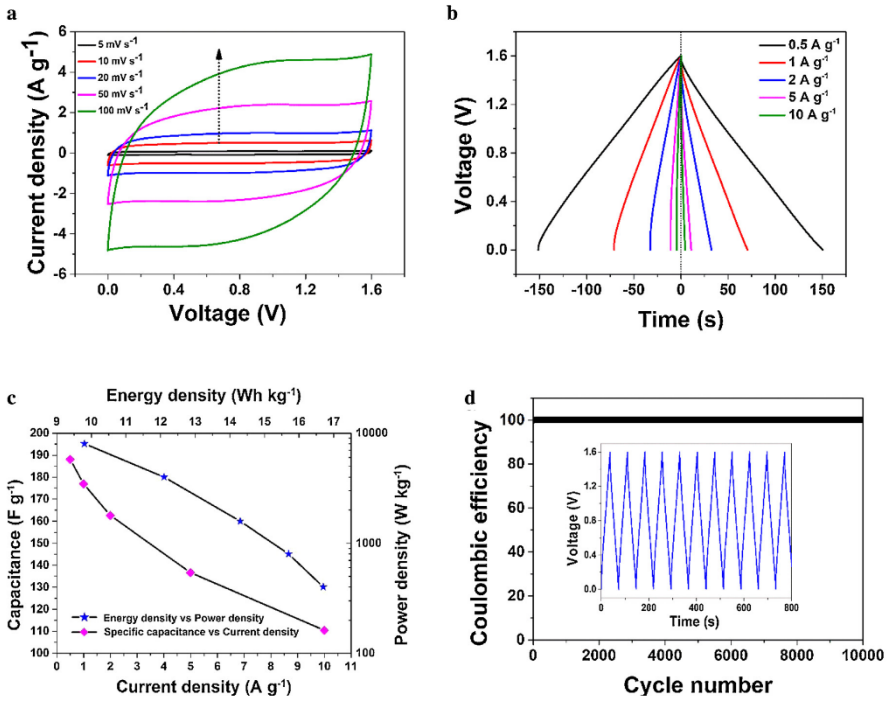

Fig. 5. (a) CV curves at scan rates from 5 to 100 mV s^{-1}, (b) The galvanostatic charge/discharge curves from 0.5 to 10 A g^{-1}, (c) Ragone plot and the specific capacitance as function of the current density, and (d) Cycle stability at a constant current density of 2 A g^{-1}.

performance of the 3D-PGP-1 electrode material was attributed to: (i) The ability of the material to work in both the negative and positive potential window, thus extending the total potential of the fabricated cell; (ii) the unique porous architecture of the 3D-PGP-1 material and (iii) the large accessible surface area, which consists of micropores for trapping the ions and adequate proper-sized mesopores, which enable rapid and reversible ion transport [30]. Although, it is difficult to compare accurately the performance of all types of supercapacitors due to a large number of varying parameters such as material mass loadings and testing configurations, but a rough estimation and comparison show that the results presented in this work are good or even better than those in some previous reports on symmetric carbons devices in aqueous media [26,31].

As shown in Fig. 5(d), the symmetric cell shows no capacitance loss after 10,000 cycles at a current density of 2 A g^{-1}, demonstrating that repeated charge/discharge cycles never caused a significant structural change in the 3D-PGP-1 electrode. Nevertheless, a small increase in the capacitance (~0.1 %) was observed after the cycling process. A similar increase was observed by Ren et .al [32]

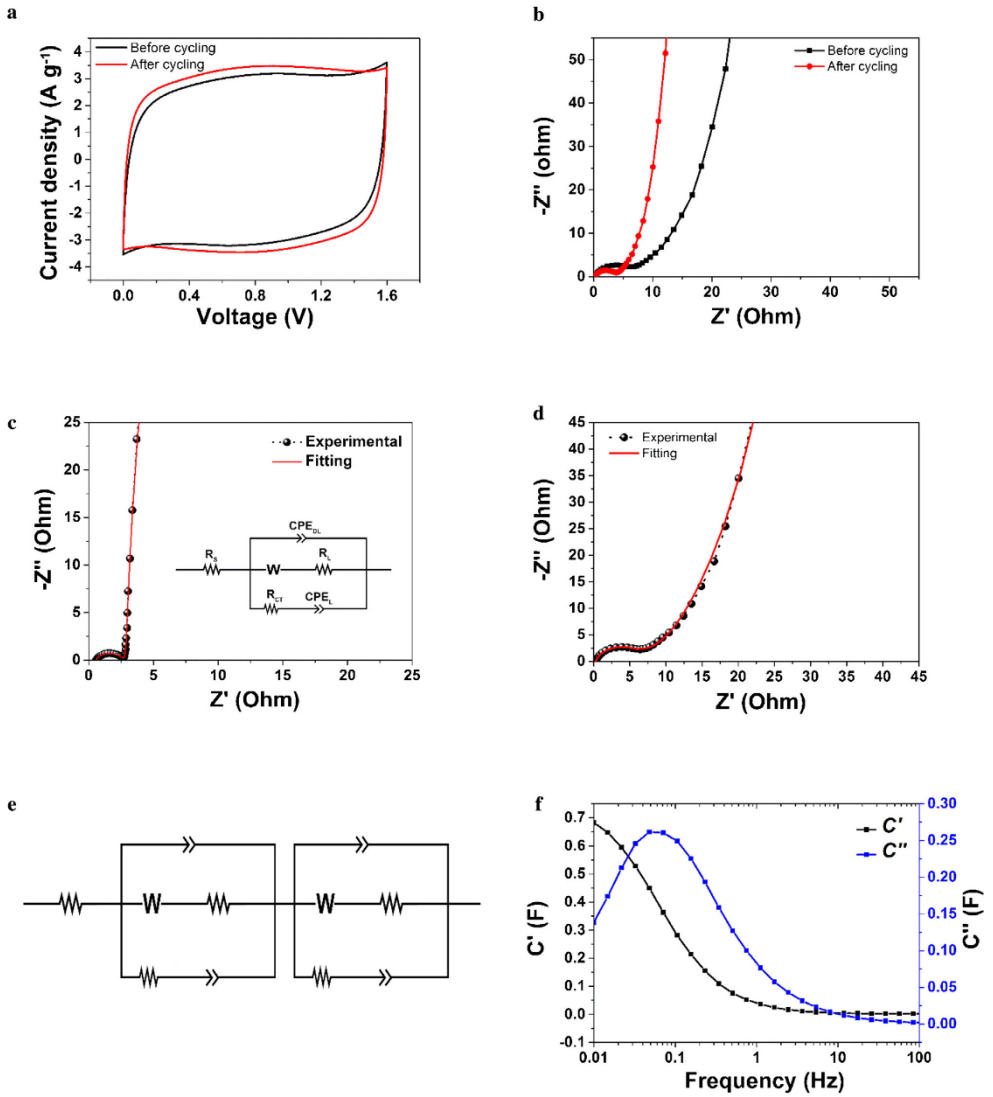

Fig. 6. (a) CV curves at a scan rate of 20 mV s^{-1} before and after cycling, (b) EIS before and after cycling, (c) EIS plot and fitting curve for single electrode with the inset to the figure being equivalent circuit used for fitting the data, (d) EIS plot and fitting curve for the symmetric cell, (e) Equivalent circuit used for fitting of the symmetric cell data in (d) and (f) the real and the imaginary part of the cells capacitance as a function of frequency.

which was tentatively attributed to the swelling of the graphene at some defective sites. This promoted the intercalation of electrolyte ions in the space created by the swelling, or the creation of more pores after many CD cycles leading to a more accessible surface area and hence an increase in efficiency [32].

The CV curves at a scan rate of 20 mV s^{-1} before and after cycling are shown in Fig. 6(a). The cell showed an improved rate capability after 10, 000 cycles, which indicates that there was no decay in the capacitive performance of the cell, as shown in Fig. 5(d). Furthermore, no significant change to or degradation of the unique microstructure of the porous electrodes was revealed. In order to confirm the improved electrochemical performance of the cell after cycling, EIS measurements were also done before and after cycling (Fig. 6(b)). In general, at high frequencies, current flow in the cell is a result of the capacitance of the electrode materials. The intercept on the real axis (left side of the semicircle) of the Nyquist plot in the high-frequency region provides information about the combined resistance of the electrolyte, the contact leads and the porous carbon materials also known as the equivalent series resistance (ESR), denoted by R_S. The semicircle is a result of the charging of the double layer which appeared in the medium-frequency region. This is attributed to the interfacial charge transfer resistance and mass transport through the porous architecture of the material, and is denoted by R_{CT}. The Nyquist plot shows a deviation from the vertical line in the low-frequency region, indicating a near-ideal capacitive behavior. This represents the diffusion of ions to the interface between electrode and electrolyte. At these low frequencies, the current flowing through the cell usually has resistance and a Warburg impedance characteristic element denoted by W, which is expressed as $A/(j\omega)^{0.5}$ [33,34] where A is the Warburg coefficient and ω is the angular frequency.

The relatively low value of the R_S (0.29 Ω) of the electrode material studied here reveals the fair conductivity and high quality of the 3D-PGP-1 electrodes. After 10,000 cycles there is a decrease in the semicircle indicating a decrease in the R_{CT} value from 6.40 to 3.88 Ω. This observation is expected as EIS is a more sensitive technique, and it also confirms the results observed from the CV after cycling from the rectangular shape.

The capacitive behavior of the 3D-PGP-1 capacitor was also confirmed using impedance analysis. Fig. 6 shows the Nyquist plot in the frequency range of 100 kHz to 10 mHz measured at the open circuit potential (0 V). The performance analyses based on Nyquist plot interpretations were represented and modelled by a modified Randles circuit [35] with a set of resistors and capacitors in series and parallel to extract the series and charge-transfer resistances. The fitting of the impedance expression data obtained from the experimental data of the Nyquist plot was performed with a fitting program ZFIT/EC-Lab version 10.38 and is represented in Fig. 6(c) along with the experimental data for a single electrode. In the equivalent circuit, a solution resistance (R_s) is connected in series with a constant phase element (CPE_{DL}), and the CPE_{DL} is connected in parallel with the charge transfer resistance (R_{CT}) and the mass capacitance (CPE_L), while the Warburg and the leakage current resistance, R_L are all in series with R_s. CPE_{DL} represents the double-layer capacitance related to the porous electrode. CPE_L represents the ideal polarizable capacitance which would give rise to a straight line parallel to the imaginary axis. The deviation from the ideal situationsuggests that a resistive element R_L is associated with CPE_L. The impedance of CPE_{DL} is defined as $T(j\omega)^{-n}$ [34] where T and n are frequency-independent constants and ω is the angular frequency. The exponent n is a correction factor which is related to the capacitive kinetics and roughness of electrode surfaces. The values for n range between 0 and 1; n = 1 denotes that the CPE is an ideal capacitor, for n = -1, CPE behaves as an inductor, while n = 0 and 0.5 denote a resistance and Warburg behavior respectively [34].

Table 1
Fitting parameters for the single electrode

R_S (Ω)	Q_{DL} ($F.s^{(a-1)}$)	a_{DL}	A_W ($\Omega.s^{0.5}$)	R_L (Ω)	R_{CT} (Ω)	Q_L ($F.s^{(a-1)}$)	a_L
0.300	0.0002	1	75.34	0.413	2.314	0.433	1

$X^2 = 0.4, X/\sqrt{N} = 0.1, PEP_{DL} - Q_{DL}, CPL_L - Q_L, a_{DL} - n$

Fig. 6(c) shows the Nyquist plot of the 3D-PGP-1 sample and its fitting using circuit in the inset to the figure obtained in a three-electrode configuration, while Fig. 6(d) shows the Nyquist plot and its fitting using the circuit in Fig. 6(e) of the symmetric cell of the 3D-PGP-1 sample. Both fittings show that the impedance spectroscopy of the electrodes fits perfectly with the experimental data. The inset to Fig. 6(c) shows the equivalent circuit of the single electrode, while Fig. 6(e) shows the equivalent circuit diagram of the symmetric cell by combining the two sets of fitting parameters listed in Table 1 for a single electrode in series. The R_S and R_{CT} values and other parameters fit perfectly without any further adjustment, which indicates an optimized minimization of experimental data with the design of the cell with an error of 0.1. X^2 represents the criterion for minimization of the fit. $X/\sqrt{N}$, where N is the number of points, is a normalized expression of X^2, whose value is independent of the number of points and is represented as the error above.

The real and imaginary parts of the capacitance of the cell as a function of the frequency are shown in Fig. 6(f). C′ represents the real accessible capacitance of the cell at the corresponding frequency (0.01 Hz), representing the deliverable capacitance which is 0.68 F, while C″ represents the energy loss due to the irreversible process of the electrodes. It is also used to define the transition frequency between pure capacitive and pure resistive behavior of the 3D-PGP-1 sample [36]. A small knee in the figure at a frequency of 0.1 Hz is an indication that the full capacitance of the cell can be reached at a slow recharging time $\tau = 1/f$, which is 10 s in this case. This is an indication of the excellent and unique porous structures with a good distribution of micro- and mesopores which provide the highly accessible pathway to ions from the electrolyte. Figure S4 in the supporting information presents the phase angle as a function of frequency. The phase angle for the electrodes is about ∼−80°, which is close to −90° and which defines ideal capacitive response.

4. CONCLUSION

In this work, we reported on the successful hydrothermal synthesis of three-dimensional porous carbons derived from various carbon precursors. The 3D material exhibited an interconnected carbon network with a superior surface area of 2994 $m^2 g^{-1}$. The symmetric supercapacitor electrodes fabricated from these materials exhibited excellent electrochemical storage properties, including a high areal capacitance of 6.3 μF cm^{-2}, high energy of 0.56 μWh cm^{-2} (16.71 Wh kg^{-1}) and power densities of 13.39 μW cm^{-2} (401 W kg^{-1}) with a stable operation voltage between 0 and 1.6 V and excellent long-term stability at a current density of 2 A g^{-1}. The stable potential window in aqueous KOH electrolyte was attributed to the presence of functional groups in the porous carbon material which could prevent the over potential of di-hydrogen and di-oxygen evolution in water-containing electrolyte. We believe that these interesting and promising results give the potential of these three-dimensional porous carbons the potential to be excellent electrode materials for high energy supercapacitors.

ACKNOWLEDGEMENT

This work is based upon research supported by the South African Research Chairs Initiative (SARChi) in Carbon Technology and Materials of the Department of Science and Technology (DST) and the National Research Foundation (NRF). Any opinions, findings and conclusions or recommendations expressed in this work are those of authors, and the NRF and the DST do not accept any liability with regard thereto. F. Barzegar and D. Y. Momodu acknowledge financial support from the University of Pretoria and the NRF for their PhD bursaries. A. Bello and O.O. Fashedemi acknowledge the University of Pretoria's financial support for their Postdoctoral fellowship. Prof. Yury Gogotsi's group at Drexel University is thanked for the help in XPS measurements.

Appendix A. Supplementary data

Supplementary data associated with this article can be found, in the online version, at http://dx.doi.org/10.1016/j.electacta.2015.08.148.

References

[1] B.E. Conway, Electrochemical Supercapacitors: Scientific Fundamentals and Technological Applications, Kluwer Academic/Plenum, New York, 1999.
[2] E. Frackowiak, F. Béguin, F.F. Frackowiak, E. Béguin, Carbon materials for the electrochemical storage of energy in capacitors, Carbon 39 (2001) 937–950.
[3] J. Yan, Q. Wang, T. Wei, Z. Fan, Recent Advances in Design and Fabrication of Electrochemical Supercapacitors with High Energy Densities, Adv. Energy Mater. 4 (2014) 1–43.
[4] M. Galiński, A. Lewandowski, I. Stępniak, Ionic liquids as electrolytes, Electrochim. Acta 51 (2006) 5567–5580.
[5] K. Fic, G. Lota, M. Meller, E. Frackowiak, Novel insight into neutral medium as electrolyte for high-voltage supercapacitors, Energy Environ. Sci. 5 (2012) 5842–5850.
[6] V. Khomenko, E. Raymundo-Piñero, F. Béguin, A new type of high energy asymmetric capacitor with nanoporous carbon electrodes in aqueous electrolyte, J. Power Sources 195 (2010) 4234–4241.
[7] D.-W. Wang, F. Li, M. Liu, G.Q. Lu, H.-M. Cheng, 3D aperiodic hierarchical porous graphitic carbon material for high-rate electrochemical capacitive energy storage, Angew. Chem. Int. Ed. Engl. 47 (2008) 373–376.
[8] C. Zhang, K.B. Hatzell, M. Boota, B. Dyatkin, M. Beidaghi, D. Long, et al., Highly porous carbon spheres for electrochemical capacitors and capacitive flowable suspension electrodes, Carbon 77 (2014) 155–164.
[9] B. You, L. Wang, N. Li, C. Zheng, Improving the Energy Storage Performance of Graphene through Insertion of Pristine CNTs and Ordered Mesoporous Carbon Coating, ChemElectroChem 1 (2014) 772–778.
[10] B. You, P. Yin, J. Zhang, D. He, G. Chen, F. Kang, et al., Hydrogel-derived non-precious electrocatalysts for efficient oxygen reduction, Sci. Rep. 5 (2015) 11739.
[11] B. You, P. Yin, L. An, Multifunctional electroactive heteroatom-doped carbon aerogels, Small 10 (2014) 4352–4361.
[12] J. Zhang, G. Chen, Q. Zhang, F. Kang, B. You, Self-Assembly Synthesis of N-Doped Carbon Aerogels for Supercapacitor and Electrocatalytic Oxygen Reduction, ACS Appl. Mater. Interfaces 7 (2015) 12760–12766.
[13] N. Rajeswari, S. Selvasekarapandian, S. Karthikeyan, C. Sanjeeviraja, Y. Iwai, J. Kawamura, Structural, vibrational, thermal, and electrical properties of PVA/PVP biodegradable polymer blend electrolyte with CH_3COONH_4, Ionics (Kiel) 19 (2013) 1105–1113.
[14] A.K. Swain, D. Bahadur, Enhanced Stability of Reduced Graphene Oxide Colloid Using Cross-Linking Polymers, J. Phys. Chem. C 118 (2014) 9450–9457.
[15] D.J.T. Hill, A.K. Whittaker, Water diffusion into radiation crosslinked PVA–PVP network hydrogels, Radiat. Phys. Chem. 80 (2011) 213–218.
[16] R. Meena, R. Lehnen, B. Saake, Microwave-assisted synthesis of kC/Xylan/PVP-based blend hydrogel materials: physicochemical and rheological studies, Cellulose 21 (2013) 553–568.
[17] A. Bello, O.O. Fashedemi, J.N. Lekitima, M. Fabiane, D. Dodoo-Arhin, K.I. Ozoemena, et al., High-performance symmetric electrochemical capacitor based on graphene foam and nanostructured manganese oxide, AIP Adv. 3 (2013) 082118.
[18] L. Zhang, F. Zhang, X. Yang, G. Long, Y. Wu, T. Zhang, et al., Porous 3D graphene-based bulk materials with exceptional high surface area and excellent conductivity for supercapacitors, Sci. Rep. 3 (2013) 1408.
[19] Y. Zhu, S. Murali, M.D. Stoller, K.J. Ganesh, W. Cai, P.J. Ferreira, et al., Carbon-based supercapacitors produced by activation of graphene, Science 332 (2011) 1537–1541.
[20] Y. Shi, D. Xiong, Microstructure and friction properties of PVA/PVP hydrogels for articular cartilage repair as function of polymerization degree and polymer concentration, Wear 305 (2013) 280–285.
[21] Z. Ping, Q.T. Nguyen, J. Néel, Investigations of poly(vinyl alcohol)/poly(N-vinyl #24Ω24#pyrrolidone) blends, 2. Influence of the molecular weights of the polymer components on crystallization, Makromol Chem. 191 (1990) 185–198.
[22] Z. Chen, W. Ren, L. Gao, B. Liu, S. Pei, H.-M. Cheng, Three-dimensional flexible and conductive interconnected graphene networks grown by chemical vapour deposition, Nat. Mater. 10 (2011) 424–428.
[23] J. Wang, S. Kaskel, KOH activation of carbon-based materials for energy storage, J. Mater. Chem. 22 (2012) 23710–23725.
[24] M.P. Bichat, E. Raymundo-Piñero, F. Béguin, High voltage supercapacitor built with seaweed carbons in neutral aqueous electrolyte, Carbon 48 (2010) 4351–4361.
[25] Z.-S. Wu, W. Ren, D.-W. Wang, F. Li, B. Liu, H.-M. Cheng, High-energy MnO2 nanowire/graphene and graphene asymmetric electrochemical capacitors, ACS Nano 4 (2010) 5835–5842.
[26] L. Demarconnay, E. Raymundo-Piñero, F. Béguin, A symmetric carbon/carbon supercapacitor operating at 1. 6V by using a neutral aqueous solution, Electrochem. Commun. 12 (2010) 1275–1278.
[27] H. Wang, Z. Xu, A. Kohandehghan, Z. Li, K. Cui, X. Tan, et al., Interconnected carbon nanosheets derived from hemp for ultrafast supercapacitors with high energy, ACS Nano 7 (2013) 5131–5141.
[28] W. Tian, Q. Gao, Y. Tan, K. Yang, L. Zhu, C. Yang, et al., Bio-inspired beehive-like hierarchical nanoporous carbon derived from bamboo-based industrial by-product as a high performance supercapacitor electrode material, J. Mater. Chem. A 3 (2015) 5656–5664.
[29] Y. Gogotsi, P. Simon, True performance metrics in electrochemical energy storage, Science 334 (2011) 917–918.
[30] M. Zhi, F. Yang, F. Meng, M. Li, A. Manivannan, N. Wu, Effects of Pore Structure on Performance of An Activated-Carbon Supercapacitor Electrode Recycled from Scrap Waste Tires, ACS Sustain. Chem. Eng. 2 (2014) 1592–1598.
[31] B. Xu, F. Wu, R. Chen, G. Cao, S. Chen, G. Wang, et al., Room temperature molten salt as electrolyte for carbon nanotube-based electric double layer capacitors, J. Power Sources 158 (2006) 773–778.
[32] G. Ren, X. Pan, S. Bayne, Z. Fan, Kilohertz ultrafast electrochemical supercapacitors based on perpendicularly-oriented graphene grown inside of nickel foam, Carbon 71 (2014) 94–101.
[33] Y. Zhou, H. Xu, N. Lachman, M. Ghaffari, S. Wu, Y. Liu, et al., Advanced asymmetric supercapacitor based on conducting polymer and aligned carbon nanotubes with controlled nanomorphology, Nano Energy 9 (2014) 176–185.
[34] H. Li, J. Wang, Q. Chu, Z. Wang, F. Zhang, S. Wang, Theoretical and experimental specific capacitance of polyaniline in sulfuric acid, J. Power Sources 190 (2009) 578–586.
[35] C. Masarapu, H.F. Zeng, K.H. Hung, B. Wei, Effect of temperature on the capacitance of carbon nanotube supercapacitors, ACS Nano 3 (2009) 2199–2206.
[36] P.L. Taberna, P. Simon, J.-F.F. Fauvarque, Electrochemical Characteristics and Impedance Spectroscopy Studies of Carbon-Carbon Supercapacitors, J. Electrochem. Soc. 150 (2003) A292–300.

Supplementary Information

Synthesis of 3D porous carbon based on cheap polymers and graphene foam for high-performance electrochemical capacitors

Farshad Barzegar[a], Abdulhakeem Bello[a], Omobosede. O Fashedemi[b], Julien. K. Dangbegnon[a], Damilola. Y. Momodu[a], Fatemeh. Taghizadeh[a], and Ncholu. Manyala[a*]

[a]Department of Physics, Institute of Applied Materials, SARCHI Chair in Carbon Technology and Materials, University of Pretoria, Pretoria 0028, South Africa.

[b]Department of Chemistry, University of Pretoria, Pretoria 0002, South Africa.

***Email address**: ncholu.manyala@up.ac.za (N. Manyala)

Corresponding author Tel: +27 (0)12 420 3549, Fax: +27 (0)12 420 2516

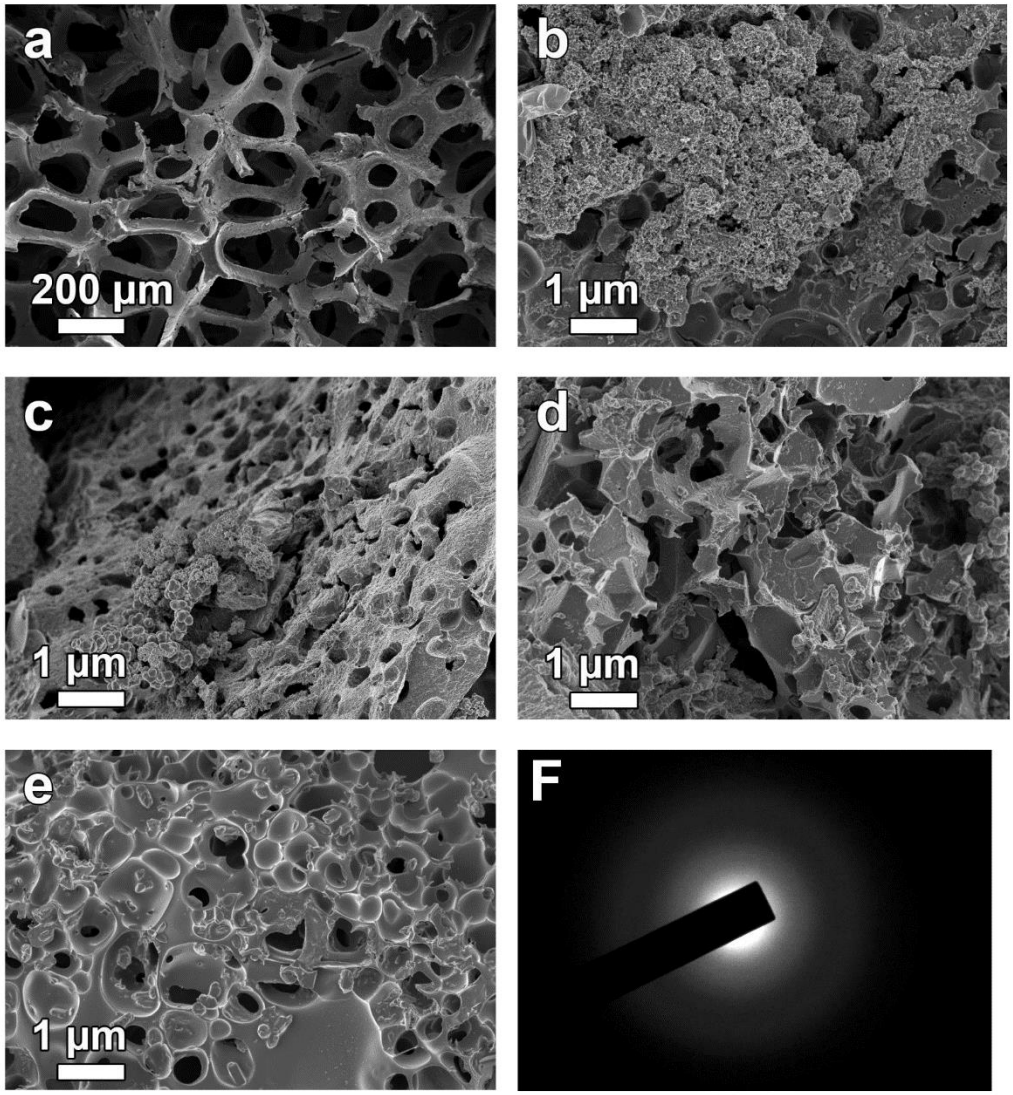

Supplementary figure S1. SEM images of (a) GF (b) 3D-PG-1 (c) 3D-PG-2 (d) 3D-PG-3 (e) 3D-PGP-2 (f) SAED image of 3D-PGP-1

Supplementary Table S1. Elemental analysis of 3D-PGP-1

C at.%	N at.%	O at.%
89.4 ± 0.1	1.1 ± 0.1	9.5 ± 0.1

Supplementary Table S2. XPS peak fitting results for 3D-PGP-1

Region	BE [eV]	FWHM [eV]	Fraction	Assigned to	Reference
C 1s	284.7	0.9	0.45	C-C	[1]
	285.2	1.0	0.36	CH_x	[2]
	286.2	1.5	0.16	C-O-/C-N	[1]
	288.1	1.5	0.03	COO	[1]
N 1s	400.6	2.1	1.00	Nitrile/Pyrrole	[3]
O 1s	532.0	2.3	0.53	C-O-	[1]
	533.5	2.1	0.47	COO	[1]

The EDX below shows that the 3D-PGP-1 sample consist mainly of carbon with little or no traces of impurities.

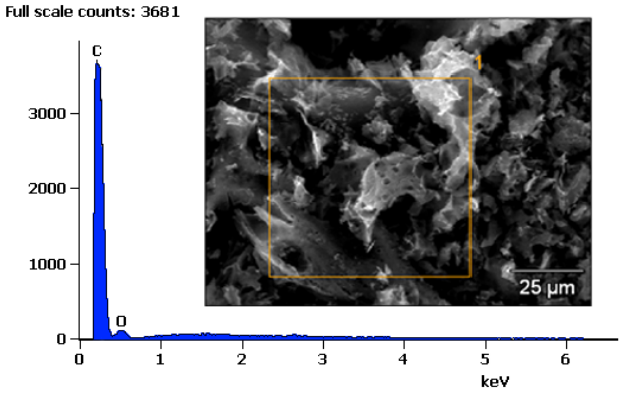

Supplementary figure S2. EDX pattern of 3D-PGP-1

The Raman spectra of the GF show the two prominent G and 2D peaks at 1582.2 cm^{-1} and 2705.7 cm^{-1}, respectively. The relative intensity 2D/G ratio of 1.2 and FWHM of 38.8 cm^{-1} were attributed to few layer graphene. The absence of the D-peak (disorder) at 1350 cm^{-1} showed that the graphene foam was of good quality, with a low defect density. SEM shows the three-dimensional (3D) porous network structure of the GF after CVD synthesis.

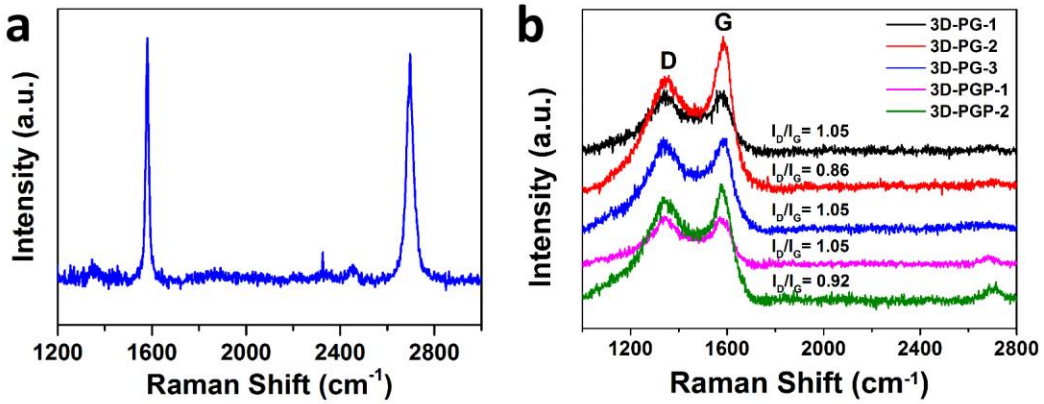

Supplementary figure S3. Raman spectra (a) GF and (b) 3D-PG-1, 3D-PG-2, 3D-PG-3, 3D-PGP-1, 3D-PGP-2.

These spectra were investigated using a Jobin Yvon Horiba TX 6400 micro-Raman spectrometer with a 514 nm argon excitation laser (1.5 mW laser power on the sample to avoid possible thermal effects). The ratio of the I_D and I_G intensity peaks were used to approximate the degree of graphitization.

The structural properties such as BET and pore volume of the produced materials with different ration of GF is summarized in Table S1. BET was measured based on adsorption branch in the relative pressure range (P/P_0) of 0.01 to 0.2.

Supplementary Table S3. BET and Pore volume of all the samples

Sample	BET ($m^2 g^{-1}$)	Pore volume ($cm^3 g^{-1}$)
3D-PG-1	502	0.026548
3D-PG-2	673	0.112935
3D-PG-3	1063	0.131153
3D-PGP-1	2994	0.455646
3D-PGP-2	1040	0.248939

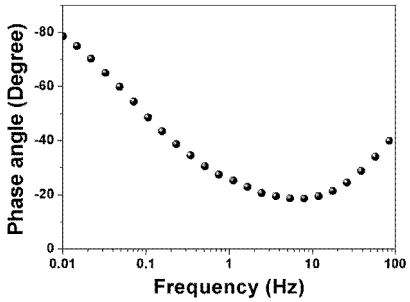

Supplementary figure S4. the phase angle versus frequency of the symmetric cell in 6 M KOH electrolyte. Showing a phase angle of ~-80 ° which is close to -90° indicating a nearly ideal capacitive behaviour.

References

[1] A.P. Terzyk, The influence of activated carbon surface chemical composition on the adsorption of acetaminophen (paracetamol) in vitro, Colloids Surfaces A Physicochem. Eng. Asp. 177 (2001) 23–45.

[2] R.J.J. Jansen, H. van Bekkum, XPS of nitrogen-containing functional groups on activated carbon, Carbon N. Y. 33 (1995) 1021–1027.

[3] P.M. Jayaweera, E.L. Quah, H. Idriss, Photoreaction of Ethanol on TiO2(110) Single-Crystal Surface, J. Phys. Chem. C. 111 (2007) 1764–1769.

4.1.1.3 Concluding Remarks

In summary, hydrothermal synthesis of 3D-PGP porous carbons, derived from various carbon precursors, with a very high surface area of 2994 m^2 g^{-1} has been successfully produced. The symmetric supercapacitor electrodes fabricated from this material showed excellent electrochemical storage properties, including a high specific capacitance of 188 F g^{-1}, high energy density of 16.71 Wh kg^{-1} and power density of 401 W kg^{-1} at 0.5 A g^{-1} with a stable operating voltage of 1.6 V and excellent long-term stability at a current density of 2 A g^{-1}. These are interesting and promising results which shows that 3D-PGP carbons electrode could be excellent materials for high energy supercapacitors applications.

4.1.2 Effect of different carbon material on polymer based AC and their applications in high performance supercapacitors electrodes

4.1.2.1 Introduction

In section 4.1.1, activated carbon base on low cost polymer with GF was presented. This section present results obtained when used in the previous section GF was replaced with other carbon materials such as carbon nanotube (CNT) and expanded graphite (EG) in the polymer matrix. The morphological, structural and electrochemical properties of the synthesized ACs materials were studied. The produced material were designated ACEG when 100 mg of EG added into PVA/PVP matrix solution, ACGF when 100 mg of CNTs was added to the PVA/PVP matrix

solution and 3D-PGP-1 when 100 mg of GF was added to the PVA/PVP matrix solution.

4.1.2.2 Result and discussions

A publication obtained from this work which details all the processes with the supporting information from the article is attached.

Electrochimica Acta 186 (2015) 277–284

Contents lists available at ScienceDirect

Electrochimica Acta

journal homepage: www.elsevier.com/locate/electacta

Effect of addition of different carbon materials on hydrogel derived carbon material for high performance electrochemical capacitors

Farshad Barzegar[a], Abdulhakeem Bello[a], Ouanassa Guellati[b], Damilola Y. Momodu[a], Aicha Harat[b], Julien K. Dangbegnon[a], Mohamed Guerioune[b], Ncholu Manyala[a,*]

[a] Department of Physics, Institute of Applied Materials, SARCHI Chair in Carbon Technology and Materials, University of Pretoria, Pretoria 0028, South Africa
[b] LEREC Laboratory, Department of Physics, Badji Mokhtar University of Annaba, Annaba 23000, BP. 12, Algeria

ARTICLE INFO

Article history:
Received 14 July 2015
Received in revised form 28 October 2015
Accepted 30 October 2015
Available online 3 November 2015

Keywords:
activated carbon
electrical double layer capacitor
specific surface area

ABSTRACT

Activated carbon (AC) materials derived from addition of graphene foam, carbon nanotube and expended graphite mixed with polyvinyl alcohol and polyvinylpyrrolidone were synthesized and tested for supercapacitor application. Although the AC obtained from expended graphite shows the smallest specific surface area (SAA), it exhibits the highest electrical double layer capacitance (EDLC) performance with high rate capability and specific capacitance. This material tested in the symmetric configuration works in a large potential window of 1.6 V. More interestingly, the device made out this material gets better in terms of electrochemical performance when subjected to ageing effect with voltage holding for 100 hours. Some tentative reasons for such discrepancy between the SAA and the EDLC are explained.

1. Introduction

The increasing demand for sustainable sources of energy for numerous applications has generated the need for the design and fabrication of efficient as well as reliable energy storage systems which could meet the requirements of present day technological developments. Supercapacitors (SCs) have been considered as potential energy storage devices suitable for such advanced applications due to their fascinating properties, which include high power density long cycle life and low maintenance cost when compared to other common storage devices like the conventional capacitors and batteries currently in use [1–3].

Supercapacitors can be generally classified into two types based on the charge storage mechanisms of the active materials used. These include the electric double-layer capacitors (EDLCs, composed of mainly carbonaceous material with a high surface area) based on reversible adsorption of ion across the electrode/electrolyte interface when biased and the faradic materials composed of mainly redox materials such as transition metal oxides/hydroxides, conducting polymers etc. [3]. SCs are however characterized with low energy densities ($<10\,Wh\,kg^{-1}$) as compared to batteries which creates a major setback and has limited their use in applications such as backup power sources, hybrid electric vehicles, renewable energy systems and industrial energy management [4–6]. To overcome this problem, many research activities have focused on developing nanostructured active electrode materials with reasonable electrical conductivity, surface area and porosity to increase the energy density without sacrificing their intrinsic high-power density and cycle life [7–9]. Furthermore, increased energy densities can also be attained by exploring different electrolytes with large potential window such as ionic or organic electrolytes. For this reason, SCs are projected with the propensity to have both high power and energy densities if the entire device design is effectively optimized.

Recent studies have shown the fabrication of high performance SCs to be linked to materials with porous morphology containing available mesopores and micropores required for efficient charge transport and storage [10–12]. The pore structure, surface area, size of the electrolyte ions and the pore size distribution governs the measured capacitance, energy storage and power delivery capability of the electrode material [13,14]. Detailed information on the pores sites are directly related to the specific surface area (SSA) and pore size distribution (PSD) obtained from the Brunauer–Emmett–Teller (BET) analysis even though no direct relationship between the capacitance and SSA of the active electrode material has so far been fully established [14,15].

Activated carbons (ACs) are the most widely used material for EDLC applications due to their highly porous nature, high specific

* Corresponding author. Tel.: +27 0 12 420 3549; fax: +27 0 12 420 2516.
E-mail address: ncholu.manyala@up.ac.za (N. Manyala).

http://dx.doi.org/10.1016/j.electacta.2015.10.189
0013-4686/

surface area (SSA), chemical stability, relatively low synthesis cost, adjustable structural properties, and electrical conductivity etc. [9]. The recent cost-effective synthesis method for producing large amounts of activated carbon with highly tunable properties is by the chemical and physical activation technique of carbon-based materials and polymers [16–19]. The chemical treatment usually yields aerogel or hydrogel materials while the physical activation leads to the formation of porous activated carbons and is commonly done with KOH, $ZnCl_2$ and H_3PO_4. For example, the formation mechanism of activated carbon using KOH has been attributed to carbon gasification associated with the removal of carbon dioxide (CO_2) and the oxygen related material contained in the matrix which reacts with carbon atoms to open up closed pores and enlarge existing micropores during the activation process [17,20,21].

For this reason, optimizing the micro/meso-porous architecture as well as the conductivity of activated carbon is ideal in order to improve the overall device electrochemical performance. Recent reports by researchers [13,18,19,22] clearly show that in order to achieve this, conducting carbon material additives need to be integrated with the main carbon source for producing activated carbons. Although numerous studies have been reported which adopt different carbon additives to the main polymer matrix to enhance the SSA, there are very few or no studies which compares different carbon additives as a way of perfecting the intrinsic properties of the fabricated activated carbon.

In this study, graphene foam (GF), carbon nanotube (CNT) and expanded graphite (EG) samples were integrated into the polyvinyl alcohol (PVA) and polyvinylpyrrolidone (PVP) polymer to obtain various types of activated carbon samples. A subsequent study on the morphological, structural and electrochemical properties of the synthesized products is carried out to fully understand the effect of introducing the different carbon material additives. Analysis of the scanning microscopy images reveal the presence of a notably large amount of pores in the activated carbon sample containing expanded graphite denoted as ACEG, which is confirmed from the micropore volume results displayed. Notably, the ACEG electrode when tested in a full cell configuration with the least surface area showed a superior electrochemical performance from the electrochemical tests compared to activated carbon with GF (ACGF) and activated carbon with CNTs (ACCNT). These results are a considerable improvement over our earlier work on activated carbon nanostructures for supercapacitor applications [19], wherein a similar KOH activation approach was adopted to synthesize AC electrodes in a symmetric configuration. These results show the potential application of polymer based activated carbons with high energy density as suitable electrodes for EDLCs.

2. Experimental

2.1. Synthesis and activation

Scheme 1 presents the preparation process of activated carbons. Briefly, graphene foam (GF) and carbon nanotube (CNT) were first prepared by chemical vapor deposition (CVD) following the procedure used in our previous works [23,24]. The expanded graphite (EG) samples were synthesized by exfoliation of expandable graphite in a quartz boat using a microwave oven at a power of 900 W, irradiated for 1 minute. The hydrogels were synthesised via the hydrothermal process. Briefly, 50 mg of GF, CNT and EG were dispersed by ultrasonication in separate containers with 100 ml of water containing 11.11 g of polyvinyl alcohol (PVA) and 3.5 g of polyvinylpyrrolidone (PVP) respectively. 1.50 ml of hydrochloric acid (HCl) was then added to the solution as a cross linker [18]. The mixture was further sonicated for few minutes and stirred for 30 min to obtain a homogeneous dispersion before being transferred into a 120 ml Teflon-lined autoclave system. The solution was heated at 190 °C for 12 h. The resulting hydrogels were crushed and washed with deionized water and dried for 6 h. The hydrogels obtained was then soaked in aqueous KOH solution (7 M) with a KOH/hydrogel mass ratio of 5, for 24 h and dried at 120 °C for 12 h before carbonization [18,25]. The composites were then placed in a horizontal tube furnace ramped from room temperature to 800 °C at 10 °C/min under argon gas flow before starting the activation process for 2 h. This procedure transforms the hydrogel into carbon materials consisting of a continuous pore network distribution. The obtained powders were washed with 3 M HCl to remove the remaining KOH and subsequently washed with deionized water. Samples were designated as **ACGF,ACCNT** and **ACEG** when 100 mg of GF, CNT and EG were added in a PVA/PVP solution, respectively.

2.2. Structural characterization

The SEM images of the samples were obtained using a Zeiss Ultra Plus 55 field emission scanning electron microscope (FE-SEM) operated at an accelerating voltage of 2.0 kV. Nitrogen adsorption–desorption isotherms were measured at −196 °C using a Micromeritics ASAP 2020. All the samples were initially degassed at 180 °C for more than 12 h under high vacuum conditions. The surface area was calculated by the Brunauer–Emmett–Teller (BET) method from the adsorption branch in the relative pressure range (P/P_0) of 0.01 - 0.2. The X-ray diffraction (XRD) spectra was recorded using an XPERT-PRO diffractometer (PANalytical BV, the Netherlands) operated with a Cu-Kα X-rays of 1·5405 Å wavelength. The qualitative phase of samples was analysed with the X'pert Highscore search match software at room temperature.

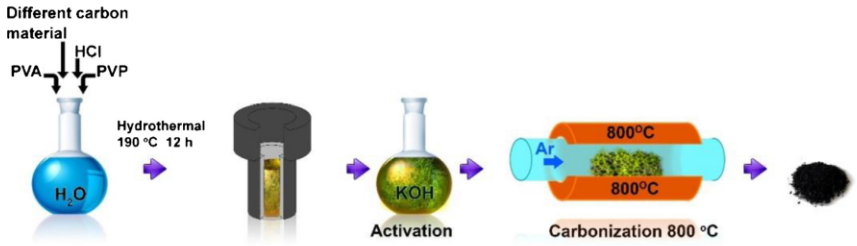

Scheme 1. Schematic diagram of the preparation process of activated carbons.

Raman spectroscopy measurements were carried out using a Jobin Yvon Horiba TX 6400 micro-Raman spectrometer equipped with a triple monochromator system to eliminate contributions from Rayleigh lines. LabSpec (Ver. 5.78.24) analytical software was used to analyze the obtained Raman spectra. All the samples were excited with a 514 nm argon laser line with a laser power of 1.5 mW to avoid possible thermal effects.

2.3. Electrochemical testing

The electrodes were fabricated as follows: firstly, known masses of the active materials and Polyvinylidene fluoride (PVdF) serving as a binder, were mixed with a mass ratio of 90:10 and dispersed in N-methylpyrrolidone (NMP) solution. The resulting mixture was then uniformly coated on a nickel foam current collector and dried at 60 °C in an oven for 8 hours to ensure complete evaporation of the NMP. The electrochemical test of the symmetric cell was carried out in two-electrode cell configuration with coin-type cells and a glass microfiber filter paper was used as the separator in 6 M KOH aqueous electrolyte solution. All electrochemical measurements were carried out using a Bio-logic VMP-300 potentiostat namely cyclic voltammetry (CV), chrono-potentiometry (CP) and electrochemical impedance spectroscopy (EIS). The CV tests were carried out in the potential range of 0 to 1.6 V at different scan rates ranging from 5 mV s^{-1} -50 mV s^{-1}. Electrochemical impedance spectroscopy (EIS) measurements were conducted in the frequency range from 0.1 Hz to 100 kHz with an open circuit potential (~0 V).

2.4. Results and discussion

The images obtained from SEM analysis are shown in Fig. 1. The high magnification SEM showed that all ACs material possesses interconnected carbon frameworks. The Fig. 1 (e) and (f) suggests the existence of a more abundant and uniform pore structure in the ACEG. ACEG material showed a well-developed porous network which could be related to the addition of expanded graphite. This type of porous carbon structure which should in principle exhibits a high surface area is favourable for electrodes in supercapacitor applications.

The gas sorption analysis of the samples was made by N_2 adsorption–desorption isotherms to measure the specific surface area (SSA) by BET method, while the Pore size distributions (PSD) were obtained using Barrett Joyner Halenda (BJH) method. Fig. 2 (a) presents a typical type II adsorption–desorption with H4 hysteresis isotherm that characterize complex materials containing micropores and mesopores. At high pressure, the inflection point occurs near completion of the first monolayer. The Brunauer–Emmett–Teller surface area of the ACEG is 627 $m^2 g^{-1}$ while those of ACGF and ACCNT are 1124 $m^2 g^{-1}$ and 1071 $m^2 g^{-1}$,

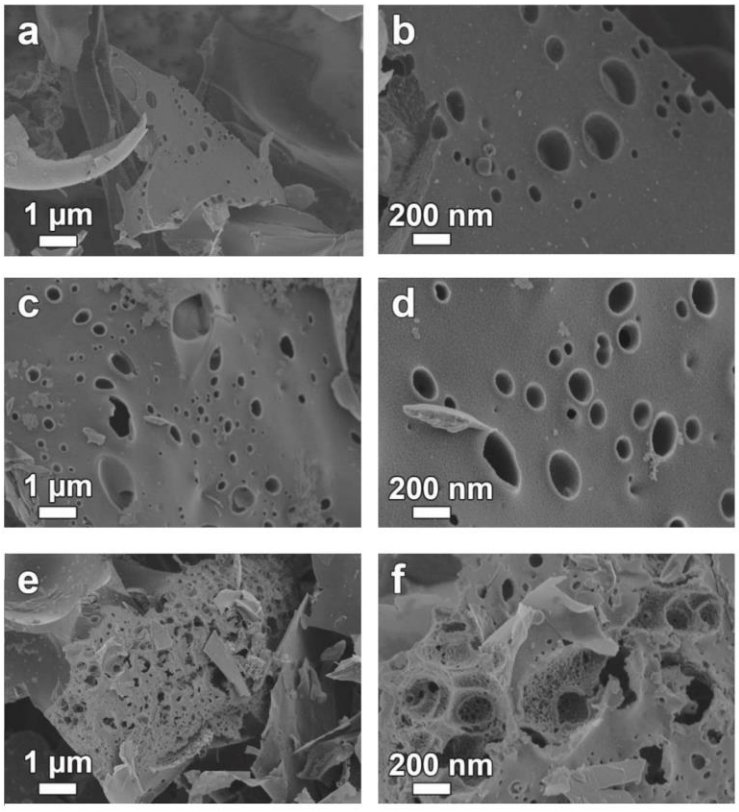

Fig. 1. Low and high magnification SEM images of (a) & (b) ACGF, (c) & (d) ACCNT, (e) and (f) ACEG respectively.

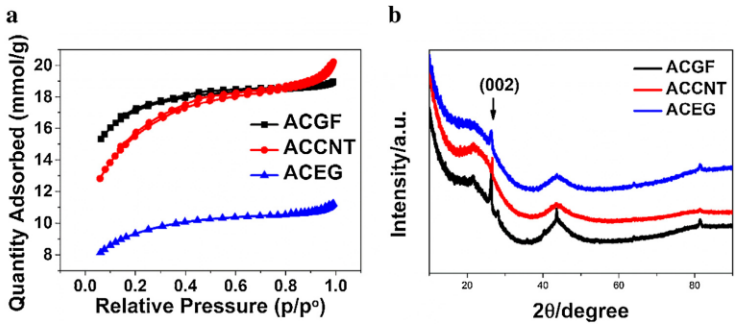

Fig. 2. (a) the N_2 adsorption-desorption isotherm and (b) the X-ray diffraction of different samples as labeled in the figure legends.

Table 1
Surface area, micropore and cumulative volume and pore size of the samples.

Sample	Surface area (m^2/g)	Micropore volume[a] (cm^3/g)	Cumulative volume[b] (cm^3/g)	Pore diameter[c] (nm)
ACGF	1124	0.388	0.173	2.8
ACCNT	1071	0.186	0.370	3.1
ACEG	627	0.177	0.024	29.8

[a] t-Plot micropore volume.
[b] BJH Desorption cumulative volume of pores between 1.7000 nm and 300.0000 nm diameter.
[c] BJH Desorption average pore diameter (4 V/A).

respectively. The properties obtained for the three samples are summarised in Table 1. Fig. 2 (b) shows the XRD patterns for the all synthesized samples. It is noted that the XRD peak of ACEG (JCPDS 00-008-0415), ACGF and ACCNT (JCPDS 01-089-8487) are identified as graphite peaks.

To evaluate the samples' performance as EDLC electrode materials, cyclic voltammetry (CV), galvanostatic charge/discharge (CD) and electrochemical impedance spectroscopy (EIS) measurements were performed. The symmetric devices fabricated based on these materials show good rate capability in aqueous electrolyte as

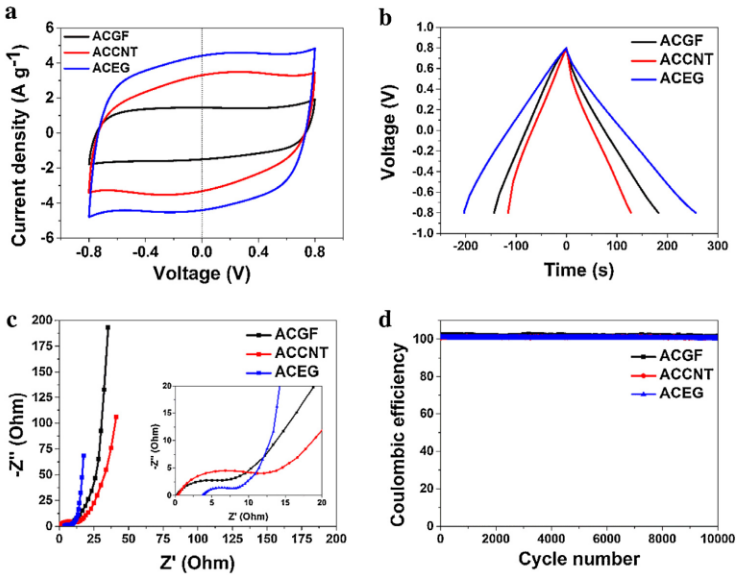

Fig. 3. (a) CV curves in 6 M KOH electrolytes at the scan rate of 20 mV s^{-1}, (b) galvanostatic charge/discharge curves at 0.5 g^{-1}, (c) Nyquist plots, and (d) Cycle stability at a constant current density of 5 A g^{-1} of the ACGF, ACCNT, ACEG samples.

observed in Fig. 3. Fig. 3 (a) presents CV curves of the three fabricated cells at a scan rate of 20 mV s^{-1}. A quasi rectangular shape is observed in the potential window of -0.8 to 0.8 V indicating an excellent rate performance. However, the ACEG device exhibited a higher current response which suggests higher capacitance performance when compared with the other two devices fabricated from the ACGF and ACCNT.

The galvanostatic CD profiles in Fig. 3 (b), show similar trend for the three samples with the ACEG exhibiting a higher CD time at a current density 0.5 Ag^{-1} suggesting higher electrochemical capacity. All the CD profiles for the three fabricated device show a relatively triangular shape with no obvious IR drop indicating the formation of a double layer capacitor mechanism with good electrode conductivity. The specific capacitances for these symmetric cells were calculated using the following expression [19]:

$$\mathbf{C_S = 2\frac{I\Delta t}{m\Delta U}} \quad (1)$$

Where I is the current, ΔU is the potential window, m is the mass of single electrode and Δt is the discharge time. The values obtained at a current density of 0.5 A g^{-1} were 157 F g^{-1}, 227 F g^{-1} and 320 F g^{-1} for the ACCNT, ACGF and ACEG electrodes, respectively. Even though the ACEG exhibits the smallest SSA and pore volume, it has the highest specific capacitance amongst these three electrodes materials. The enhanced electrochemical performance of the ACEG could be attributed to the continuous interconnected porous carbon network when compared with the other two samples that show non-uniform undulating irregular pore structure as observed from the SEM images which is deemed unfavourable for mass ion transport.

The capacitance for the ACEG corresponds to an areal capacitance 51 μF/cm^2 which is within the same order of areal capacitance values obtained so far when compared to previous reports [26,27]. Although a direct mechanism of this high areal capacitance has not been ascertained, the high area density of the ACEG could be due to the presence of carbonyl and oxygen functional groups in the ACEG material can give rise to pseudocapacitance, thus contributing to the total capacitance of the cell. The concentration of these functional groups might be higher in ACEG compared to ACCNT, ACGF owing to the higher concentration of these functional groups in the EG than in CNT and GF.

EIS was further used to understand the performance of these materials [28] by providing information about the movement or restriction of ion transport in the porous architecture of these materials. The Nyquist plots for all fabricated devices are shown in Fig. 3 (c). At high frequency the intercept on the X-axis represents the Ohmic internal resistance denoted by R_S or equivalent series resistance (ESR) of the electrode material and electrolyte [29]. The transition from the high- to mid-frequency region denoted by the diameter of the semicircle is a measure of the charge transfer resistance; R_{CT}. The low frequency region in aqueous electrolyte should be in principle a vertical line however; there is usually deviation from this ideal behaviour which is usually associated to Warburg impedance. From the figure, the ACEG device exhibits a more ideal behaviour when compared to the others which show more deviation which could be attributed to the diffusion of inner mesopores in this materials which is largely dependent on the measured potential [30]. Also, from the graph, the ACEG exhibits the shortest diffusion length indicating a faster response of the device. The estimated values of R_S and R_{CT} are 0.26, 0.34, 3.73 and 6.15, 11.77, 4.01 Ω, respectively for ACGF, ACCNT and ACEG. The low R_{CT} value observed for the ACEG indicates a well-connected interface nature of electrolyte ions and electrode probably due to its unique porous structure. Furthermore, the apparent high R_S value observed for this material show an order of magnitude decrease after cycling (see Fig. 5(b)) and this could already happen during the first cycling after the effective penetration of the electrolyte ions into the porous structure of this material.

Long cycling test is also very important for practical applications in supercapacitors. The cycling stability of these materials are studied and shown in Fig. 3 (d). From the results obtained, all the devices show excellent and stable cycling ability in aqueous 6 M KOH electrolyte with no obvious decay or capacitance drop observed after 10,000CD cycles at a current density of 5 A g^{-1}. Based on the above analysis detailed electrochemical characterization was performed on the ACEG material which showed a higher and promising electrochemical behaviour.

Fig. 4 (a) present the CV curves of the ACEG symmetric supercapacitor device at the scan rate from 5 to 50 mV s^{-1}. It maintained a quasi-rectangular shape as the scan rate increases, suggesting an EDLC behaviour and a good rate capability. Typical CD curves of the ACEG-based symmetrical supercapacitors were also measured and presented in Fig. 4 (b) with relatively symmetric triangular shapes for the symmetrical supercapacitors which confirms the quick ion/charge transport and dominant electric double-layer capacitor formation mechanism at the interface of electrode and electrolyte. The specific capacitance was calculated from the CD using the recommended rules and standards for reporting the performance of supercapacitor devices using equation 1 [31,32] and the result is presented in Fig. 4 (c). It is worth noting that the lines through the data of Figs. 4 (c)-4 (e) are for guide to the eye and not a sort of fitting to the data. The energy density (E (Wh kg^{-1})) and power density (P (W kg^{-1})) of SCs can then be calculated using the following equations [33] with the same meaning for the parameters as in Eq. (1):

$$\mathbf{E = \frac{C_s \times \Delta U^2}{28.8}} \quad (2)$$

$$\mathbf{P = \frac{3.6 \times E}{\Delta t}} \quad (3)$$

A highest specific capacitance of 320 F g^{-1} at 0.5 A g^{-1} was obtained, and the capacitance value of 111 F g^{-1} was retained at 10 A g^{-1}, indicating a capacitance loss of about 35%, with a current variation from 0.5 A g^{-1} to 10 A g^{-1}, as shown in Fig. 4 (c). The Ragone plots based on the total mass of active electrode materials is given in Fig. 4 (d). The symmetric device exhibits a high gravimetric energy density of 28.4 Wh kg^{-1} at a power density of 400 W kg^{-1}. These results show that symmetric supercapacitors devices based on this material can deliver a high energy-power densities owing to its morphology and porous structure that ensure ultrafast ion transport. Cycling test based on floating (voltage holding) has been used to investigate the long-term stability of devices [34].

Fig. 4 (e) shows the floating performance of the ACEG symmetric device at 1 A g^{-1}. An increase in specific capacitance after the first 20 hours is observed and thereafter the value of the specific capacitance stabilises. The first increase could be due to the time required for the complete penetration and adsorption of the ions contained in the electrolyte. The stabilization of the capacitance value after 100 hours of floating at a high current density, demonstrates that repeated floating stability does not cause any significant structural change to the ACEG electrode structure or even improves the electrode/ions interface. This was further confirmed by the higher current response in the CV curve after voltage holding shown in Fig. 4 (f), evidencing an improvement on the capacitance. The increase in capacitance could also be associated to the expansion and swelling of the ACEG porous

structure during the ageing time, creating more accessible surface for adsorption of ion from the electrolyte thus increasing the capacitance of the cell.

EIS measurements of the ACEG sample were further carried out analysed in detail. Fig. 5 presents the experiment and fitting data of the ACEG cell with the equivalent circuit diagram shown in the inset to the figure. A semicircle in the high frequency region and a straight line in the low frequency region are observed. The R_S includes the intrinsic resistances of the active electrode materials, the current collectors, electrolyte and the contact resistance of the electrodes [35]. The charge transfer resistance at the interface between the electrode and electrolytes denoted as R_1 in the circuit diagram. As reported above, the device possesses a R_S value of 3.61 Ω and charge transfer resistance R_1 value of 4.01 Ω. The circuit

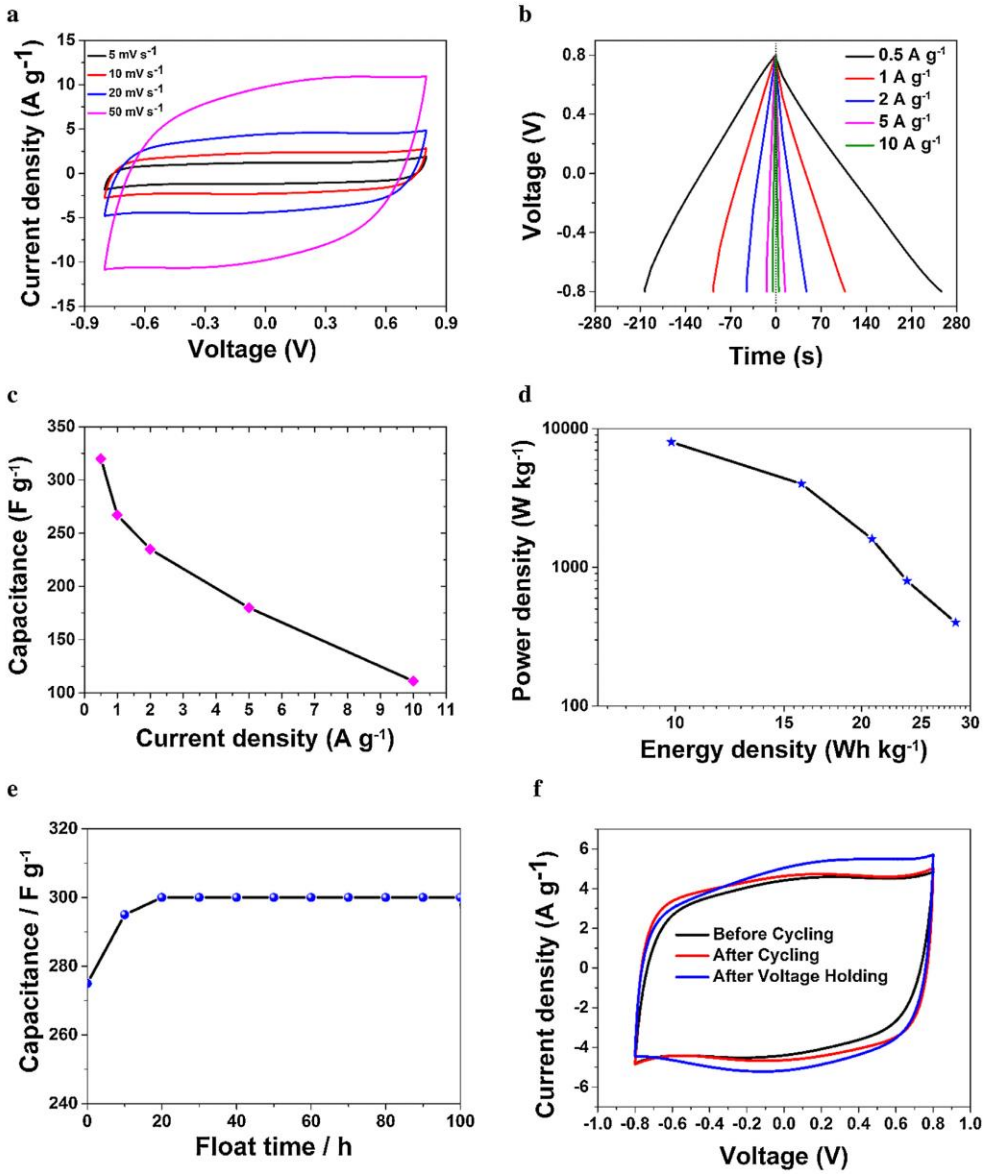

Fig. 4. (a) CV curves at scan rates from 5 to 50 mV s^{-1}, (b) the galvanostatic charge/discharge curves from 0.5 to 10 A g^{-1}, (c) the specific capacitance as function of the current density, (d) Ragone plot, (e) voltage holding vs. capacitance and (f) CV before stability, after stability and voltage holding at 20 mV s^{-1} of ACEG respectively.

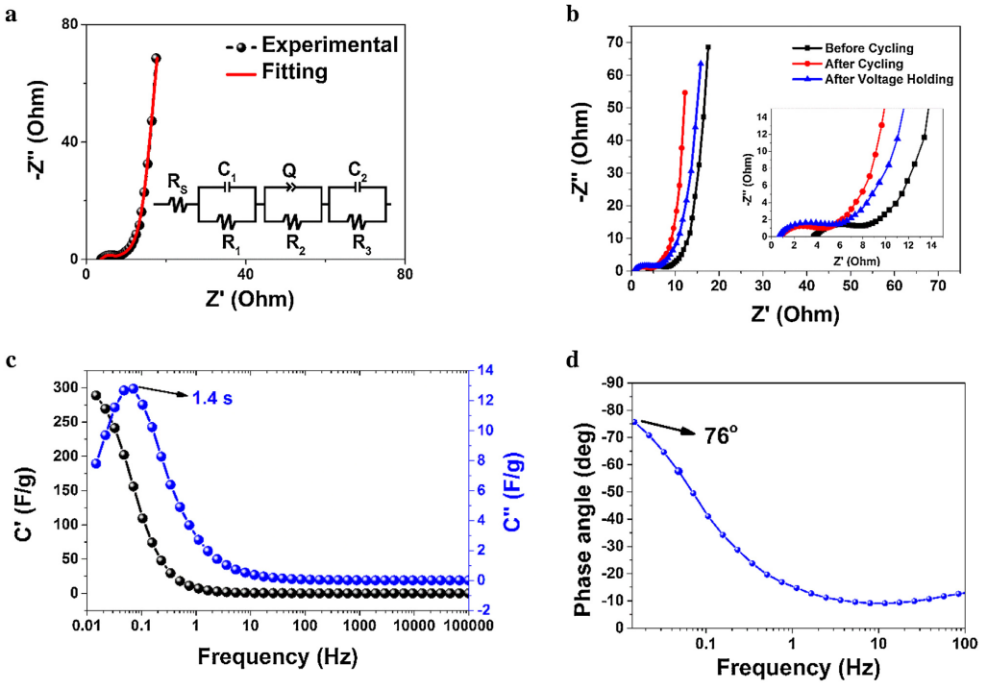

Fig. 5. (a) EIS plot and fitting curve for the symmetric cell with the inset to the figure being equivalent circuit used for fitting the data, (b) EIS before stability, after stability and voltage holding, (c) the real and the imaginary part of the cells specific capacitance as a function of frequency and (d) Bode phase angle of ACEG respectively.

in the inset was fitted from the EIS experimental data with a fitting program ZFIT/EC-Lab version 10.40. In the circuit R_S is connected in series with the interface contact capacitance C_1 between the active material and charge transfer resistance R_1 that are connected in parallel to each other. A constant phase element (Q), representing double layer capacitance, which occurs at the interface between materials and electrolytes due to charge separation, is connected in parallel with a charge separation resistance R_2 and C_2 represents the ideal polarizable capacitance which would give rise to a straight line parallel to the imaginary axis. The deviation from the ideal situation suggests that a resistive element R_3 is associated with C_2. R_3 is the leakage resistance which is placed in parallel with C_2. This resistance (R_3) is usually very high and can be ignored in the circuit. The R_S and R_1 values and other parameters agree quiet well with the experimental data, indicating an optimized minimization of experimental data with the design of the cell with an error of 0.0075. X^2 represents the criterion for minimization of the fit. $X/\sqrt{N}$, where N is the number of points is a normalized expression of X^2, whose value is independent of the number of points and is represented as the error above. Fig. 5 (b) shows the Nyquist plots before and after cycling and also after voltage holding. There was a significant decrease in the R_S and the charge transfer resistance possibly due to the increased available surface area during repeated CD cycle which could improve the supercapacitor performance.

Fig. 5 (c) presents real ($C'(\omega)$) and imaginary ($C''(\omega)$) specific capacitances as a function of frequency. The equations to derive $C'(\omega)$ and $C''(\omega)$ have been clearly stated by Taberna *et. al.*, [36]. $C'(\omega)$ represents the real accessible capacitance of the cell at the corresponding frequency, representing the deliverable capacitance, while $C''(\omega)$ represents the energy dissipated. A relaxation time τ can be calculated from knee frequency of 0.07 Hz in the figure; from $\tau = 1/f$ where f is the characteristic frequency of the cell, corresponding to the maximum on the $C''(\omega)$ curve. τ was found to be 1.4 s and it is the time required to efficiently deliver the stored energy. This represents the boundary between a pure capacitive and resistive behavior of the supercapacitor electrode. At low frequency, a phase angles of −76° was observed (Fig. 5 (d)) which is a characteristic of the purely capacitive behaviour

3. CONCLUSION

We have produced porous carbons from different carbon source such as CNTs, graphene foam, expanded graphite and low cost polymer materials. Structural and morphological characterizations show that the produced materials mainly consisted of porous structures with a good distribution of mesopores and micropore volume; that could lead to high electrochemical activity and high stability, with good performance as electrodes in supercapacitors. Overall, the porous material made from expanded graphite (ACEG), although exhibiting the smallest SSA, demonstrated the highest specific capacitance of 320 $F g^{-1}$, gravimetric energy density of 28.4 $Wh kg^{-1}$ and a power density of 400 $W kg^{-1}$ at 0.5 $A g^{-1}$, showing excellent performance in aqueous electrolyte. Similar results of material with low SSA and high electrochemical performance has been reported for MXene material [37,38] with the possible storage mechanism not well understood yet. Our results show that porous carbons adapted from low cost polymer and carbon materials with desired properties can be fine-tuned for high performance electrochemical capacitors.

ACKNOWLEDGEMENT

This work is based upon research supported by the South African Research Chairs Initiative (SARChi) in carbon Technology and Materials of the Department of Science and Technology (DST) and the National Research Foundation (NRF) as well as General Direction of Scientific Research and Technological Development (DGRSDT) via Algerian Ministry of Higher Education and Scientific Research through Algeria/South Africa collaboration programme. Any opinion, findings and conclusions or recommendations expressed in this work are those of authors and therefore the NRF and DST do not accept any liability with regard thereto. F. Barzegar and D. Y. Momodu acknowledge financial support from University of Pretoria and NRF for their PhD bursaries, while A. Bello acknowledges University of Pretoria financial support for Postdoc fellowship.

Appendix A. Supplementary data

Supplementary data associated with this article can be found, in the online version, at http://dx.doi.org/10.1016/j.electacta.2015.10.189.

References

[1] R. Kötz, M. Carlen, Principles and applications of electrochemical capacitors, Electrochim. Acta 45 (2000) 2483–2498.
[2] L.L. Zhang, X.S. Zhao, Carbon-based materials as supercapacitor electrodes, Chem. Soc. Rev. 38 (2009) 2520–2531.
[3] B.E. Conway, Electrochemical Supercapacitors: Scientific Fundamentals and Technological Applications, Kluwer Academic/Plenum, New York, 1999.
[4] A. Burke, A. Burke, R&D considerations for the performance and application of electrochemical capacitors, Electrochim. Acta 53 (2007) 1083–1091.
[5] J.R. Miller, A.F. Burke, Electrochemical capacitors: Challenges and opportunities for real-world applications, Electrochem. Soc. 17 (2008) 53–57.
[6] P.J. Hall, M. Mirzaeian, S.I. Fletcher, F.B. Sillars, A.J.R. Rennie, G.O. Shitta-Bey, et al., Energy storage in electrochemical capacitors: designing functional materials to improve performance, Energy Environ. Sci. 3 (2010) 1238–1251.
[7] L.L. Zhang, R. Zhou, X.S. Zhao, Graphene-based materials as supercapacitor electrodes, J. Mater. Chem. 20 (2010) 5983–5992.
[8] E. Frackowiak, F. Béguin, F.F. Frackowiak, E. Beguin, Carbon materials for the electrochemical storage of energy in capacitors, Carbon 39 (2001) 937–950.
[9] P. Simon, Y. Gogotsi, Materials for electrochemical capacitors, Nat. Mater. 7 (2008) 845–854.
[10] M. Zhi, C. Xiang, J. Li, M. Li, N. Wu, Nanostructured Carbon-Metal Oxide Composite Electrodes for Supercapacitors: Review, Nanoscale. 5 (2012) 72–88.
[11] M. Zhi, F. Yang, F. Meng, M. Li, A. Manivannan, N. Wu, Effects of Pore Structure on Performance of An Activated-Carbon Supercapacitor Electrode Recycled from Scrap Waste Tires, ACS Sustain. Chem. Eng. 2 (2014) 1592–1598.
[12] B. Batalla Garci'a, A.M. Feaver, Q. Zhang, G. Champion, et al., Effect of pore morphology on the electrochemical properties of electric double layer carbon cryogel supercapacitors, J. Appl. Phys. 104 (2008) 014305.
[13] A. Bello, F. Barzegar, D. Momodu, F. Taghizadeh, M. Fabiane, J. Dangbegnon, et al., Morphological characterization and impedance spectroscopy study of porous 3D carbons based on graphene foam-PVA/phenol-formaldehyde resin composite as an electrode material for supercapacitors, RSC Adv 4 (2014) 39066–39072.
[14] M. Inagaki, H. Konno, O. Tanaike, Carbon materials for electrochemical capacitors, J. Power Sources 195 (2010) 7880–7903.
[15] T.A. Centeno, M. Sevilla, A.B. Fuertes, F. Stoeckli, On the electrical double-layer capacitance of mesoporous templated carbons, Carbon 43 (2005) 3012–3015.
[16] M. a. Lillo-Ródenas, D. Cazorla-Amorós, A. Linares-Solano, Understanding chemical reactions between carbons and NaOH and KOH: An insight into the chemical activation mechanism, Carbon N. Y. 41 (2003) 267–275.
[17] J. Wang, S. Kaskel, KOH activation of carbon-based materials for energy storage, J. Mater. Chem. 22 (2012) 23710–23725.
[18] L. Zhang, F. Zhang, X. Yang, G. Long, Y. Wu, T. Zhang, et al., Porous 3D graphene-based bulk materials with exceptional high surface area and excellent conductivity for supercapacitors, Sci. Rep. 3 (2013) 1408.
[19] A. Bello, F. Barzegar, D. Momodu, J. Dangbegnon, F. Taghizadeh, N. Manyala, Symmetric supercapacitors based on porous 3D interconnected carbon framework, Electrochim. Acta 151 (2015) 386–392.
[20] T. Wang, S. Tan, C. Liang, Preparation and characterization of activated carbon from wood via microwave-induced ZnCl2 activation, Carbon 47 (2009) 1880–1883.
[21] Q.-S. Liu, T. Zheng, P. Wang, L. Guo, Preparation and characterization of activated carbon from bamboo by microwave-induced phosphoric acid activation, Ind. Crops Prod. 31 (2010) 233–238.
[22] A. Bello, F. Barzegar, D. Momodu, J. Dangbegnon, F. Taghizadeh, M. Fabiane, et al., Asymmetric supercapacitor based on nanostructured graphene foam/polyvinyl alcohol/formaldehyde and activated carbon electrodes, J. Power Sources 273 (2015) 305–311.
[23] A. Bello, O.O. Fashedemi, J.N. Lekitima, M. Fabiane, D. Dodoo-Arhin, K.I. Ozoemena, et al., High-performance symmetric electrochemical capacitor based on graphene foam and nanostructured manganese oxide, AIP Adv. 3 (2013) 082118.
[24] O. Guellati, I. Janowska, D. Bégin, M. Guerioune, Z. Mekhalif, J. Delhalle, et al., Influence of ethanol in the presence of H2 on the catalytic growth of vertically aligned carbon nanotubes, Appl. Catal. A Gen. 423–424 (2012) 7–14.
[25] Y. Zhu, S. Murali, M.D. Stoller, K.J. Ganesh, W. Cai, P.J. Ferreira, et al., Carbon-based supercapacitors produced by activation of graphene, Science 332 (2011) 1537–1541.
[26] R. Signorelli, D.C. Ku, J.G. Kassakian, J.E. Schindall, Electrochemical Double-Layer Capacitors Using Carbon Nanotube Electrode Structures, Proc. IEEE. 97 (2009) 1837–1847.
[27] Z.-S. Wu, K. Parvez, X. Feng, K. Müllen, Photolithographic fabrication of high-performance all-solid-state graphene-based planar micro-supercapacitors with different interdigital fingers, J. Mater. Chem. A. 2 (2014) 8288.
[28] X. Li, J. Rong, B. Wei, Electrochemical behavior of single-walled carbon nanotube supercapacitors under compressive stress, ACS Nano. 4 (2010) 6039–6049.
[29] B.G. Choi, J. Hong, W.H. Hong, P.T. Hammond, H. Park, Facilitated ion transport in all-solid-state flexible supercapacitors, ACS Nano. 5 (2011) 7205–7213.
[30] W. Sugimoto, H. Iwata, K. Yokoshima, Y. Murakami, Y. Takasu, Proton and electron conductivity in hydrous ruthenium oxides evaluated by electrochemical impedance spectroscopy: the origin of large capacitance, J. Phys. Chem. B. 109 (2005) 7330–7338.
[31] M.D. Stoller, R.S. Ruoff, Best practice methods for determining an electrode material's performance for ultracapacitors, Energy Environ. Sci. 3 (2010) 1294–1301.
[32] Y. Gogotsi, P. Simon, True performance metrics in electrochemical energy storage, Science 334 (2011) 917–918.
[33] F. Barzegar, A. Bello, D.Y. Momodu, J.K. Dangbegnon, F. Taghizadeh, M.J. Madito, et al., Asymmetric supercapacitor based on an α-MoO 3 cathode and porous activated carbon anode materials, RSC Adv. 5 (2015) 37462–37468.
[34] P. Ratajczak, K. Jurewicz, F. Béguin, Factors contributing to ageing of high voltage carbon/carbon supercapacitors in salt aqueous electrolyte, J. Appl. Electrochem. 44 (2013) 475–480.
[35] B.G. Choi, M. Yang, W.H. Hong, J.W. Choi, Y.S. Huh, 3D macroporous graphene frameworks for supercapacitors with high energy and power densities, ACS Nano 6 (2012) 4020–4028.
[36] P.L. Taberna, P. Simon, J.-F.F. Fauvarque, Electrochemical Characteristics and Impedance Spectroscopy Studies of Carbon-Carbon Supercapacitors, J. Electrochem. Soc. 150 (2003) A292–A300.
[37] Z. Ling, C.E. Ren, M.-Q. Zhao, J. Yang, J.M. Giammarco, J. Qiu, et al., Flexible and conductive MXene films and nanocomposites with high capacitance, Proc. Natl. Acad. Sci. U. S. A. 111 (2014) 16676–16681.
[38] M.D. Levi, M.R. Lukatskaya, S. Sigalov, M. Beidaghi, N. Shpigel, L. Daikhin, et al., Solving the Capacitive Paradox of 2D MXene using Electrochemical Quartz-Crystal Admittance and In Situ Electronic Conductance Measurements, Adv. Energy Mater. 5 (1) (2015) 400815.

Supplementary data

Effect of addition of different carbon materials on hydrogel derived carbon material for high performance electrochemical capacitors

Farshad Barzegar[a], Abdulhakeem Bello[a], Ouanassa Guellati[b], Damilola Y. Momodu[a], Aicha Harat[b], Julien K. Dangbegnon[a], Mohamed Guerioune[b], and Ncholu Manyala[a]*

[a]Department of Physics, Institute of Applied Materials, SARCHI Chair in Carbon Technology and Materials, University of Pretoria, Pretoria 0028, South Africa.

[b]LEREC Laboratory, Department of Physics, Badji Mokhtar University of Annaba, Annaba 23000, BP.12, Algeria.

Corresponding Author: *Email address: ncholu.manyala@up.ac.za (N. Manyala)

Tel: +27 (0)12 420 3549, Fax: +27 (0)12 420 2516

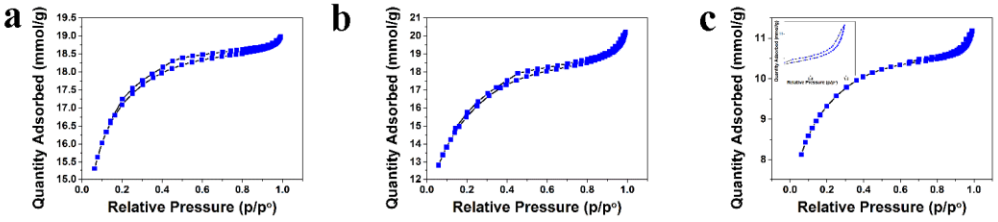

Figure S1 N_2 adsorption-desorption isotherm and pore size distributions of the (a) ACGF (b) ACCNT (c) ACEG

4.1.2.3 Concluding Remarks

Porous carbons materials from low-cost polymer materials with different carbon source such as CNTs, GF and EG from dispersed into a matrix polymer have been successfully characterized. The low cost porous material made from expanded graphite (ACEG), exhibited the smallest SSA, but demonstrated the highest specific capacitance of 320 F g^{-1}, energy density of 28.4 Wh kg^{-1} and a power density of 400 W kg^{-1} at 0.5 A g^{-1}, in aqueous electrolyte. The results showed that the EG can be a good candidate for production of carbon material from polymer based matrix to improve the performance of electrode materials for high energy supercapacitors.

4.1.3 Synthesis and characterization of ACs from expanded graphite (EG) for high-voltage supercapacitors.

4.1.3.1 Introduction

In section 4.1.1 and 4.1.2, activated carbon based on low-cost polymer with different carbon materials such as graphene (G), carbon nanotube (CNT) and expanded graphite (EG) were produced and characterized as possible electrodes for EDLCs applications. In this section, porous carbon material from EG were synthesized as it has not been reported based on our knowledge of the literature on energy storage system. EG was activated as explained in (3.1.4.2) and the produced material was denoted as AEG. The whole concept and the idea was to create pores and by

opening up the interlayer spaces between the layers of the EG material and by the chemical activation process.

4.1.3.2 Result and discussions

The results of this section are currently under review for publication, and the will be presented below as submitted to the journal.

Journal of Power Sources 309 (2016) 245–253

Contents lists available at ScienceDirect

Journal of Power Sources

journal homepage: www.elsevier.com/locate/jpowsour

Preparation and characterization of porous carbon from expanded graphite for high energy density supercapacitor in aqueous electrolyte

Farshad Barzegar, Abdulhakeem Bello, Damilola Momodu, Moshawe Jack Madito, Julien Dangbegnon, Ncholu Manyala*

Department of Physics, Institute of Applied Materials, SARCHI Chair in Carbon Technology and Materials, University of Pretoria, Pretoria 0028, South Africa

HIGHLIGHTS

- Activated carbon made from expanded graphite dispersed in polyvinylpyrrolidone.
- KOH activation and carbonization expanded graphite solid precipitate.
- Produced carbon had a specific surface area of 457 $m^2 g^{-1}$.
- Activated expanded graphite electrodes exhibit good electrochemical performance.
- Device exhibited excellent floating stability for 120 h.

ARTICLE INFO

Article history:
Received 14 November 2015
Received in revised form
18 January 2016
Accepted 27 January 2016
Available online xxx

Keywords:
Expanded graphite
Supercapacitor
Energy storage
Activated carbon nanosheets

ABSTRACT

In this work, we present the synthesis of low cost carbon nanosheets derived from expanded graphite dispersed in Polyvinylpyrrolidone, subsequently activated in KOH and finally carbonized in Ar/H_2 atmosphere. Interconnected sheet-like structure with low concentration of oxygen (9.0 at.%) and a specific surface area of 457 $m^2 g^{-1}$ was obtained. The electrochemical characterization of the carbon material as supercapacitor electrode in a 2-electrode configuration shows high specific capacitance of 337 $F g^{-1}$ at a current density of 0.5 A g^{-1} as well as high energy density of 37.9 Wh kg^{-1} at a power density of 450 W kg^{-1}. This electrical double layer capacitor electrode also exhibits excellent stability after floating test for 120 h in 6 M KOH aqueous electrolyte. These results suggest that this activated expanded graphite (AEG) material has great potential for high performance electrode in energy storage applications.

1. Introduction

The energy industry is currently facing a global crisis due to the rising cost associated with the high energy demand, a growing population and serious depletion of fossils fuels which raises some environmental issue such as global warming. Thus, there is an urgent need to explore alternative renewable energy resources as well as storage devices with high power and energy densities. In other words, the alternative energy sources are expected to be clean, low cost, environmentally friendly and sustainable [1–3]. Furthermore, new technology has to be implemented for the storage of the energy that can be released during high demand and at any time. In the search for high energy density and high power density energy storage devices, electrochemical technologies demonstrate the aptitude to provide the means for electrical energy storage. Amongst the various electrochemical energy storage devices, supercapacitors have drawn much interest due to their extremely high power density, good cycling stability and fast charge-discharge rate compared to conventional capacitors and lithium-ion batteries which possess a low power density and a short cycle life [4–6]. However, the relatively low energy density of supercapacitors has not yet met the requirements of electrical systems, ranging from portable electronics to hybrid electric vehicles [7,8]. Hence, all research efforts are geared towards improving on the energy density of supercapacitors without sacrificing their high power density and high cyclability. Generally, supercapacitors can be classified into two categories

* Corresponding author.
E-mail addresses: farshadbarzegar@gmail.com (F. Barzegar), bellohakeem@gmail.com (A. Bello), dymomodu@yahoo.com (D. Momodu), jack.madito@gmail.com (M.J. Madito), dangbegnon01@googlemail.com (J. Dangbegnon), ncholu.manyala@up.ac.za (N. Manyala).

http://dx.doi.org/10.1016/j.jpowsour.2016.01.097
0378-7753/

according to their different energy storage mechanisms: Electrical double-layer capacitors (EDLCs) and pseudocapacitors (RuO and MnO) [4,9]. EDLCs energy storage mechanism is based on electrical double layer charge accumulation at the interface between the electrode and electrolyte. Advances in the field of EDLCs research have shown that the high electrochemical performance of these devices is highly dependent on the development of active electrode materials and also on the electrolyte used. In other words, materials with high micropore volume and good representation of the pore structure are needed to improve on the energy density. Carbon-based materials with high specific surface area (SSA) have been widely studied as electrode materials for EDLCs owing to their good electrochemical performances which include reasonably high specific capacitance and long-term cyclability, excellent physico-chemical properties, high electrical conductivity. In addition, their synthesis is generally easy and cost effective. While activated carbon is the material of choice for commercial supercapacitors, other forms of carbon materials such as carbide-derived carbons (CDCs) [10], onion-like carbons (OLCs) [11], carbon nanotubes (CNTs) [12] and graphene [13] are currently being considered as next generation EDLC electrodes. In general, the electrochemical performance of carbon based EDLC device is highly dependent on its SSA, pore size and pore size distribution (PSD) [14]. Therefore, it is necessary to control these parameters during the production of the carbon materials. This is usually done through physical activation using steam or CO_2 on one hand or through the traditional chemical activation using activating agents such as KOH, $ZnCl_2$, and H_3PO_4, on the other hand. Recently, highly porous carbon nanosheets made from a three-dimensional graphene/polymer-based hydrogel with exceptional properties was reported by Zhang et al. [15]. The Hydrogel was activated with KOH and the porous materials produced demonstrated a superior supercapacitor performance in ionic liquid. Since the report of Zhang et al., several other reports based on similar method for production of porous carbons have since been published [16–19]. Herein we explore a two-step synthesis of highly porous carbon using Polyvinylpyrrolidone (PVP) and expanded graphite (EG) as carbon precursors. The choice of PVP is based on its ability to disperse and exfoliate carbon material such as graphite [20]. The obtained carbon with unique interconnected sheet-like morphology designated as AEG which stands for activated expanded graphite, exhibits high specific surface area (457 $m^2 g^{-1}$) and specific capacitance (337 F g^{-1}). High energy density value of 37.9 Wh kg^{-1} at a power density of 450 W kg^{-1} was obtained. These excellent electrochemical performances were attributed to the unique porous and interconnected morphology of the carbon nanosheets which could facilitate a fast charge transport mechanism.

2. Experimental

Scheme 1 presents the preparation process of the AEG material. Firstly, graphite sample (grade ES 250 B5 from Qingdao Kropfmuehl Graphite) was expanded using a microwave oven at an irradiation power of 300 W for 5 min 1 g of the expanded graphite (EG) was dispersed in 100 ml of 10 wt% Polyvinylpyrrolidone (PVP) and the mixture was sonicated for 12 h. 5 g of KOH was then added to the solution, and the mixture was further stirred for 2 h at 60 °C. The solid precipitate obtained was collected and dried at 70 °C for 12 h. The dried solid precipitate was then placed in a horizontal tube furnace which was ramped from room temperature to 800 °C at 5 °C/min under argon and hydrogen gas flow and kept at this temperature for 2 h of carbonization. This procedure transforms the EG solid precipitate into flakes of carbon material denoted as activated expanded graphite (AEG). The black powder obtained was washed with 1 M HCl to remove the remaining KOH and subsequently with deionized water and dried at 60 °C.

3. Structural and electrochemical characterization

The morphology of the samples was studied using a Zeiss Ultra Plus 55 field emission scanning electron microscope (FE-SEM) operated at an accelerating voltage of 2.0 kV. Transmission electron microscopy (TEM) analysis was performed at 200 kV on a JEOL JEM-2100F microscope with field-emission gun. TEM samples were prepared by dispersing the samples in ethanol and which were dropped on a lacey carbon grid. X-ray diffraction (XRD) was recorded using an XPERT-PRO diffractometer (PANalytical BV, the Netherlands) with theta/theta geometry. Qualitative phase analysis of samples was conducted using the X'pert Highscore search match software at room temperature. Raman spectroscopy analysis of the sample was performed using a T64000 micro-Raman spectrometer from HORIBA Scientific equipped with a triple monochromator system to eliminate contributions from the Rayleigh line. All the samples were excited with a 514 nm line of an Ar laser with a power of 12 mW to avoid any thermal effect. Nitrogen adsorption-desorption isotherms were measured at −196 °C using a Micromeritics TriStar II 3020 (version 2.00) analyzer. All the samples were degassed at 180 °C for more than 12 h under high vacuum condition. The surface area was calculated with the Brunauer-Emmett-Teller (BET) method from the adsorption branch in the relative pressure range (P/P_0) of 0.01–0.2. X-ray photoelectron spectroscopy (XPS) was used to determine the chemistry of the carbon sample. A Physical Electronics VersaProbe 5000 instrument was used which employs a 100 μm monochromatic Al-Kα to irradiate the sample surface. Photoelectrons were collected by a 180° hemispherical electron energy analyzer. Samples were analyzed at a 45° angle between the sample surface and the path to the analyzer. Survey spectra were taken at pulse energy of 117.5 eV, with a step size of 0.1 eV, which was used to obtain the elemental analysis of the powders. High-resolution spectra of C1s, N1s, and O1s regions were taken at pulse energy of 23.5 eV, with a step size

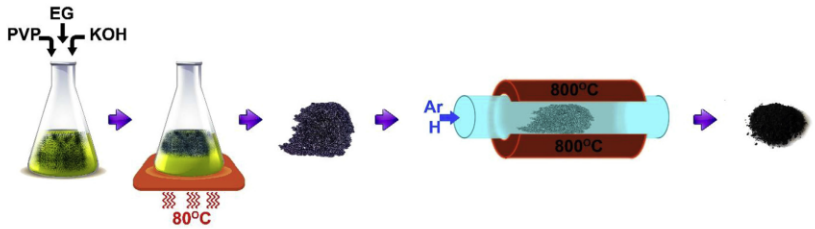

Scheme 1. Schematic diagram of the preparation process of AEG.

of 0.05 eV. All binding energies were referenced to that of the binding energy of C–C at 284.7 eV. Peak fitting for the high-resolution spectra was performed using CasaXPS Version 2.3.16 RP 1.6. Prior to the peak fitting the background contribution was subtracted using a Shirley function. The preparation of electrodes was done by mixing the active materials and Polytetrafluoroethylene (PTFE) as a binder with a weight ratio of 90:10, which was homogenized and dispersed in N-methylpyrrolidone (NMP) solution. The resulting paste was then uniformly coated on a nickel foam current collector and dried at 60 °C in an oven for 8 h to ensure complete evaporation of the NMP. The electrochemical test of the symmetric cell was carried out in a two electrode cell configuration in a coin cells with a thickness of 0.2 mm and a diameter of 16 mm. A glass microfiber filter paper was used as separator and the electrolyte was 6 M KOH. All electrochemical measurements were carried out using a Bio-logic VMP-300 potentiostat.

4. Results and discussion

Typical morphology and microstructure of the AEG sample were characterized by scanning electron microscopy (SEM) and transmission electron microscopy (TEM). Fig. 1(a) and (b) show low and high magnification SEM of the AEG sample, respectively. The sample displays a network of interconnected sheet-like material. TEM images in Fig. 1(c) and (d) also reveal a unique morphology with a well-developed porous mesh or porous graphene-like flakes. This type of interconnected porous nanosheets would provide a unique open pore system with high active surface area and a short diffusion path for electrolyte ions. Such structure promises to be a good electrode material for improved electrochemical performance for energy storage applications.

X-ray powder diffraction (XRD) was used to analyze the crystallinity after carbonization. Fig. 2(a) represents the XRD patterns for AEG powders. It is noted that all the XRD peaks are indexed to graphite peaks (COD: 96-900-0047) exhibiting orthorhombic structure with a space group *Fmmm* (69), with the following lattice parameters: a = 2.4560 Å, b = 4.2540 Å and c = 6.6960 Å. The XRD confirms that the material produced is indeed carbon.

In Fig. 2(b), EG Raman spectrum shows characteristic of an undisturbed graphitic structure with only the first-order band (G band) and second order 2D band visible. Such spectrum is commonly observed in highly oriented polycrystalline graphite (HOPG) [20]. On the other hand, the spectrum of the AEG shows additional first-order band (D band), which is the Raman fingerprint of disorder in the graphitic structure. This broad band can be deconvoluted in 4 bands using a curve fitting with Lorentzian distribution (Fig. 2(c)). The D1 band has been suggested to arise from the carbon atoms at the edge of a graphene layer and also from the edge planes perpendicular to the graphene layers of large single crystals graphite and HOPG [21]. The D2 band origin is related to the lattice vibration corresponding to that of the G band but involving graphene layers at the surface of graphite which are not directly incorporated between two other graphene layers [22]. The D3 band is known to originate from the distribution of amorphous carbon in interstitial sites in the disturbed graphitic lattice [23,24]. The D4 band is related to lattice vibrations corresponding to sp^2-sp^3 bonds [25,26]. In brief, Raman spectra suggest that the AEG, compared to EG, consists of a significant fraction of non-intercalated graphene layers and some amount of interstitial amorphous carbon in the lattice structure. The Raman curve fitting presented in Fig. 2 agrees well with Raman data reported for other carbonaceous material (e.g. soot) [27]. The porous texture of the two samples was analyzed by N_2 physisorption. The nitrogen adsorption-desorption isotherms of AEG curves are shown in Fig. 2(d), and the porous properties of the EG and AEG are listed in Table 1. AEG sample shows a type-II isotherms (definition by IUPAC) with H4 hysteresis loop in the range of ca. 0.20–0.99 P/P_0,

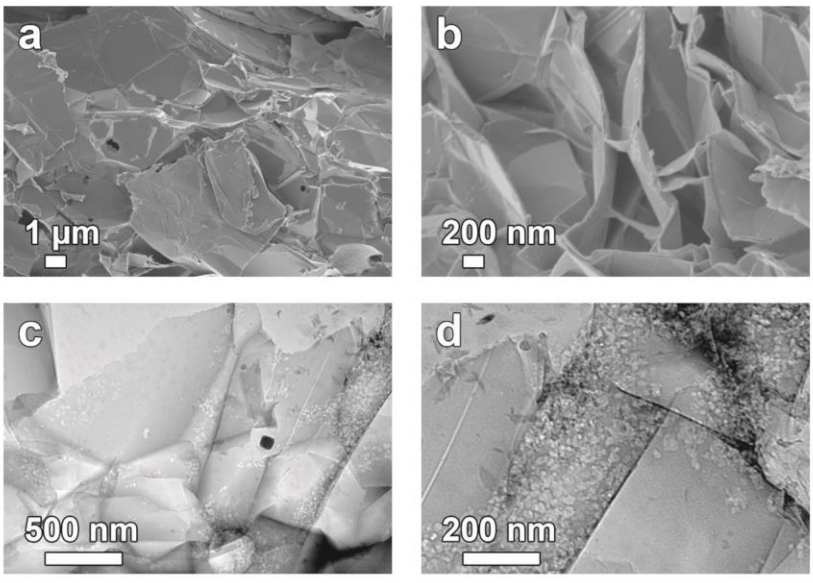

Fig. 1. Low and high magnification (a) and (b) SEM images and (c) and (d) TEM images of AEG.

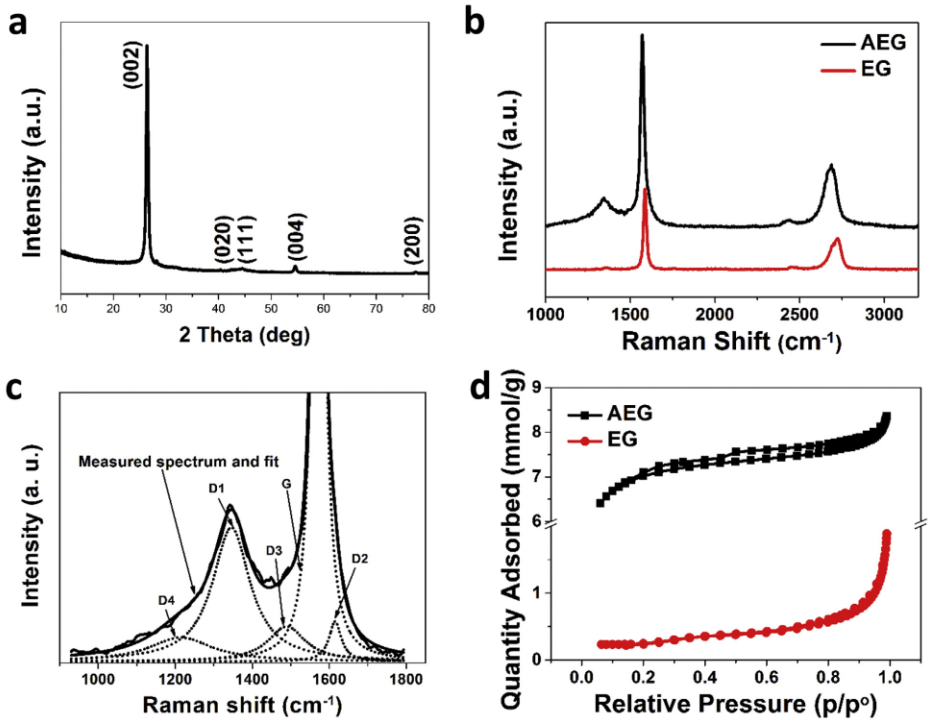

Fig. 2. (a) The X-ray diffraction pattern, (b) Raman spectra, (c) Curve fitting (Lorentzian) of different combinations of D and G Raman bands and (d) The N_2 adsorption-desorption isotherms of the EG and AEG as indicated in the figure.

Table 1
Surface area, micropore and cumulative volume and pore size of AEG.

Sample name	Surface area (m^2/g)	Micropore volume[a] (cm^3/g)	Cumulative volume[b] (cm^3/g)	Pore diameter[c] (nm)
EG	20	0.004	0.066	11.23
AEG	457	0.174	0.076	4.053

[a] t-Plot micropore volume.
[b] BJH Desorption cumulative volume of pores between 1.7000 nm and 300.0000 nm diameter.
[c] BJH Desorption average pore diameter (4 V/A).

suggesting the presence of micropores and mesopores whereas the EG sample shows a type III isotherm with H3 hysteresis loop, suggesting non-rigid aggregates of plate-like structure As observed from Table 1, there is a drastic increase in the micropore volume after activation and carbonization of EG material. Furthermore, high concentration of mesopores with smaller diameters was observed for AEG as compared to EG. Moreover, the surface area of the EG material after activation significantly increased from 20 $m^2\ g^{-1}$ to 457 $m^2\ g^{-1}$ which corresponds to an increase of over two orders of magnitude.

The elemental composition of the AEG was obtained from XPS characterization. The results of the peak fit of the high resolution spectra of C, N, and O are shown in Fig. 3 and summarized in Table 2. The C 1s region (Fig. 3(a)) was fitted by four components corresponding to graphitic carbon, hydrocarbons (CH_x), alcoholic (C–O–) and/or carbon nitrogen structures (C–N–) and carboxyl or ester (COO) [28]. The N 1s (Fig. 3(b)) at ~400 eV [29] was fitted by two components corresponding to pyridine/amine (P/A) and/or Nitrile/Pyrrole (N/P). The ratio of P/A to N/P ranges from 2 to 8. Finally, the O 1s region (Fig. 3(c)) was fitted with only one component corresponding to C–O. From the survey spectra (see Table 2), carbon is the main element in the sample, followed by oxygen. Also, the sample can be considered doped with nitrogen owning to the small amount of nitrogen in this sample (0.5 at.%). Furthermore, about 0.6 at.% of Si which is believed to originate from the quartz tube during carbonization is also present in the AEG sample.

To analyze the electrochemical properties and quantify the working potential windows of the AEG electrode material, cyclic voltammograms (CVs), in a 6 M KOH aqueous solution, in a three-electrode configuration was primarily performed. Fig. 4(a) and (b) show the CV of the AEG electrode at a scan rate of 50 mV s^{-1}. The CV of the AEG electrode is measured within a negative potential window of −1.2 to 0.0 V vs. Ag/AgCl as well as within a positive

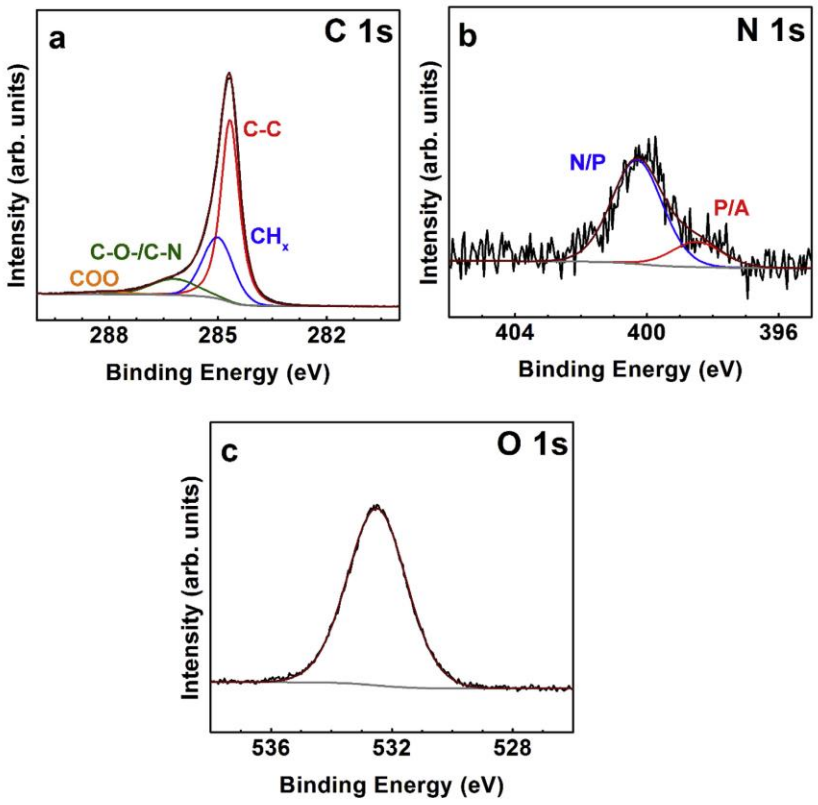

Fig. 3. XPS spectra of C 1s, N 1s and O 1s regions for AEG.

Table 2
Elemental analysis of AEG obtained from XPS characterization of the survey spectra.

Sample	C at.%	N at.%	O at.%	Si at.%
AEG	89.9 ± 0.1	0.5 ± 0.1	9.0 ± 0.1	0.6 ± 0.1

voltage window of 0.0–1.0 V vs. Ag/AgCl. The CV curves show rectangular shape in both potential windows, which indicate a good current response behavior. Below −1.0 V and above 0.9 V, cathodic and anodic current leaps are observed which are

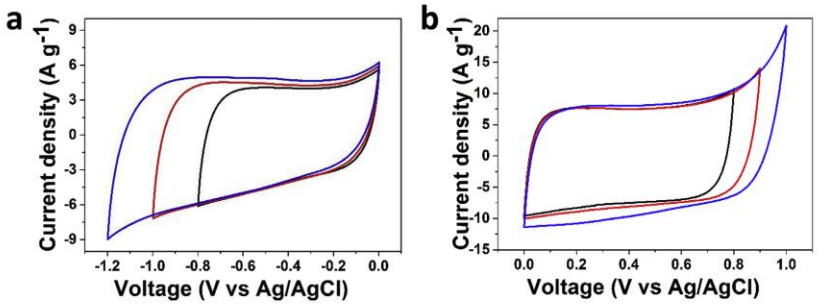

Fig. 4. Three electrode CV measurements in 6 M KOH aqueous electrolyte at 50 mV s^{-1} at different potential windows in (a) the negative voltage range and (b) the positive voltage range.

indications of di-hydrogen and oxygen evolution as the potential approaches −1 V and 0.9 V. On the basis of these results, it is expected that the operating symmetric two electrode cell voltage could be extended to about 1.9 V in 6 M KOH solution since the best potential windows for positive electrode can be up to 0.9 V and that of the negative one can be up to −1.0 V.

A two-electrode symmetric supercapacitor was fabricated to further test the electrochemical performance of the supercapacitor device based on the AEG electrode. Fig. 5(a) shows the combined CV in both the positive and negative voltage windows to the extended potential window of 2.4 V. The CV curves seem to still keep a rectangular shape with increasing total potential window, however, at about ±1.2 V current leaps on both sides of the CV curves were observed. These current leaps correspond to the evolution of oxygen and hydrogen on both side of the electrode as mentioned above [30,31]. To avoid these phenomena, the working voltage of the symmetric cell was kept to 1.8 V (from −0.9 to 0.9 V). At this voltage the CV curves maintained a symmetric reversible rectangular shape indicating ideal capacitive behavior and outstanding reversibility as shown in Fig. 5(b). The CV curves of the symmetric cell at different scan rates from 5 to 100 mV s^{-1} are shown in Fig. 5(b). The CV shapes does not change significantly

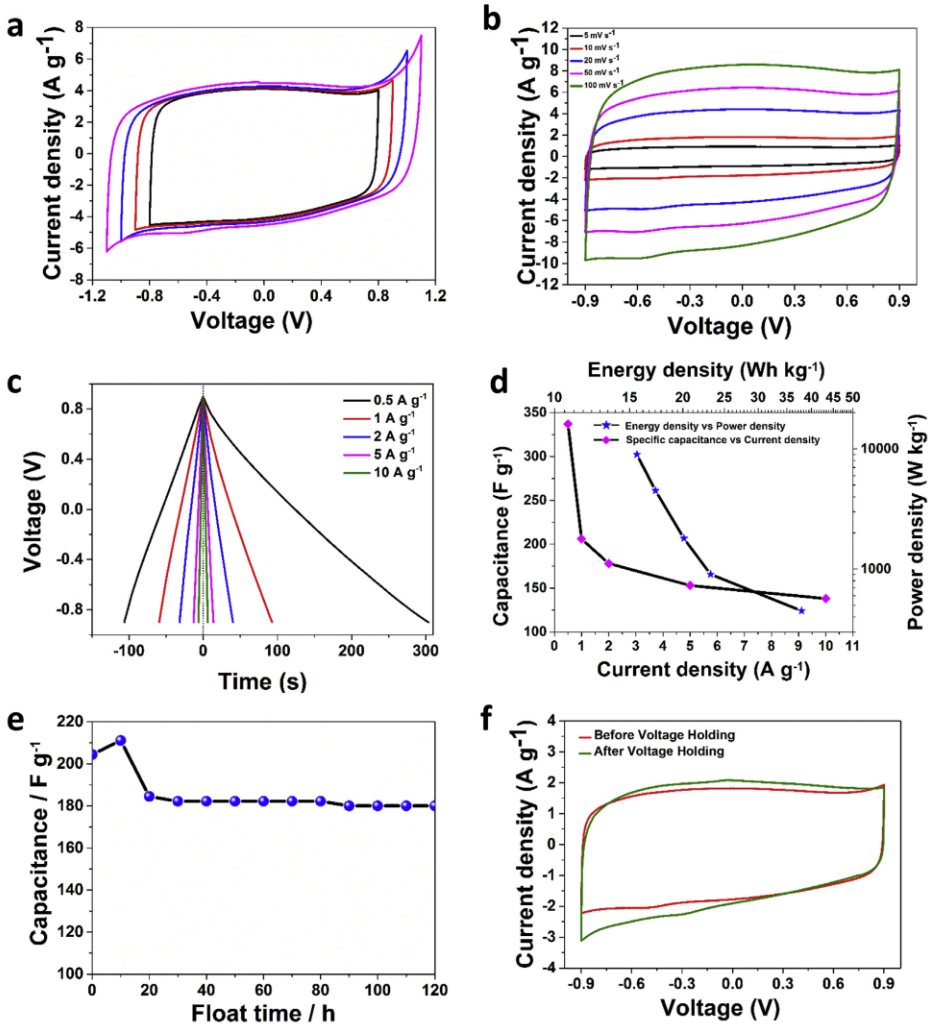

Fig. 5. (a) CV curves at 50 mV s^{-1} at different voltage windows, (b) CV curves at scan rates from 5 to 100 mV s^{-1}, (c) The galvanostatic charge/discharge curves from 0.5 to 10 A g^{-1}, (d) Ragone plot and the specific capacitance as function of the current density, (e) voltage holding vs. capacitance at a constant current density of 1 A g^{-1}, and (f) CV curves at scan rate of 10 mV s^{-1} before and after cycling of symmetric AEG two electrode cell, respectively.

even at high scan rate of 100 mV s^{-1}, indicating rapid ions transportation and good rate capability. The broad peak at ~0.6 V on the CV curves can be associated to the redox activities of nitrogen and oxygen in the matrix of the electrode material. The constant current charge-discharge (CD) curves are shown in Fig. 5(c). Surprisingly, the CD curves exhibits a linear voltage-time function with non-symmetric triangular shape with longer discharge time compared to the charging time. This could be tentatively attributed to the presence of nitrogen and oxygen in the electrode materials which could promote faradaic reaction, influencing the discharge time. The corresponding electrode specific capacitance and Ragone plot (Fig. 5(d)) showing the energy density versus the power density of the symmetric supercapacitor are calculated from the CD curves according to the equations below [32,33]:

$$C_{sp} = 4 \times I\,\Delta t / m\,\Delta V \quad (1)$$

$$E_{max} = 0.5\,C(\Delta V)^2 = \left(C_{sp} \times \Delta V^2\right)/28.8 \quad (2)$$

$$P_{max} = 3.6 \times E_{max}/\Delta t \quad (3)$$

Where C_{sp} is the specific capacitance (F g^{-1}), E_{max}, the maximum energy density (Wh kg^{-1}), P_{max}, the power density (kW kg^{-1}), I is the discharge current (A), m is the total mass of the active material in both electrodes (g), Δt is the discharge time (s), and ΔV is the applied potential (V).

The device exhibits a specific capacitance of 337 F g^{-1} at a current density of 0.5 A g^{-1} and an outstanding energy density of 37.9 Wh kg^{-1} at a power density of 450 W kg^{-1} at the same current density. The energy density of AEG based symmetric supercapacitor is higher than those previously reported for carbon-based symmetric supercapacitors in aqueous electrolyte [34–36]. Table 3 compares the C_{sp}, E_{max} values obtained in this work with previous values reported.

Cycling test based on floating (ageing) has been used to investigate the long-term stability of the symmetric device based on AEG. During ageing, a 10 h period of potentiostatic mode (called 'floating') was followed by five galvanostatic charge-discharge at 1 A g^{-1} and the specific capacitance value was estimated from the fifth discharge. The floating and galvanostatic sequences were repeated 12 times, i.e. for a total floating time of 120 h [46]. Fig. 5(e) shows the stability during voltage-holding over 120 h. Floating has a significant impact on the specific capacitance which rapidly increases and decreases during the first 20 h of ageing, before stabilizing at a constant value throughout the remaining ageing time. The increase is due to the insertion of ions into the matrix of the electrode at the initial stage of the holding, while the decrease could be related to partial removal of surface functional groups. Only ~10% of capacitance loss was observed during the first 20 h of ageing. The excellent stability of the AEG electrode material showed that this device can be charged and discharged with little degree of degradation. Fig. 5(f) shows the CV curves at a scan rate of 10 mV s^{-1} before and after voltage holding. The cell showed no significant degradation with only a small current leap at the negative electrode. Overall, the CV indicates that there was very little decay in the capacitive performance of the cell, confirming the result obtained in Fig. 5(e).

EIS analysis is crucial to investigate the behavior of the electrodes. The impedance measurement was taken in an open circuit potential, in the frequency range of 100 kHz–0.01 Hz. The Nyquist impedance plot is presented in Fig. 6(a) which features a small arc in the high and middle frequency region indicating charge transfer resistance (R_{CT}), and a nearly vertical line in the low frequency region, indicating ideal capacitive behavior and good electrical conductivity of the AEG electrode material. The intersection with the real Z′ axis from Nyquist is the solution resistance (R_S) which includes the total resistance of the ionic resistance of electrolyte, the intrinsic resistance of the active materials and the contact resistance at the interface between the active electrode material and current collector [47]. From the Figure, the R_S and R_{CT} values of the device are 0.4 Ω and 1.6 Ω, respectively. The fitting of the Nyquist plot was performed with a fitting program ZFIT/EC-Lab version 10.40 using the equivalent circuit shown as inset of Fig. 6(a). The fitting is also shown in Fig. 6(a). In the equivalent circuit, the solution resistance (R_s) is connected in series with a constant phase element Q, which is connected in parallel with the charge transfer resistance (R_{CT}). The transition from high-low frequency region is modelled by Warburg diffusion element and represented by W which is in series with R_{CT}. Ideally, at very low frequencies, an ideal polarizable capacitive electrode with the mass capacitance (C_L) should give rise to a straight line parallel to the imaginary axis, However, from the Nyquist plot in Fig. 6(a) there is a divergence from this ideal behavior. This divergence is attributed to the existence of a resistive element associated to C_L. This resistance is denoted as leakage resistance R_L and is in parallel with C_L. Table 4 below summarizes all the parameters obtained from the fitting. The result indicates an optimized minimization of experimental data with the design of the cell with an error of 0.03. X^2 represents the criterion for minimization of the fit. $X/\sqrt{N}$ where N is the number of data points, is a normalized expression of X^2, whose value is independent to the number of points and is represented as the error. EIS measurements were made after voltage holding and the result is presented in Fig. 6 (b). The result shows that there was no much deviation to the initial Nyquist plot confirming that indeed only very little degradation of the electrode material occurred

Table 3
Performance comparison of AEG symmetric cell with previous reported electrodes.

Precursor	Activation agent	S_{BET} (m^2 g^{-1})	Potential (V)	Capacitance (F g^{-1})	Scan rate	Electrolyte	Energy (W h kg^{-1})	Ref.
Coal tar pitch	KOH	1003	1	224 (2)	0.1 A g^{-1}	6 M KOH	7.8	[37]
Poly-aniline (PANI)	–	400	1	125 (3)	0.2 A g^{-1}	6 M KOH	–	[38]
polystyrene	KOH	2350	1	258 (3)	5 mV s^{-1}	6 M KOH	–	[39]
Polyvinyl alcohol/graphene	KOH	2994	1.6	188 (2)	0.5 A g^{-1}	6 M KOH	16.7	[40]
Bamboo	KOH	1472	1	301 (3)	0.1 A g^{-1}	6 M KOH	-	[41]
Bamboo	KOH	1472	3.5	146 (2)	0.2 A g^{-1}	EMIM TFSI	6.1	[41]
3D graphene	–	3523	3.5	202 (2)	1 A g^{-1}	1 M TEABF4/AN	51	[15]
Graphite	HNO_3/H_2SO_4 (1:1)	–	2.5	1071 (3)	–	0.1 M KOH	–	[42]
Poly(vinylidene chloride) (PVDC)	KOH	2050	4	38 (2)	1 mV s^{-1}	1 M $TEABF_4$ in PC	–	[43]
Phenol-formaldehyde resin	KOH	1902	1.3	105 (2)	–	1 M H_2SO_4	–	[44]
Polypyrrole (PPy)	KOH	3432	2.3	290 (2)	0.1 A g^{-1}	$EMImBF_4$	–	[45]
Expanded graphite	KOH	457	1.8	337	0.5 A g^{-1}	6 M KOH	37.9	This work

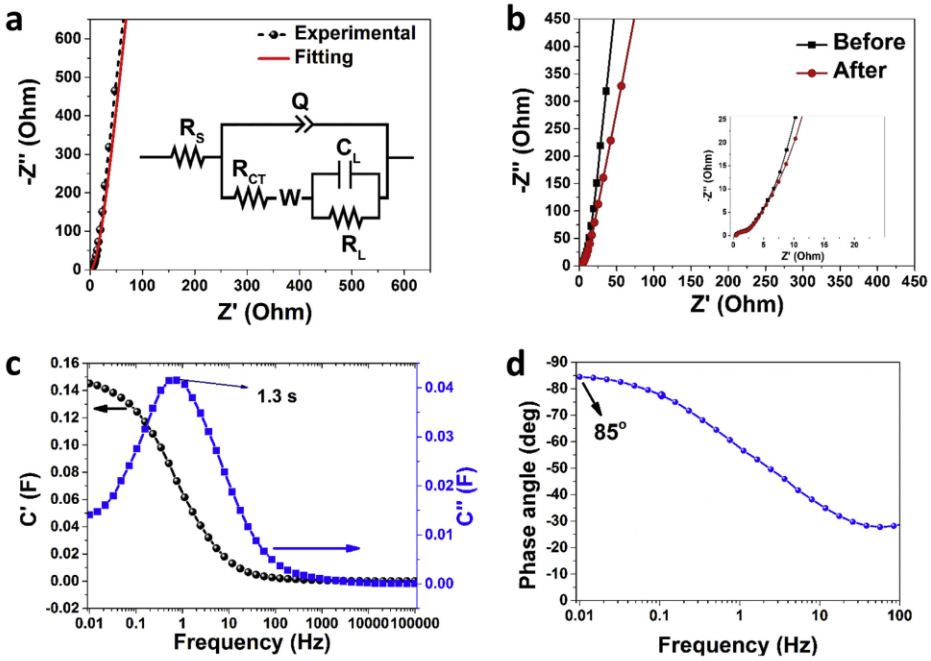

Fig. 6. (a) EIS plot and fitting curve, (b) EIS before and after cycling, (c) the real and the imaginary part of the cells capacitance against frequency, (d) the phase angle versus frequency in 6 M KOH aqueous electrolytes of symmetric AEG two electrode cell respectively.

Table 4
Fitting parameters of EIS.

R_S (Ω)	Q ($F\ s^{(a-1)}$)	a	R_{CT} (Ω)	A_W ($\Omega\ s^{-0.5}$)	C_L (F)
0.411	0.0002	0.786	1.772	13.07	0.023

$X^2 = 0.03$, $X/\sqrt{N} = 0.029$, CPE ≡ Q, a ≡ n.

except small change in slope in the low frequency region. This deviation could be attributed to the repeated cycling effect such as increment voltage drop, polarization and less utilization or insufficient active material during the cycling because of the high current density used. Furthermore, the deviation could also be due to the formation of inactive sites caused by the collapse of some part of sheet-like structures during the cycle test.

The real and imaginary parts of the capacitance of the cell as a function of the frequency are shown in Fig. 6(c). C′ represents the real accessible capacitance of the cell at the corresponding frequency (0.01 Hz), representing the deliverable capacitance which is 0.145 F. The evolution of C″ which defines the transition frequency between a pure capacitive and a pure resistive behavior is also shown in the figure which also represents the energy loss due to the irreversible process of the electrodes. C″ is also used to define the transition between pure capacitive and pure resistive behavior of the AEG sample [48]. From the figure, C″ as a function of frequency shows a peak which appears at a maximum frequency of 0.75 Hz defining a relaxation time of ~1.3 s obtained from $\tau = 1/\omega_{max} = 1/(2\pi f_{max})$. This value indicates that the full capacitance of the cell can be reached within a fast charging time of 1.3 s.

Finally Fig. 6(d) presents the phase angle as a function of frequency. The phase angle for the electrodes is about ~−84.5°, very close to −90° which defines ideal capacitive response.

5. Conclusion

In summary, novel carbon nanosheets derived from expanded graphite was synthesized. The produced AEG material possesses a sheet-like morphology with presence of small amount of oxygen and nitrogen as revealed by XPS. An improved SSA of 457 $m^2\ g^{-1}$ compared to the that of EG results in high specific capacitance of 337 $F\ g^{-1}$, high energy density of 37.9 Wh kg^{-1} and power density of 450 W kg^{-1} at 0.5 A g^{-1} with excellent rate capability in 6 M KOH aqueous electrolyte. No significant degradation or capacitance loss of the supercapacitor cell was observed after 120 h of floating test. These results suggest that the AEG material has great potential in high performance energy storage device applications and is also expected to be useful to the broader scientific community on electrochemical capacitors if fully explored.

Acknowledgement

This work is based upon research supported by the South African Research Chairs Initiative of the Department of Science and Technology and National Research Foundation of South Africa (Grant No. 97994). Any opinions, findings and conclusions or recommendations expressed in this work are those of authors, and the NRF and the DST do not accept any liability with regard thereto. F. Barzegar, M. J. Madito and D. Y. Momodu acknowledge financial

support from the University of Pretoria and the NRF for their PhD bursaries. A. Bello acknowledge the University of Pretoria's financial support for their Postdoctoral fellowship.

References

[1] J. Ding, H. Wang, Z. Li, K. Cui, D. Karpuzov, X. Tan, et al., Peanut shell hybrid sodium ion capacitor with extreme energy–power rivals lithium ion capacitors, Energy Environ. Sci. 8 (2015) 941–955.
[2] X. Peng, L. Peng, C. Wu, Y. Xie, Two dimensional nanomaterials for flexible supercapacitors, Chem. Soc. Rev. 43 (2014) 3303–3323.
[3] H. Sun, L. Cao, L. Lu, Bacteria promoted hierarchical carbon materials for high-performance supercapacitor, Energy Environ. Sci. 5 (2012) 6206.
[4] P. Simon, Y. Gogotsi, Materials for electrochemical capacitors, Nat. Mater 7 (2008) 845–854.
[5] J. Pu, F. Cui, S. Chu, T. Wang, E. Sheng, Z. Wang, Preparation and electrochemical characterization of hollow hexagonal NiCo 2 S 4 nanoplates as pseudocapacitor materials, ACS Sustain. Chem. Eng. 2 (2014) 809–815.
[6] H. Jiang, P.S. Lee, C. Li, 3D carbon based nanostructures for advanced supercapacitors, Energy Environ. Sci. 6 (2013) 41–53.
[7] H. Wang, Z. Xu, A. Kohandehghan, Z. Li, K. Cui, X. Tan, et al., Interconnected carbon nanosheets derived from hemp for ultrafast supercapacitors with high energy, ACS Nano 7 (2013) 5131–5141.
[8] D. Higgins, Z. Chen, D.U. Lee, Z. Chen, Activated and nitrogen-doped exfoliated graphene as air electrodes for metal–air battery applications, J. Mater. Chem. A 1 (2013) 2639.
[9] T. Brousse, D. Belanger, J.W. Long, To be or not to be pseudocapacitive? J. Electrochem. Soc. 162 (2015) A5185–A5189.
[10] V. Presser, M. Heon, Y. Gogotsi, Carbide-derived carbons – from porous networks to nanotubes and graphene, Adv. Funct. Mater. 21 (2011) 810–833.
[11] Y. Gao, Y.S. Zhou, M. Qian, X.N. He, J. Redepenning, P. Goodman, et al., Chemical activation of carbon nano-onions for high-rate supercapacitor electrodes, Carbon 51 (2013) 52–58.
[12] E. Iyyamperumal, S. Wang, L. Dai, Vertically aligned BCN nanotubes with high capacitance, ACS Nano 6 (2012) 5259–5265.
[13] L.L. Zhang, R. Zhou, X.S. Zhao, Graphene-based materials as supercapacitor electrodes, J. Mater. Chem. 20 (2010) 5983–5992.
[14] X. Li, B. Wei, Supercapacitors based on nanostructured carbon, Nano Energy 2 (2013) 159–173.
[15] L. Zhang, F. Zhang, X. Yang, G. Long, Y. Wu, T. Zhang, et al., Porous 3D graphene-based bulk materials with exceptional high surface area and excellent conductivity for supercapacitors, Sci. Rep. 3 (2013) 1408.
[16] L. Zhang, X. Yang, F. Zhang, G. Long, T. Zhang, K. Leng, et al., Controlling the effective surface area and pore size distribution of sp2 carbon materials and their impact on the capacitance performance of these materials, J. Am. Chem. Soc. 135 (2013) 5921–5929.
[17] A. Bello, F. Barzegar, D. Momodu, F. Taghizadeh, M. Fabiane, J. Dangbegnon, et al., Morphological characterization and impedance spectroscopy study of porous 3D carbons based on graphene foam-PVA/phenol-formaldehyde resin composite as an electrode material for supercapacitors, RSC Adv. 4 (2014) 39066–39072.
[18] L. Dong, Z. Chen, D. Yang, H. Lu, Hierarchically structured graphene-based supercapacitor electrodes, RSC Adv. 3 (2013) 21183.
[19] Y. Ito, Y. Tanabe, H.-J. Qiu, K. Sugawara, S. Heguri, N.H. Tu, et al., High-quality three-dimensional nanoporous graphene, Angew. Chem. 126 (2014) 4922–4926.
[20] H. Aoki, M.S. Dresselhaus (Eds.), Physics of Graphene, Springer International Publishing, Cham, 2014.
[21] Y. Wang, D.C. Alsmeyer, R.L. McCreery, Raman spectroscopy of carbon materials: structural basis of observed spectra, Chem. Mater. 2 (1990) 557–563.
[22] M. Cardona, G. Güntherodt (Eds.), Light Scattering in Solids III, Springer Berlin Heidelberg, Berlin, Heidelberg, 1982.
[23] A. Cuesta, P. Dhamelincourt, J. Laureyns, A. Martínez-Alonso, J.M.D. Tascón, Raman microprobe studies on carbon materials, Carbon 32 (1994) 1523–1532.
[24] T. Jawhari, A. Roid, J. Casado, Raman spectroscopic characterization of some commercially available carbon black materials, Carbon 33 (1995) 1561–1565.
[25] S. Sze, Raman spectroscopic characterization of carbonaceous aerosols, Atmos. Environ. 35 (2001) 561–568.
[26] B. Dippel, H. Jander, J. Heintzenberg, NIR FT Raman spectroscopic study of flame soot, Phys. Chem. Chem. Phys. 1 (1999) 4707–4712.
[27] A. Sadezky, H. Muckenhuber, H. Grothe, R. Niessner, U. Pöschl, Raman microspectroscopy of soot and related carbonaceous materials: spectral analysis and structural information, Carbon 43 (2005) 1731–1742.
[28] A.P. Terzyk, The influence of activated carbon surface chemical composition on the adsorption of acetaminophen (paracetamol) in vitro, Colloids Surf. A Physicochem. Eng. Asp. 177 (2001) 23–45.
[29] R.J.J. Jansen, H. van Bekkum, XPS of nitrogen-containing functional groups on activated carbon, Carbon 33 (1995) 1021–1027.
[30] M.P. Bichat, E. Raymundo-Piñero, F. Béguin, High voltage supercapacitor built with seaweed carbons in neutral aqueous electrolyte, Carbon N. Y. 48 (2010) 4351–4361.
[31] L. Demarconnay, E. Raymundo-Piñero, F. Béguin, A symmetric carbon/carbon supercapacitor operating at 1.6V by using a neutral aqueous solution, Electrochem. Commun. 12 (2010) 1275–1278.
[32] M.D. Stoller, R.S. Ruoff, Best practice methods for determining an electrode material's performance for ultracapacitors, Energy Environ. Sci. 3 (2010) 1294–1301.
[33] Y. Gogotsi, P. Simon, True performance metrics in electrochemical energy storage, Science 334 (2011) 917–918.
[34] M. Sevilla, W. Gu, C. Falco, M.M. Titirici, A.B. Fuertes, G. Yushin, Hydrothermal synthesis of microalgae-derived microporous carbons for electrochemical capacitors, J. Power Sources 267 (2014) 26–32.
[35] S. Shivakumara, B. Kishore, T.R. Penki, N. Munichandraiah, Symmetric supercapacitor based on partially exfoliated and reduced graphite oxide in neutral aqueous electrolyte, Solid State Commun. 199 (2014) 26–32.
[36] Q. Gao, L. Demarconnay, E. Raymundo-Piñero, F. Béguin, Exploring the large voltage range of carbon/carbon supercapacitors in aqueous lithium sulfate electrolyte, Energy Environ. Sci. 5 (2012) 9611.
[37] X. He, R. Li, J. Qiu, K. Xie, P. Ling, M. Yu, et al., Synthesis of mesoporous carbons for supercapacitors from coal tar pitch by coupling microwave-assisted KOH activation with a MgO template, Carbon 50 (2012) 4911–4921.
[38] K.-S. Kim, S.-J. Park, Easy synthesis of polyaniline-based mesoporous carbons and their high electrochemical performance, Microporous Mesoporous Mater. 163 (2012) 140–146.
[39] S.-J. Han, Y.-H. Kim, K.-S. Kim, S.-J. Park, A study on high electrochemical capacitance of ion exchange resin-based activated carbons for supercapacitor, Curr. Appl. Phys. 12 (2012) 1039–1044.
[40] F. Barzegar, A. Bello, O.O. Fashedemi, J.K. Dangbegnon, D.Y. Momodu, F. Taghizadeh, et al., Synthesis of 3D porous carbon based on cheap polymers and graphene foam for high-performance electrochemical capacitors, Electrochim. Acta 180 (2015) 442–450.
[41] W. Tian, Q. Gao, Y. Tan, K. Yang, L. Zhu, C. Yang, et al., Bio-inspired beehive-like hierarchical nanoporous carbon derived from bamboo-based industrial by-product as a high performance supercapacitor electrode material, J. Mater. Chem. A 3 (2015) 5656–5664.
[42] R. Nandhini, P.A. Mini, B. Avinash, S.V. Nair, K.R.V. Subramanian, Supercapacitor electrodes using nanoscale activated carbon from graphite by ball milling, Mater. Lett. 87 (2012) 165–168.
[43] Y. Kim, Y. Horie, S. Ozaki, Y. Matsuzawa, H. Suezaki, C. Kim, et al., Correlation between the pore and solvated ion size on capacitance uptake of PVDC-based carbons, Carbon 42 (2004) 1491–1500.
[44] H. Teng, Y.-J. Chang, C.-T. Hsieh, Performance of electric double-layer capacitors using carbons prepared from phenol–formaldehyde resins by KOH etching, Carbon 39 (2001) 1981–1987.
[45] L. Wei, M. Sevilla, A.B. Fuertes, R. Mokaya, G. Yushin, Polypyrrole-derived activated carbons for high-performance electrical double-layer capacitors with ionic liquid electrolyte, Adv. Funct. Mater. 22 (2012) 827–834.
[46] P. Ratajczak, K. Jurewicz, F. Béguin, Factors contributing to ageing of high voltage carbon/carbon supercapacitors in salt aqueous electrolyte, J. Appl. Electrochem. 44 (2013) 475–480.
[47] J. Luo, H.D. Jang, J. Huang, Effect of sheet morphology on the scalability of graphene-based ultracapacitors, ACS Nano 7 (2013) 1464–1471.
[48] P.L. Taberna, P. Simon, J.-F.F. Fauvarque, Electrochemical characteristics and impedance spectroscopy studies of carbon-carbon supercapacitors, J. Electrochem. Soc. 150 (2003) A292–A300.

4.1.3.3 Concluding Remarks

Novel carbon nanosheets (AEG) derived from EG were synthesized with presence of small amount of oxygen and nitrogen in the sample. An improved SSA of 457 m^2 g^{-1} for AEG as compared to the that of EG results gives high specific capacitance of 337 F g^{-1}, high energy density of 37.9 Wh kg^{-1} and power density of 450 W kg^{-1} at 0.5 A g^{-1} with excellent rate capability in 6 M KOH aqueous electrolyte and no capacitance loss after 120 h of floating test. These results suggest that the AEG material has a great potential for high performance energy storage applications and is also expected to be useful to the broader scientific community on electrochemical capacitors if fully explored.

4.1.4 Synthesis and characterization of supercapacitor electrodes based on AC derived from pine tree cones.

4.1.4.1 Introduction

Commercially available activated carbons (ACs) used as electrode materials for ECs are usually fabricated from coconut shells, coal, wood and pitch [71,237–239]. Recently attention has been shifted to the use of biomass or organic waste materials for the production of efficient, low-cost, scalable, locally available and renewable carbon materials for absorbents or energy storage applications [240]. These include materials such as waste tea-leaves [73], potato starch [74], fish scale [75], waste coffee beans [76], etc. as a source of carbon materials for ECs applications [241].

However, there are few reports on the use of activated carbon from pine cones for supercapacitor application. Pines are coniferous trees in the genus *Pinus* family of the *Pinaceae*; they are among the most important species of tree that are highly valued throughout the world and are mostly composed of cellulose, hemicellulose, lignin, resin and tannins [242,243]. The common methods of activation have been extensively carried out earlier by other researchers for the production of activated carbons for absorbent applications [243–245]. Our choice of the pin econe is due to the fact that pine trees naturally abundant in large amounts especially in Africa and many countries across the world and can be easily activated by a facile activation method.

4.1.4.2 Result and discussions

Figure 4-1 (a) and (b) shows the morphology of the surface of the pine cone before activation. As seen from the figure, the surface of the sample composes of two different surfaces with an interconnected porous architecture and some flat surface which could be beneficial in providing a large ion-accessible platform for fast ion transport for high-performance supercapacitors. Figure 4-1 (c) shows the XRD patterns of the pine activated carbons (PACS) using a Co-Kα x-ray source with a wavelength of 1.7890 Å. It is noted that the XRD peak of PAC (JCPDS 00-008-0415) are identified with graphite peaks. It is observed that the PAC has a low crystallinity with the characteristic graphitic (carbon) peaks recorded, at a 2θ value of 26° (002). The surface area and pore size distribution of the pine activated carbon was measured from the nitrogen adsorption–desorption isotherms at 77 K. Figure 4-1 (d)

shows that the sample exhibits a type II isotherm with an H4 hysteresis behavior. A little hysteresis loop at a relative pressure P/P_0 of about 0.45 - 0.65 was observed which is attributed to capillary condensation of the mesopores in the solid material [246]. The BET specific surface area of 808 m^2 g^1 was measured based on the standard BET method. The pore size distribution as analyzed by the Barrett Joyner Halenda (BJH) method indicates the presence of micro and mesopores in the material. The size of the mesopores likely arises from slit-like structures formed by randomly collapsed nanostructures with most of other micropores of diameters less than 2 nm. A small fraction of the meso/macro-pores with a wide pore diameter range of values greater than 4 nm originates from the bottleneck-like pores. The results from the surface area and pore volume distributions are summarized in Table 1. These results suggest that the material is suitable as a supercapacitor electrode material and that the microstructural properties are beneficial in improving the volumetric energy and power characteristics of the pine-based supercapacitors.

Table 1 Surface area, micropore and cumulative volume and pore size of PAC

Surface area (m^2/g)	micropore volume[a] (cm^3/g)	cumulative volume[b] (cm^3/g)	Pore diameter[c] (nm)
808	0.28	0.13	2.98

[a] t-Plot micropore volume

[b] BJH Desorption cumulative volume of pores between 1.7000 nm and 300.0000 nm diameter

[c] BJH Desorption average pore diameter (4V/A)

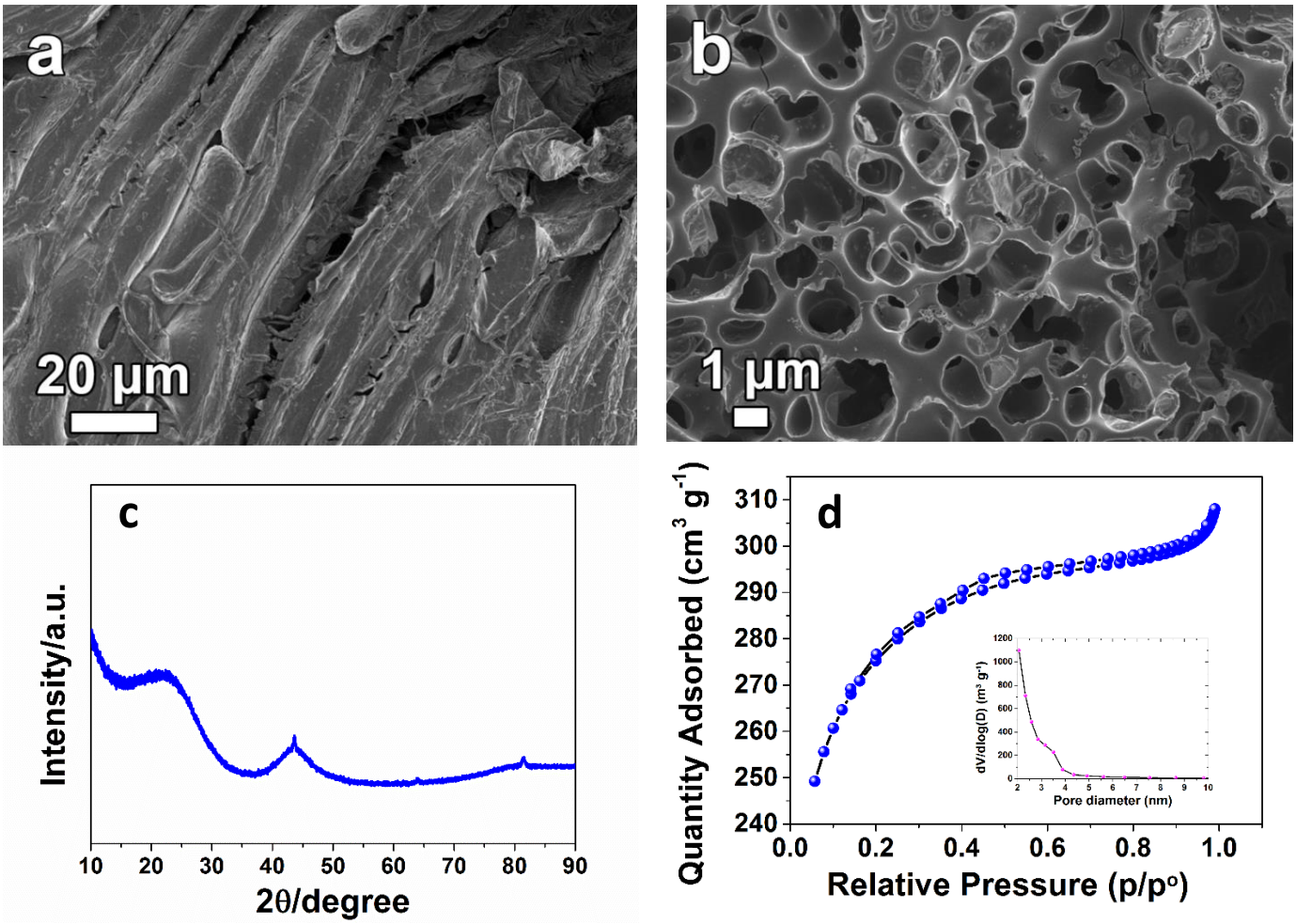

Figure 4-1 (a) SEM micrographs of raw pine cone, (b) SEM micrographs of PAC (c) X-ray photoelectron spectroscopy and (d) the N_2 adsorption-desorption isotherm of PAC

Figure 4-2 (a) shows CV curves of PAC material at different operating voltages ranging from 0.8 V to 1.2 V in a three electrode system. Figure 4-2 (b) shows the results of the CV plots for the PAC material at scan rates ranging from 5 to 50 mV s^{-1} in a 1.2 V potential window. The CV plots are characterized with no oxidation or reduction peaks indicating a typical EDL capacitor behavior.

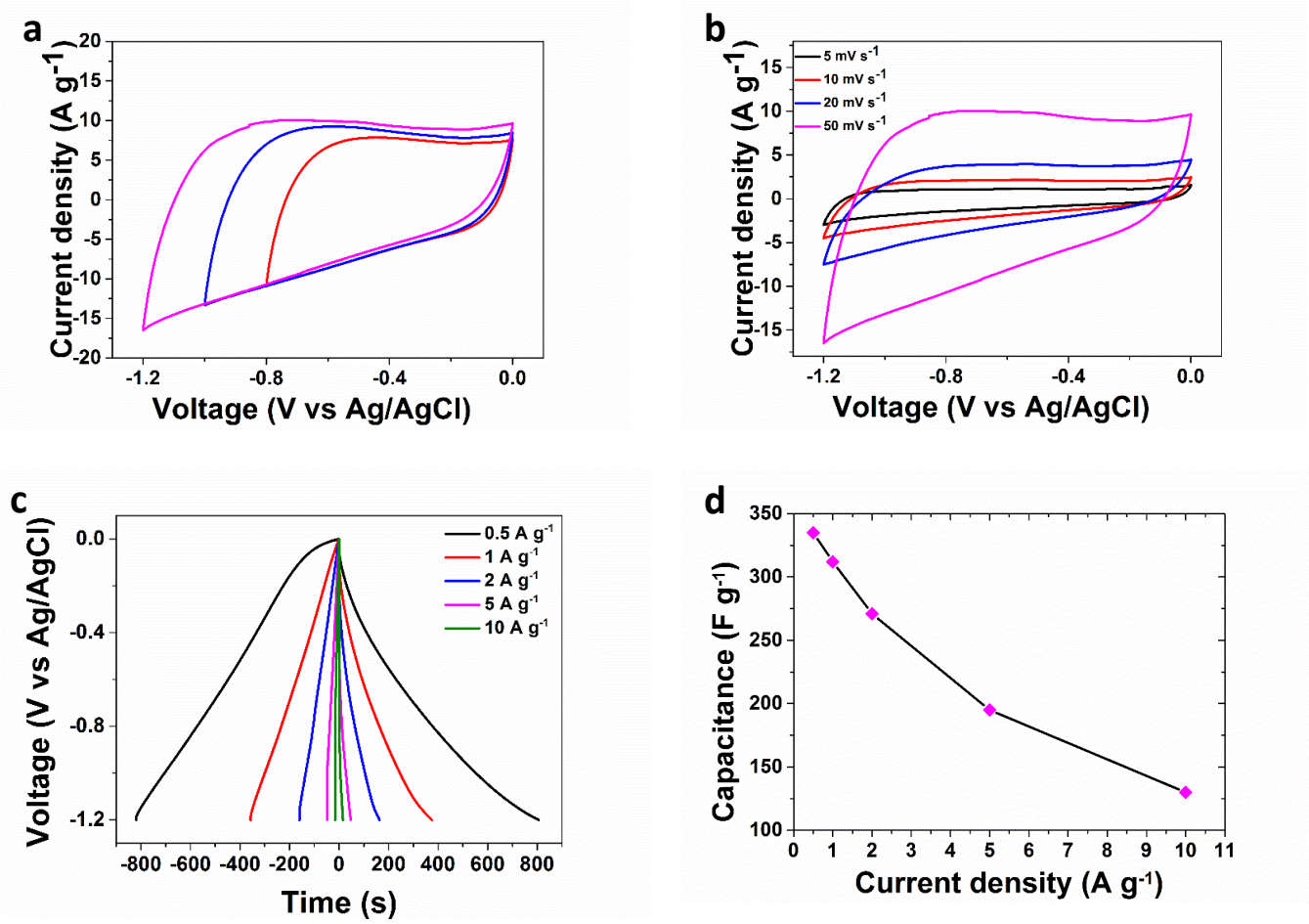

Figure 4-2 (a) CV at different voltage windows in 6 M KOH aqueous electrolytes in three electrode system, (b) CV curves at scan rates from 5 to 50 mV s^{-1}, (c) the galvanostatic charge/discharge curves from 0.5 to 10 A g^{-1} for PAC, (d) the specific capacitance as function of the current density.

The galvanostatic charge and discharge curves at different current densities are shown in Figure 4-2 (c). The charge –discharge plots are almost triangular and symmetric which indicates a fast I-V response [177]. The measured value of the specific capacitance (C_s) of the PAC is 335 F g^{-1} at a current density of 0.5 A g^{-1}. The

C_s value decreases from 335 F g^{-1} to 130 F g^{-1} with an increase in current density from 0.5 to 10 A g^{-1} as shown in figure 2 (d). This shows a quite stable reduction in the capacitance of the PAC electrode material with a considerable increase in current density.

Figure 4-3 (a) demonstrates the stability of the electrode material by subjecting it to continuous charging and discharging at a constant current density over several cycles. The PAC shows no capacitance loss even after 10000 cycles at a current density of 2 A g^{-1}. However, a small increase in the capacitance (~2.8 %) was observed after the initial cycling process which is similar to observations made by Ren et al.[247]. In their work, they attributed this occurrence to the possible swelling of the carbon material at some defective sites, which promotes electrolyte ions intercalation into the space created by the swelling or creation of more pores. This leads to the more accessible surface area and hence increase in the efficiency of the cell which was stable and maintained throughout the cycling process [247].

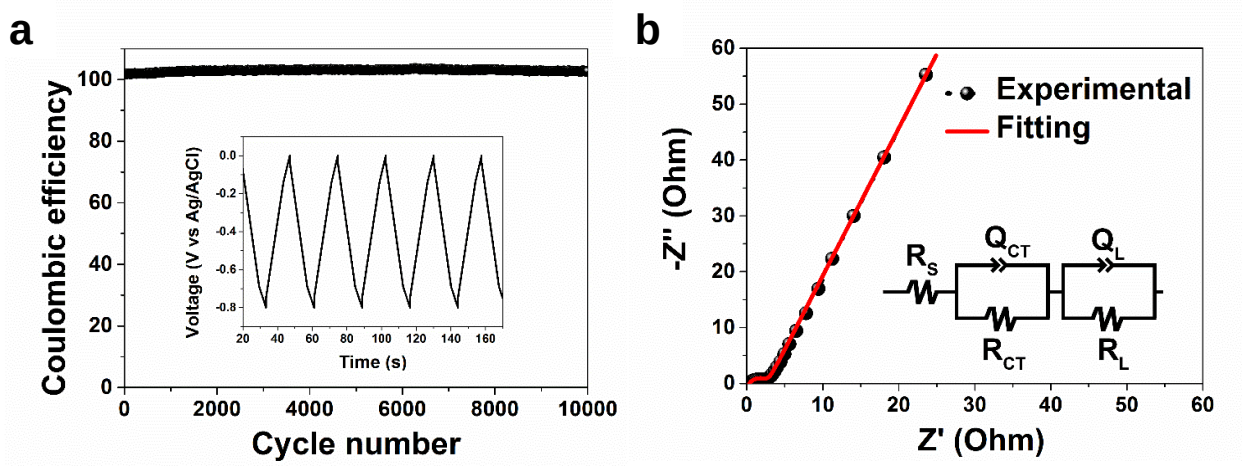

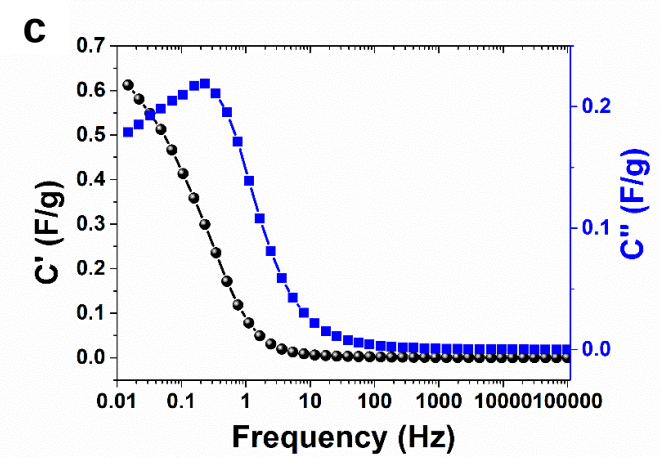

Figure 4-3 (a) cycle stability at a constant current density of 2 A g^{-1} (b) EIS plot and fitting curve with the equivalent circuit (c) the real and imaginary part of the cell's capacitance against frequency

The electrochemical impedance spectroscopy (EIS) was used to study the rate capability of an electrode material. The Nyquist spectrum of the electrode material is shown in figure 4-3 (b). The EIS plot shows a semi-circle in the high-frequency region and a sloping line in the low-frequency region. The intercept on the real Z - axis denoted by R_S represents the combined resistance of the electrolyte, the contact between the current collector, the metal leads and the electrode material. An Ohmic resistance (R_S) value of 0.35 Ω was obtained which shows a good conductivity and high quality of the activated carbon electrode [248]. The diameter of the semi-circle in the high-frequency region corresponds to the charge transfer resistance (R_{CT}) with a value of 2.1 Ω which is attributed to the double layer capacitance C_{DL} and the redox reaction that might occur at the surface of the electrode material. At the low-frequency region, the plot should be a parallel line to the imaginary axis. However,

the resulting curve shows a deviation from this theoretical behavior which is due to the presence of leakage current denoted by R_L. The impedance spectrum was further analyzed with the complex nonlinear least-squares (CNLS) fitting method using the ZFIT software and the equivalent circuit as shown in the inset to figure 4-3 (b) based on the equivalent RC model. The obtained plot also shows that the model used fits well with the experimental data. The capacitance as a function of the frequency (figure 3 (c)) was also used to check the charge propagation of the electrode material and was calculated. From figure 4-3 (c) above, the capacitance (C′) of the cell is 0.15 F (from topmost part of the C′ graph) while C" which defines the transition frequency between a pure capacitive and a pure resistive behaviour has a relaxation time of ~4.3 seconds obtained by taking the reciprocal of the maximum frequency in the C″ graph [183].

4.1.4.3 Concluding Remarks

In this section, for the first time, an excellent EDLC behaviour of porous and high surface area AC derived from pine cones (PAC) material synthesized obtained locally in South Africa and pyrolyzed by direct carbonization of chemically activated pine cones was successfully demonstrated. The choice of organic waste from biological-based raw materials was inspired by its relative abundance, low cost and ultimately the environmental friendly nature associated with them.

The PAC electrode material when electrochemically tested exhibited a superior electrochemical performance due to the presence of a porous network which allows the efficient transport of electrolyte ions and the storage of charges within the material. An outstanding specific capacitance of 335 F g^{-1} at a current density of 0.5 A g^{-1} with no capacitance loss after 10,000 charge–discharge cycles at current density of 2 A g^{-1}. Thus, the results demonstrate the potential for applying pine cone activated carbon material as a suitable and promising electrode material for fabricating low cost energy storage devices. Although this study is still at its initial stage, enhancement of the results obtained so far can be further optimized with respect to the specific capacitance and the adoption of this electrode material in asymmetrical capacitors in order to boost the energy density of the entire supercapacitor device.

4.2 STUDY THE EFFECT OF DIFFERENT ELECTROLYTES ON THE ELECTROCHEMICAL BEHAVIOR OF SUPERCAPACITORS BASED ON AC

4.2.1 Effect of different aqueous electrolytes on AC based supercapacitors.

4.2.1.1 Introduction

Organic and ionic electrolytes are commonly used for commercial energy storage applications due to their wide operating voltages [19,249] which increase the overall energy density. However, organic and ionic liquids are plagued with some demerits which include high cost, low conductivity, generally complicated handling procedures

involved, high flammability and electrolyte leakage [22]. In contrast, aqueous electrolytes have lower cost, environmentally friendly nature, facile preparation methods and operating stability, high ionic conductivity and proton transport which is necessary for obtaining lower internal resistance [250]. A major step to achieving best results in energy storage for AC is by studying the effect of different aqueous electrolytes on the electrochemical behavior of activated porous carbons in order to fully understand the adaptability of these porous networks with the associated electrolyte. Unfortunately, very few reports presently exist in which a detailed study have been carried out regarding this area. This study, therefore, investigates and elucidates the effect of different aqueous electrolytes on AC (3.1.4.1). The results obtained demonstrate a complete analysis of the electrochemical performance of carbon-based supercapacitors tested in KOH, LiCl and Na_2SO_4 electrolytes. The choice of these aqueous electrolytes is based on their unique properties which include the crystal radius, ionic mobility, Gibbs free energy amongst other properties mentioned earlier. The results show the potential for adopting activated porous carbons as suitable material for SC electrodes.

4.2.1.2 Result and discussions

A publication obtained from this work which details all the processes with the supporting information from the article is attached.

RSC Advances

PAPER

View Article Online
View Journal | View Issue

CrossMark click for updates

Cite this: *RSC Adv.*, 2015, **5**, 107482

Investigation of different aqueous electrolytes on the electrochemical performance of activated carbon-based supercapacitors†

F. Barzegar,[a] D. Y. Momodu,[a] O. O. Fashedemi,[b] A. Bello,[a] J. K. Dangbegnon[a] and N. Manyala*[a]

Received 20th October 2015
Accepted 11th December 2015

DOI: 10.1039/c5ra21962k

www.rsc.org/advances

In this study, porous activated carbons (AC) were synthesized by an environmentally friendly technique involving chemical activation and carbonization, with an in-depth experimental study carried out to understand the electrochemical behaviour in different aqueous electrolytes (KOH, LiCl, and Na_2SO_4). The electrochemical performance of the AC electrode was evaluated by different techniques such as cyclic voltammetry, galvanostatic charge/discharge and impedance spectroscopy. The results obtained demonstrate that the AC materials in different electrolytes exhibit unique double layer properties. In particular, the AC electrode tested in 6 M KOH showed the best electrochemical performance in terms of specific capacitance and efficiency. A specific capacitance of 129 F g^{-1} was obtained at 0.5 A g^{-1} with a corresponding solution resistance of 0.66 Ω in an operating voltage window of 0.8 V, with an efficiency of ~100% at different current densities.

Introduction

Supercapacitors (SCs) which are also referred to as electrochemical capacitors (ECs) have been extensively studied recently due to their unique capabilities for use in high power storage applications. This is due to their characteristic higher energy density as compared to conventional capacitors and much higher power densities than batteries presently in use.[1–3] The mechanism of storage in supercapacitors can be used to broadly classify SCs into two groups namely; the electric double layer capacitors (EDLCs) and faradaic or pseudocapacitors.[4] The energy storage mechanism in EDLCs depends on the efficient electrostatic accumulation of charges at the interface between electrode and electrolyte.[5] In this charge storage process, there is no transfer of charges. On the other hand, energy storage in pseudocapacitors is governed by fast redox processes involving the transfer of charges between the electrode/electrolyte interfaces.[6]

The most common materials used for EDLCs are the carbon-based materials[7–9] due to their low cost, controllable porous nature with a corresponding high specific surface area (SSA), suitable conductivity, chemical stability, adjustable structural properties and excellent electrochemical behavior which makes them ideal for use in different advanced applications.[8,10–12] Such applications include; hybrid vehicles, regenerative braking systems, memory back-up systems in electronic devices, storage components in combination with batteries to enhance battery life.[13,14]

Numerous studies[5,12,14–17] have been carried out in order to fully understand the influence of electrolyte on the performance of carbon-based SCs. Activated porous carbons derived from chemical activation of polymer hydrogels[18] have particularly received growing interest from researchers worldwide due to their facile preparation method involved in obtaining the final products with the relatively high specific surface area. Since the capacitance in EDLCs largely depends on charge accumulation and adsorption at the electrode/electrolyte interface, the specific capacitance of carbon electrodes is generally influenced by changes in its specific surface area.[19] Although it is well known that a relatively high SSA carbon-based material with the abundant porous network is ideal for enhancing the performance of EDLC electrodes, there is still no clear-cut relationship between the capacitance and SSA.[20,21] It has however been established that the pore structure governs the energy storage and power delivery capability of the material.[21]

The availability of adequate mesopores and micropores within the porous morphology provides an avenue for sufficient movement of ions in the electrolyte. These result from contribution from the volume of active micropores (<2 nm in size) serve as the ion traps for energy storage, while mesopores (2–50 nm) act as the ion transport pathways for power delivery,[22,23] and the macropores (>50 nm in size) playing the role of an ion buffering reservoir.[23] Furthermore, the pore size distribution in

[a]*Department of Physics, Institute of Applied Materials, SARCHI Chair in Carbon Technology and Materials, University of Pretoria, Pretoria 0028, South Africa. E-mail: ncholu.manyala@up.ac.za; Fax: +27 12 420 2516; Tel: +27 12 420 3549*
[b]*Department of Chemistry, University of Pretoria, Pretoria 0002, South Africa*

† Electronic supplementary information (ESI) available: Electrochemical characterization at 0.5 potential window. See DOI: 10.1039/c5ra21962k

relation to the size of the electrolyte ions significantly affects the electrochemical properties of the EDLC carbon electrodes.[24]

Organic and ionic electrolytes are commonly used for commercial applications involving carbon-based materials due to their wide operating voltages[25,26] which improves the overall energy density. This is due to the direct relationship between the energy density of the SC with respect to the operating voltage. However, organic and ionic liquids are plagued with some demerits which include high cost, low conductivity (large internal resistance), generally complicated handling procedures involved, high flammability and electrolyte leakage.[27] In contrast, aqueous electrolytes have lower cost, environmentally friendly nature, facile preparation methods and operating stability, high ionic conductivity and proton transport which is necessary for obtaining lower internal resistance.[28] It is worthy to state that even though aqueous electrolytes are characterized with a limited operating voltage in comparison with organic electrolytes, the ions present in the former are still capable of much faster transport rates in relation to the latter.[10] Thus, efforts are geared towards extending the operating voltage window of these electrolytes in order to improve the overall working potential and energy density of the SC device.

A major step to achieving this is by studying the effect of different aqueous electrolytes on the electrochemical behavior of activated porous carbons in order to fully understand the adaptability of these porous networks with the associated electrolyte. Unfortunately, very few reports presently exist in which a detailed study have been carried out regarding this area. Zhu *et al.*[29] investigated the effect of various electrolyte cations (Li^+, Na^+, K^+, H^+) on the electrochemical performance of polypyrrole/RGO based supercapacitors. They report that H^+ cation has a significantly improved result which is due to ionic conductivity, efficient ion/charge diffusion/exchange and relaxation time of the 3 M HCl compare to the rest of electrolyte that they investigated. Eliad *et al.*[30] investigated the estimating effective ion size in electrolytic solutions for porous carbon electrodes. They report that the capacitance of the material will be controlled by the relationship between the average pore size of material and the effective size of electrolyte ion.

This study therefore investigates and elucidates the effect of different aqueous electrolytes on highly conductive activated porous carbons obtained from chemically activating graphene-doped polymer gels. The results obtained demonstrate a complete analysis of the electrochemical performance of carbon-based supercapacitors tested in KOH, LiCl and Na_2SO_4 electrolytes. The choice of these aqueous electrolytes is based on their unique properties which include the crystal radius, ionic mobility, Gibbs energy amongst other properties mentioned earlier. The results show the potential for adopting activated porous carbons as suitable material for SC electrodes.

Experimental

Preparation of activated carbon electrode

Activated carbon (AC) was first prepared by the process reported in our previous work.[31] The electrode was prepared by mixing the active material (AC) and polyvinylidene fluoride (PVDF) as a binder with a weight ratio of 9 : 1, homogenized and dispersed in *N*-methylpyrrolidone (NMP) solution, and the slurry was then uniformly pasted on a nickel foam current collector and dried at 60 °C in an oven for 8 hours to ensure complete evaporation of the NMP. The three electrode measurements were performed with AC as the working electrode, Ag/AgCl (3 M KCl) serving as the reference and glassy carbon plate as the counter electrode in different electrolyte solutions of 6.0 M KOH, 1.0 M Na_2SO_4 and 6.0 M LiCl for evaluation of the electrochemical behavior.

Characterization

The sample was characterized using powder X-ray diffraction (XRD). An XPERT-PRO diffractometer (PANalytical BV, Netherlands) with theta/theta geometry, operating a cobalt tube at 35 kV and 50 mA was used to study the crystal structure of the AC material. Nitrogen adsorption–desorption isotherms were measured at −196 °C using a Micromeritics TriStar II 3020 (version 2.00) analyzer. The sample was degassed at 180 °C for more than 12 h under high vacuum condition before measurements were made. The surface area was calculated by the Brunauer–Emmett–Teller (BET) method from the adsorption desorption isotherm. The morphology of the AC was obtained on a Zeiss Ultra Plus 55 field emission scanning electron microscope (FE-SEM) operated at an accelerating voltage of 2.0 kV. Transmission electron microscopy (TEM) was carried out with a JEOL JEM-2100F microscope operated at 200 kV accelerating voltage. All electrochemical measurements were carried out using a Bio-logic VMP-300 potentiostat. These measurements included cyclic voltammetry (CV), chronopotentiometry (CP) and electrochemical impedance spectroscopy (EIS). The CV tests were carried out at different scan rates ranging from 5 to 100 mV s^{-1}, and the electrochemical impedance spectroscopy (EIS) measurements were conducted in the frequency range from 0.1 to 100 kHz with an open circuit potential (~0 V).

Results and discussions

Fig. 1(a) represents the XRD patterns of AC powder. The wavelength used for the XRD analysis was Cu-K_α, 1.5405 Å. The XRD pattern of the PAC sample is made of two distinctive features: broad peaks which are always overlapping with sharp ones. The broad diffraction peaks could be arising from the amorphous nature of the activated carbon with some degree of graphitization responsible to the presence of sharp and intense graphitic diffraction pattern.

It is noted that all the XRD peaks are identified to graphite peaks (COD: 96-900-8570) which crystallize in the orthorhombic system with space group *P*63*mc*(186), lattice parameters $a = 2.4560$ Å and $c = 6.6960$ Å. Fig. 1(b) represents the BET results of AC material. The nitrogen adsorption and desorption isotherm shows type II characteristics with H4 hysteresis loop corresponding to a complex mixture of micro and mesoporous structure for the AC sample. The corresponding specific surface area of AC is 1063 m^2 g^{-1}. The BJH desorption average pore diameter (4*V*/*A*) from Table 1 for AC is 2.79 nm, suggesting that the pore diameter of our material is bigger than all ions for all

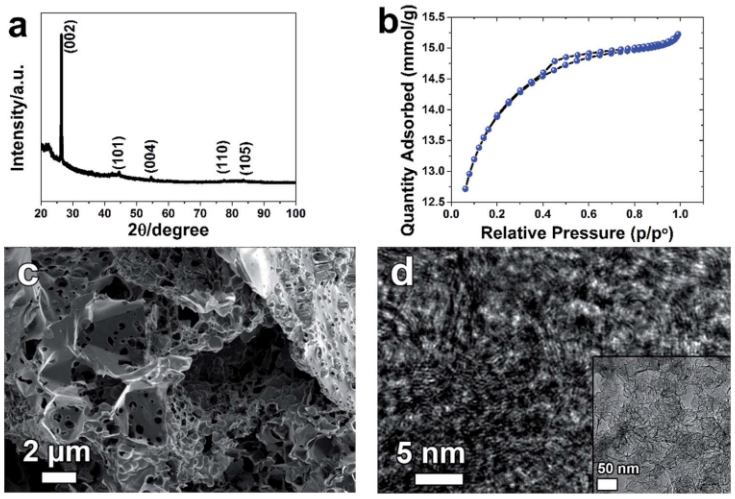

Fig. 1 (a) the X-ray diffraction, (b) N_2 adsorption–desorption isotherm, (c) SEM image, and (d) TEM image of AC.

the electrolytes that were used as observed from Table 2. Fig. 1(c) represents the SEM image of AC. It clearly shows mesoporous structure resulting from the KOH activation and carbonization process. This type of structure could provide ion path way for efficient transport during electrochemical measurement and hence suitable for fast ion transport for high performance supercapacitors. The TEM image (Fig. 1(d)) verifies that the pores are homogeneously and uniformly distributed throughout the structure of the sample. Partially crystallized carbon material is suggested by the appearance of fringes which could be due to the separation of graphite sheet. The measured interlayer distances are in the range of 0.35–0.38 nm, a little larger than the *d*-spacing of (002) crystal plane (0.335 nm) of bulk graphite due to slight expansion and distortion.[32]

The electrochemical behavior of the carbon nanosheets was evaluated in a three-electrode system with various aqueous electrolytes. The cyclic voltammetry (CV) comparison profiles measured at a scan rate of 5 mV s^{-1} are shown in Fig. 2(a). The CV profiles of the carbon material in different electrolytes show a fairly rectangular shape indicating EDLC response. The differences observed in current response and CV behaviors of AC in different electrolytes come from different physical properties of the ions from these different electrolytes. Some of these properties include the ionic radius, radius of ionic hydration sphere, molar conductivity and ionic mobility.

Table 1 Surface area, micropore and cumulative volume and pore size of AC

Surface area (m^2 g^{-1})	Micropore volume[a] (cm^3 g^{-1})	Cumulative volume[b] (cm^3 g^{-1})	Pore diameter[c] (nm)
1063	0.33	0.13	2.79

[a] *t*-Plot micropore volume. [b] BJH desorption cumulative volume of pores between 1.7000 nm and 300.0000 nm diameter. [c] BJH desorption average pore diameter (4*V*/*A*).

Table 2 represents the ionic radius, radius of water of hydration, free energy formation of water of hydration and conductivity of Li, Na, K ions. Generally, alkali metal ions are strongly solvated in water, therefore, the radius of hydration sphere decreases in the following order: $Li^+ > Na^+ > K^+$.[14] As seen in the table Li^+ is a highly solvated cation with a radius hydration sphere of 3.82 Å, while the radii hydration sphere values of the other two cations are somewhat in the same range, though lower. As the bulk electrolyte is a dynamic system, the number of water molecules around alkali metal ions cannot be strictly defined. Therefore, the main factors in determining super capacitive performance using different electrolytes have to be those of mobility and conductivity of the ions. From Table 2, K^+ ions have the highest molar conductivity with a value of 73.5 cm^2 Ω^{-1} mol^{-1}; a value which is almost two folds as compared to that of Li^+ ion, while Na^+ ion has a value of 50.1 cm^2 Ω^{-1} mol^{-1}, thus making Li^+ the cation with the lowest conductivity. Consequently, K^+ ions being characterized by the highest mobility can easily migrate into the electrode/electrolyte surface during charging and into the electrolyte bulk during discharging. The presence of the bigger SO_4^{2-} anion will reduce the mobility of Na^+ cation thus making the electrochemical behavior of the capacitor in the Na_2SO_4 electrolyte less favorable. Thus capacitive performance may be reduced in Na_2SO_4 despite the lower molar conductivity of Li^+ compared to that of Na^+ cation. The specific capacitance (C_S) can be calculated from CV curves according to the following equation:[33]

Table 2 Crystal radius, radius of hydration sphere, free energy of hydration, conductivity of alkali ions (in water solution at 25 °C)[14,34–36]

Alkali ion	Crystal radius (Å)	Radius of hydration sphere (Å)	Gibbs energy (kcal mol^{-1})	Molar conductivity (cm^2 Ω^{-1} mol^{-1})	Ionic mobility (μ 10^{-5} cm^2 s^{-1} V^{-1})
Li^+	0.60	3.82	138.4	38.6	—
Na^+	0.95	3.58	162.3	50.1	5.2
K^+	1.33	3.31	179.9	73.5	7.6
Cl^-	1.70	3.14	—	76.4	—
SO_4^{2-}	—	3.79	—	79.8	8.3
OH^-	—	3.00	—	198.0	20.6

$$C_S = \frac{\int I dU}{vm\Delta U} \quad (1)$$

or C_S can be calculated from charge–discharge curves according to the equation:[33]

$$C_S = \frac{I\Delta t}{m\Delta U} \quad (2)$$

where I is the current, ΔU is the voltage difference, v is the potential sweep rate (mV s^{-1}), m is the mass of total electrode active materials and Δt is the discharge time.

From Fig. 2(a) the CV curves for AC in KOH and Na_2SO_4 electrolytes show fairly rectangular shape while the LiCl demonstrate a highly resistive CV shape due to the molar conductivity which is less than that of KOH and Na_2SO_4 as shown in Table 1. The loading amount of active materials for electrochemical performance in KOH, LiCl and Na_2SO_4 electrolytes are 3.8 mg, 4.5 mg and 5.5 mg respectively.

Fig. 2(c) shows the specific capacitance as function of sweep rate. As expected from the molar conductivity of K^+, Na^+ and Li^+, the highest specific capacitive was obtained in KOH electrolyte followed by Na_2SO_4 and LiCl with the lowest molar conductivity. In other words, specific capacitance values of 123, 102 and 99 F g^{-1} were obtained at a sweep rate of 5 mV s^{-1} in KOH, Na_2SO_4 and LiCl electrolytes respectively. At a higher sweep rate of 100 mV s^{-1}, the specific capacitance values remained at 79, 55 and 54 F g^{-1} in the same order of electrolyte. This is in striking agreement with the molar conductivity of the cation molar conductivity, *i.e.*, the higher the molar conductivity, the higher the specific capacitance. Also, the specific capacitance has direct relationship with hydration radius, as observed from Table 2, by reducing hydration radius, the specific capacitances are increased.

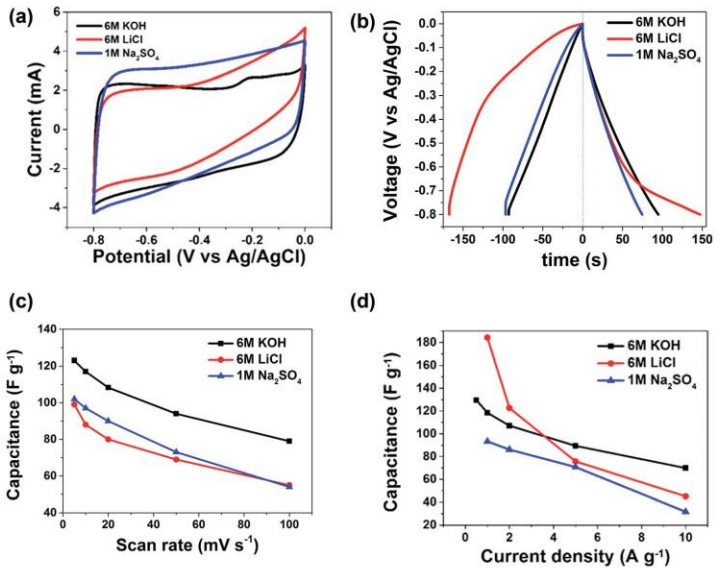

Fig. 2 (a) CV curves at scan rates of 5 mV s^{-1}, (b) the galvanostatic charge/discharge curves at 1 A g^{-1}, (c) the specific capacitance as function of the scan rate and (d) the specific capacitance as function of the current density at 0.8 V of AC different for different electrolytes as shown in the figures.

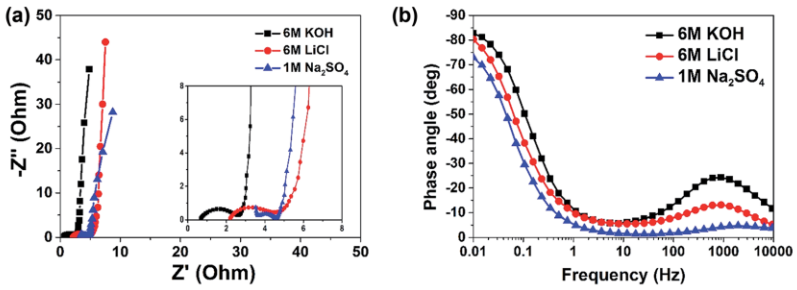

Fig. 3 (a) The Nyquist plots and (b) Bode phase angle plots in different electrolytes.

Furthermore, with increasing scan rates, the KOH reveals a stable capacitance when compared with the other two electrolytes; demonstrating a 65% capacitance retention at 100 mV s^{-1} as observed from Fig. 2(c). This stability is tentatively attributed to the presence of surface carbonyl and oxygen functional groups in the AC that may lead to redox reactions with the KOH electrolyte thereby leading to increase and stability of the electrode material.[14]

Galvanostatic experiments were performed for more accurate capacitance assessment as the measurements from the CV are not sometimes reliable. They were measured at current densities ranging from 0.5 to 10 A g^{-1}. A typical charge/discharge curves in the three electrolytes is shown in Fig. 2(b). The highest capacitance value was obtained at 1 A g^{-1} in the LiCl electrolyte. However, as observed from Fig. 2(b) and (d), the AC material shows better symmetric triangular charge–discharge curves in KOH and Na_2SO_4 electrolyte. This suggests that the LiCl electrolyte was stretched beyond its capacity at 0.8 V. This was demonstrated by a non-symmetric charge–discharge curves thus resulting in higher capacitance values. For the purpose of clarification the experiment was repeated at a potential window of 0.5 V and the results are presented in Fig. S1 in the ESI.† From the CV shape of the LiCl presented in Fig. S1b and d,† it is clearly seen that AC electrode gives a better EDLCs characteristics within a potential window of 0.5 V *vs.* Ag/AgCl. At a current density of 1 A g^{-1} and maximum potential window of 0.8 V the specific capacitance values are 118, 84 and 184 F g^{-1} in KOH, Na_2SO_4 and LiCl aqueous electrolyte respectively. The charge/discharge curves in 6 M KOH are almost perfect isosceles lines, with a charge/discharge efficiency of approximate 100%. This shows the stability of the AC in the electrolyte.[14] At higher current density of 10 A g^{-1} reduced capacitance values in all three solutions are expected due to the capacitance *vs.* current load dependence. However, the same trend observed in the CV measurement at high scan rate is maintained and values obtained in the three electrolytes are 70 F g^{-1} for KOH, compared to 32 F g^{-1} and 45 F g^{-1} in Na_2SO_4 and LiCl respectively. From Tables S1, S2 and S3,† it is very evident that the charge/discharge efficiency (η (%)) of the electrode at different current densities, that of 6 M KOH electrolyte is higher than the other two electrolytes.

Fig. 3(a) shows Nyquist plots of AC in the different electrolytes obtained from the EIS experiments. Although all the three plots appear to have the nearly typical capacitive shape and vertical profile at lower frequencies with low diffusion resistance, the magnified image/spectra inset to Fig. 3(a) gives the differences in the solution resistance (R_S) values of AC in the three electrolytes. R_S is 0.66 Ω, for KOH solution as compared to much higher values of 2.10 Ω and 3.5 Ω for LiCl and in Na_2SO_4 electrolytes respectively. The charge transfer resistance (R_{CT}) values are seen to increase in the same trend. The EIS results also confirms that K^+ ions have the highest molar conductivity as compared to that of Li^+ and Na^+ ions, thus resulting in the smallest R_S and R_{CT} values.

Fig. 3(b) represents Bode plot for the AC in different electrolytes. It can be seen that in 6.0 M KOH electrolyte compared to other electrolytes gives the fastest response time demonstrating a phase angle of −83° which is close to −90° for ideal capacitors at lower frequency. Overall, the obtained results and analysis show good capacitive property of the AC in 6.0 M KOH electrolyte for supercapacitors.

Conclusion

Cyclic voltammetry, galvanostatic charge/discharge and electrochemical impedance spectroscopy have been used to compare the electrochemical behaviors for the supercapacitors electrode based on the mesoporous AC material in 6.0 M KOH, 1.0 M Na_2SO_4 and 6.0 M LiCl electrolyte solutions. AC electrode in 6.0 M KOH exhibited excellent electrochemical storage properties including a highest specific capacitance of 124 F g^{-1} at 0.5 A g^{-1}. The charge/discharge efficiency of electrode at different current densities of 6 M KOH electrolyte is higher than both 1.0 M Na_2SO_4 and 6.0 M LiCl electrolytes and it's close to 100%. The smallest R_S is obtained for the 6.0 M KOH electrolyte (0.66 Ω). These results suggest and confirm that 6.0 M KOH is the ideal aqueous electrolyte and concentration for AC based electrode materials.

Acknowledgements

This work is based on the research supported by the South African Research Chairs Initiative of the Department of Science

and Technology and National Research Foundation of South Africa (Grant No. 97994). Any opinion, finding and conclusion or recommendation expressed in this material is that of the author(s) and the NRF does not accept any liability in this regard. F. Barzegar and D. Y. Momodu acknowledge financial support from the University of Pretoria and the NRF while A. Bello acknowledge the University of Pretoria's financial support for their postdoctoral fellowships.

References

1 R. Kötz and M. Carlen, *Electrochim. Acta*, 2000, **45**, 2483–2498.
2 B. Conway, *J. Electrochem. Soc.*, 1991, **138**, 1539–1548.
3 J. P. Zheng, *J. Electrochem. Soc.*, 1997, **144**, 2417–2420.
4 B. E. Conway, *Electrochemical Supercapacitors: Scientific Fundamentals and Technological Applications*, Kluwer Academic/Plenum, New York, 1999.
5 F. Béguin, V. Presser, A. Balducci and E. Frackowiak, *Adv. Mater.*, 2014, **26**, 2219–2251.
6 B. E. Conway, V. Birss and J. Wojtowicz, *J. Power Sources*, 1997, **66**, 1–14.
7 L. L. Zhang and X. S. Zhao, *Chem. Soc. Rev.*, 2009, **38**, 2520–2531.
8 A. G. Pandolfo and A. F. Hollenkamp, *J. Power Sources*, 2006, **157**, 11–27.
9 E. Frackowiak and F. Béguin, *Carbon*, 2001, **39**, 937–950.
10 T. E. Rufford, D. Hulicova-Jurcakova, E. Fiset, Z. Zhu and G. Q. Lu, *Electrochem. Commun.*, 2009, **11**, 974–977.
11 W. Li, D. Chen, Z. Li, Y. Shi, Y. Wan, J. Huang, J. Yang, D. Zhao and Z. Jiang, *Electrochem. Commun.*, 2007, **9**, 569–573.
12 D.-W. Wang, F. Li, M. Liu, G. Q. Lu and H.-M. Cheng, *Angew. Chem., Int. Ed.*, 2008, **47**, 373–376.
13 A. Bello, F. Barzegar, D. Momodu, F. Taghizadeh, M. Fabiane, J. Dangbegnon and N. Manyala, *RSC Adv.*, 2014, **4**, 39066–39072.
14 X. Zhang, X. Wang, L. Jiang, H. Wu, C. Wu and J. Su, *J. Power Sources*, 2012, **216**, 290–296.
15 C. Lin, *J. Electrochem. Soc.*, 1999, **146**, 3639–3643.
16 C. Vix-Guterl, E. Frackowiak, K. Jurewicz, M. Friebe, J. Parmentier and F. Béguin, *Carbon*, 2005, **43**, 1293–1302.
17 C. Zhong, Y. Deng, W. Hu, J. Qiao, L. Zhang and J. Zhang, *Chem. Soc. Rev.*, 2015, **44**, 7484–7539.
18 L. Zhang, F. Zhang, X. Yang, G. Long, Y. Wu, T. Zhang, K. Leng, Y. Huang, Y. Ma, A. Yu and Y. Chen, *Sci. Rep.*, 2013, **3**, 1408.
19 T. E. Rufford, D. Hulicova-Jurcakova, Z. Zhu and G. Q. Lu, *Electrochem. Commun.*, 2008, **10**, 1594–1597.
20 T. A. Centeno, M. Sevilla, A. B. Fuertes and F. Stoeckli, *Carbon*, 2005, **43**, 3012–3015.
21 M. Inagaki, H. Konno and O. Tanaike, *J. Power Sources*, 2010, **195**, 7880–7903.
22 M. Zhi, F. Yang, F. Meng, M. Li, A. Manivannan and N. Wu, *ACS Sustainable Chem. Eng.*, 2014, **2**, 1592–1598.
23 M. Zhi, C. Xiang, J. Li, M. Li and N. Wu, *Nanoscale*, 2012, **5**, 72–88.
24 C. Largeot, C. Portet, J. Chmiola, P.-L. Taberna, Y. Gogotsi and P. Simon, *J. Am. Chem. Soc.*, 2008, **130**, 2730–2731.
25 P. Simon and Y. Gogotsi, *Nat. Mater.*, 2008, **7**, 845–854.
26 P. Hapiot and C. Lagrost, *Chem. Rev.*, 2008, **108**, 2238–2264.
27 A. Bello, F. Barzegar, D. Momodu, J. Dangbegnon, F. Taghizadeh and N. Manyala, *Electrochim. Acta*, 2015, **151**, 386–392.
28 Q. T. Qu, B. Wang, L. C. Yang, Y. Shi, S. Tian and Y. P. Wu, *Electrochem. Commun.*, 2008, **10**, 1652–1655.
29 J. Zhu, Y. Xu, J. Wang, J. Lin, X. Sun and S. Mao, *Phys. Chem. Chem. Phys.*, 2015, **17**, 28666–28673.
30 L. Eliad, G. Salitra, A. Soffer and D. Aurbach, *J. Phys. Chem. B*, 2001, **105**, 6880–6887.
31 F. Barzegar, A. Bello, O. O. Fashedemi, J. K. Dangbegnon, D. Y. Momodu, F. Taghizadeh and N. Manyala, *Electrochim. Acta*, 2015, **180**, 442–450.
32 J. Wang, R. Ma, Z. Zhou, G. Liu and Q. Liu, *Sci. Rep.*, 2015, **5**, 9304.
33 W. Zhang, C. Ma, J. Fang, J. Cheng, X. Zhang, S. Dong and L. Zhang, *RSC Adv.*, 2013, **3**, 2483–2490.
34 R. N. Reddy and R. G. Reddy, *J. Power Sources*, 2003, **124**, 330–337.
35 I. Waluyo, C. Huang, D. Nordlund, U. Bergmann, T. M. Weiss, L. G. M. Pettersson and A. Nilsson, *J. Chem. Phys.*, 2011, **134**, 064513.
36 P. Yates, *Chemical Calculations: Mathematics for Chemistry*, CRC Press, 2nd edn, 2007.

Supplementary Information

Investigation of different aqueous electrolytes on the electrochemical performance of activated carbon-based supercapacitors

Farshad Barzegar[a], Damilola. Y. Momodu[a], Omobosede. O Fashedemi[b,c], Abdulhakeem Bello[a], Julien. K. Dangbegnon[a], and Ncholu. Manyala[a*]

[a]Department of Physics, Institute of Applied Materials, SARCHI Chair in Carbon Technology and Materials, University of Pretoria, Pretoria 0028, South Africa.

[b]Department of Chemistry, University of Pretoria, Pretoria 0002, South Africa.

[c]Department of Chemistry, Augustine University, Ilara-Epe, Lagos 106103, Nigeria.

Corresponding Author: *Email address: ncholu.manyala@up.ac.za (N. Manyala)

Tel: +27 (0)12 420 3549, Fax: +27 (0)12 420 2516

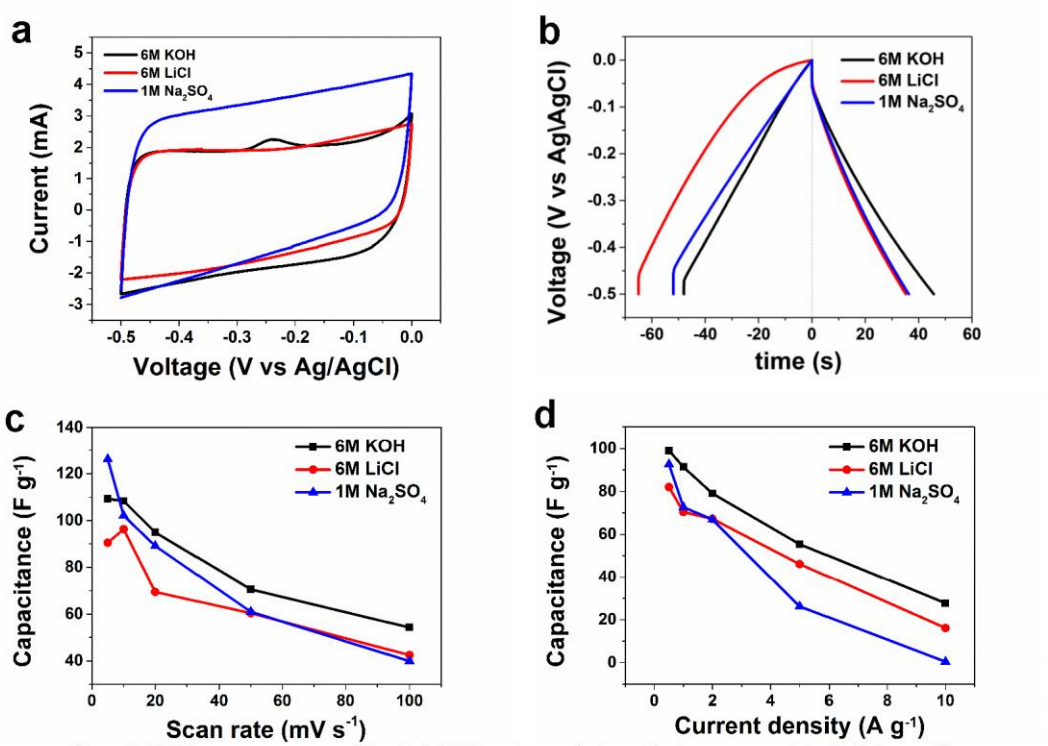

Figure S1 (a) CV curves at scan rates of 5 m Vs^{-1}, (b) The galvanostatic charge/discharge curves at 1 A g^{-1}, (c) the specific capacitance as function of the scan rate and (d) the specific capacitance as function of the current density at 0.5 potential window

Table S1 Result of the specific capacitance as function of the current density at 0.8 V potential window of 6 M KOH

6 M KOH	Current density (A g^{-1})				
	0.5	1	2	5	10
C_{Deh} (F g^{-1}) [a]	129.5	118.49	107.11	89.38	69.88
C_{Ch} (F g^{-1}) [a]	126.21	115.8	107.23	89.55	70.14
$C_{Average}$ (F g^{-1})	127.86	117.15	107.17	89.47	70.01
η (%) [b]	102.6	102.32	99.89	99.81	99.63

[a] $\overline{C_{Deh}}$ and $\overline{C_{Ch}}$ refer, respectively, to discharge and charge capacitance.

[b] $\eta = C_{Deh}/C_{Ch}$, the charge/discharge efficiency of electrode with current density

Table S2 Result of the specific capacitance as function of the current density at 0.8 V potential window of 6 M LiCl

6 M LiCl	**Current density (A g^{-1})**				
	0.5	**1**	**2**	**5**	**10**
C_{Dch} (F g^{-1})	-	184.22	122.63	75.75	45.05
C_{Ch} (F g^{-1})	-	209.16	129.23	78.53	46.59
$C_{Average}$ (F g^{-1})	-	196.69	125.93	77.14	45.82
η (%)	-	88.07	94.89	96.46	96.69

Table S3 Result of the specific capacitance as function of the current density at 0.8 V potential window of 1 M Na_2SO_4

1 M Na_2SO_4	**Current density (A g^{-1})**				
	0.5	**1**	**2**	**5**	**10**
C_{Dch} (F g^{-1})	-	93.3	86.09	70.71	31.58
C_{Ch} (F g^{-1})	-	120.9	96.78	74.43	32.38
$C_{Average}$ (F g^{-1})	-	106.65	80.26	72.57	31.98
η (%)	-	77.17	88.95	95	97.52

4.2.1.3 Concluding Remarks

From this study, AC electrode in 6.0 M KOH exhibited excellent electrochemical storage properties. The charge/discharge efficiency of electrode at different current densities of 6 M KOH electrolyte is higher than both 1.0 M Na_2SO_4 and 6.0 M LiCl electrolytes and it's close to 100%. The smallest R_s was obtained for the 6.0 M KOH electrolyte (0.66 Ω). These results suggest and confirm that 6.0 M KOH is an ideal aqueous electrolyte and concentration for AC based electrode materials.

4.2.2 Effect of different gel electrolytes on AC supercapacitors

4.2.2.1 Introduction

A key component for application of supercapacitors in mobile communication and computing electronics is the solid-state electrolyte [251]. Solid state polymer based gel electrolytes comprise a polymer and an ionic component and have recently been explored because of their several advantages which include its anticorrosive characteristic, compatibility with metal current collectors, good physical contact, exhibit ion of liquid-like ionic conductivity with high stability over cycling, higher surface to volume - ratio, low internal corrosion, simple principle and mode of fabrication, higher reliability, environmentally friendly and handling safety [252–255]. Various polymer gel based electrolytes have been used in electrochemical supercapacitors applications. Here we report on the electrochemical performance of the

symmetric supercapacitors based on highly porous activated carbon material and solid-state polyvinyl alcohol (PVA) and potassium hydroxide (KOH) hydrogel membrane electrolytes with different additives such as carbon black (CB) and a conducting polymer Polyaniline (PANI). A comparative electrochemical study with four different gel electrolytes in terms of their specific capacitance, energy and power densities were elucidated. The gel polymer electrolytes obtained at the different dopants were denoted as PK, PKC, and PKP for PVA-KOH, PVA-KOH-CB and PVA-KOH-PANI hydrogels respectively.

4.2.2.2 Result and discussions

The result of effect of different gel electrolytes on AC supercapacitors together with supporting information are presented in paper below.

AIP ADVANCES 5, 097171 (2015)

Effect of conductive additives to gel electrolytes on activated carbon-based supercapacitors

Farshad Barzegar,[1] Julien K. Dangbegnon,[1] Abdulhakeem Bello,[1] Damilola Y. Momodu,[1] A. T. Charlie Johnson, Jr.,[2] and Ncholu Manyala[1,a]
[1]*Department of Physics, Institute of Applied Materials, SARCHI Chair in Carbon Technology and Materials, University of Pretoria, Pretoria 0028, South Africa*
[2]*Department of Physics and Astronomy, University of Pennsylvania, Philadelphia, PA 19104, USA*

(Received 19 June 2015; accepted 16 September 2015; published online 24 September 2015)

This article is focused on polymer based gel electrolyte due to the fact that polymers are cheap and can be used to achieve extended potential window for improved energy density of the supercapacitor devices when compared to aqueous electrolytes. Electrochemical characterization of a symmetric supercapacitor devices based on activated carbon in different polyvinyl alcohol (PVA) based gel electrolytes was carried out. The device exhibited a maximum energy density of 24 Wh kg^{-1} when carbon black was added to the gel electrolyte as conductive additive. The good energy density was correlated with the improved conductivity of the electrolyte medium which is favorable for fast ion transport in this relatively viscous environment. Most importantly, the device remained stable with no capacitance lost after 10,000 cycles. [http://dx.doi.org/10.1063/1.4931956]

INTRODUCTION

There has been a tremendous increase on sustainable storage technology due to rapid depletion of current sources of energy (fossil fuel). Supercapacitors, batteries and fuel cells are all under investigation for sustainable energy technologies such as energy generation, energy conversion and energy storage. Electric double-layer capacitors (EDLCs), also known as ultracapacitors or supercapacitors, are high power density devices with long cycle life and are considered as a leading candidate for zero CO_2 emission vehicles by providing peak power for start-stop, acceleration and regenerative braking systems.[1,2]

EDLCs store energy by accumulation of charge at the interface between the electrode and electrolyte. The material of choice for most common and commercially available EDLCs is carbon due to its fair conductivity and high surface area ranging from 500 $m^2\ g^{-1}$ to 3000 $m^2\ g^{-1}$.[3] Current research activities focus on trying to increase the energy density of EDLCs without sacrificing their intrinsic high power density and long cycle life as well as minimizing fabrication cost by using abundant sources of carbon which are also environmentally friendly. One approach to achieve this is the use of electrolyte with a large potential window since the energy density of EDLCs is a function of the voltage squared ($E = 0.5CV^2$)[4] while the voltage range is limited or governed by the type of electrolyte used.

Recently three dimensional porous carbons have become attractive as materials for EDLCs because of their texture, structural composition, and high density of micropores. It has been shown that the pore size distribution of the material influences the electrochemical performance of the electrode material in various electrolytes.[5] The size distribution can be classified into macro-, meso- and micropores, while the electrolytes are categorized as ionic liquids, and organic and aqueous electrolytes. These different electrolytes have different advantages and disadvantages. Aqueous

[a]Corresponding author: N. Manyala (Ncholu.Manyala@up.ac.za)

electrolytes are characterized by high conductivity and high mobility of proton transport but suffer from low potential range (limited to ~1.2 V due to water decomposition) in power sources and are also associated with leakage resistance and corrosion.[6] On the other hand, organic and ionic liquids allow EDLCS to operate between 2.3 and 4 V in different solvents leading in principle to high energy density,[7] but suffer from low conductivity, high viscosity which slows ion transport and hence high resistance of the EDLCS, which can lead to low power density.

For application of supercapacitors in mobile communication and computing electronics, a key component is the solid-state electrolyte.[8] Solid state polymer-based gel electrolytes, comprising of a polymer and an ionic component, have recently been explored because of their anticorrosive properties, making them compatible with metal current collectors which exhibit good physical contact and good ionic conductivity with high stability over cycling, simple principle and mode of fabrication which are more reliable, environmentally friendly and safe to handle.[9–12] They are also characterized by wider electro-chemical potential window (> 4 V).[13,14] Polymer gel based electrolytes have been used in electrochemical supercapacitors applications, for example polyvinyl alcohol (PVA)–KOH,[15] PVA–H_2SO_4[16] and PVA-H_3PO_4.[17] Recently, Ma *et al.* reported a redox-mediated P-phenylenediamine doped polyvinyl alcohol gel electrolyte (PVA-KOH-PPD) as electrolyte and separator, and activated carbon as electrodes for symmetric supercapacitor with excellent electrochemical performance.[18] The same activated carbon electrode was tested in PVA-KOH-$K_3[Fe(CN)_6]$ gel electrolyte by the same authors and the material showed a specific capacitance as high as 431 F g^{-1}, energy and power densities values of 57.94 Wh kg^{-1} and 59.84 kW kg^{-1}, respectively.[19] The excellent good electrochemical performance was attributed to high ionic conductivity of gel electrolyte and the contribution from the reversible redox reaction of $K_3[Fe(CN)_6]$ and its quick electron relay at the electrode-electrolyte interface.[19] Ramasamy *et al.* reported activated carbon supercapacitor using a gel electrolyte of sodium salt-polyethylene oxide in an organic mixture solvent with the cell operating at a stable potential window of 2.5 V and exhibiting a specific capacitance of 24 F g^{-1}, real power of 0.52 kW kg^{-1}, and energy density of 18.7 Wh kg^{-1}. Gao *et al.* also tested an asymmetric capacitor via paper-like carbon nanotube-manganese oxide electrodes based on potassium polyacrylate gel-based with a cell voltage of 1.8 V, a stable cycling performance (capacitance retention of 86.0 % after 10,000 continuous charge/discharge cycles) and energy of density (32.7 Wh kg^{-1}).[20] Here we report on the electrochemical performance of the symmetric supercapacitors based on highly porous activated carbon material and solid-state poly-vinyl alcohol (PVA) and potassium hydroxide (KOH) hydrogel electrolyte with different additives such as carbon black (CB) and a conducting polymer Polyaniline (PANI). A comparative electrochemical study with four different electrolytes in terms of their specific capacitance, energy and power density was performed. The gel polymer electrolytes obtained at the different dopants were denoted as PK, PKC, and PKP for PVA-KOH, PVA-KOH-CB and PVA-KOH-PANI hydrogels respectively. The PKC sample exhibited a maximum energy density of 24 Wh kg^{-1} with no capacitance loss after 10,000 galvanostatic charge/discharge cycles.

EXPERIMENTAL

Preparation of gel polymer electrolytes

The gel polymer electrolytes were prepared by a modification of the procedure in Ref. 18. First, 5 ml PVA 10 wt% and 5 ml KOH 6 M were mixed by continuous stirring at 85 °C until homogeneous viscous mixture was obtained and allowed to cool to room temperature. This mixture of PVA–KOH gel polymer was designated as **PK**. To this PVA-KOH electrolyte, 5 mg carbon black was added to obtain PVA-KOH-carbon black electrolyte denoted as **PKC**, and 5 mg polyaniline was added to another mixture of **PK** to obtain PVA-KOH- polyaniline denoted as **PKP** respectively.

Preparation of activated carbon electrode

The AC used in this work was prepared as follows; graphene foam (GF) was first prepared by chemical vapour deposition (CVD) onto a catalytic nickel foam (Alantum Innovations in Alloy

Foam Munich, Germany) following the procedure described in our previous report.[21] To provide mechanical support for the graphene during removal of nickel, polymethylmethacrylate (PMMA) was drop coated on the sample and baked at 180 °C for 30 minutes. The samples were then placed in 3 M HCl solution at 80 °C overnight to ensure that nickel was completely etched away. The resulting GF sample was placed in acetone at 50 °C for 30 minutes to remove the PMMA. The samples were then rinsed in deionised water and dried.[22]

The hydrogel was synthesised via the hydrothermal process. Typically, 100 mg of GF were dispersed in 100 ml of water containing 11.11 g of polyvinyl alcohol (PVA) followed by the addition of different masses of 1.76 g Polyvinylpyrrolidone (PVP) in a glass vial by ultrasonication, 1.50 ml of hydrochloric acid (HCl) was added to the solution as a cross linker. The mixture was sonicated for few minutes and further stirred for 30 min to obtain a homogeneous dispersion before being transferred into a 120 ml Teflon-lined autoclave system operated at 190 °C for 12 h. The resulting hydrogel was crushed and washed with deionized water and dried for 6 h. The hydrogel obtained was then soaked in aqueous KOH solution with a KOH/hydrogel mass ratio of 5 for 24 h and dried at 120 °C for 12 h before carbonization. The composite was then placed in a horizontal tube furnace ramped from room temperature to 800 °C at 10 °C/min under argon gas flow for 1 h of activation. This procedure transforms the hydrogel into carbon materials consisting of a continuous pore network distribution. After which sample was washed with 3 M HCl to remove the remaining KOH and further washed with deionized water and dried in an electric oven. To prepare the electrode, the AC and binder polyvinylidene fluoride (PVDF) were homogeneously mixed in an agate mortar with respective weight ratio 90:10 at room temperature and dispersed in N-methylpyrrolidone (NMP) solution to form slurry. The slurry was then uniformly coated on a nickel foam current collector and dried at 60 °C in an oven for 8 hours to ensure complete evaporation of the NMP.

Supercapacitor assembly

A symmetric supercapacitor was fabricated by dropping the hydrogel electrolyte between the AC electrodes and filter paper separator as shown in scheme 1 below.

Characterization

Nitrogen adsorption–desorption isotherms were measured at −196 °C using a Micromeritics ASAP 2020 analyzer. All the samples were degassed at 180 °C for more than 12 h under high vacuum conditions. The surface area was calculated by the Brunauer–Emmett–Teller (BET) method from the adsorption branch in the relative pressure range (P/P_0) of 0.01 – 0.2. The sample was also characterized using powder X-ray diffraction (XRD). An XPERT-PRO diffractometer (PANalytical

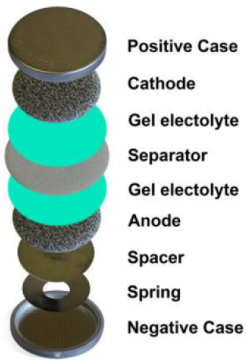

SCHEME 1. Assembly of supercapacitor device.

BV, Netherlands) with theta/theta geometry, operating a cobalt tube at 35 kV and 50 mA was used. The SEM images were obtained on a Zeiss Ultra Plus 55 field emission scanning electron microscope (FE-SEM) operated at an accelerating voltage of 2.0 kV. Transmission electron microscopy (TEM) was carried out with a JEOL JEM-2100F microscope operated at 200 kV accelerating voltage. The electrochemical test of the symmetric cell was carried out in a two-electrode cell configuration by means of coin-type cells with a mass loading of ~3.3 mg for both electrodes, a thickness of 0.2 mm and a diameter of 16 mm, using a glass microfiber filter paper as the separator, in KOH and three different hydrogel electrolytes respectively. All electrochemical measurements were carried out using a Bio-logic VMP-300 potentiostat. These measurements included cyclic voltammetry (CV), chronopotentiometry (CP) and electrochemical impedance spectroscopy (EIS). The CV tests were carried out at different scan rates ranging from 5 to 100 mV s^{-1}, and the electrochemical impedance spectroscopy (EIS) measurements were conducted in the frequency range from 0.1 to 100 kHz with an open circuit potential (~ 0 V).

RESULTS AND DISCUSSIONS

Figure 1 shows SEM images for the structural characterization of the activated carbon used in this work. Figure 1(a) and 1(b) show the low and high magnification micrograph of the activated carbon. Highly porous network are observed which could be beneficial in providing easy ion mobility for fast ion transport for high-performance supercapacitors. To study the crystallinity of the carbon material, XRD was performed and the spectrum is shown in figure 2(a). All the XRD peaks are identified as graphite peaks (COD: 96-900-8570) which crystallizes in the orthorhombic structure with space group P63mc(186), lattice parameters a = 2.4560 Å and c = 6.6960 Å. Figure 2(b) shows the N_2 gas sorption analysis of the sample showing a H4 adsorption and desorption hysteresis, characteristic of complex materials containing both micropores and mesopores. The sample exhibits a high BET surface area of 2994 m^2 g^{-1} and an average Barrett-Joyner-Halenda (BJH) pore size (inset to Figure 2(b)) centered at about 8 nm depicting substantial amount of mesopores. The sharp increase of the curve for diameter below 2 nm also hints the presence of micropores in this sample. The presence of micropores and mesopores in this sample are highly desirable for energy storage application since micropores store the charges whereas mesopores allow ion accessibility to the micropores. Also from the SEM micrographs, macropores are also observed which could act as buffer.

Electrochemical characterization

Cyclic voltammetry measurements of the activated carbon were performed with the different polymer gel electrolytes in a two electrode configuration and the results obtained were compared with results obtained using KOH aqueous electrolyte alone. Figure 3 shows the different CV curves obtained in different polymer gel electrolytes at the scan rate of 10 mV s^{-1}. The CV curves of the activated carbon in the aqueous electrolyte operate up to a potential window of 1.6 V while

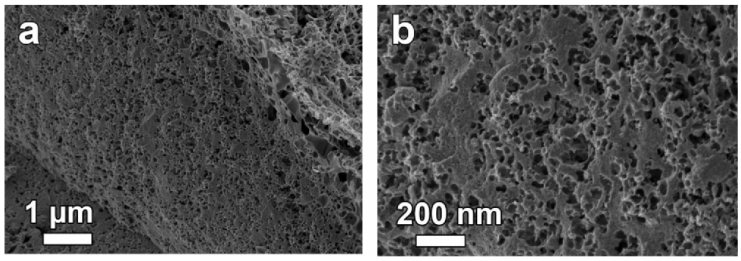

FIG. 1. (a) and (b) low magnification and high magnification SEM images of AC respectively.

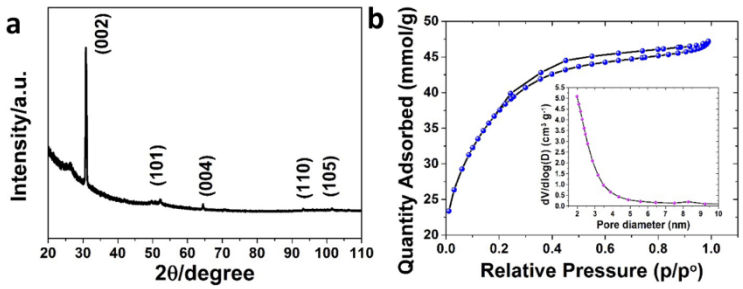

FIG. 2. (a) X-ray diffraction and (b) the N_2 adsorption-desorption isotherm of the AC.

those in the gel electrolytes operate up to a potential window of 2.0 V. Furthermore, these results show that the CV curves for all these cells show fairly rectangular shape, indicating EDLC behavior with good capacitive behavior with rapid current responses. Moreover, a clear increase in current response is observed from aqueous to gel electrolytes. Furthermore, the devices using PK and PKP electrolytes show current leap at a potential of ~1.9 V and towards the 0 V mark, which is attributed to the evolution of gases or oxygenated surface functionalities generated from the electrode and the reactions with the electrolyte during the scanning process. Compared with other two polymer gel electrolytes, devices made with the PKC electrolyte showed a stable and rectangular shape during scanning, which is an indication of pure electrochemical double layer behavior.

Galvanostatic charge-discharge measurements were also performed to evaluate the electrochemical performance of activated carbon in a symmetric capacitor using different polymer gel electrolytes media. At a current density of 1 A g^{-1}, all the cells show symmetric triangular charge/discharge features, which are characteristic of ideal capacitor behavior (Figure 4(a)). The gravimetric capacitance of the devices was calculated from these curves using the expression $C_{SP} = 2I/((dV/dt)m)$, where I is the current (A), dV/dt is the slope of the discharge curve (V) and m is the mass of carbon in one electrode (g). Figure 4(b) shows the specific capacitance as a function of the current density of the symmetric devices. The device with KOH electrolyte showed the highest gravimetric capacitance of 188 F g^{-1} at a current density of 0.5 A g^{-1}, which can be ascribed to the small size of ion in the electrolyte as well as the low viscosity of the electrolyte which enhances a rapid transport mechanism at the interface between the electrode and electrolyte

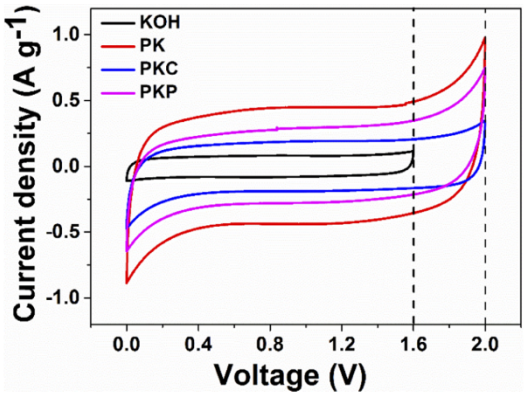

FIG. 3. The CV curves of the supercapacitors in various electrolytes at 10 mV s^{-1}.

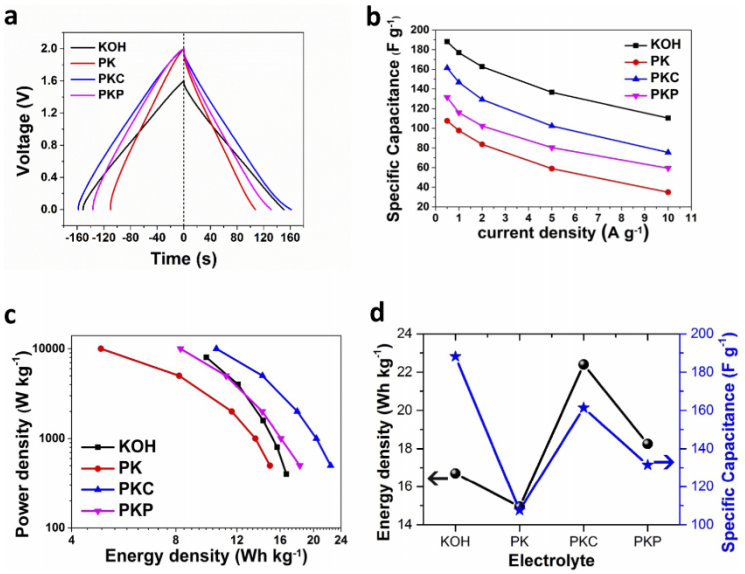

FIG. 4. The comparison of electrolytes dependence of (a) the galvanostatic charge/discharge curves at 0.5 A g^{-1} (b) specific capacitance vs. current density (c) Ragone plot and (d) energy density and specific capacitance vs. electrolytes used in the devices fabricated.

for improved electrochemical performance. Comparing the gel electrolyte-based devices, the device with the PKC performed the best, which could be due to the addition of the carbon black which improves the conductivity of the PVA-KOH gel and hence high capacitance value. The lower values of specific capacitances when the gel electrolytes were used compared to the aqueous electrolyte, could be due to the increase in solution viscosity in the gel electrolyte which reduces the ion conductivity and consequently the ability to accommodate ions in the micropore volume of the electrodes. Although no electrical conductivity measurements were done in this work, carbon black is believed to be a more conducting additive than PANI which was both used as additives in the PK electrolyte as shown by low equivalent series resistance (R_S) that will be discussed below. This is also supported by the higher specific capacitance obtained from the PKC electrolyte in comparison to that obtained in PKP. These specific capacitance values are reasonable for activated carbon as double-layer capacitor and compare favorably to previous values in the literature.[20,23] In order to discard the possibility of the contribution of carbon black and PANI in the total specific capacitance when PKC and PKP electrolytes were used, carbon black and PANI were prepared as electrode material on the nickel foam and the galvanostatic charge- discharge measurements were performed in PVA-KOH electrolyte. This setting will indeed give the contribution of carbon black and PANI in PVA-KOH-CB and PVA-KOH-PANI electrolytes respectively. Figure S1 in the supporting information[25] shows very small discharge time for both materials compared to AC with similar mass of AC as electrode materials. This implies a very little or negligible contribution of these materials in the specific capacitance in PKC and PKP electrolytes, but rather improve the conductivity of the PK electrolyte as stated above.

The Ragone plot of all the devices is shown in figure 4(c) which shows that the lowest value of the energy density was obtained for the PVA-KOH (PK) electrolyte (16 Wh kg^{-1}) which is the electrolyte with the lowest conductivity based on the obtained results. Furthermore, it confirms that the device with the PKC electrolyte has the highest energy density of 24 Wh kg^{-1} which is higher than the value in PKP electrolyte (18 Wh kg^{-1}) at 0.5 A g^{-1}. The energy density values from

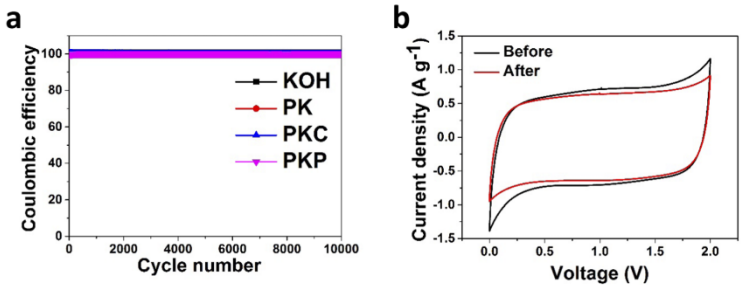

FIG. 5. (a) Cycle stability of different electrolytes at a constant current density of 5 A g^{-1} and (b) CV curves of AC in PKC electrolyte at scan rate of 20 mV s^{-1} before and after cycling.

PKC and PKP electrolytes are due to the extended potential window up to 2.0 V combined with the improved conductivity of the electrolyte medium which also impacts on specific capacitance. This leads to an increase in the energy density and overall performance of the device. This is also evidenced in Figure 4(d) where the energy density and specific capacitance are plotted against the different electrolytes. It is observed that although KOH gives the best specific capacitance, the low voltage window negatively influences the energy density whereas for the PKC electrolyte, a specific capacitance close to that of KOH was obtained with a larger working voltage window which leads to the highest energy density.

Figure 5(a) show the cycle stability of the cell in the different electrolytes at a constant current density of 5 A g^{-1}. The stability of the active material in all electrolytes shows no capacitance loss after 10,000 cycles. The CV curves of PKC at scan rate of 20 mV s^{-1} before and after cycling are shown in Figure 5(b). The Similar CV curves were obtained before and after the 10,000th cycle with better rectangular shape after cycling, implying better EDLC performance after cycling which could be attributed to the fact that during cycling more surface area get exposed to the electrolyte, hence increase in the electrochemical behavior.

Electrochemical impedance spectroscopy (EIS) measurements were performed in the frequency range from 100 kHz to 10 MHz for capacitors operating in the different cells but show similar tendencies as observed in figure 6. The Nyquist plot shown in Fig. 6(a) presents a typical capacitive shape with partial semi-circle in the high-frequency region and vertical line in the low frequency region.

The KOH electrolyte showed a more vertical behavior when compared with gel electrolytes presented in the figure due to its higher conductivity thus demonstrating a better electrochemical diffusion mechanism. At high frequency, the intercept on the real axis (Z′) gives information about the Ohmic resistance (R_s) also known as equivalent series resistance (ESR) of the device. This

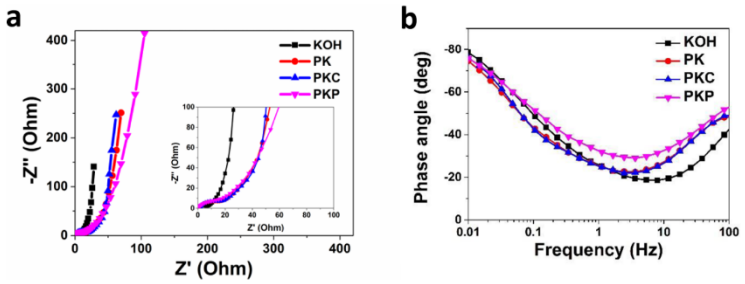

FIG. 6. (a) The Nyquist plots and (b) Bode phase angle plots of AC in different electrolytes.

resistance value includes the intrinsic resistances of the active electrode materials, the substrate and electrolyte, and the contact resistance of the electrodes with the external circuit.[24] From the Nyquist plot above the device with the KOH electrolyte has R_s value of 0.29 Ω. This small R_s value proves that the current can easily diffuse through the electrode-electrolyte interface due to the high mobility of K^+ cation. The three devices made with the gel electrolytes have R_S values of 0.47 Ω, 0.52 Ω and 0.53 Ω for PKC, PK and PKP respectively. The device with the PKC gel electrolyte has a relatively smaller value than the other two gel electrolytes. This difference in R_s can be attributed to the presence of the carbon black in the electrolyte which improves on the conductivity of the gel electrolyte PK much better than PANI. However, comparing with the R_s value from the KOH electrolyte the PKC value is higher. This demonstrates the superiority of aqueous electrolyte over organic and ionic liquid electrolyte which exhibit low conductivity. Fig. 6(b) shows Bode plot for all devices in different electrolytes. It is observed that the cell using KOH aqueous electrolyte shows a phase angle approximately −80° close to −90° for ideal capacitive behavior while the others cells using other three gel electrolytes show a phase angle of ∼78°, which also evidences the good capacitive property of the fabricated supercapacitor cells in these gel electrolytes.

CONCLUSION

The work has demonstrated a simple way to improve the energy density of EDLCs material through using correct electrolyte. The use of conductive additives such as carbon black additive in particular in the gel electrolyte, improved the energy density of the supercapacitor when compared to aqueous electrolyte or simple gel electrolyte. This was correlated with the improved conductivity of the electrolyte medium which is favorable to fast ion transport in this relatively viscous environment. In particular, in this work a maximum energy density of 24 Wh kg^{-1} was obtained when carbon black was added to the gel electrolyte as conductive additive. This value is higher than that obtained in KOH (17 Wh kg^{-1}) and other gel electrolytes PVA-KOH (16 Wh kg^{-1}). Most importantly the cell remained stable with no capacitance loss after 10000 cycles for all devices with PKC device showing slightly higher stability value throughout.

ACKNOWLEDGEMENTS

This work is based on research supported by the South African Research Chair Initiative (SARChi) in Carbon Technology and Materials of the Department of Science and Technology (DST) and the National Research Foundation (NRF). Any opinion, findings and conclusions or recommendations expressed in this work are those of authors and therefore the NRF and the DST do not accept any liability with regard thereto. F. Barzegar and D. Y. Momodu acknowledge financial support from the University of Pretoria and the NRF for their PhD bursaries, while A. Bello acknowledges NRF through SARChI in Carbon Technology and Materials and University of Pretoria for his Postdoctoral financial support. A.T. C. Johnson acknowledges support from the Laboratory for Research on the Structure of Matter, National Science Foundation MRSEC, grant number DMR-1120901.

[1] P.J. Hall, M. Mirzaeian, S.I. Fletcher, F.B. Sillars, A.J.R. Rennie, G.O. Shitta-Bey, G. Wilson, A. Cruden, and R. Carter, Energy Environ. Sci. **3**, 1238 (2010).
[2] P. Simon, Y. Gogotsi, and B. Dunn, Science **343**, 1210 (2014).
[3] M. Inagaki, H. Konno, and O. Tanaike, J. Power Sources **195**, 7880 (2010).
[4] M.D. Stoller and R.S. Ruoff, Energy Environ. Sci. **3**, 1294 (2010).
[5] L. Zhang, F. Zhang, X. Yang, G. Long, Y. Wu, T. Zhang, K. Leng, Y. Huang, Y. Ma, A. Yu, and C. Yongsheng, Sci. Rep. **3** (2013).
[6] W.G. Pell and B.E. Conway, J. Power Sources **136**, 334 (2004).
[7] P. Hapiot and C. Lagrost, Chem. Rev. **108**, 2238 (2008).
[8] G.P. Pandey and A.C. Rastogi, J. Electrochem. Soc. **159**, A1664 (2012).
[9] H. Yu, J. Wu, L. Fan, K. Xu, X. Zhong, Y. Lin, and J. Lin, Electrochim. Acta **56**, 6881 (2011).
[10] C. Ramasamy, J. Palma del vel, and M. Anderson, J. Solid State Electrochem. **18**, 2217 (2014).
[11] P. Sivaraman, A. Thakur, R.K. Kushwaha, D. Ratna, and A.B. Samui, Electrochem. Solid-State Lett. **9**, A435 (2006).
[12] P. Yang, W. Cui, L. Li, L. Liu, and M. An, Solid State Sci. **14**, 598 (2012).

[13] M. Armand, F. Endres, D.R. MacFarlane, H. Ohno, and B. Scrosati, Nat. Mater. **8**, 621 (2009).
[14] P. Simon and Y. Gogotsi, Nat. Mater. **7**, 845 (2008).
[15] C.-C. Yang, S.-T. Hsu, and W.-C. Chien, J. Power Sources **152**, 303 (2005).
[16] C. Meng, C. Liu, L. Chen, C. Hu, and S. Fan, Nano Lett. **10**, 4025 (2010).
[17] S.A. Hashmi, R.J. Latham, R.G. Linford, and W.S. Schlindwein, Polym. Int. **47**, 28 (1998).
[18] G. Ma, E. Feng, K. Sun, H. Peng, J. Li, and Z. Lei, Electrochim. Acta **135**, 461 (2014).
[19] G. Ma, J. Li, K. Sun, H. Peng, J. Mu, and Z. Lei, J. Power Sources **256**, 281 (2014).
[20] H. Gao, F. Xiao, C.B. Ching, and H. Duan, ACS Appl. Mater. Interfaces **4**, 7020 (2012).
[21] A. Bello, K. Makgopa, M. Fabiane, D. Dodoo-Ahrin, K.I. Ozoemena, and N. Manyala, J. Mater. Sci. (2013).
[22] A. Bello, O.O. Fashedemi, J.N. Lekitima, M. Fabiane, D. Dodoo-Arhin, K.I. Ozoemena, Y. Gogotsi, A.T. Charlie Johnson, and N. Manyala, AIP Adv. **3**, 82118 (2013).
[23] L. Demarconnay, E. Raymundo-Pinero, and F. Béguin, Electrochem. Commun. **12**, 1275 (2010).
[24] J. Luo, H.D. Jang, and J. Huang, ACS Nano **7**, 1464 (2013).
[25] See supplementary material at http://dx.doi.org/10.1063/1.4931956 for comparison of galvanostatic charge/discharge at 0.5 A g-1 AC and CB electrode materials in PKC and PK gel electrolytes respectively and AC and PANI electrode materials in PKP and PK gel electrolytes respectively.

Effect of conductive additives to gel electrolytes on Activated Carbon-based supercapacitors

Farshad Barzegar[1], Julien K. Dangbegnon[1], Abdulhakeem Bello[1], Damilola Y. Momodu[1], A. T. Charlie Johnson, Jr.[2] and Ncholu Manyala[1,a]

[1]Department of Physics, Institute of Applied Materials, SARCHI Chair in Carbon Technology and Materials, University of Pretoria, Pretoria 0028, South Africa.

[2]Department of Physics and Astronomy, University of Pennsylvania, Philadelphia, PA 19104, USA

[a] Corresponding author: N. Manyala (Ncholu.Manyala@up.ac.za)

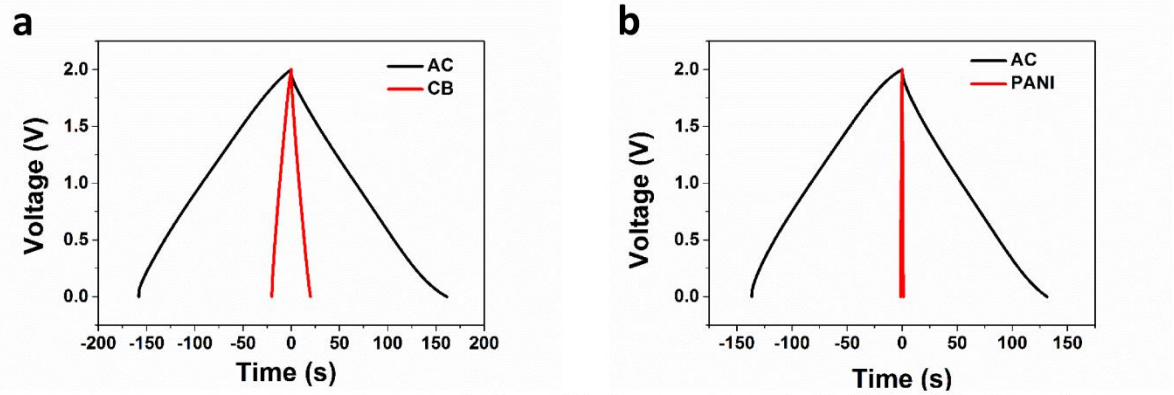

Figure S1 Comparison of galvanostatic charge/discharge at 0.5 A g^{-1} of (a) AC and CB electrode materials in PKC and PK gel electrolytes respectively and (b) AC and PANI electrode materials in PKP and PK gel electrolytes respectively.

4.2.2.3 Concluding Remarks

Gel electrolytes based on PVA polymer and KOH were produced and studied their electrochemical behavior for EDLCs application based on the produced AC material. The use of conductive additives such as carbon black in particular in the gel electrolyte, improves the energy density of the supercapacitor when compared to aqueous electrolyte or simple gel electrolyte. This was correlated with the improved conductivity of the electrolyte medium which is favorable for fast ion transport in the relatively viscous environment. In particular, this work produced a maximum energy density of 24 Wh kg^{-1} when carbon black was added to the gel electrolyte as conductive additive. This value is higher than that obtained in KOH (17 Wh kg^{-1}) and other gel electrolytes PVA-KOH (16 Wh kg^{-1}). Most importantly the cell remained stable with no capacitance loss after 10000 cycles for all devices with PKC device showing slightly higher stability value throughout.

4.3 PREPARATION AND CHARACTERIZATION OF AC CATHODE MATERIAL AND A-MoO_3 TRANSITION METAL OXIDE AS ANODE MATERIAL FOR HIGH-PERFORMANCE ASYMMETRIC SUPERCAPACITORS

4.3.1 Introduction

Aqueous asymmetric supercapacitors (AASs) are promising hybrid energy storage devices as they have been shown to provide a wider operating voltage

and higher energy density compared to symmetric capacitors [256,257] by combining a battery-type electrode Faradaic cathode (transition metal oxide) material and a capacitor-type electrode anode material (usually activated carbon). AASs make use of the different potential windows in the anode and cathode leading to an increased operational voltage of the aqueous electrolyte [257] and significantly improving the energy density of devices. Generally most AASs ECs make use of activated carbon (AC) as the negative electrode [258,259] because of the anomalous faradaic capacitance mechanism at the surfaces of carbon-based electrodes when scanned at negative potentials in aqueous electrolytes [260]. For the positive electrode, conductive polymers and various transition metal oxides [261–265] are widely studied due to rapid and reversible electron exchange reactions at the electrode interface which contribute to the high energy and power densities of AASs. In order to achieve high-performance AASs, MoO_3 has been shown to exhibit good performance in energy storage devices [139]. In this study, AC from polymer based materials discussed earlier was used as the anode and α-MoO_3 as the cathode material in an aqueous electrolyte media respectively.

4.3.2 Result and discussions

The result of asymmetric cell made from AC/ α-MoO_3 is presented in the attached paper below with its supporting information.

RSC Advances

PAPER

View Article Online
View Journal | View Issue

Cite this: RSC Adv., 2015, 5, 37462

Asymmetric supercapacitor based on an α-MoO_3 cathode and porous activated carbon anode materials†

F. Barzegar, A. Bello, D. Y. Momodu, J. K. Dangbegnon, F. Taghizadeh, M. J. Madito, T. M. Masikhwa and N. Manyala*

Received 3rd March 2015
Accepted 17th April 2015

DOI: 10.1039/c5ra03579a

www.rsc.org/advances

Low cost porous carbon materials were produced from cheap polymer materials and graphene foam materials which were tested as a negative electrode material in an asymmetric cell configuration with α-MoO_3 as a positive electrode. These materials were paired to maximize the specific capacitance and to extend the potential window, hence improving the energy density of the device. The asymmetrical device exhibits significantly higher energy density of 16.75 W h kg^{-1} and a power density of 325 W kg^{-1}.

Introduction

In the last few decades, there has been a tremendous growth in the development of new hybrid energy storage technology to address the challenges of renewable and sustainable energy sources. Supercapacitors are at the forefront of this research and are recognized as a special type of device for next generation energy storage due to their high power densities and excellent cycling ability, which make them suitable for use in hybrid electric vehicles, memory backup systems and industrial equipment that relies on long cycle-life times and uninterruptable power supply.[1]

Aqueous asymmetric supercapacitors (AASs) are promising hybrid energy storage devices as they have been shown to provide a wider operating voltage at higher energy density compared to symmetric capacitors[2,3] by combining a battery-type electrode Faradaic cathode (transition metal oxide) material and a capacitor-type electrode anode material (usually an activated carbon). AASs make use of the different potential windows in the anode and cathode leading to an increased operational voltage of the aqueous electrolyte[3] and significantly improving the energy density of devices. Generally most AASs ECs make use of activated carbon (AC) as the negative electrode[4,5] because of the anomalous pseudocapacitance mechanism at the surfaces of carbon-based electrodes when scanned at a negative potentials in aqueous electrolytes.[6] For the positive electrode, conductive polymers and various transition metal oxides[7–11] are widely studied due to rapid and reversible electron exchange reactions at the electrode interface which contribute to the high energy and power densities of AASs.

In order to achieve high performance AASs, several AASs systems have been developed for example AC//$Ni(OH)_2$,[12] graphene//$Ni(OH)_2$,[13] carbon nanotubes//MnO_2 (ref. 9) and activated carbon(AC)//MoO_3 (ref. 14) were all fabricated and exhibited high energy storage capabilities. Nevertheless, the energy capabilities of these devices are still far from commercialization due to the poor capacitive performance of positive electrode materials at the high current loading and the corresponding carbon negative materials in a low utilization.[15] Thus, the synergistic effect in energy storage from positive electrode and power delivery from negative electrode is greatly limited in the asymmetric configuration.[15] The activated carbon(AC)//MoO_3 (ref. 14) AAS involves a two-dimensional (2D) material: MoO_3 which is part of the family of phyllosilicates. The interest for this 2D layered material was boosted by the unique properties of graphene. In fact, similar properties to those of graphene are expected for this 2D material. In other words, owing to the exceptional electrochemical performance of graphene, it is conceivable to also expect such performance for MoO_3. Although numerous research has been carried out so far there are still few studies reporting the fabrication of AASs with activated carbon from polymer based materials as the anode and MoO_3 as the cathode in an aqueous electrolyte media. In this work, we report on a design of AASs based on activated carbon with 3D interconnected pores derived from a combination of polymer materials such as polyvinyl alcohol (PVA), polyvinylpyrrolidone (PVP) and graphene foam (GF) on a nickel foam current collector as the anode electrode and using mesoporous MoO_3 nanosheets as cathode electrode material. The hybrid material showed high rate capability compared to a pure MoO_3 electrode. The optimized AAS showed a specific capacitance of 179 F g^{-1} at 0.5 A g^{-1} and a maximum energy density of

Department of Physics, Institute of Applied Materials, SARCHI Chair in Carbon Technology and Materials, University of Pretoria, Pretoria 0028, South Africa. E-mail: ncholu.manyala@up.ac.za; Fax: +27 (0)12 420 2516; Tel: +27 (0)12 420 3549

† Electronic supplementary information (ESI) available: Fitting parameters for the single electrodes and electrochemical characterization of three electrode system for each electrode. See DOI: 10.1039/c5ra03579a

16.75 W h kg $^{-1}$ based on the total mass of active materials operating at a potential window of 1.3 V.

Experimental

Synthesis of electrode materials

Activated carbon was first prepared by the process reported in our previous work,[16] while α-MoO_3 prepared by hydrothermal system as recommended by Wang *et al.*[17] First, ammonium paramolybdate $\{(NH_4)_6Mo_7O_{24}\cdot 4H_2O\}$ and sodium diethyldithiocarbamate $\{(C_2H_5)_2NCS_2Na\cdot 3H_2O\}$ were dissolved in deionized water and magnetically stirred for 12 h and the solution mixture was kept stationary under the ambient condition for another 12 h. The resulting yellow precipitate $\{Mo\{(C_2H_5)_2NCS_2\}_2O_2\}$ was filtered, washed with deionized water and dried at 70 °C for 12 h. After, which the $Mo\{(C_2H_5)_2NCS_2\}_2O_2$ was placed into a Teflon-lined stainless steel autoclave and the deionized water was added with stirring. The autoclave was sealed and maintained at 200 °C for 24 h. The resulting precipitates was filtered, washed with deionized water and ethanol and dried in vacuum at 100 °C for 6 h. Nanostructured α-MoO_3 was obtained by heating the hydrothermally synthesized powder in air at 370 °C for 6 h.

Microstructural characterization

Nitrogen adsorption–desorption isotherms were measured at −196 °C using a Micromeritics ASAP 2020. All the samples were degassed at 180 °C for more than 12 h under vacuum conditions. The surface area was calculated by the Brunauer–Emmett–Teller (BET) method from the adsorption branch in the relative pressure range (P/P_0) of 0.01–0.2. The samples were also characterized using powder X-ray diffraction (XRD). An XPERT-PRO diffractometer (PANalytical BV, Netherlands) with theta/theta geometry, operating a cobalt tube at 35 kV and 50 mA, was used. The XRD patterns of all specimens were recorded in the 10.0–80.0° 2θ range with a counting time of 5.240 seconds per step. The SEM images were obtained on a Zeiss Ultra Plus 55 field emission scanning electron microscope (FE-SEM) operated at an accelerating voltage of 2.0 kV.

Electrochemical characterization

All electrochemical measurements were carried out using a Biologic SP-300 potentiostat such as cyclic voltammetry (CV), chronopotentiometry (CP) and electrochemical impedance spectroscopy (EIS). The negative electrode was prepared by mixing the active material (AC), and polyvinylidene fluoride (PVDF) binder with a weight ratio of 9 : 1 which was homogenized and dispersed in *N*-methylpyrrolidone (NMP) solution, and the slurry was then uniformly pasted on a nickel foam current collector and dried at 60 °C in an oven for 8 hours to ensure complete evaporation of the NMP. The positive electrode was made by mixing the active material (α-MoO_3), polyvinylidene fluoride (PVDF) binder and carbon black (CB) to improve the conductivity of material with a weight ratio of 8 : 1:1 and dispersed in *N*-methylpyrrolidone (NMP) solution, and the slurry was then uniformly pasted on a nickel foam current collector and dried at 60 °C in an oven for 8 hours. The electrochemical test of the asymmetric cell was carried out in a two electrode cell configuration by means of coin-type cells with thickness of 0.2 mm and diameter of 16 mm, using a glass microfiber filter paper as the separator in 6 M KOH aqueous electrolyte solution. The three electrode measurements were performed for both AC and α-MoO_3 as the working electrodes, glassy carbon plate as the counter electrode and Ag/AgCl (3 M KCl) serving as the reference. The specific capacitance (C_s) can be calculated from CV curves according to the following equation:[18]

$$C_s = \frac{\int I\, dU}{vm\Delta U} \quad (1)$$

or C_s can be calculated from charge–discharge curves according to the equation:[18]

$$C_s = \frac{I\,\Delta t}{m\,\Delta U} \quad (2)$$

where I is the current, ΔU is the potential window, v is the sweep rate (mV s $^{-1}$), m is the mass of total electrode active materials and Δt is the discharge time. The energy density (E (W h kg $^{-1}$)) and power density (P (W kg $^{-1}$)) of ECs can be then calculated from C_s according to the following equations:

$$E = \frac{1}{2}\, C_s \Delta U^2 = \frac{1000 \times C_s \times \Delta U^2}{2 \times 4 \times 3600} = \frac{C_s \times \Delta U^2}{28.8} \quad (3)$$

$$P = \frac{E}{t} = \frac{3600 \times E}{1000 \times \Delta t} = \frac{3.6 \times E}{\Delta t} \quad (4)$$

In construction of an asymmetric ECs, the voltage split is dependent on the capacitance of the active material in each electrode. Therefore, it is very important to take care of the mass balancing of each electrode by taking into account the charge equality: $Q_+ = Q_-$, where Q_+ and Q_- are the charges stored in the positive and negative electrodes, respectively. The charge can be expressed by:[19]

$$Q = C_s M \Delta U \quad (5)$$

where C_s is the specific capacitance of active material, M is the mass of each active material and ΔU is the potential range during charge–discharge process. In order to get $Q_+ = Q_-$, the mass balancing will follow the equation:

$$\frac{M_+}{M_-} = \frac{C_{s-}\ \Delta U_-}{C_{s+}\ \Delta U_+} \quad (6)$$

Results and discussion

Fig. 1(a) and (b) represent the BET results of MoO_3 and AC materials respectively. The nitrogen adsorption and desorption isotherm shows type 3 characteristics for MoO_3 and type 1 characteristics for AC. The corresponding specific surface area of MoO_3 is approximately 5.5 m^2 g $^{-1}$ and for Ac is about 2923 m^2 g $^{-1}$. Moreover, the pores constructed in MoO_3 are mainly

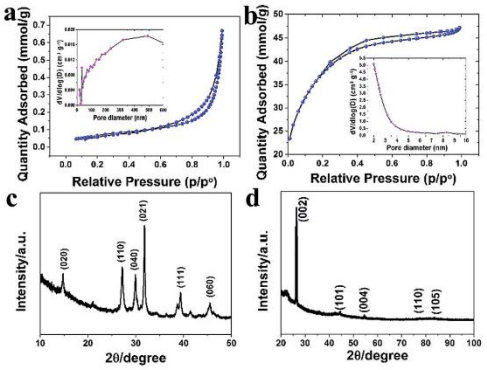

Fig. 1 (a) and (b) the N_2 adsorption–desorption isotherm of the α-MoO_3 and AC respectively (insets show pore size distribution), (c) and (d) the X-ray diffraction of the α-MoO_3 and AC respectively.

mesopore structure (inset to Fig. 1(a)) and in AC are mainly micropore structure with a broad pore size distribution of 2–7 nm and an average pore size of 2.7 nm (inset to Fig. 1(b)).

Fig. 1(c) represents the XRD patterns of MoO_3 powder. The wavelength used for the XRD analysis was Co-K_α, 1.7890 Å. After the synthesis, it was found that the peaks corresponding to (0 2 0), (1 1 0), (0 4 0), (0 2 1), (1 1 1), (0 6 0) planes are of orthorhombic crystal structure of MoO_3.[20,21] It is noted that all the XRD peaks are identified to be MoO_3 peaks (COD: 96-900-9670) which crystallizes in the orthorhombic system with space group *Pbnm* (62), and lattice parameters $a = 3.9616$ Å, $b = 13.8560$ Å, $c = 3.6978$ Å. The (020) peaks were clearly detected, and indicated the presence of orthorhombic phase rather than the monoclinic. From lattice parameters we can identify the phase of the MoO_3 to be α-phase (see Fig. 2). Fig. 1(d) represents the XRD patterns of AC powder. The wavelength used for the XRD analysis was Cu-K_α, 1.5405 Å. It is noted that all the XRD peaks are identified to Graphite peaks (COD: 96-900-8570) which crystallizes in the orthorhombic system with space group *P*63*mc*(186), lattice parameters $a = 2.4560$ Å and $c = 6.6960$ Å.

Fig. 3(a) and (b) show the low and high magnification SEM of the α-MoO_3. It can be seen from these figure that the α-MoO_3 comprises clusters of interleaving nano-platelets, whose

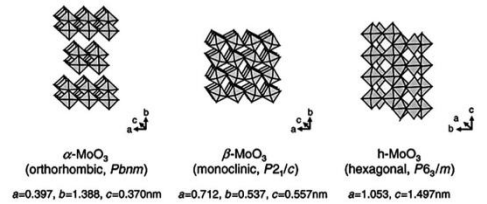

Fig. 2 Illustrations of three MoO_3 crystal structures of α, β, and h phases.[22]

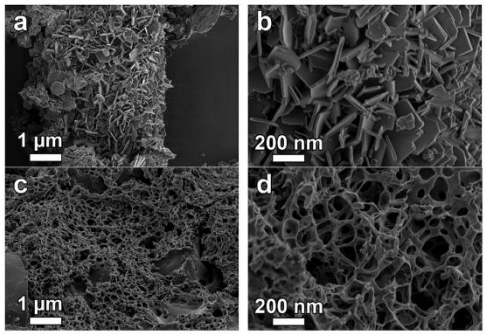

Fig. 3 Low and high magnification SEM image of (a) and (b) α-MoO_3 (c) and (d) AC.

thicknesses range from 20 to 85 nm. Fig. 3(c) and (d) present the low and high magnification SEM of the AC. As observed, the porosity of this AC is very high hence making it suitable for large ion-accessible surface for fast ion transport in high performance supercapacitors.

To evaluate the electrochemical properties and quantify the specific capacitance of the as-prepared AC and α-MoO_3, we performed cyclic voltammetry (CV) measurements on these two electrode materials in a 6 M KOH aqueous solution using a three electrode system (Fig. 4). The CV for AC electrode was measured within a potential window of −0.8 to 0.0 V and for α-MoO_3 was measured within a potential window of 0.0 to 0.5 V *vs.* Ag/AgCl at a scan rate of 10 mV s^{-1}. The detailed three electrode electrochemical measurements of each single electrode are documented in Fig. S1 and S2† in the ESI.† From the CV curve (Fig. 4) of AC electrode, no peaks of oxidation and reduction are observed, indicating a typical characteristic of EDL capacitor behavior, while the CV shape of the α-MoO_3 electrode in the potential range of 0.0 to 0.5 V is of pseudocapacitance type showing oxidation and reduction peaks.

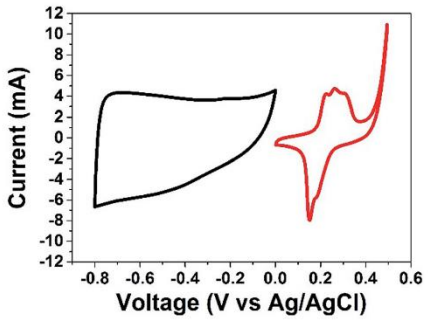

Fig. 4 CV curves of α-MoO_3 (red curve) and AC (black curve) electrodes performed in three electrode system in 6 M KOH solution at a scan rate of 10 mV s^{-1}.

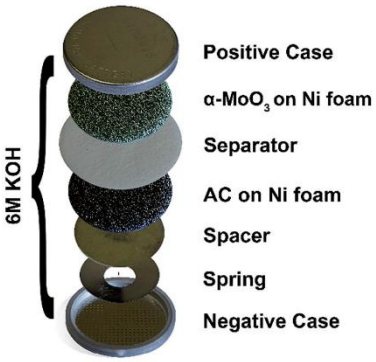

Fig. 5 Schematic of the assembled structure of asymmetric ECs based on α-MoO_3 as positive electrode and AC as negative electrode.

On the basis of these results, it is expected that the operating cell voltage could be extended to about 1.3 V in 6 M KOH solutions as electrolyte if the α-MoO_3 electrode as a cathode and the AC electrode as an anode are assembled into asymmetric ECs (Fig. 5).

For making two electrode cell, according to eqn (6), the mass of the MoO_3 should be two times mass of the AC $\left(\frac{M_{\alpha\text{-}MoO_3}}{M_{AC}} = 2\right)$. Fig. 6(a) shows a typical CV of the asymmetric EC at scan rates from 5 to 100 m Vs^{-1} in a potential window of 1.3 V. The mirror image shape of the CV indicates excellent reversible reaction at the electrode/electrolyte interface.[23] An asymmetric charge–discharge curve showing EDLCs with little pseudocapacitive behavior at all current densities (Fig. 6(b)) were observed. The specific capacitance of the MoO_3/AC can reach 179 F g^{-1} at a scan rate of 0.5 A g^{-1}. The Ragone plot and the specific capacitance as function of the current density of the asymmetric device are shown in Fig. 6(c). The specific capacitance decreases from 179 F g^{-1} to 37 F g^{-1} with increasing current density from 0.5 to 10 A g^{-1}. The maximum energy density of the device was recorded as 16.75 W h kg^{-1} and power density of 325 W Kg^{-1} at a current density of 0.5 A g^{-1}. The energy density is higher than those reported symmetric and asymmetric supercapacitor such as MoO_3/MWCNTs//MoO_3/MWCNTs (7.28 W h kg^{-1}),[24] $Ni(OH)_2$/UGF//a-MEGO (13.4 W h kg^{-1})[25] but smaller than those reported for $GrMnO_2$//$GrMoO_3$ (42.6 W h kg^{-1})[26] and PANI//MoO_3 (71.9 W h kg^{-1}).[27] Nevertheless, our electrode material presents better stability compared to $GrMnO_2$//$GrMoO_3$ and PANI//MoO_3 materials. The latter already degrading after 200 cycles.

As shown in Fig. 6(d), the AASs cell shows no capacitance loss after 10 000 cycles at current density of 2 A g^{-1}. However, a small increase in the capacitance (~1.13%) was observed after the initial cycling process which is similar to what was observed by Ren *et al.*[28] and this was tentatively attributed to the swelling of the carbon material at some defective sites, promoting electrolyte ions to intercalate into the space created by the swelling or creation of more pores after many CD cycles and leading to more accessible surface area and hence increase in the efficiency of the cell which was stable and maintained throughout the cycling process.[28]

EIS is an important parameter for investigating the electrical conductivity of electrodes. We measured the impedance of the electrode materials in the frequency range of 0.01 to 10^5 Hz.

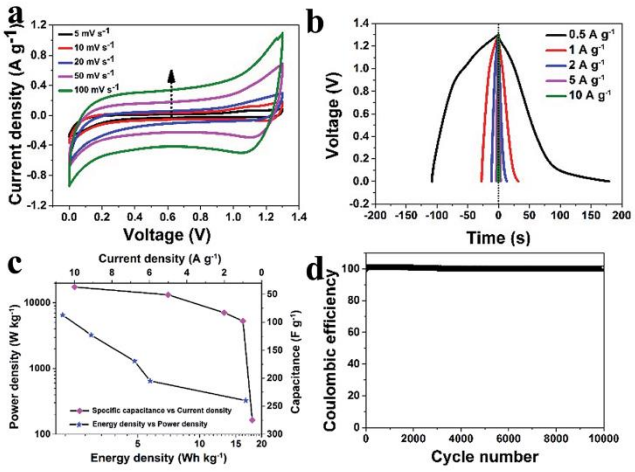

Fig. 6 (a) CV curves at scan rates of 5 to 100 mV s^{-1}, (b) the galvanostatic charge–discharge curves from 0.5 to 10 A g^{-1} current densities, (c) Ragone plot and the specific capacitance as function of the current density and (d) cycle stability at a constant current density of 2 A g^{-1} of asymmetric cell of α-MoO_3/AC.

The intercept on the x-axis of the Nyquist plot (Fig. 7(a) and (b)) in the high-frequency region represents the electronic resistance of the device, also known as the equivalent series resistance (ESR), denoted as R_S. The semicircle is a result of the charging of the double layer of the activated carbon (Fig. 7(b)). The charge transfer resistance (R_{CT}) and the double-layer capacitance C_{DL} lie in the high-frequency to mid-frequency region. The Nyquist plot shows a nearly vertical line in the low-frequency region representing the diffusion of ions to the interface between electrode and electrolyte. The deviation from the ideal vertical behavior is attributed to the presence of resistance with a Warburg impedance characteristic element denoted by W, which is expressed as $A/(j\omega)^{0.5}$,[29] where A is the Warburg coefficient, ω is the angular frequency.

The circuits used for fitting of the EIS experimental data of the Nyquist plot for each electrode material was performed with a fitting program ZFIT/EC-Lab version 10.38 and are represented in the inset to Fig. 7(a) and (b) for MoO_3 and AC respectively. In Fig. 7(a) the equivalent circuits, has a solution resistance (R_S) connected in series with a constant phase element (CPE_{DL}), and the CPE_{DL} is connected in parallel with the charge-transfer resistance (R_{CT}) and the mass capacitance (CPE_L), while the Warburg element (W) and the leakage current R_L are all in series with R_S. Fig. 7(b) CPE_{DL}, CPE_L, and R_{CT} are all parallel to each other and are in series with the R_S which is also in series with both the R_L and W. CPE_{DL} representing the double-layer capacitance related to the porous electrode. CPE_L represents the ideal polarizable capacitance that would give rise to a straight line parallel to the imaginary axis. The deviation from the ideal situation suggests that a resistive element R_L is associated with CPE_L. The impedance of CPE_{DL} is defined as $Z_{CPE} = T(j\omega)^{-n}$,[30] where T and n are frequency-independent constants and ω is the angular frequency. The n is a correction factor which is related to the capacitive kinetics and roughness of electrode surfaces. The values for n range between 0 and 1: $n = 1$ denotes that the CPE element is an ideal capacitor, for $n = -1$, CPE behaves as an inductor, while $n = 0$ and 0.5 denote a resistance and Warburg behaviors respectively.[30] Fig. 7(c) presents the Nyquist plot of the asymmetric device fabricated with ESR value of 0.39 Ohms while Fig. 7(d) shows the fitting which combine the two sets of fitting parameters listed in Tables S1 and S3 in the ESI† for a single electrodes in series. The fittings show that the impedance spectra of the electrodes fit perfectly with the experimental data without further adjustments. The Nyquist plot before and after cycling is shown in Fig. 7(e).

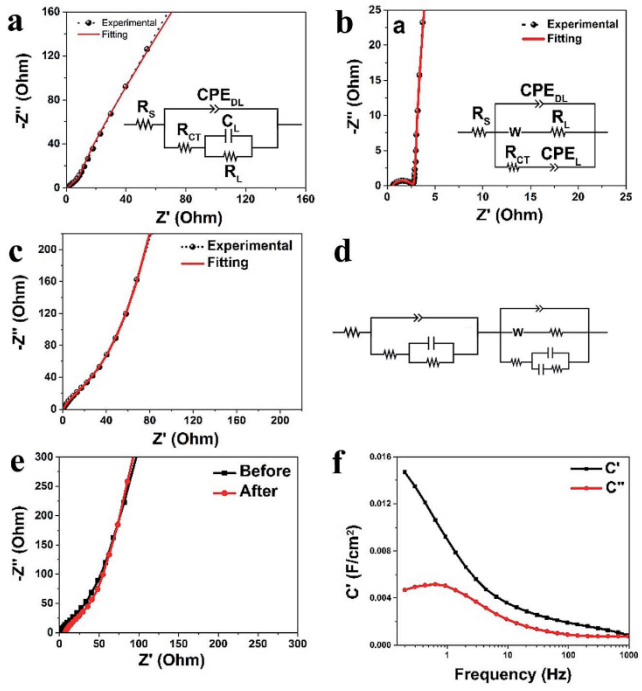

Fig. 7 (a) and (b) EIS plot and fitting curve for single electrode with the insets to the figure being equivalent circuits used for fitting the data of the α-MoO_3 and AC respectively, (c) EIS plot and fitting curve for the asymmetric cell, (d) equivalent circuit used for fitting the asymmetric cell data in (c), (e) EIS before and after cycling, (f) the real and the imaginary part of the cells capacitance against frequency.

The supercapacitors behave as a series combination of a resistance and capacitance and both of them depend on the frequency. In the low frequency region, the capacitance $\{C(\omega)\}$ can be defined as the combination of imaginary part of the capacitance $\{C''(\omega)\}$ and real part of the capacitance $\{C'(\omega)\}$, and they can be expressed by the following equations:[31,32]

$$C(\omega) = C'(\omega) + jC''(\omega) \quad (7)$$

$$C'(\omega) = -\frac{Z''(\omega)}{\omega\left|Z(\omega)^2\right|} \quad (8)$$

$$C''(\omega) = -\frac{Z'(\omega)}{\omega\left|Z(\omega)^2\right|} \quad (9)$$

where $C'(\omega)$ corresponds to the static capacitance which is tested during the constant current discharge, $C''(\omega)$ corresponds to energy dissipation of the supercapacitor by IR drop and an irreversible faradic charge transfer process, which can cause the hysteresis of the electrochemical processes. $|Z(\omega)|$ is the impedance modulus, and ω is the angular frequency.[31,32] Based on the above formulae, the capacitance $\{C'\}$ of the cell is 0.015 F (from topmost part of the C' graph) as shown in Fig. 7(f), C'' define the transition frequency between a pure capacitive and a pure resistive behavior of the AASs with a relaxation time of ~1.7 s obtained by taking the reciprocal of the maximum frequency in the C'' graph (Fig. 7(f)). These values show that the cells can be fully discharged within a very short time with an efficiency of more than 50%.[30]

Conclusions

We have successfully fabricated an asymmetric supercapacitor device based on porous activated carbon material as negative electrodes and α-MoO_3 as positive electrode. The asymmetrical device shows high specific capacitance of 179 F g^{-1}, energy density of 16.75 W h kg^{-1}, power density of 325 W Kg^{-1} and good stability after 10 000 cycles at an operating voltage of about 1.3 V in 6 M KOH aqueous electrolytes. It shows that pairing such hybrid material could be an excellent approach to produce supercapacitors with high energy and power densities. These encouraging results could open up new possibility of three dimensional porous carbons based on cheap polymer materials and graphene foam for applications in asymmetric supercapacitors with high potential window, high energy and high power densities to meet the increasing energy demand of the global society.

Acknowledgements

This work is based on research supported by the South African Research Chairs Initiative (SARChi) in Carbon Technology and Materials of the Department of Science and Technology (DST) and the National Research Foundation (NRF). Any opinion, findings and conclusions or recommendations expressed in this work are those of authors and therefore the NRF and the DST do not accept any liability with regard thereto. F. Barzegar and D. Y. Momodu acknowledge financial support from the University of Pretoria and the NRF for their PhD bursaries, while A. Bello acknowledge the University of Pretoria's financial support for their postdoctoral fellowships.

Notes and references

1 B. E. Conway, *Electrochemical Supercapacitors: Scientific Fundamentals and Technological Applications*, Kluwer Academic/Plenum, New York, 1999.
2 J. W. Long, D. Bélanger, T. Brousse, W. Sugimoto, M. B. Sassin and O. Crosnier, *MRS Bull.*, 2011, **36**, 513–522.
3 K. Naoi, S. Ishimoto, J. Miyamoto and W. Naoi, *Energy Environ. Sci.*, 2012, **5**, 9363.
4 Y. Zhai, Y. Dou, D. Zhao, P. F. Fulvio, R. T. Mayes and S. Dai, *Adv. Mater.*, 2011, **23**, 4828–4850.
5 N. W. Duffy, W. Baldsing and A. G. Pandolfo, *Electrochim. Acta*, 2008, **54**, 535–539.
6 F. Béguin, K. Kierzek, M. Friebe, A. Jankowska, J. Machnikowski, K. Jurewicz and E. Frackowiak, *Electrochim. Acta*, 2006, **51**, 2161–2167.
7 Z. Algharaibeh, X. Liu and P. G. Pickup, *J. Power Sources*, 2009, **187**, 640–643.
8 V. Khomenko, E. Raymundo-Piñero and F. Béguin, *J. Power Sources*, 2006, **153**, 183–190.
9 H. Jiang, C. Li, T. Sun and J. Ma, *Nanoscale*, 2012, **4**, 807–812.
10 Y. Cheng, S. Lu, H. Zhang, C. V. Varanasi and J. Liu, *Nano Lett.*, 2012, **12**, 4206–4211.
11 X. Liu, R. Ma, Y. Bando and T. Sasaki, *Adv. Mater.*, 2012, **24**, 2148–2153.
12 S. Nohara, T. Asahina, H. Wada, N. Furukawa, H. Inoue, N. Sugoh, H. Iwasaki and C. Iwakura, *J. Power Sources*, 2006, **157**, 605–609.
13 J. Yan, Z. Fan, W. Sun, G. Ning, T. Wei, Q. Zhang, R. Zhang, L. Zhi and F. Wei, *Adv. Funct. Mater.*, 2012, **22**, 2632–2641.
14 W. Tang, L. Liu, S. Tian, L. Li, Y. Yue, Y. Wu and K. Zhu, *Chem. Commun.*, 2011, **47**, 10058–10060.
15 R. Wang and X. Yan, *Sci. Rep.*, 2014, **4**, 3712.
16 A. Bello, F. Barzegar, D. Momodu, J. Dangbegnon, F. Taghizadeh and N. Manyala, *Electrochim. Acta*, 2015, **151**, 386–392.
17 T. Wang, J. Li and G. Zhao, *Powder Technol.*, 2014, **253**, 347–351.
18 W. Zhang, C. Ma, J. Fang, J. Cheng, X. Zhang, S. Dong and L. Zhang, *RSC Adv.*, 2013, **3**, 2483.
19 A. Bello, F. Barzegar, D. Momodu, J. Dangbegnon, F. Taghizadeh, M. Fabiane and N. Manyala, *J. Power Sources*, 2015, **273**, 305–311.
20 T. Mizushima, K. Fukushima, H. Ohkita and N. Kakuta, *Appl. Catal., A*, 2007, **326**, 106–112.
21 A. Ganguly and R. George, *Bull. Mater. Sci.*, 2007, **30**, 183–185.
22 K. Koike, R. Wada, S. Yagi, Y. Harada, S. Sasa and M. Yano, *Jpn. J. Appl. Phys.*, 2014, **53**, 05FJ02.
23 Z.-S. Wu, W. Ren, D.-W. Wang, F. Li, B. Liu and H.-M. Cheng, *ACS Nano*, 2010, **4**, 5835–5842.

24 L. S. Aravinda, U. Bhat and B. R. Bhat, *Electrochim. Acta*, 2013, **112**, 663–669.
25 J. Ji, L. L. Zhang, H. Ji, Y. Li, X. Zhao, X. Bai, X. Fan, F. Zhang and R. S. Ruoff, *ACS Nano*, 2013, **7**, 6237–6243.
26 J. Chang, M. Jin, F. Yao, T. H. Kim, V. T. Le, H. Yue, F. Gunes, B. Li, A. Ghosh, S. Xie and Y. H. Lee, *Adv. Funct. Mater.*, 2013, **23**, 5074–5083.
27 H. Peng, G. Ma, J. Mu, K. Sun and Z. Lei, *J. Mater. Chem. A*, 2014, **2**, 10384.
28 G. Ren, X. Pan, S. Bayne and Z. Fan, *Carbon*, 2014, **71**, 94–101.
29 Y. Zhou, H. Xu, N. Lachman, M. Ghaffari, S. Wu, Y. Liu, A. Ugur, K. K. Gleason, B. L. Wardle and Q. M. Zhang, *Nano Energy*, 2014, **9**, 176–185.
30 D. Pech, M. Brunet, H. Durou, P. Huang, V. Mochalin, Y. Gogotsi, P.-L. Taberna and P. Simon, *Nat. Nanotechnol.*, 2010, **5**, 651–654.
31 X. Zhang, X. Wang, L. Jiang, H. Wu, C. Wu and J. Su, *J. Power Sources*, 2012, **216**, 290–296.
32 P. L. Taberna, P. Simon and J. F. Fauvarque, *J. Electrochem. Soc.*, 2003, **150**, A292.

Electronic Supplementary Material (ESI) for RSC Advances.

Supplementary Information

Asymmetric supercapacitor based on α-MoO_3 cathode and porous activated carbon anode materials

F. Barzegar[a], A. Bello[a], D. Y. Momodu[a], J. K. Dangbegnon[a], F. Taghizadeh[a], M.J. Madito[a], T.M. Masikhwa[a] and N. Manyala[a]*

[a]Department of Physics, Institute of Applied Materials, SARCHI Chair in Carbon Technology and Materials, University of Pretoria, Pretoria 0028, South Africa.

***Email address**: ncholu.manyala@up.ac.za (N. Manyala)

Corresponding author Tel: +27 (0)12 420 3549, Fax: +27 (0)12 420 2516

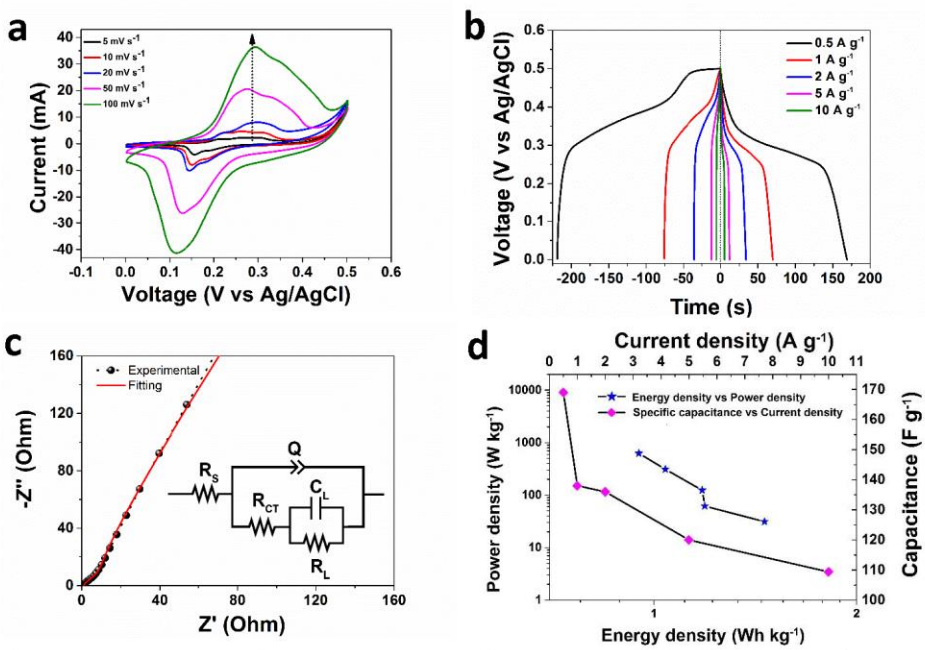

Figure S1. (a) CV curves of α-MoO_3 at scan rates of 5 to 100 m Vs^{-1}, (b) The galvanostatic charge/discharge curves of α-MoO_3 from 0.5 to 10 A g^{-1}, (c) EIS plot and fitting curve for single electrode with the inset to the figure being equivalent circuit used for fitting the data of the α-MoO_3 and (d) Ragone plot and the specific capacitance as function of the current density of α-MoO_3

Table S1 Fitting parameters for the single electrode of α-MoO_3

R_S (Ω)	Q ($F.s^{a-1}$)	n	R_{CT} (Ω)	C_L (F)	R_L (Ω)
0.8	0.013	0.7	32	5.34 e-3	800

$X^2 = 0.016$ $X/\sqrt{N} = 0.021$ CPE ≡ Q

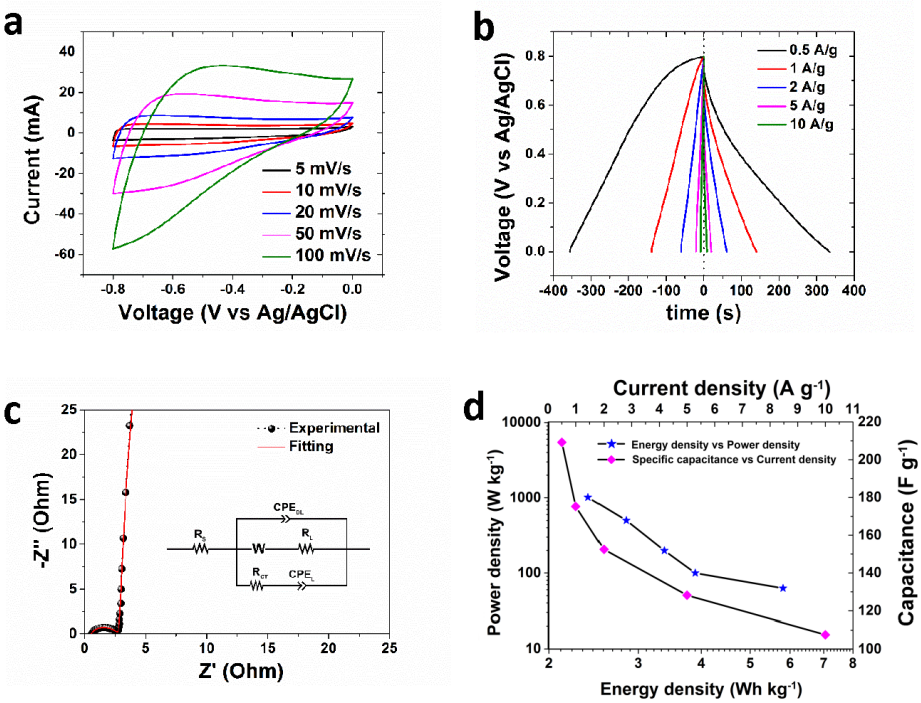

Figure S2. (a) CV curves of AC at scan rates of from 5 to 100 m Vs^{-1}, (b) The galvanostatic charge/discharge curves of AC from 0.5 to 10 A g^{-1}, (c) EIS plot and fitting curve for single electrode with the inset to the figure being equivalent circuit used for fitting the data of the AC and (d) Ragone plot and the specific capacitance as function of the current density of AC

Table S2 Fitting parameters for the single electrode of AC

R_S (Ω)	Q_{DL} ($F.s^{a-1}$)	a_{DL}	A_W ($\Omega.s^{-0.5}$)	R_L (Ω)	R_{CT} (Ω)	Q_L ($F.s^{a-1}$)	a_L
0.596	0.0002	1	75.34	0.413	2.314	0.433	1

$X^2 = 0.4$ $X/\sqrt{N} = 0.1$ $CPE_{DL} \equiv Q_{DL}$ $CPE_L \equiv Q_L$ $a_{DL} \equiv a_L \equiv n$

4.3.3 Concluding Remarks

Asymmetric supercapacitor device based on porous activated carbon material as negative electrodes and α-MoO3 as positive electrode has been successfully fabricated. The asymmetrical device shows high specific capacitance, energy density and power density with good stability after 10000 cycles at an operating voltage of about 1.3 V in 6 M KOH aqueous electrolytes. It shows that pairing such hybrid device could be an excellent approach to produce supercapacitors with high energy and power densities.

CHAPTER 5

GENERAL CONCLUSIONS AND FUTURE WORK

In this chapter, the main results reported and discussed in chapter 4 are summarized Activated carbons (ACs) from different sources are produced in this work to obtain the best AC for high-performance electrochemical capacitors. First, ACs based on polymers and a different carbon material such as graphene foam (GF), carbon nanotubes (CNTs) and expanded graphite (EG) were synthesized using a hydrothermal and CVD technique. Secondly novel source of the carbons to produce AC was explored and thirdly the novel pine cone source was also explored for the production of the AC materials. The ACs, have been studied and optimized through all the parameters that could be important in activation and carbonization such as the ratio of the carbon/KOH during activation or effect of the time and temperature during carbonization time to get the best porous material.

Each of the produced materials was characterized by scanning electron microscope (SEM), transmission electron microscope (TEM), X-ray diffraction (XRD), X-ray photoelectron spectroscopy (XPS), N_2 adsorption-desorption isotherm (BET) and Raman. All produced materials were also analyzed in the electrochemical system as electrodes for supercapacitors both in the two and three electrode configurations. The asymmetric cell was further produced by combining the ACs produced as negative electrode and some metal oxide as a positive electrode for the asymmetric cell. All the cell tested in this study achieved very good electrochemical performance

based on common techniques for testing electrodes such as cyclic voltammetry (CV), galvanostatic charge/discharge (GCD), internal resistance, cyclic life, self-discharge and electrochemical impedance spectroscopy (EIS).

In section 4.1, the synthesis and characterization of ACs for high-performance electrochemical capacitors from different carbon sources have been elucidated. In section 4.1.1, Report on the hydrothermal synthesis of three-dimensional porous carbons with a high SSA (2994 m^2 g^{-1}) based on two low-cost polymers namely polyvinyl alcohol (PVA) and polyvinylpyrrolidone (PVP) with graphene foam (GF) dispersed in the polymer matrix solution and fabricated symmetric supercapacitor was presented. The symmetric cell showed excellent electrochemical storage properties, including high specific capacitance (188 F g^{-1}) with high energy densities (16.71 Wh kg^{-1}) and power densities (401 W kg^{-1}) at 0.5 A g^{-1} with a stable 1.6 V operation voltage and excellent long-term stability. These promising results show the potential of these three-dimensional porous carbons as electrodes for high energy and power densities supercapacitor devices. Section 4.1.2 presents the results of the addition of different carbon material such as carbon nanotube (CNT) and expanded graphite (EG) rather than the GF into the polymer matrix solution during the synthesis of the porous carbon material and studied the morphological, structural and electrochemical properties of the synthesized products materials. The result showed AC material made from these polymers by dispersing expanded graphite in the polymer matrix (ACEG) exhibiting the smallest SSA (627 F g^{-1}) compared to ACGF and yet demonstrating the highest specific capacitance (320 F g^{-1}) and energy

density (28.4 Wh kg^{-1}) at 0.5 A g^{-1}. The results showed that the EG is a good candidate that could be easily dispersed in a polymer matrix solution to produce ACs for high energy density supercapacitors. In section 4.1.3, It was shown that the EG material could be a good candidate as the base material for the production of ACs. Novel carbon nanosheets (AEG) derived from EG was synthesized and showed a high SSA (457 m^2 g^{-1}) compared to EG alone (20 m^2 g^{-1}). AEG showed highest specific capacitance (337 F g^{-1}), high energy density (37.9 Wh kg^{-1}) and power density (450 W kg^{-1}) at 0.5 A g^{-1} with excellent rate capability in 6 M KOH aqueous electrolyte with no capacitance loss after 120 h of floating test. It showed that AEG material has great potential for high-performance energy storage device applications.

Section 4.1.4 reported for the first time, an excellent EDLC behavior of porous and high surface area (808 m^2 g^{-1}) Pine cone activated carbon (PAC) material synthesized by direct carbonization of chemically activated pine cones obtained locally in South Africa. The electrochemical behavior of the PAC was a study in the three-electrode system and results obtained show that it works as a negative electrode in KOH electrolyte exhibiting a specific capacitance (335 F g^{-1}) at a current density of 0.5 A g^{-1} with no capacitance loss after 10,000 charge–discharge cycles at a current density of 2 A g^{-1}. Thus, demonstrating the potential of the PAC as a suitable and promising electrode material for fabricating low-cost green energy storage devices.

In section 4.2, results based on the effect of different electrolytes on the electrochemical behavior of supercapacitors based on AC were presented. As

identified, the failure and destruction of ECs are also related to the electrolyte that it used in the ECs system. Section 4.2.1 showed that carbon material exhibit excellent electrochemical storage properties in 6 M KOH compared to other aqueous electrolyte and this electrolyte was adopted for all materials in section 4.1. To improve the electrochemical behavior of EDLCs material, in section 4.2.2, different gel electrolytes were produced, and their effect on symmetric ACs based supercapacitors was studied. A comparative electrochemical study with four different gel electrolytes in terms of their specific capacitance, energy, and power density was elucidated. In this study, solid-state KOH and PVA hydrogel membrane electrolytes with different additives such as carbon black (CB) and a conducting polymer polyaniline (PANI) were made and tested. The gel electrolyte made of PVA/KOH/CB (PKC) showed improved potential window and energy density of the supercapacitor when compared to aqueous electrolyte or simple gel electrolyte. In particular, in this work a maximum energy density of 24 Wh kg^{-1} was obtained from ACGF porous carbon when carbon black was added to the gel electrolyte as a conductive additive. This value is higher than that obtained in KOH (~17 Wh kg^{-1}) for the same material. The results demonstrate the potential of this gel electrolyte for EDLCs material.

Finally in section 4.3 Asymmetric supercapacitor devices based on porous activated carbon material as negative electrodes and α-MoO3 as positive electrode was successfully fabricated. The asymmetrical device shows good specific capacitance, energy density and power density with good stability after 10000 cycles with an operating voltage of about 1.3 V in 6 M KOH aqueous electrolyte.

In summary, the results clearly show the great potential of activated carbon drive from a different carbon sources, especially expanded graphite, as energy storage device electrodes and also showed that the potential of working on the nontoxic gel electrolyte such as PKC to improve the electrochemical behavior of supercapacitors.

Future work could be further exploration of the EG as an active material for EDLCs and also explore other sources of carbon such as a coconut shell or biomass material as electrode materials for the improved electrochemical behavior of the EDLCs. Improve on the morphology and porosity of the pores of the produced carbon material to fully explore the potential of the produced carbon materials for optimum electrochemical performance. Finally, explore the possibility of novel electrolyte to improve the operating voltage window which will also improve the energy density and specific capacitance of the supercapacitor device.

References

[1] F. Béguin, V. Presser, A. Balducci, E. Frackowiak, Carbons and electrolytes for advanced supercapacitors., Adv. Mater. 26 (2014) 2219–2251. doi:10.1002/adma.201304137.

[2] H.I. Becker, low voltage electrolytic capacitor, US 2800616 A, 1957.

[3] R. Kötz, M. Carlen, Principles and applications of electrochemical capacitors, Electrochim. Acta. 45 (2000) 2483–2498. doi:10.1016/S0013-4686(00)00354-6.

[4] D.P. Dubal, O. Ayyad, V. Ruiz, P. Gómez-Romero, Hybrid energy storage: the merging of battery and supercapacitor chemistries., Chem. Soc. Rev. 44 (2015) 1777–1790. doi:10.1039/c4cs00266k.

[5] Y. Zhang, H. Feng, X. Wu, L. Wang, A. Zhang, T. Xia, et al., Progress of electrochemical capacitor electrode materials: A review, Int. J. Hydrogen Energy. 34 (2009) 4889–4899. doi:10.1016/j.ijhydene.2009.04.005.

[6] G. Wang, L. Zhang, J. Zhang, A review of electrode materials for electrochemical supercapacitors, Chem. Soc. Rev. 41 (2012) 797–828. doi:10.1039/c1cs15060j.

[7] M. Galiński, A. Lewandowski, I. Stępniak, Ionic liquids as electrolytes, Electrochim. Acta. 51 (2006) 5567–5580. doi:10.1016/j.electacta.2006.03.016.

[8] H. Wang, Z. Xu, A. Kohandehghan, Z. Li, K. Cui, X. Tan, et al., Interconnected carbon nanosheets derived from hemp for ultrafast supercapacitors with high energy., ACS Nano. 7 (2013) 5131–5141. doi:10.1021/nn400731g.

[9] A. Bello, F. Barzegar, D. Momodu, F. Taghizadeh, M. Fabiane, J. Dangbegnon, et al., Morphological characterization and impedance spectroscopy study of porous 3D carbons based on graphene foam-PVA/phenol-formaldehyde resin composite as an electrode material for supercapacitors, RSC Adv. 4 (2014) 39066–39072. doi:10.1039/C4RA05425C.

[10] K.H. An, Supercapacitors using singlewalled carbon nanotube electrodes, in: AIP Conf. Proc., AIP, 2001: pp. 241–244. doi:10.1063/1.1420099.

[11] X. Lang, A. Hirata, T. Fujita, M. Chen, Nanoporous metal/oxide hybrid electrodes for electrochemical supercapacitors., Nat. Nanotechnol. 6 (2011) 232–236. doi:10.1038/nnano.2011.13.

[12] T. Cottineau, M. Toupin, T. Delahaye, T. Brousse, D. Bélanger, Nanostructured transition metal oxides for aqueous hybrid electrochemical supercapacitors, Appl. Phys. A. 82 (2005) 599–606. doi:10.1007/s00339-005-3401-3.

[13] Y. Liu, B.H. Zhang, S.Y. Xiao, L.L. Liu, Z.B. Wen, Y.P. Wu, A nanocomposite of MoO3 coated with PPy as an anode material for aqueous sodium rechargeable batteries with excellent electrochemical performance, Electrochim. Acta. 116 (2014) 512–517. doi:10.1016/j.electacta.2013.11.077.

[14] M. Beidaghi, C. Wang, Micro-supercapacitors based on three dimensional interdigital polypyrrole/C-MEMS electrodes, Electrochim. Acta. 56 (2011) 9508–9514. doi:10.1016/j.electacta.2011.08.054.

[15] Y.S. Yun, H.H. Park, H.-J. Jin, Pseudocapacitive Effects of N-Doped Carbon Nanotube Electrodes in Supercapacitors, Materials (Basel). 5 (2012) 1258–1266. doi:10.3390/ma5071258.

[16] L. Zhang, F. Zhang, X. Yang, G. Long, Y. Wu, T. Zhang, et al., Porous 3D graphene-based bulk materials with exceptional high surface area and excellent conductivity for supercapacitors, Sci. Rep. 3 (2013) 1408. doi:10.1038/srep01408.

[17] C. Zhang, K.B. Hatzell, M. Boota, B. Dyatkin, M. Beidaghi, D. Long, et al., Highly porous carbon spheres for electrochemical capacitors and capacitive flowable suspension electrodes, Carbon . 77 (2014) 155–164. doi:10.1016/j.carbon.2014.05.017.

[18] P. Simon, Y. Gogotsi, Capacitive energy storage in nanostructured carbon-electrolyte systems, Acc. Chem. Res. 46 (2013) 1094–1103. doi:10.1021/ar200306b.

[19] P. Simon, Y. Gogotsi, Materials for electrochemical capacitors, Nat. Mater. 7 (2008) 845–854. doi:10.1038/nmat2297.

[20] M. a. Lillo-Ródenas, D. Cazorla-Amorós, A. Linares-Solano, Understanding chemical reactions between carbons and NaOH and KOH: An insight into the chemical activation mechanism, Carbon . 41 (2003) 267–275. doi:10.1016/S0008-6223(02)00279-8.

[21] J. Wang, S. Kaskel, KOH activation of carbon-based materials for energy storage, J. Mater. Chem. 22 (2012) 23710–23725. doi:10.1039/c2jm34066f.

[22] A. Bello, F. Barzegar, D. Momodu, J. Dangbegnon, F. Taghizadeh, N. Manyala, Symmetric supercapacitors based on porous 3D interconnected carbon framework, Electrochim. Acta. 151 (2015) 386–392. doi:10.1016/j.electacta.2014.11.051.

[23] A.G. Pandolfo, A.F. Hollenkamp, Carbon properties and their role in supercapacitors, J. Power Sources. 157 (2006) 11–27. doi:10.1016/j.jpowsour.2006.02.065.

[24] C. Bouchelta, M.S. Medjram, O. Bertrand, J.-P. Bellat, Preparation and characterization of activated carbon from date stones by physical activation with steam, J. Anal. Appl. Pyrolysis. 82 (2008) 70–77. doi:10.1016/j.jaap.2007.12.009.

[25] A. Burke, Ultracapacitors: why, how, and where is the technology, J. Power Sources. 91 (2000) 37–50. doi:10.1016/S0378-7753(00)00485-7.

[26] X. Zhang, X. Wang, L. Jiang, H. Wu, C. Wu, J. Su, Effect of aqueous electrolytes on the electrochemical behaviors of supercapacitors based on hierarchically porous carbons, J. Power Sources. 216 (2012) 290–296. doi:10.1016/j.jpowsour.2012.05.090.

[27] B. Wang, Q. Liu, Z. Qian, X. Zhang, J. Wang, Z. Li, et al., Two steps in situ structure fabrication of Ni–Al layered double hydroxide on Ni foam and its electrochemical performance for supercapacitors, J. Power Sources. 246 (2014) 747–753. doi:10.1016/j.jpowsour.2013.08.035.

[28] E. Frackowiak, F. Béguin, Electrochemical storage of energy in carbon nanotubes and nanostructured carbons, Carbon . 40 (2002) 1775–1787. doi:10.1016/S0008-6223(02)00045-3.

[29] V.S. Bagotsky, A.M. Skundin, Y.M. Volfkovich, Electrochemical Power Sources: Batteries, Fuel Cells, and Supercapacitors, Wiley; 1 edition, 2015.

[30] F. Beguin, E. Frackowiak, Carbons for Electrochemical Energy Storage and Conversion Systems, CRC Press, 2010.

[31] M. Kim, I. Oh, J. Kim, Hierarchical porous silicon carbide with controlled micropores and mesopores for electric double layer capacitors, J. Power Sources. 282 (2015) 277–285. doi:10.1016/j.jpowsour.2015.02.040.

[32] M. Winter, R.J. Brodd, What are batteries, fuel cells, and supercapacitors?, Chem. Rev. 104 (2004) 4245–4269. doi:10.1021/cr020730k.

[33] A.G. Kashkooli, S. Farhad, V. Chabot, A. Yu, Z. Chen, Effects of structural design on the performance of electrical double layer capacitors, Appl. Energy. 138 (2015) 631–639. doi:10.1016/j.apenergy.2014.09.033.

[34] H. Helmholtz, Ueber einige Gesetze der Vertheilung elektrischer Ströme in körperlichen Leitern mit Anwendung auf die thierisch-elektrischen Versuche, Ann. Der Phys. Und Chemie. 165 (1853) 211–233. doi:10.1002/andp.18531650603.

[35] H. Helmholtz, Studien über electrische Grenzschichten, Ann. Der Phys. Und Chemie. 243 (1879) 337–382. doi:10.1002/andp.18792430702.

[36] H. Wang, L. Pilon, Mesoscale modeling of electric double layer capacitors with three-dimensional ordered structures, J. Power Sources. 221 (2013) 252–260. doi:10.1016/j.jpowsour.2012.08.002.

[37] J. Kang, J. Wen, S.H. Jayaram, A. Yu, X. Wang, Development of an equivalent circuit model for electrochemical double layer capacitors (EDLCs) with distinct electrolytes, Electrochim. Acta. 115 (2014) 587–598. doi:10.1016/j.electacta.2013.11.002.

[38] V. Augustyn, P. Simon, B. Dunn, Pseudocapacitive oxide materials for high-rate electrochemical energy storage, Energy Environ. Sci. 7 (2014) 1597-1614. doi:10.1039/c3ee44164d.

[39] T. Brousse, D. Belanger, J.W. Long, To Be or Not To Be Pseudocapacitive?, J. Electrochem. Soc. 162 (2015) A5185–A5189. doi:10.1149/2.0201505jes.

[40] B.E. Conway, Electrochemical Supercapacitors: Scientific Fundamentals and Technological Applications, Kluwer Academic/Plenum, New York, 1999.

[41] M.A. Herman, W. Richter, H. Sitter, Epitaxy: Physical Principles and Technical Implementation, Springer Science & Business Media, 2013.

[42] V. Sudha, M. V. Sangaranarayanan, Underpotential Deposition of Metals: Structural and Thermodynamic Considerations, J. Phys. Chem. B. 106 (2002) 2699–2707. doi:10.1021/jp013544b.

[43] A.J. Motheo, E.R. Gonzalez, G. Tremilliosi-Filho, A. Rakotondrainibe, J.-M. Léger, B. Beden, et al., A Study of the Underpotential Deposition of Lead on Gold by UV-Visible Differential Reflectance Spectroscopy, J. Braz. Chem. Soc. 9 (1998) 31–38. doi:10.1590/S0103-50531998000100006.

[44] V. Augustyn, J. Come, M.A. Lowe, J.W. Kim, P.-L. Taberna, S.H. Tolbert, et al., High-rate electrochemical energy storage through Li^+ intercalation pseudocapacitance., Nat. Mater. 12 (2013) 518–22. doi:10.1038/nmat3601.

[45] C.-C. Hu, K.-H. Chang, M.-C. Lin, Y.-T. Wu, Design and tailoring of the nanotubular arrayed architecture of hydrous RuO2 for next generation supercapacitors., Nano Lett. 6 (2006) 2690–2695. doi:10.1021/nl061576a.

[46] H. Zhang, G. Cao, Z. Wang, Y. Yang, Z. Shi, Z. Gu, Growth of manganese oxide nanoflowers on vertically-aligned carbon nanotube arrays for high-rate electrochemical capacitive energy storage., Nano Lett. 8 (2008) 2664–2668. doi:10.1021/nl800925j.

[47] H.B. Li, M.H. Yu, F.X. Wang, P. Liu, Y. Liang, J. Xiao, et al., Amorphous nickel hydroxide nanospheres with ultrahigh capacitance and energy density as electrochemical pseudocapacitor materials., Nat. Commun. 4 (2013) 1894.

doi:10.1038/ncomms2932.

[48] Y. Zhu, C. Cao, S. Tao, W. Chu, Z. Wu, Y. Li, Ultrathin nickel hydroxide and oxide nanosheets: synthesis, characterizations and excellent supercapacitor performances., Sci. Rep. 4 (2014) 5787. doi:10.1038/srep05787.

[49] T. Yan, R. Li, Z. Li, Nickel–cobalt layered double hydroxide ultrathin nanoflakes decorated on graphene sheets with a 3D nanonetwork structure as supercapacitive materials, Mater. Res. Bull. 51 (2014) 97–104. doi:10.1016/j.materresbull.2013.11.044.

[50] R.S.L. Liu, T.-C., Pell W.G., Conway B.E., Behavior of Molybdenum Nitrides as Materials for Electrochemical Capacitors, J. Electrochem. Soc. 145 (1998) 1882-1888. doi:10.1149/1.1838571.

[51] D. Choi, G.E. Blomgren, P.N. Kumta, Fast and Reversible Surface Redox Reaction in Nanocrystalline Vanadium Nitride Supercapacitors, Adv. Mater. 18 (2006) 1178–1182. doi:10.1002/adma.200502471.

[52] T.A. Centeno, F. Stoeckli, The role of textural characteristics and oxygen-containing surface groups in the supercapacitor performances of activated carbons, Electrochim. Acta. 52 (2006) 560–566. doi:10.1016/j.electacta.2006.05.035.

[53] W. Li, D. Chen, Z. Li, Y. Shi, Y. Wan, G. Wang, et al., Nitrogen-containing carbon spheres with very large uniform mesopores: The superior electrode materials for EDLC in organic electrolyte, Carbon 45 (2007) 1757–1763. doi:10.1016/j.carbon.2007.05.004.

[54] L.L. Zhang, X.S. Zhao, Carbon-based materials as supercapacitor electrodes., Chem. Soc. Rev. 38 (2009) 2520–2531. doi:10.1039/b813846j.

[55] H. Wang, M. Yoshio, A.K. Thapa, H. Nakamura, From symmetric AC/AC to asymmetric AC/graphite, a progress in electrochemical capacitors, J. Power Sources. 169 (2007) 375–380. doi:10.1016/j.jpowsour.2007.02.088.

[56] B. Fang, L. Binder, Enhanced surface hydrophobisation for improved performance of carbon aerogel electrochemical capacitor, Electrochim. Acta.

52 (2007) 6916–6921. doi:10.1016/j.electacta.2007.05.004.

[57] H. Wang, M. Yoshio, Graphite, a suitable positive electrode material for high-energy electrochemical capacitors, Electrochem. Commun. 8 (2006) 1481–1486. doi:10.1016/j.elecom.2006.07.016.

[58] S.R.C. Vivekchand, C.S. Rout, K.S. Subrahmanyam, a. Govindaraj, C.N.R. Rao, Graphene-based electrochemical supercapacitors, J. Chem. Sci. 120 (2008) 9–13. doi:10.1007/s12039-008-0002-7.

[59] Y. Wang, Z. Shi, Y. Huang, Y. Ma, C. Wang, M. Chen, et al., Supercapacitor Devices Based on Graphene Materials, J. Phys. Chem. C. 113 (2009) 13103–13107. doi:10.1021/jp902214f.

[60] Y. Honda, T. Haramoto, M. Takeshige, H. Shiozaki, T. Kitamura, M. Ishikawa, Aligned MWCNT Sheet Electrodes Prepared by Transfer Methodology Providing High-Power Capacitor Performance, Electrochem. Solid-State Lett. 10 (2007) A106. doi:10.1149/1.2437665.

[61] B. Xu, F. Wu, S. Chen, C. Zhang, G. Cao, Y. Yang, Activated carbon fiber cloths as electrodes for high performance electric double layer capacitors, Electrochim. Acta. 52 (2007) 4595–4598. doi:10.1016/j.electacta.2007.01.006.

[62] K. Honda, M. Yoshimura, K. Kawakita, A. Fujishima, Y. Sakamoto, K. Yasui, et al., Electrochemical Characterization of Carbon Nanotube/Nanohoneycomb Diamond Composite Electrodes for a Hybrid Anode of Li-Ion Battery and Super Capacitor, J. Electrochem. Soc. 151 (2004) A532. doi:10.1149/1.1649752.

[63] E. Frackowiak, Q. Abbas, F. Béguin, Carbon/carbon supercapacitors, J. Energy Chem. 22 (2013) 226–240. doi:10.1016/S2095-4956(13)60028-5.

[64] D. Mohan, C.U. Pittman, Activated carbons and low cost adsorbents for remediation of tri- and hexavalent chromium from water., J. Hazard. Mater. 137 (2006) 762–811. doi:10.1016/j.jhazmat.2006.06.060.

[65] D. Mohan, C.U. Pittman, Arsenic removal from water/wastewater using adsorbents--A critical review., J. Hazard. Mater. 142 (2007) 1–53. doi:10.1016/j.jhazmat.2007.01.006.

[66] S. Choi, J.H. Drese, C.W. Jones, Adsorbent materials for carbon dioxide capture from large anthropogenic point sources., ChemSusChem. 2 (2009) 796–854. doi:10.1002/cssc.200900036.

[67] F. Rodríguez-reinoso, The role of carbon materials in heterogeneous catalysis, Carbon . 36 (1998) 159–175. doi:10.1016/S0008-6223(97)00173-5.

[68] E. Auer, A. Freund, J. Pietsch, T. Tacke, Carbons as supports for industrial precious metal catalysts, Appl. Catal. A Gen. 173 (1998) 259–271. doi:10.1016/S0926-860X(98)00184-7.

[69] L. Khezami, A. Chetouani, B. Taouk, R. Capart, Production and characterisation of activated carbon from wood components in powder: Cellulose, lignin, xylan, Powder Technol. 157 (2005) 48–56. doi:10.1016/j.powtec.2005.05.009.

[70] M. Jasieńko-Hałat, K. Kędzior, Comparison of molecular sieve properties in microporous chars from low-rank bituminous coal activated by steam and carbon dioxide, Carbon . 43 (2005) 944–953. doi:10.1016/j.carbon.2004.11.024.

[71] K. Yang, J. Peng, C. Srinivasakannan, L. Zhang, H. Xia, X. Duan, Preparation of high surface area activated carbon from coconut shells using microwave heating., Bioresour. Technol. 101 (2010) 6163–6169. doi:10.1016/j.biortech.2010.03.001.

[72] J. Laine, S. Yunes, Effect of the preparation method on the pore size distribution of activated carbon from coconut shell, Carbon . 30 (1992) 601–604. doi:10.1016/0008-6223(92)90178-Y.

[73] C. Peng, X. Yan, R. Wang, J. Lang, Y. Ou, Q. Xue, Promising activated carbons derived from waste tea-leaves and their application in high performance supercapacitors electrodes, Electrochim. Acta. 87 (2013) 401–408. doi:10.1016/j.electacta.2012.09.082.

[74] S. Zhao, C.-Y. Wang, M.-M. Chen, J. Wang, Z.-Q. Shi, Potato starch-based activated carbon spheres as electrode material for electrochemical capacitor, J.

Phys. Chem. Solids. 70 (2009) 1256–1260. doi:10.1016/j.jpcs.2009.07.004.

[75] W. Chen, H. Zhang, Y. Huang, W. Wang, A fish scale based hierarchical lamellar porous carbon material obtained using a natural template for high performance electrochemical capacitors, J. Mater. Chem. 20 (2010) 4773-4775. doi:10.1039/c0jm00382d.

[76] T.E. Rufford, D. Hulicova-Jurcakova, Z. Zhu, G.Q. Lu, Nanoporous carbon electrode from waste coffee beans for high performance supercapacitors, Electrochem. Commun. 10 (2008) 1594–1597. doi:10.1016/j.elecom.2008.08.022.

[77] J. Rouquerol, F. Rouquerol, P. Llewellyn, G. Maurin, K.S.W. Sing, Adsorption by Powders and Porous Solids: Principles, Methodology and Applications, Academic Press, 2013.

[78] R.E. Franklin, Crystallite Growth in Graphitizing and Non-Graphitizing Carbons, Proc. R. Soc. A Math. Phys. Eng. Sci. 209 (1951) 196–218. doi:10.1098/rspa.1951.0197.

[79] Drinking Water and Health, Volume 2, National Academies, 1977.

[80] P.J.F. Harris, Z. Liu, K. Suenaga, Imaging the atomic structure of activated carbon, J. Phys. Condens. Matter. 20 (2008) 362201. doi:10.1088/0953-8984/20/36/362201.

[81] M. Sánchez-Polo, J. Rivera-Utrilla, Adsorbent-adsorbate interactions in the adsorption of Cd(II) and Hg(II) on ozonized activated carbons., Environ. Sci. Technol. 36 (2002) 3850–4.

[82] P. Somasundaran, Encyclopedia of Surface and Colloid Science, Volume 7, CRC Press, 2006.

[83] H.S. Nalwa, ed., Handbook of Surfaces and Interfaces of Materials, Five-Volume Set, Academic Press, 2001.

[84] S. Barany, ed., Role of Interfaces in Environmental Protection, Springer

Science & Business Media, 2012.

[85] S. Biniak, M. Pakuła, G.S. Szymański, A. Świątkowski, Effect of Activated Carbon Surface Oxygen- and/or Nitrogen-Containing Groups on Adsorption of Copper(II) Ions from Aqueous Solution †, Langmuir. 15 (1999) 6117–6122. doi:10.1021/la9815704.

[86] Z.Q.-F. LI Na, ZHU Jian, Quantitative and Qualitative Analyses of Oxygen-containing Surface Functional Groups on Activated Carbon, Chem. J. Chinese Univ. 33 (2012) 548–554. doi:10.3969/j.issn.0251-0790.2012.03.022.

[87] R.C. Bansal, M. Goyal, Activated Carbon Adsorption, CRC Press, 2005.

[88] Chemistry & Physics of Carbon, CRC Press, 2000.

[89] G. Meurant, Applications in Industry, Elsevier, 1998.

[90] New Carbon Based Materials for Electrochemical Energy Storage Systems: Batteries, Supercapacitors and Fuel Cells, Springer Science & Business Media, 2006.

[91] P. Simon, Y. Gogotsi, Charge storage mechanism in nanoporous carbons and its consequence for electrical double layer capacitors., Philos. Trans. A. Math. Phys. Eng. Sci. 368 (2010) 3457–67. doi:10.1098/rsta.2010.0109.

[92] K.S. Novoselov, a K. Geim, S. V Morozov, D. Jiang, Y. Zhang, S. V Dubonos, et al., Electric field effect in atomically thin carbon films., Science. 306 (2004) 666–669. doi:10.1126/science.1102896.

[93] a K. Geim, K.S. Novoselov, The rise of graphene., Nat. Mater. 6 (2007) 183–191. doi:10.1038/nmat1849.

[94] A. Yasmin, J.-J. Luo, I.M. Daniel, Processing of expanded graphite reinforced polymer nanocomposites, Compos. Sci. Technol. 66 (2006) 1182–1189. doi:10.1016/j.compscitech.2005.10.014.

[95] E. Duplock, M. Scheffler, P. Lindan, Hallmark of Perfect Graphene, Phys. Rev.

Lett. 92 (2004) 225502. doi:10.1103/PhysRevLett.92.225502.

[96] K. Novoselov, A. Geim, S. Morozov, Two-dimensional gas of massless Dirac fermions in graphene, Nature. 438 (2005) 197-200. doi:10.1038/nature04233

[97] X. Wang, L. Zhi, K. Müllen, Transparent, conductive graphene electrodes for dye-sensitized solar cells, Nano Lett. 8 (2008) 323–327. doi:10.1021/nl072838r

[98] T. Yumura, K. Kimura, H. Kobayashi, R. Tanaka, N. Okumura, T. Yamabe, The use of nanometer-sized hydrographene species for support material for fuel cell electrode catalysts: a theoretical proposal, Phys. Chem. Chem. Phys. 11 (2009) 8275-8284. doi:10.1039/b905866d.

[99] W.H. Jr, R. Offeman, Preparation of graphitic oxide, J. Am. Chem. Soc. 80 (1958) 1339–1339. doi:10.1021/ja01539a017

[100] F. Bonaccorso, A. Lombardo, T. Hasan, Z. Sun, L. Colombo, A.C. Ferrari, Production and processing of graphene and 2d crystals, Mater. Today. 15 (2012) 564–589. doi:10.1016/S1369-7021(13)70014-2.

[101] P.L. Chiu, D.D.T. Mastrogiovanni, D. Wei, C. Louis, M. Jeong, G. Yu, et al., Microwave- and nitronium ion-enabled rapid and direct production of highly conductive low-oxygen graphene., J. Am. Chem. Soc. 134 (2012) 5850–5856. doi:10.1021/ja210725p.

[102] C.N.R. Rao, K.S. Subrahmanyam, H.S.S. Ramakrishna Matte, B. Abdulhakeem, A. Govindaraj, B. Das, et al., A study of the synthetic methods and properties of graphenes, Sci. Technol. Adv. Mater. 11 (2010) 054502. doi:10.1088/1468-6996/11/5/054502.

[103] Y. Zhu, S. Murali, W. Cai, X. Li, J.W. Suk, J.R. Potts, et al., Graphene and graphene oxide: Synthesis, properties, and applications, Adv. Mater. 22 (2010) 3906–3924. doi:10.1002/adma.201001068.

[104] D. Wei, Y. Liu, Y. Wang, H. Zhang, L. Huang, G. Yu, Synthesis of N-doped graphene by chemical vapor deposition and its electrical properties., Nano Lett. 9 (2009) 1752–1758. doi:10.1021/nl803279t.

[105] P. A. Basnayaka, M. K. Ram, L. Stefanakos, A. Kumar, Graphene/Polypyrrole Nanocomposite as Electrochemical Supercapacitor Electrode: Electrochemical Impedance Studies, Graphene. 02 (2013) 81–87. doi:10.4236/graphene.2013.22012.

[106] X. Li, Z. Wang, Y. Qiu, Q. Pan, P. Hu, 3D graphene/ZnO nanorods composite networks as supercapacitor electrodes, J. Alloys Compd. 620 (2015) 31–37. doi:10.1016/j.jallcom.2014.09.105.

[107] L. Huang, B. Wu, G. Yu, Y. Liu, Graphene: learning from carbon nanotubes, J. Mater. Chem. 21 (2011) 919–929. doi:10.1039/c0jm02225j.

[108] R. Saito, G. Dresselhaus, M.S. Dresselhaus, Physical Properties of Carbon Nanotubes, Imperial College Press, 1998.

[109] J.L. Hutchison, N.A. Kiselev, E.P. Krinichnaya, A.V. Krestinin, R.O. Loutfy, A.P. Morawsky, et al., Double-walled carbon nanotubes fabricated by a hydrogen arc discharge method, Carbon . 39 (2001) 761–770. doi:10.1016/S0008-6223(00)00187-1.

[110] C.D. Scott, S. Arepalli, P. Nikolaev, R.E. Smalley, Growth mechanisms for single-wall carbon nanotubes in a laser-ablation process, Appl. Phys. A Mater. Sci. Process. 72 (2001) 573–580. doi:10.1007/s003390100761.

[111] M.J. Bronikowski, P.A. Willis, D.T. Colbert, K.A. Smith, R.E. Smalley, Gas-phase production of carbon single-walled nanotubes from carbon monoxide via the HiPco process: A parametric study, J. Vac. Sci. Technol. A Vacuum, Surfaces, Film. 19 (2001) 1800. doi:10.1116/1.1380721.

[112] J. Kong, A.M. Cassell, H. Dai, Chemical vapor deposition of methane for single-walled carbon nanotubes, Chem. Phys. Lett. 292 (1998) 567–574. doi:10.1016/S0009-2614(98)00745-3.

[113] O. Guellati, I. Janowska, D. Bégin, M. Guerioune, Z. Mekhalif, J. Delhalle, et al., Influence of ethanol in the presence of H2 on the catalytic growth of vertically aligned carbon nanotubes, Appl. Catal. A Gen. 423-424 (2012) 7–14. doi:10.1016/j.apcata.2012.02.036.

[114] J.-F. Colomer, C. Stephan, S. Lefrant, G. Van Tendeloo, I. Willems, Z. Kónya, et al., Large-scale synthesis of single-wall carbon nanotubes by catalytic chemical vapor deposition (CCVD) method, Chem. Phys. Lett. 317 (2000) 83–89. doi:10.1016/S0009-2614(99)01338-X.

[115] A. Pandey, R.S. Chouhan, Y. Gurbuz, J.H. Niazi, A. Qureshi, S. cerevisiae whole-cell based capacitive biochip for the detection of toxicity of different forms of carbon nanotubes, Sensors Actuators B Chem. 218 (2015) 253–260. doi:10.1016/j.snb.2015.05.008.

[116] D.N. Futaba, K. Hata, T. Yamada, T. Hiraoka, Y. Hayamizu, Y. Kakudate, et al., Shape-engineerable and highly densely packed single-walled carbon nanotubes and their application as super-capacitor electrodes., Nat. Mater. 5 (2006) 987–94. doi:10.1038/nmat1782.

[117] B. Zhang, J. Liang, C.. Xu, B.. Wei, D.. Ruan, D.. Wu, Electric double-layer capacitors using carbon nanotube electrodes and organic electrolyte, Mater. Lett. 51 (2001) 539–542. doi:10.1016/S0167-577X(01)00352-4.

[118] W. Lu, R. Hartman, L. Qu, L. Dai, Nanocomposite Electrodes for High-Performance Supercapacitors, J. Phys. Chem. Lett. 2 (2011) 655–660. doi:10.1021/jz200104n.

[119] M. Toupin, T. Brousse, D. Bélanger, Charge Storage Mechanism of MnO 2 Electrode Used in Aqueous Electrochemical Capacitor, Chem. Mater. 16 (2004) 3184–3190. doi:10.1021/cm049649j.

[120] N. Nagarajan, H. Humadi, I. Zhitomirsky, Cathodic electrodeposition of MnOx films for electrochemical supercapacitors, Electrochim. Acta. 51 (2006) 3039–3045. doi:10.1016/j.electacta.2005.08.042.

[121] A. Bello, O.O. Fashedemi, J.N. Lekitima, M. Fabiane, D. Dodoo-Arhin, K.I. Ozoemena, et al., High-performance symmetric electrochemical capacitor based on graphene foam and nanostructured manganese oxide, AIP Adv. 3 (2013) 082118. doi:10.1063/1.4819270.

[122] H. Wang, H.S. Casalongue, Y. Liang, H. Dai, Ni(OH)2 nanoplates grown on graphene as advanced electrochemical pseudocapacitor materials., J. Am. Chem. Soc. 132 (2010) 7472–7477. doi:10.1021/ja102267j.

[123] V. Srinivasan, An Electrochemical Route for Making Porous Nickel Oxide Electrochemical Capacitors, J. Electrochem. Soc. 144 (1997) L210. doi:10.1149/1.1837859.

[124] M.-S. Wu, H.-H. Hsieh, Nickel oxide/hydroxide nanoplatelets synthesized by chemical precipitation for electrochemical capacitors, Electrochim. Acta. 53 (2008) 3427–3435. doi:10.1016/j.electacta.2007.12.005.

[125] A. Bello, K. Makgopa, M. Fabiane, D. Dodoo-Ahrin, K.I. Ozoemena, N. Manyala, Chemical adsorption of NiO nanostructures on nickel foam-graphene for supercapacitor applications, J. Mater. Sci. 48 (2013) 6707–6712. doi:10.1007/s10853-013-7471-x.

[126] T. Liu, W.G. Pell, B.E. Conway, Self-discharge and potential recovery phenomena at thermally and electrochemically prepared RuO2 supercapacitor electrodes, Electrochim. Acta. 42 (1997) 3541–3552. doi:10.1016/S0013-4686(97)81190-5.

[127] Y.R. Ahn, M.Y. Song, S.M. Jo, C.R. Park, D.Y. Kim, Electrochemical capacitors based on electrodeposited ruthenium oxide on nanofibre substrates, Nanotechnology. 17 (2006) 2865–2869. doi:10.1088/0957-4484/17/12/007.

[128] T.-S. Hyun, J.-E. Kang, H.-G. Kim, J.-M. Hong, I.-D. Kim, Electrochemical Properties of MnO_x–RuO_2 Nanofiber Mats Synthesized by Co-Electrospinning, Electrochem. Solid-State Lett. 12 (2009) A225-A228. doi:10.1149/1.3224899.

[129] J.-K. Chang, C.-M. Wu, I.-W. Sun, Nano-architectured $Co(OH)^2$ electrodes constructed using an easily-manipulated electrochemical protocol for high-performance energy storage applications, J. Mater. Chem. 20 (2010) 3729–3735. doi:10.1039/b925176f.

[130] X. Xia, J. Tu, Y. Mai, X. Wang, C. Gu, X. Zhao, Self-supported hydrothermal synthesized hollow Co3O4 nanowire arrays with high supercapacitor capacitance, J. Mater. Chem. 21 (2011) 9319-9325. doi:10.1039/c1jm10946d.

[131] S.K. Meher, G.R. Rao, Ultralayered Co3O4 for High-Performance Supercapacitor Applications, J. Phys. Chem. C. 115 (2011) 15646–15654.

doi:10.1021/jp201200e.

[132] Y. Gao, S. Chen, D. Cao, G. Wang, J. Yin, Electrochemical capacitance of Co3O4 nanowire arrays supported on nickel foam, J. Power Sources. 195 (2010) 1757–1760. doi:10.1016/j.jpowsour.2009.09.048.

[133] N. Miura, S. Oonishi, K. Rajendra Prasad, Indium Tin Oxide/Carbon Composite Electrode Material for Electrochemical Supercapacitors, Electrochem. Solid-State Lett. 7 (2004) A247-A249. doi:10.1149/1.1763773.

[134] D.L. da Silva, R.G. Delatorre, G. Pattanaik, G. Zangari, W. Figueiredo, R.-P. Blum, et al., Electrochemical Synthesis of Vanadium Oxide Nanofibers, J. Electrochem. Soc. 155 (2008) E14-E17. doi:10.1149/1.2804856.

[135] C.-M. Huang, C.-C. Hu, K.-H. Chang, J.-M. Li, Y.-F. Li, Pseudocapacitive Characteristics of Vanadium Oxide Deposits with a Three-Dimensional Porous Structure, J. Electrochem. Soc. 156 (2009) A667-A671. doi:10.1149/1.3138703.

[136] L.S. Aravinda, U. Bhat, B. Ramachandra Bhat, Binder free MoO3/multiwalled carbon nanotube thin film electrode for high energy density supercapacitors, Electrochim. Acta. 112 (2013) 663–669. doi:10.1016/j.electacta.2013.08.114.

[137] B. Mendoza-Sánchez, T. Brousse, C. Ramirez-Castro, V. Nicolosi, P. S. Grant, An investigation of nanostructured thin film α-MoO3 based supercapacitor electrodes in an aqueous electrolyte, Electrochim. Acta. 91 (2013) 253–260. doi:10.1016/j.electacta.2012.11.127.

[138] H. Peng, G. Ma, J. Mu, K. Sun, Z. Lei, Low-cost and high energy density asymmetric supercapacitors based on polyaniline nanotubes and MoO3 nanobelts, J. Mater. Chem. A. 2 (2014) 10384–10388. doi:10.1039/c4ta01899k.

[139] W. Tang, L. Liu, S. Tian, L. Li, Y. Yue, Y. Wu, et al., Aqueous supercapacitors of high energy density based on MoO3 nanoplates as anode material., Chem. Commun. (Camb). 47 (2011) 10058–10060. doi:10.1039/c1cc13474d.

[140] T. Wang, J. Li, G. Zhao, Synthesis of MoS2 and MoO3 hierarchical

nanostructures using a single-source molecular precursor, Powder Technol. 253 (2014) 347–351. doi:10.1016/j.powtec.2013.12.005.

[141] G.A. Snook, P. Kao, A.S. Best, Conducting-polymer-based supercapacitor devices and electrodes, J. Power Sources. 196 (2011) 1–12. doi:10.1016/j.jpowsour.2010.06.084.

[142] Y. Zhou, H. Xu, N. Lachman, M. Ghaffari, S. Wu, Y. Liu, et al., Advanced asymmetric supercapacitor based on conducting polymer and aligned carbon nanotubes with controlled nanomorphology, Nano Energy. 9 (2014) 176–185. doi:10.1016/j.nanoen.2014.07.007.

[143] M.E. Roberts, D.R. Wheeler, B.B. McKenzie, B.C. Bunker, High specific capacitance conducting polymer supercapacitor electrodes based on poly(tris(thiophenylphenyl)amine), J. Mater. Chem. 19 (2009) 6977-6979. doi:10.1039/b916666a.

[144] H.J. Ahonen, J. Lukkari, J. Kankare, n- and p-Doped Poly(3,4-ethylenedioxythiophene): Two Electronically Conducting States of the Polymer, Macromolecules. 33 (2000) 6787–6793. doi:10.1021/ma0004312.

[145] J. Hu, Adaptive and Functional Polymers, Textiles and Their Applications, World Scientific, 2010.

[146] M. Halper, J. Ellenbogen, Supercapacitors : A Brief Overview, Virginia, USA, 2006.

[147] K.S. Ryu, K.M. Kim, N.G. Park, Y.J. Park, S.H. Chang, Symmetric redox supercapacitor with conducting polyaniline electrodes, J. Power Sources. 103 (2002) 305–309. doi:10.1016/S0378-7753(01)00862-X.

[148] G.P. Nanofiber, Q. Wu, Y. Xu, Z. Yao, A. Liu, G. Shi, Supercapacitors Based on Flexible, ACS Nano. 4 (2010) 1963–1970. doi:10.1021/nn1000035.

[149] Clemente, A, Solid-state, polymer-based, redox capacitors, Solid State Ionics. 85 (1996) 273–277. doi:10.1016/0167-2738(96)00070-7.

[150] C. Arbizzani, M. Mastragostino, L. Meneghello, Polymer-based redox supercapacitors: A comparative study, Electrochim. Acta. 41 (1996) 21–26. doi:10.1016/0013-4686(95)00289-Q.

[151] J. Zhang, X.S. Zhao, Conducting Polymers Directly Coated on Reduced Graphene Oxide Sheets as High-Performance Supercapacitor Electrodes, J. Phys. Chem. C. 116 (2012) 5420–5426. doi:10.1021/jp211474e.

[152] H. An, Y. Wang, X. Wang, L. Zheng, X. Wang, L. Yi, et al., Polypyrrole/carbon aerogel composite materials for supercapacitor, J. Power Sources. 195 (2010) 6964–6969. doi:10.1016/j.jpowsour.2010.04.074.

[153] P. Pieta, I. Obraztsov, F. D'Souza, W. Kutner, Composites of Conducting Polymers and Various Carbon Nanostructures for Electrochemical Supercapacitors, ECS J. Solid State Sci. Technol. 2 (2013) M3120–M3134. doi:10.1149/2.015310jss.

[154] J. Wang, Y. Xu, X. Chen, X. Sun, Capacitance properties of single wall carbon nanotube/polypyrrole composite films, Compos. Sci. Technol. 67 (2007) 2981–2985. doi:10.1016/j.compscitech.2007.05.015.

[155] V. Khomenko, E. Frackowiak, F. Béguin, Determination of the specific capacitance of conducting polymer/nanotubes composite electrodes using different cell configurations, Electrochim. Acta. 50 (2005) 2499–2506. doi:10.1016/j.electacta.2004.10.078.

[156] L.L. Zhang, T. Wei, W. Wang, X.S. Zhao, Manganese oxide–carbon composite as supercapacitor electrode materials, Microporous Mesoporous Mater. 123 (2009) 260–267. doi:10.1016/j.micromeso.2009.04.008.

[157] Y.M. Shulga, S.A. Baskakov, V.V. Abalyaeva, O.N. Efimov, N.Y. Shulga, A. Michtchenko, et al., Composite material for supercapacitors formed by polymerization of aniline in the presence of graphene oxide nanosheets, J. Power Sources. 224 (2013) 195–201. doi:10.1016/j.jpowsour.2012.09.105.

[158] W. Liu, X. Yan, J. Lang, J. Pu, Q. Xue, Supercapacitors based on graphene nanosheets using different non-aqueous electrolytes, New J. Chem. 37 (2013) 2186-2195. doi:10.1039/c3nj00335c.

[159] G. Xiong, A. Kundu, T.S. Fisher, Thermal Effects in Supercapacitors, Springer, 2015.

[160] Z. Salameh, Renewable Energy System Design, Academic Press, 2014.

[161] V.V.N. Obreja, Supercapacitors specialities - Materials review, in: 1st Int. Freib. Conf. Electrochem. Storage Mater., 2014: pp. 98–120. doi:10.1063/1.4878482.

[162] V. Khomenko, E. Raymundo-Piñero, E. Frackowiak, F. Béguin, High-voltage asymmetric supercapacitors operating in aqueous electrolyte, Appl. Phys. A Mater. Sci. Process. 82 (2006) 567–573. doi:10.1007/s00339-005-3397-8.

[163] Y. Wang, W. Yang, S. Zhang, D.G. Evans, X. Duan, Synthesis and Electrochemical Characterization of Co–Al Layered Double Hydroxides, J. Electrochem. Soc. 152 (2005) A2130-A2137. doi:10.1149/1.2041107.

[164] V. Ruiz, C. Blanco, E. Raymundo-Piñero, V. Khomenko, F. Béguin, R. Santamaría, Effects of thermal treatment of activated carbon on the electrochemical behaviour in supercapacitors, Electrochim. Acta. 52 (2007) 4969–4973. doi:10.1016/j.electacta.2007.01.071.

[165] C. Zhao, W. Zheng, A Review for Aqueous Electrochemical Supercapacitors, Front. Energy Res. 3 (2015) Article 23. doi:10.3389/fenrg.2015.00023.

[166] H. OHNO, K. FUKUMOTO, Progress in Ionic Liquids for Electrochemical Reaction Matrices, Electrochemistry. 76 (2008) 16–23. doi:10.5796/electrochemistry.76.16.

[167] A. Balducci, R. Dugas, P.L. Taberna, P. Simon, D. Plée, M. Mastragostino, et al., High temperature carbon–carbon supercapacitor using ionic liquid as electrolyte, J. Power Sources. 165 (2007) 922–927. doi:10.1016/j.jpowsour.2006.12.048.

[168] H. Ohno, ed., Electrochemical Aspects of Ionic Liquids, John Wiley & Sons, 2011.

[169] R. Lin, P.-L. Taberna, S. Fantini, V. Presser, C.R. Pérez, F. Malbosc, et al.,

Capacitive Energy Storage from −50 to 100 °C Using an Ionic Liquid Electrolyte, J. Phys. Chem. Lett. 2 (2011) 2396–2401. doi:10.1021/jz201065t.

[170] J.F. Wishart, Energy applications of ionic liquids, Energy Environ. Sci. 2 (2009) 956-961. doi:10.1039/b906273d.

[171] G. Lakshminarayana, M. Nogami, Inorganic–organic hybrid membranes with anhydrous proton conduction prepared from tetramethoxysilane/methyl-trimethoxysilane/trimethylphosphate and 1-ethyl-3-methylimidazolium-bis (trifluoromethanesulfonyl) imide for H2/O2 fuel cells , Electrochim. Acta. 55 (2010) 1160–1168. doi:10.1016/j.electacta.2009.10.020

[172] A. Lewandowski, A. Olejniczak, M. Galinski, I. Stepniak, Performance of carbon--carbon supercapacitors based on organic, aqueous and ionic liquid electrolytes, J. Power Sources. 195 (2010) 5814–5819. doi:10.1016/j.jpowsour.2010.03.082

[173] F. Béguin, E. Frąckowiak, Supercapacitors: Materials, Systems and Applications, John Wiley & Sons, 2013.

[174] S. Shivakumara, B. Kishore, T.R. Penki, N. Munichandraiah, Symmetric supercapacitor based on partially exfoliated and reduced graphite oxide in neutral aqueous electrolyte, Solid State Commun. 199 (2014) 26–32. doi:10.1016/j.ssc.2014.08.014.

[175] R.P. Deshpande, ULTRACAPACITORS, McGraw Hill Education, 2014.

[176] J.P. Zheng, The Limitations of Energy Density of Battery/Double-Layer Capacitor Asymmetric Cells, J. Electrochem. Soc. 150 (2003) A484-A492. doi:10.1149/1.1559067.

[177] W. Zhang, C. Ma, J. Fang, J. Cheng, X. Zhang, S. Dong, et al., Asymmetric electrochemical capacitors with high energy and power density based on graphene/CoAl-LDH and activated carbon electrodes, RSC Adv. 3 (2013) 2483–2490. doi:10.1039/c2ra23283a.

[178] L. Demarconnay, E. Raymundo-Piñero, F. Béguin, Adjustment of electrodes potential window in an asymmetric carbon/MnO2 supercapacitor, J. Power

Sources. 196 (2011) 580–586. doi:10.1016/j.jpowsour.2010.06.013.

[179] C. Wall, Z. Zhao-Karger, M. Fichtner, Corrosion Resistance of Current Collector Materials in Bisamide Based Electrolyte for Magnesium Batteries, ECS Electrochem. Lett. 4 (2014) C8–C10. doi:10.1149/2.0111501eel.

[180] Allen J. Bard, L.R. Faulkner, Electrochemical Methods: Fundamentals and Applications, 2nd Editio, Wiley Online Library, New York, 2001.

[181] X.-Z. Yuan, C. Song, H. Wang, J. Zhang, Electrochemical Impedance Spectroscopy in PEM Fuel Cells, Springer London, London, 2010.

[182] M. Arulepp, L. Permann, J. Leis, A. Perkson, K. Rumma, A. Jänes, et al., Influence of the solvent properties on the characteristics of a double layer capacitor, J. Power Sources. 133 (2004) 320–328. doi:10.1016/j.jpowsour.2004.03.026.

[183] P.L. Taberna, P. Simon, J.-F.F. Fauvarque, Electrochemical Characteristics and Impedance Spectroscopy Studies of Carbon-Carbon Supercapacitors, J. Electrochem. Soc. 150 (2003) A292–A300. doi:10.1149/1.1543948.

[184] M.E. Orazem, B. Tribollet, Electrochemical Impedance Spectroscopy, John Wiley & Sons, 2011.

[185] Polymer Electrolyte Fuel Cells: Science, Applications, and Challenges, CRC Press, 2013.

[186] X.-Z.R. Yuan, C. Song, H. Wang, J. Zhang, Electrochemical Impedance Spectroscopy in PEM Fuel Cells: Fundamentals and Applications, Springer Science & Business Media, 2009.

[187] J. Bisquert, G. Garcia-Belmonte, P. Bueno, E. Longo, L.O.. Bulhões, Impedance of constant phase element (CPE)-blocked diffusion in film electrodes, J. Electroanal. Chem. 452 (1998) 229–234. doi:10.1016/S0022-0728(98)00115-6.

[188] Impedance Spectroscopy: Theory, Experiment, and Applications, John Wiley &

Sons, 2005.

[189] L. Cui, J. Li, X.-G. Zhang, Preparation and properties of Co3O4 nanorods as supercapacitor material, J. Appl. Electrochem. 39 (2009) 1871–1876. doi:10.1007/s10800-009-9891-5.

[190] W. Sun, R. Zheng, X. Chen, Symmetric redox supercapacitor based on micro-fabrication with three-dimensional polypyrrole electrodes, J. Power Sources. 195 (2010) 7120–7125. doi:10.1016/j.jpowsour.2010.05.012.

[191] A. Jorio, G. Dresselhaus, M. Dresselhaus, Carbon nanotubes: advanced topics in the synthesis, structure, properties and applications, 2008.

[192] N. Yahya, Carbon and Oxide Nanostructures: Synthesis, Characterisation and Applications. Springer Science & Business Media, 2011.

[193] G.B. Stringfellow, Organometallic Vapor-Phase Epitaxy: Theory and Practice, Second Edi, Academic Press, 1999.

[194] A. Guermoune, T. Chari, F. Popescu, S.S. Sabri, J. Guillemette, H.S. Skulason, et al., Chemical vapor deposition synthesis of graphene on copper with methanol, ethanol, and propanol precursors, Carbon . 49 (2011) 4204–4210. doi:10.1016/j.carbon.2011.05.054.

[195] Y. Zhang, L. Zhang, C. Zhou, Review of Chemical Vapor Deposition of Graphene and Related Applications, Acc. Chem. Res. (2013).

[196] Z. Chen, W. Ren, L. Gao, B. Liu, S. Pei, H.-M. Cheng, Three-dimensional flexible and conductive interconnected graphene networks grown by chemical vapour deposition., Nat. Mater. 10 (2011) 424–428. doi:10.1038/nmat3001.

[197] X. Li, W. Cai, L. Colombo, R.S. Ruoff, Evolution of Graphene Growth on Ni and Cu by Carbon Isotope Labeling, 12 (2009).

[198] A. Umair, H. Raza, Controlled synthesis of bilayer graphene on nickel, Nanoscale Res. Lett. 7 (2012) 437. doi:10.1186/1556-276X-7-437.

[199] Q. Yu, J. Lian, S. Siriponglert, H. Li, Y.P. Chen, S.S. Pei, Graphene segregated on Ni surfaces and transferred to insulators, Appl. Phys. Lett. 93 (2008) 113103. doi:10.1063/1.2982585.

[200] A. Reina, S. Thiele, X. Jia, S. Bhaviripudi, M.S. Dresselhaus, J. a. Schaefer, et al., Growth of large-area single- and Bi-layer graphene by controlled carbon precipitation on polycrystalline Ni surfaces, 2 (2009) 509-516. doi:10.1007/s12274-009-9059-y.

[201] X. Li, C.W. Magnuson, A. Venugopal, J. An, J.W. Suk, B. Han, et al., Graphene films with large domain size by a two-step chemical vapor deposition process, Nano Lett. 10 (2010) 4328–4334. doi:10.1021/nl101629g.

[202] A. Bello, M. Fabiane, D. Dodoo-Arhin, K.I. Ozoemena, N. Manyala, Silver nanoparticles decorated on a three-dimensional graphene scaffold for electrochemical applications, J. Phys. Chem. Solids. 75 (2014) 109–114. doi:10.1016/j.jpcs.2013.09.006.

[203] A. Kopp Alves, C.P. Bergmann, F.A. Berutti, Novel Synthesis and Characterization of Nanostructured Materials, Springer Berlin Heidelberg, Berlin, Heidelberg, 2013.

[204] M. Yoshimura, K. Byrappa, Hydrothermal processing of materials: past, present and future, J. Mater. Sci. 43 (2007) 2085–2103. doi:10.1007/s10853-007-1853-x.

[205] W. Yang, Z. Gao, J. Wang, J. Ma, M. Zhang, L. Liu, Solvothermal one-step synthesis of Ni-Al layered double hydroxide/carbon nanotube/reduced graphene oxide sheet ternary nanocomposite with ultrahigh capacitance for supercapacitors., ACS Appl. Mater. Interfaces. 5 (2013) 5443–5454. doi:10.1021/am4003843

[206] Y. Song, J. Wang, Z. Li, D. Guan, T. Mann, Q. Liu, et al., Self-assembled hierarchical porous layered double hydroxides by solvothermal method and their application for capacitors, Microporous Mesoporous Mater. 148 (2012) 159–165. doi:10.1016/j.micromeso.2011.08.013.

[207] Y. Zhao, F. Xiao, Q. Jiao, Hydrothermal Synthesis of Ni/Al Layered Double Hydroxide Nanorods, J. Nanotechnol. 2011 (2011) 646409.

doi:10.1155/2011/646409.

[208] Z. Gao, J. Wang, Z. Li, W. Yang, B. Wang, Graphene nanosheet/Ni2+/Al3+ layered double-hydroxide composite as a novel electrode for a supercapacitor, Chem. Mater. 23 (2011) 3509–3516. doi:10.1021/cm200975x

[209] Y. Tao, L. Ruiyi, L. Zaijun, L. Junkang, W. Guangli, G. Zhiquo, A free template strategy for the fabrication of nickel/cobalt double hydroxide microspheres with tunable nanostructure and morphology for high performance supercapacitors, RSC Adv. 3 (2013) 19416-19422. doi:10.1039/C3RA42806K

[210] M. Baghbanzadeh, L. Carbone, P.D. Cozzoli, C.O. Kappe, Microwave-Assisted Synthesis of Colloidal Inorganic Nanocrystals, Angew. Chemie Int. Ed. 50 (2011) 11312–11359. doi:10.1002/anie.201101274

[211] C.O. Kappe, Microwave dielectric heating in synthetic organic chemistry, Chem. Soc. Rev. 37 (2008) 1127–1139. doi:10.1039/B803001b

[212] A.S. Wajid, S. Das, F. Irin, H.S.T. Ahmed, J.L. Shelburne, D. Parviz, et al., Polymer-stabilized graphene dispersions at high concentrations in organic solvents for composite production, Carbon . 50 (2012) 526–534. doi:10.1016/j.carbon.2011.09.008.

[213] Y. Zhu, S. Murali, M.D. Stoller, K.J. Ganesh, W. Cai, P.J. Ferreira, et al., Carbon-based supercapacitors produced by activation of graphene, Science. 332 (2011) 1537–1541. doi:10.1126/science.1200770.

[214] J.I. Goldstein, D.E. Newbury, P. Echlin, D.C. Joy, C.E. Lyman, E. Lifshin, et al., Scanning Electron Microscopy and X-ray Microanalysis, 3rd ed., Springer US, Boston, MA, 2003.

[215] R. Egerton, Physical Principles of Electron Microscopy - An Introduction to TEM, SEM, and AEM, 1st Ed., Springer, 2005.

[216] D.B. Williams, C.B. Carter, Transmission Electron Microscopy, Springer US, Boston, MA, 2009.

[217] L.K. Wang, Y.-T. Hung, N.K. Shammas, eds., Physicochemical Treatment Processes, Springer Science & Business Media, 2007.

[218] A. Loiseau, P. Launois-Bernede, P. Petit, S. Roche, J.-P. Salvetat, eds., Understanding Carbon Nanotubes: From Basics to Applications, Springer Berlin Heidelberg, 2006.

[219] S. Brunauer, L.S. Deming, W.E. Deming, E. Teller, On a Theory of the van der Waals Adsorption of Gases, J. Am. Chem. Soc. 62 (1940) 1723–1732. doi:10.1021/ja01864a025.

[220] K.S.W. Sing, Reporting physisorption data for gas/solid systems with special reference to the determination of surface area and porosity (Recommendations 1984), Pure Appl. Chem. 57 (1982) 2201–2218. doi:10.1351/pac198557040603.

[221] S.J. Gregg, K.S.W. Sing, Adsorption, surface area, and porosity, Second, Academic Press, 1982.

[222] C. Sangwichien, G.. Aranovich, M.. Donohue, Density functional theory predictions of adsorption isotherms with hysteresis loops, Colloids Surfaces A Physicochem. Eng. Asp. 206 (2002) 313–320. doi:10.1016/S0927-7757(02)00048-1.

[223] D. Gardiner, P. Graves, H. Bowley, Practical Raman Spectroscopy, Springer-Verlag Berlin Heidelberg, 1989.

[224] Self-Healing Phenomena in Cement-Based Materials: State-of-the-Art Report of RILEM Technical Committee 221-SHC: Self-Healing Phenomena in Cement-Based Materials, Springer Science & Business Media, 2013.

[225] L.G. Cançado, K. Takai, T. Enoki, M. Endo, Y.A. Kim, H. Mizusaki, et al., General equation for the determination of the crystallite size L[sub a] of nanographite by Raman spectroscopy, Appl. Phys. Lett. 88 (2006) 163106. doi:10.1063/1.2196057.

[226] A. Jorio, C.A. Achete, E.H.M. Ferreira, L.G. Cançado, R.B. Capaz, Measuring disorder in graphene with Raman spectroscopy, INTECH Open Access

Publisher, 2011.

[227] M.A. Pimenta, G. Dresselhaus, M.S. Dresselhaus, L.G. Cançado, A. Jorio, R. Saito, Studying disorder in graphite-based systems by Raman spectroscopy., Phys. Chem. Chem. Phys. 9 (2007) 1276–1291. doi:10.1039/b613962k.

[228] C. Casiraghi, A. Hartschuh, H. Qian, S. Piscanec, C. Georgi, A. Fasoli, et al., Raman spectroscopy of graphene edges., Nano Lett. 9 (2009) 1433–1441. doi:10.1021/nl8032697.

[229] B.D. Cullity, S.R. Stock, Elements Of X Ray Diffraction, 3rd ed., Upper Saddle River, NJ : Prentice Hall, New Jersey, 2001.

[230] Charl Jeremy Jafta, Synthetic strategies to improve the performance of manganese oxide based layered and spinel materials for electrochemical energy storage, University of Pretoria, 2014.

[231] F.P. Miller, A.F. Vandome, J. McBrewster, Bragg's Law, Alphascript Publishing, 2010.

[232] Q. Cong, X. Yu, L. He, eds., Multifunctional Two- and Three-Dimensional Polycrystalline X-Ray Diffractometry, Bentham Science, Saif Zone Sharjah, U.A.E., 2011.

[233] N. Rajeswari, S. Selvasekarapandian, S. Karthikeyan, C. Sanjeeviraja, Y. Iwai, J. Kawamura, Structural, vibrational, thermal, and electrical properties of PVA/PVP biodegradable polymer blend electrolyte with CH_3COONH_4, Ionics (Kiel). 19 (2013) 1105–1113. doi:10.1007/s11581-012-0838-1.

[234] A.K. Swain, D. Bahadur, Enhanced Stability of Reduced Graphene Oxide Colloid Using Cross-Linking Polymers, J. Phys. Chem. C. 118 (2014) 9450–9457. doi:10.1021/jp500205n.

[235] D.J.T. Hill, A.K. Whittaker, Water diffusion into radiation crosslinked PVA–PVP network hydrogels, Radiat. Phys. Chem. 80 (2011) 213–218. doi:10.1016/j.radphyschem.2010.07.035.

[236] R. Meena, R. Lehnen, B. Saake, Microwave-assisted synthesis of kC/Xylan/PVP-based blend hydrogel materials: physicochemical and rheological studies, Cellulose. 21 (2013) 553–568. doi:10.1007/s10570-013-0155-5.

[237] X. Ge, F. Tian, Z. Wu, Y. Yan, G. Cravotto, Z. Wu, Adsorption of naphthalene from aqueous solution on coal-based activated carbon modified by microwave induction: Microwave power effects, Chem. Eng. Process. Process Intensif. 91 (2015) 67–77. doi:10.1016/j.cep.2015.03.019.

[238] B. Acevedo, C. Barriocanal, I. Lupul, G. Gryglewicz, Properties and performance of mesoporous activated carbons from scrap tyres, bituminous wastes and coal, Fuel. 151 (2015) 83–90. doi:10.1016/j.fuel.2015.01.010.

[239] I.I. Salame, T.J. Bandosz, Surface Chemistry of Activated Carbons: Combining the Results of Temperature-Programmed Desorption, Boehm, and Potentiometric Titrations., J. Colloid Interface Sci. 240 (2001) 252–258. doi:10.1006/jcis.2001.7596.

[240] S. Park, C. Liang, D. Sheng, N. Dudney, D. DePaoli, Mesoporous Carbon Materials as Electrodes for Electrochemical Double-Layer Capacitor, MRS Proc. 973 (2006) 903 – 916. doi:10.1557/PROC-0973-BB07-04.

[241] J. Yan, Q. Wang, T. Wei, Z. Fan, Recent Advances in Design and Fabrication of Electrochemical Supercapacitors with High Energy Densities, Adv. Energy Mater. 4 (2014) 1300816. doi:10.1002/aenm.201300816.

[242] W.W. ROBBINS, T.E. WEIER, C.R. STOCKING, Botany:An Introduction to Plant Science, Soil Sci. 84 (1957).

[243] A.E. Ofomaja, E.B. Naidoo, Biosorption of copper from aqueous solution by chemically activated pine cone: A kinetic study, Chem. Eng. J. 175 (2011) 260–270. doi:10.1016/j.cej.2011.09.103.

[244] G. V Nunell, M.E. Fernandez, P.R. Bonelli, A.L. Cukierman, Nitrate uptake improvement by modified activated carbons developed from two species of pine cones., J. Colloid Interface Sci. 440 (2015) 102–108. doi:10.1016/j.jcis.2014.10.058.

[245] M. Momčilović, M. Purenović, A. Bojić, A. Zarubica, M. Ranđelović, Removal of lead(II) ions from aqueous solutions by adsorption onto pine cone activated carbon, Desalination. 276 (2011) 53–59. doi:10.1016/j.desal.2011.03.013.

[246] M. Liu, L. Gan, W. Xiong, Z. Xu, D. Zhu, L. Chen, Development of MnO2/porous carbon microspheres with a partially graphitic structure for high performance supercapacitor electrodes, J. Mater. Chem. A. 2 (2014) 2555. doi:10.1039/c3ta14445c.

[247] G. Ren, X. Pan, S. Bayne, Z. Fan, Kilohertz ultrafast electrochemical supercapacitors based on perpendicularly-oriented graphene grown inside of nickel foam, Carbon . 71 (2014) 94–101. doi:10.1016/j.carbon.2014.01.017.

[248] M. Zhi, F. Yang, F. Meng, M. Li, A. Manivannan, N. Wu, Effects of Pore Structure on Performance of An Activated-Carbon Supercapacitor Electrode Recycled from Scrap Waste Tires, ACS Sustain. Chem. Eng. 2 (2014) 1592–1598. doi:10.1021/sc500336h.

[249] P. Hapiot, C. Lagrost, Electrochemical reactivity in room-temperature ionic liquids, Chem. Rev. 108 (2008) 2238–2264. http://pubs.acs.org/doi/pdf/10.1021/cr0680686 (accessed March 19, 2015).

[250] Q.T. Qu, B. Wang, L.C. Yang, Y. Shi, S. Tian, Y.P. Wu, Study on electrochemical performance of activated carbon in aqueous Li2SO4, Na2SO4 and K2SO4 electrolytes, Electrochem. Commun. 10 (2008) 1652–1655. doi:10.1016/j.elecom.2008.08.020.

[251] G.P. Pandey, A.C. Rastogi, Solid-State Supercapacitors Based on Pulse Polymerized Poly(3,4-ethylenedioxythiophene) Electrodes and Ionic Liquid Gel Polymer Electrolyte, J. Electrochem. Soc. 159 (2012) A1664–A1671. doi:10.1149/2.047210jes.

[252] H. Yu, J. Wu, L. Fan, K. Xu, X. Zhong, Y. Lin, et al., Improvement of the performance for quasi-solid-state supercapacitor by using PVA–KOH–KI polymer gel electrolyte, Electrochim. Acta. 56 (2011) 6881–6886. doi:10.1016/j.electacta.2011.06.039.

[253] C. Ramasamy, J. Palma del vel, M. Anderson, An activated carbon supercapacitor analysis by using a gel electrolyte of sodium salt-polyethylene

oxide in an organic mixture solvent, J. Solid State Electrochem. 18 (2014) 2217–2223. doi:10.1007/s10008-014-2466-3.

[254] P. Sivaraman, A. Thakur, R.K. Kushwaha, D. Ratna, A.B. Samui, Poly(3-methyl thiophene)-Activated Carbon Hybrid Supercapacitor Based on Gel Polymer Electrolyte, Electrochem. Solid-State Lett. 9 (2006) A435–A437. doi:10.1149/1.2213357.

[255] P. Yang, W. Cui, L. Li, L. Liu, M. An, Characterization and properties of ternary P(VdF-HFP)-LiTFSI-EMITFSI ionic liquid polymer electrolytes, Solid State Sci. 14 (2012) 598–606. doi:10.1016/j.solidstatesciences.2012.02.005.

[256] J.W. Long, D. Bélanger, T. Brousse, W. Sugimoto, M.B. Sassin, O. Crosnier, Asymmetric electrochemical capacitors—Stretching the limits of aqueous electrolytes, MRS Bull. 36 (2011) 513–522. doi:10.1557/mrs.2011.137.

[257] K. Naoi, S. Ishimoto, J. Miyamoto, W. Naoi, Second generation “nanohybrid supercapacitor”: Evolution of capacitive energy storage devices, Energy Environ. Sci. 5 (2012) 9363–73. doi:10.1039/c2ee21675b.

[258] Y. Zhai, Y. Dou, D. Zhao, P.F. Fulvio, R.T. Mayes, S. Dai, Carbon materials for chemical capacitive energy storage., Adv. Mater. 23 (2011) 4828–4850. doi:10.1002/adma.201100984.

[259] N.W. Duffy, W. Baldsing, A.G. Pandolfo, The nickel–carbon asymmetric supercapacitor—Performance, energy density and electrode mass ratios, Electrochim. Acta. 54 (2008) 535–539. doi:10.1016/j.electacta.2008.07.047.

[260] F. Béguin, K. Kierzek, M. Friebe, A. Jankowska, J. Machnikowski, K. Jurewicz, et al., Effect of various porous nanotextures on the reversible electrochemical sorption of hydrogen in activated carbons, Electrochim. Acta. 51 (2006) 2161–2167. doi:10.1016/j.electacta.2005.03.086.

[261] Z. Algharaibeh, X. Liu, P.G. Pickup, An asymmetric anthraquinone-modified carbon/ruthenium oxide supercapacitor, J. Power Sources. 187 (2009) 640–643. doi:10.1016/j.jpowsour.2008.11.012.

[262] V. Khomenko, E. Raymundo-Piñero, F. Béguin, Optimisation of an asymmetric

manganese oxide/activated carbon capacitor working at 2V in aqueous medium, J. Power Sources. 153 (2006) 183–190. doi:10.1016/j.jpowsour.2005.03.210.

[263] H. Jiang, C. Li, T. Sun, J. Ma, A green and high energy density asymmetric supercapacitor based on ultrathin MnO2 nanostructures and functional mesoporous carbon nanotube electrodes., Nanoscale. 4 (2012) 807–812. doi:10.1039/c1nr11542a.

[264] Y. Cheng, S. Lu, H. Zhang, C. V Varanasi, J. Liu, Synergistic effects from graphene and carbon nanotubes enable flexible and robust electrodes for high-performance supercapacitors., Nano Lett. 12 (2012) 4206–4211. doi:10.1021/nl301804c.

[265] X. Liu, R. Ma, Y. Bando, T. Sasaki, A general strategy to layered transition-metal hydroxide nanocones: tuning the composition for high electrochemical performance., Adv. Mater. 24 (2012) 2148–2153. doi:10.1002/adma.201104753.